
Theses and Dissertations

Summer 2016

Developing property and kinetic control strategies for radiation polymerization

Sage Marie Schissel
University of Iowa

Follow this and additional works at: <https://ir.uiowa.edu/etd>

 Part of the [Chemical Engineering Commons](#)

Copyright © 2016 Sage Marie Schissel

This dissertation is available at Iowa Research Online: <https://ir.uiowa.edu/etd/7027>

Recommended Citation

Schissel, Sage Marie. "Developing property and kinetic control strategies for radiation polymerization." PhD (Doctor of Philosophy) thesis, University of Iowa, 2016.
<https://doi.org/10.17077/etd.3417-0aqt>

Follow this and additional works at: <https://ir.uiowa.edu/etd>

 Part of the [Chemical Engineering Commons](#)

DEVELOPING PROPERTY AND KINETIC CONTROL STRATEGIES FOR
RADIATION POLYMERIZATION

by

Sage Marie Schissel

A thesis submitted in partial fulfillment
of the requirements for the Doctor of Philosophy
degree in Chemical and Biochemical Engineering in the
Graduate College of
The University of Iowa

August 2016

Thesis Supervisor: Associate Professor Julie L.P. Jessop

Copyright by
SAGE MARIE SCHISSEL
2016
All Rights Reserved

Graduate College
The University of Iowa
Iowa City, Iowa

CERTIFICATE OF APPROVAL

PH.D. THESIS

This is to certify that the Ph.D. thesis of

Sage Marie Schissel

has been approved by the Examining Committee for
the thesis requirement for the Doctor of Philosophy degree
in Chemical and Biochemical Engineering at the August 2016 graduation.

Thesis Committee:

Julie L.P. Jessop, Thesis Supervisor

Jennifer Fiegel

M. Lei Geng

C. Allan Guymon

Stephen C. Lapin

To Mom, Dad, and Garrett

Science does not know its debt to imagination.

Ralph Waldo Emerson
Poetry and Imagination, 1872

ACKNOWLEDGEMENTS

First and foremost, I would like to thank my adviser, Dr. Julie L. P. Jessop, without whom this work would not have been possible. She has supported me fully throughout this journey, always providing encouragement and guidance. No question was ever too foolish. No idea was ever too ridiculous. I will certainly miss our conversations, both about research and good books. She taught me how to be a better student and a better teacher. For all of those things, I am grateful.

Thank you to my committee members: Drs. Fiegel, Geng, Guymon, and Lapin. Their wisdom has helped shape my thoughts and ideas and is peppered throughout this thesis. I'd especially like to thank Dr. Guymon, who sat me down one summer and told me a Ph.D. in chemical engineering was the only path to take.

Thank you to the heart of the department, past and present: Jacquie Albrecht, Katie Schnedler, Wendy Meyers, Natalie Potter, and Linda Wheatley. Their kindness and wisdom has helped me navigate the intricacies of graduate school, and many a deadline has been met because of them.

Thank you to my fellow graduate students: Sara Kaalberg, Nicole Kloepfer, Jon Scholte, Amir Farnoud, Joel Coffel, Erica Ricker, Todd Thorson, Brian Dillman, Kristan Worthington, Clint Cook, Brad Forney, and others. They have passed along their knowledge, provided a sounding board for new ideas, helped me with experiments, and were always up for a good conversation.

Thank you to my undergraduate students: Katie Classon, Lu Liu, Shiqin He, Mackenzie Cole, Bobby Tempel, and Elliot Glenn. They were an immense help with experiments and always brightened the lab with laughter.

Finally, I would like to thank my friends, my grandparents, and most especially, my parents. Their love and support has truly carried me through my time at the University of Iowa. They never doubted me, even when I doubted myself. They have listened to endless hours of ranting about broken instruments and failed experiments. They have celebrated with me small triumphs and big successes. They have been my proofreader, my wiring expert, but most importantly, they have been my rock. I cannot thank you enough.

ABSTRACT

Radiation polymerization is a rapid, sustainable process, requiring no environmentally damaging solvents and less energy than thermal polymerization methods. This process is used extensively each year to produce millions of tons of films, coatings, inks, and adhesives. In this work, kinetic- and property-control strategies were developed for three underdeveloped areas of radiation polymerization: free-radical electron beam (EB) polymerization, free-radical/cationic hybrid photopolymerization, and cationic shadow cure.

Raman spectroscopy, an analytical technique for studying photopolymerization kinetics, was established as a method of determining the conversion of EB-initiated polymer films. This technique, in conjunction with dynamic mechanical analysis (DMA), was used to investigate the impact of chemical structure on the magnitude of EB dose rate effects (DREs). A strong correlation was determined between the DRE magnitude and monomer size, which may be attributed to chain transfer opportunities. A preliminary predictive relationship was developed to estimate the magnitude of the DRE using the property shift caused by changes in dose, enabling scale-up of process variables for polymers prone to dose rate effects. In addition, a protocol was developed to produce films with equivalent energy deposition for both EB and photopolymerizations, allowing the effect of the initiating radiation to be studied. Distinct kinetic and physical property differences were shown in the resulting EB- and photo-initiated films, despite equivalent initiation energies and energy rates. Monomer chemistry was determined to be an important factor in the magnitude of these differences.

In order to control the phase separation that can occur in free-radical/cationic hybrid systems, the cationic activated monomer (AM) mechanism was promoted through a hydroxyl group located on the (meth)acrylate, covalently bonding the (meth)acrylate and epoxide networks. The impact of the AM mechanism on the reaction kinetics and physical properties was studied using real-time Raman spectroscopy and DMA to compare a hydroxyl-containing acrylate and methacrylate to non-hydroxyl-containing controls. The promotion of the AM mechanism improved epoxide conversion and network homogeneity. The affect on the (meth)acrylate kinetics correlated to the propagation rate of the neat (meth)acrylate. It was also demonstrated that the glass

transition temperature of the hybrid system could be controlled by varying the ratio of (meth)acrylate to epoxide.

Cationic shadow cure, which offers a means of circumventing the light penetration limitations in photopolymerization, was modeled using a central composite design. This model was shown to be predictive of both shadow cure length and gel fraction while varying effective irradiance, exposure time, exposure area, and sample depth. Moreover, the model helped ascertain the impact of each variable and its interactions: shadow cure length was most influenced by sample depth, but the gel fraction was reliant on the other three variables. Active center mobility was also qualitatively tracked, and it was established that the section of solid polymer formed during illumination was restricting the movement of the active centers, preventing complete cure. Through this discovery, a new method of shadow cure was developed, termed transferable shadow cure (TSC). This new method separates the initiation and propagation mechanisms, and, as the name suggests, allows for the active-center-containing monomer to be transferred to areas unreachable by light before solidifying. Conversion of the TSC, as determined via Raman spectroscopy, was also modeled using a central composite design. The model predicts TSC conversion is equally dependent on effective irradiance, sample depth, and exposure time, but independent of exposure area.

Through the development of control strategies in these three areas, this work provides a better fundamental understanding of radiation polymerization, as well as guidelines that aid in product design and technology expansion.

PUBLIC ABSTRACT

Radiation polymerization is a rapid, sustainable process, requiring no environmentally damaging solvents and less energy than traditional, heat-initiated polymerization methods. This process is used extensively each year to produce millions of tons of polymer (sometimes referred to as plastic) films, coatings, inks, and adhesives. Here, strategies were developed to better control the chemical reactions and physical properties of three underdeveloped areas of radiation polymerization: free-radical electron-beam (EB) polymerization, free-radical/cationic hybrid photopolymerization, and cationic shadow cure.

In the area of free-radical electron-beam polymerization, a preliminary relationship was built between the chemical structure of the starting materials, the processing conditions, and the final properties of the polymer produced. This relationship will help predict effects caused by changes in the reaction rate.

In hybrid photopolymerization, light is used to initiate two reactions, a free-radical reaction and a cationic reaction. This work demonstrated that the two polymers could be chemically bonded through placement of a hydroxyl group on the free-radical starting material. The hydroxyl group promotes a second cationic reaction, which improves the reaction speed and polymer properties.

In cationic shadow cure, control of the reaction was established using physical cues and common processing variables. Additionally, a new method of shadow cure was developed that allows for activated starting material to be transferred and modifiers to be added before solidifying into a polymer.

Through the development of these three areas, this work provides a better fundamental understanding of radiation polymerization, as well as guidelines that aid in product design and technology expansion.

TABLE OF CONTENTS

LIST OF TABLES	xii
LIST OF FIGURES	xiv
LIST OF ABBREVIATIONS.....	xxiii
General Abbreviations.....	xxiii
Unit Abbreviations	xxv
CHAPTER 1	
INTRODUCTION AND BACKGROUND	1
1.1 Radiation Polymerization.....	1
1.1.1 Radiation Kinetics	4
1.1.2 Energy Deposition	13
1.1.3 Exposure vs. Dose	15
1.1.4 Exposure Rate and Dose Rate	16
1.2 Polymerization Systems	18
1.2.1 Free-Radical Polymerization	18
1.2.2 Cationic Polymerization	22
1.2.3 Hybrid Polymerization	29
1.3 Analytical Methods	34
1.3.1 Raman Spectroscopy	34
1.3.2 Dynamic Mechanical Analysis.....	39
1.4 References	43
CHAPTER 2	
OBJECTIVES	49
CHAPTER 3	
INTERNAL REFERENCE PEAK VALIDATION FOR EB-CURED POLYMER CONVERSIONS MEASURED VIA RAMAN SPECTROSCOPY	52
3.1 Introduction	52
3.2 Experimental	53
3.2.1 Materials	53
3.2.2 Methods	54
3.3 Results and Discussion.....	57
3.3.1 Reference Peak Stability.....	57
3.3.2 Peak Stability Comparison in UV and EB.....	62
3.4 Conclusions	64
3.5 References	66
CHAPTER 4	
DOSE RATE EFFECTS IN ELECTRON-BEAM INITIATED POLYMERIZATION: THE EFFECTS OF MONOMER CHEMISTRY	67
4.1 Introduction	67
4.2 Experimental	68

4.2.1 Materials	68
4.2.2 Methods	69
4.3 Results and Discussion.....	73
4.3.1 Influence of Dose on Dose Rate Effects.....	73
4.3.2 Influence of Monomer Structure on Dose Rate Effects	80
4.3.3 Predicting Dose-Rate-Effect Magnitude	86
4.4 Conclusions	89
4.5 References	91
CHAPTER 5	
EQUIVALENT INITIATION ENERGY COMPARISON OF PHOTO- AND ELECTRON-BEAM-INITIATED POLYMERIZATION: KINETIC AND PHYSICAL PROPERTIES	
93	
5.1 Introduction	93
5.2 Experimental	95
5.2.1 Materials	95
5.2.2 Methods	96
5.3 Results and Discussion.....	104
5.3.1 Conversion Studies and Energy Rate Effects	104
5.3.2 Physical Property Studies	115
5.4 Conclusions	119
5.5 References	121
CHAPTER 6	
EPOXIDE-(METH)ACRYLATE HYBRID PHOTOPOLYMERIZATIONS WITH HYDROXYL-CONTAINING (METH)ACRYLATES: ENHANCED KINETICS AND PHYSICAL PROPERTY TUNING	
123	
6.1 Introduction	123
6.2 Experimental	125
6.2.1 Materials	125
6.2.2 Methods	126
6.3 Results and Discussion.....	128
6.3.1 Free-radical Photopolymerization of Epoxy-Acrylate Hybrid Formulations	129
6.3.2 Cationic Ring-Opening Photopolymerization of Epoxy-Acrylate Hybrid Formulations	131
6.3.3 Free-Radical Photopolymerizations of Epoxy-Methacrylate Hybrid Formulations	135
6.3.4 Cationic Photopolymerizations of Epoxy-Methacrylate Hybrid Formulations	138
6.3.5 Impact of Viscosity on Hybrid Kinetics	141
6.3.6. Physical Properties of Epoxide-Acrylate Hybrid Photopolymers	146
6.4 Conclusions	149
6.5 References	151

CHAPTER 7	
CONTROLLING CATIONIC SHADOW CURE USING PHYSICAL CUES AND PROCESSING VARIABLES.....	154
7.1 Introduction	154
7.2 Experimental	155
7.2.1 Materials	155
7.2.2 Methods	156
7.3 Results and Discussion.....	161
7.3.1 Active Center Mobility.....	161
7.3.2 Complex Geometries	166
7.3.3 Crack and Crevice Molds	168
7.3.4 Central Composite Design (CCD).....	171
7.4 Conclusions	181
7.5 References	183
CHAPTER 8	
TRANSFERABLE SHADOW CURE: A NEW APPROACH TO ACHIEVING CATIONIC PHOTOPOLYMERIZATION IN LIGHT-RESTRICTED AREAS	184
8.1 Introduction	184
8.2 Experimental	185
8.2.1 Materials	185
8.2.2 Methods	186
8.3 Results and Discussion.....	194
8.3.1 Kinetic Characterization.....	195
8.3.2 Physical Property Characterization	197
8.3.3 TSC in Complex Geometries with Pigments, and Fillers.....	202
8.3.4 Central Composite Design 1.....	205
8.3.5 Central Composite Design 2.....	212
8.4 Conclusions	219
8.5 References	221
CHAPTER 9	
CONCLUSIONS AND RECOMMENDATIONS	222
9.1 Conclusions	222
9.2 Recommendations	227
9.2.1 Electron-beam Polymerization	227
9.2.2 Hybrid Polymerization	230
9.2.3 Cationic Shadow Cure	230
9.3 References	233
APPENDIX A	
SUPPLEMENTAL INFORMATION FOR CHAPTER 5	234
A.1 Dose Equivalents for Photo-initiated Films	234

APPENDIX B	
SUPPLEMENTAL INFORMATION FOR CHAPTER 6	240
B.1 Formulation Information	240
B.2 Hybrid Kinetics.....	241
B.3 Viscosity Studies	241
B.4 Hybrid Physical Properties	243
APPENDIX C	
SUPPLEMENTAL INFORMATION FOR CHAPTER 7	244
C.1 Light Interactions with PDMS.....	244
C.2 Preliminary Work – Hexagonal Design.....	244
C.3 Central Composite Design.....	248
C.4 CCD Models	249
C.4.1 ANOVA of the Shadow Cure Length Response.....	249
C.4.2 ANOVA of the Gel Fraction Response	251
C.5 Model Accuracy	253
C.6 Factor Math.....	255
APPENDIX D	
SUPPLEMENTAL INFORMATION FOR CHAPTER 8	257
D.1 Shadow Cure Kinetics	257
D.2 CCD Models.....	258
D.2.1 ANOVA for CCD1, Avg Conversion.....	258
D.2.2 ANOVA for CCD1, LCS wt%	260
D.2.3 ANOVA for CCD2, Average Conversion.....	262
D.2.4 ANOVA for CCD2, Average Conversion 13 wks Post-Illumination.....	264
D.2.5 ANOVA for CCD2, LCS wt%	266
D.3 Model Accuracy	268
APPENDIX E	
RAMAN HOW-TO AND TROUBLESHOOTING GUIDE	273
E.1 Raman How-To Guide.....	273
E.2 Raman Troubleshooting Guide.....	275
E.3 Procedures.....	280

LIST OF TABLES

Table 1-1. EB requires significantly less energy to dry/cure coatings compared to solvent-based and water-based systems. Adapted from Reference 3.....	3
Table 4-1. Acrylate conversion (%) for five monomer/oligomer formulations at three different doses and line speeds. Conversion was measured using Raman spectroscopy and calculated using Equation 4-2. Conversion increases with increasing dose (at a constant line speed), but decreases with increasing line speed (at a constant dose).....	74
Table 4-2. Glass transition temperature (T_g , °C) of the EB-cured films for five monomer/oligomer formulations at three different doses and line speeds. T_g was measured using DMA. T_g increases with increasing dose (at a constant line speed), but decreases with increasing line speed (at a constant dose).....	78
Table 4-3. Component viscosities of the five monomers were measured experimentally at 25°C, while the viscosity of the oligomer was reported by the manufacturer. Formulation viscosities were calculated using the Refutas equation (Equation 4-3) assuming a 50/50, by weight, mixture of monomer and oligomer.....	81
Table 4-4. The maximum R_p value and the reaction time at which it occurred for the six components and five monomer/oligomer formulations. R_p values were calculated using the conversion vs. time profiles (Figures 4-6 and 4-7). Decreasing DRE magnitude (PA > HPOPA) correlates with increasing monomer and formulation R_p values, with the exception of the HPOPA formulation.	84
Table 5-1. Effective irradiances needed, at three exposure times, to equal the initiation energies of 15, 30, and 60 kGy for the PA formulation. The irradiances were estimated using Equation 5-3 and the Kenning <i>et al.</i> model.....	102
Table 5-2. Average values of EB-initiated acrylate conversion (%) for five monomer/oligomer formulations at three different doses and line speeds. Conversion increases with increasing dose (at a constant line speed), but decreases at increasing line speed (at a constant dose).	105
Table 5-3. Average values of photo-initiated acrylate conversion (%) for five monomer/oligomer formulations at three equivalent doses and three different exposure times. Conversion increases with increasing energy (at a constant exposure time), but decreases with decreasing exposure time (at a constant dose).	106
Table 5-4. Example energy rates for the EB- and photo-cured (Set 1) exposure times, assuming 10 J of energy delivered.	109

Table 5-5. Average values of photo-initiated acrylate conversion (%) for five monomer/oligomer formulations at three equivalent doses and three different exposure times. Conversion increases with increasing energy (at a constant exposure time), but decreases with decreasing exposure time (at a constant dose).	110
Table 7-1. The different geometries of mold wells used and their dimensions (in mm).....	157
Table 7-2. Coded factor levels for the four factors used in the central composite design.....	160
Table 7-3. Conversion (%), measured by Raman spectroscopy, of the remaining liquid resin from three locations after 48 hrs, 72 hrs, and 2 wks of shadow cure. Only the conversion of the liquid resin in the cavity beneath the light-cured section (LCS) increases.	165
Table 7-4. Model accuracy of the CCD was verified using ten checkpoints external to the model. The model accurately predicts gel fraction, but is only moderately accurate in predicting shadow cure length. Standard deviation of the shadow cure length response is 2.24. Standard deviation of the gel fraction response is 0.03.	180
Table 8-1. Factor levels for the four factors used in the first central composite design (CCD 1).	192
Table 8-2. Factor levels for the four factors used in the second central composite design (CCD 2).....	194
Table 8-3. Model accuracy of CCD 1 was verified using 10 checkpoints external to the model. The model accurately predicts conversion, but is only moderately accurate in predicting LCS wt%. Standard deviation of the conversion response is 0.015. Standard deviation of the LCS wt% response is 3.21wt%.	217
Table 8-4. Model accuracy of CCD 2 was verified using 10 checkpoints external to the mode. The model accurately predicts conversion, but does not accurately predict LCS wt%. Standard deviation of the conversion response is 0.049. Standard deviation of the LCS wt% response is 3.5wt%.	218
Table 8-5. Model accuracy of CCD 2 was verified using 10 checkpoints external to the mode. The model predicts conversion 13 weeks post-illumination with moderate accuracy. Standard deviation of the conversion (13 week post-illumination) response is 0.031.....	219

LIST OF FIGURES

Figure 1-1. Electron beam radiation in comparison to the electromagnetic radiation spectrum. Wavelength is measured in meters. Adapted from Reference 2.....	1
Figure 1-2. Chain polymerization of a reactive C=C bond.....	5
Figure 1-3. Monofunctional monomers for linear polymers (A) and multifunctional monomers form cross-linked or branched networks (B).....	9
Figure 1-4. Cross-linking (A) and chain scission (B) of polymer chains by electron beam radiation. Adapted from Reference 18.....	10
Figure 1-5. A comparison of the energy deposition of UV light (A) and electron beam (B) at an increasing energy and different voltages, respectively. The units of depth of penetration (B, x-axis) become micrometers if the film density is equal to 1 g/cm^3	14
Figure 1-6. Free-radical polymerization of a (meth)acrylate.....	20
Figure 1-7. α -cleavage of DMPA to produce propagating free radicals.....	21
Figure 1-8. H-abstraction from MDEA by benzophenone to produce a propagating free radical.....	21
Figure 1-9. The X and Y groups on a benzoyl chromophore affect the wavelength range and efficiency of the photoinitiator.	22
Figure 1-10. Over time, long-lived cationic active centers can diffuse into unilluminated areas and propagate. Polymer created in these unilluminated areas is called shadow cure.....	23
Figure 1-11. The cationic active chain end (ACE) propagation mechanism. Adapted from Reference 48.	24
Figure 1-12. The cationic activated monomer (AM) propagation mechanism. This mechanism is promoting in the presence of hydroxyl groups. Adapted from Reference 48.....	24
Figure 1-13. The architecture of the polymer network is influenced by whether the ACE mechanism (A) or the AM mechanism dominates (B). Adapted from Reference 51.....	25
Figure 1-14. Examples of monomers that photopolymerize via the cationic mechanism. Adapted from Reference 52.	26
Figure 1-15. General structures of diaryliodonium (A) and triarylsulfonium salts (B)....	27
Figure 1-16. Photoactivation of a diaryliodonium hexafluoroantimonate photoacid generator (DAI).	28
Figure 1-17. Two proposed mechanisms of EB-initiated cationic polymerization.	29

Figure 1-18. In an interpenetrating network (IPN), Polymer A (dashed line) is mechanically entangled to Polymer B (solid line), but each polymer is only covalently bonded (circles) to itself. In a semi-IPN (A), Polymer A is linear and Polymer B is cross-linked, and in a full-IPN (B), both polymers are cross-linked. Adapted from Reference 62.....	31
Figure 1-19. A laser scanning confocal microscopy image of phase separation	32
Figure 1-20. In a grafted network, Polymer A (dashed line) is covalently bonded (circles) to Polymer B (solid line). In a semi-grafted network (A), Polymer A is linear and Polymer B is cross-linked, and in a full-grafted network (B), both polymers are cross-linked. Adapted from Reference 62.	33
Figure 1-21. A hybrid resin can consist of a single hybrid monomer containing two different functional groups (A) or a solution of two or more monomers with different functional groups (B).....	34
Figure 1-22. Raman spectroscopy relies on the inelastic scattering of photons by either Stokes or anti-Stokes scattering.	35
Figure 1-23. Example of a Raman spectrum of 2-hydroxy-3-phenoxypropyl acrylate....	37
Figure 1-24. An example of the disappearance of the –C=C– acrylate bond, represented by the 1640 cm ⁻¹ peak (arrow), during photopolymerization.	38
Figure 1-25. Schematic illustrating confocal Raman microscopy, adapted from Reference 72. The beam splitter is angled 45° to the incident laser beam. Only the laser scattered at the focal plane (red, solid line) reaches the detector.....	39
Figure 1-26. A DMA graph illustrating how the loss modulus (green), storage modulus (blue) and tan δ (red) change with temperature. The temperature at which the maximum of the tan δ peak occurs is taken as the glass transition temperature (T _g). Below the T _g , the polymer is in the glassy region, and above the T _g the polymer is in the rubbery region.	41
Figure 3-1. Chemical structures of acrylate monomers used in this study: (A) TMPTA and (B) BADGEDA.....	53
Figure 3-2. Real-time Raman spectra for photopolymerization of TMPTA. A reaction peak of 1636 cm ⁻¹ and a reference peak of 1070 cm ⁻¹ were identified.....	55
Figure 3-3. Depth profile of an EB-cured sample of TMPTA. Conversion was expected to be constant as a function of depth, but instead increases with sample depth.	57
Figure 3-4. A comparison of the standard deviation of the Raman peak intensity ratios: (A) $I_{1636}:I_{1070}$ for UV-cured and EB-cured TMPTA coatings and (B) $I_{1636}:I_{1613}$ for UV-cured and EB-cured TMPTA/BADGEDA coatings. The small and equal standard deviations for the TMPTA/BADGEDA coatings suggest the reference peak I_{1613} is stable under EB radiation.....	58

Figure 3-5. Raman confocal depth profile of a silicon wafer. The sample surface occurs at the maximum peak intensity of the characteristic silicon peak (520 cm^{-1}).....	59
Figure 3-6. A comparison of UV and EB-cured Raman confocal depth profiles of the 1613 cm^{-1} peak intensity for the TMPTA/BADGEDA formulation. The UV and EB samples reach a maximum peak intensity within $2\text{ }\mu\text{m}$ of each other, suggesting the 1613 cm^{-1} peak is stable under EB radiation. Depth values refer to microscope stage movement, not actual sample depth.....	60
Figure 3-7. A comparison of UV and EB-cured Raman confocal depth profiles of the 1070 cm^{-1} peak intensity for the TMPTA formulation. The UV and EB samples reach a maximum peak intensity at very different depths, suggesting the 1070 cm^{-1} peak is unstable under EB radiation. Depth values refer to microscope stage movement, not actual sample depth.	61
Figure 3-8. Depth profile of an EB-cured sample of TMPTA/BADGEDA. Conversion is constant as a function of depth considering the typical ± 3 to 4% instrumental deviation.	62
Figure 3-9. Real-time Raman profile of the TMPTA/BADGEDA photopolymerization. The C-O-C bending (665 cm^{-1}) and the aromatic =CH bond (1185 cm^{-1}) were determined to be unaltered during the reaction.....	63
Figure 3-10. Depth profile of an EB-cured sample of TMPTA/BADGEDA. The 665 and 1185 cm^{-1} peaks, both stable in UV polymerization, are altered in EB polymerization.	64
Figure 4-1. The chemical structures of the 5-monomer series: (A) PA, (B) BA, (C) PEA, (D) POEA, and (E) HPOPA.....	69
Figure 4-2. The conversion DREs, at three different doses, for three monomer/oligomer formulations. In general, the DRE magnitude decreases with increasing dose and with increasing monomer size.	75
Figure 4-3. The EB polymerization reaction mechanism.	76
Figure 4-4. The T_g DREs, at three different doses, for five monomer/oligomer formulations. In general, the DRE magnitude decreases with increasing dose and with increasing monomer size.	79
Figure 4-5. The monomer/oligomer formulation T_g values, as estimated by the Flory-Fox equation (Equation 4-8), presented in order of decreasing DRE magnitude (PA > HPOPA). T_g and DRE magnitude do not correlate.	82
Figure 4-6. Real-time conversions from UV-initiated reactions of neat monomer collected using Raman spectroscopy. The R_p increases and the DRE decreases with increasing monomer size.	83
Figure 4-7. UV-initiated reactions of monomer/oligomer formulations collected using Raman spectroscopy.	85

Figure 4-8. Using T_g -shift comparisons, a demonstration of the relationship between increasing dose 4-fold and line speed 10-fold. DE (20 ft/min) is the magnitude of the T_g shift from 15 kGy to 60 kGy at a constant line speed of 20 ft/min. DRE (60 kGy) is the magnitude of the T_g shift from 20 ft/min to 200 ft/min at a constant dose of 60 kGy. To be perfectly predictive, the bar values in gray should be equal to those in black, and light-textured bar values should equal dark-textured bar values.	87
Figure 4-9. Using conversion-shift comparisons, a demonstration of the relationship between increasing dose 4-fold and line speed 10-fold. DE (20 ft/min) is the magnitude of the conversion shift from 15 kGy to 60 kGy at a constant line speed of 20 ft/min. DRE (60 kGy) is the magnitude of the conversion shift from 20 ft/min to 200 ft/min at a constant dose of 60 kGy. To be perfectly predictive, the bar values in gray should be equal to those in black, and light-textured bar values should equal dark-textured bar values.....	88
Figure 5-1. The chemical structures of the 5-monomer series: (A) PA, (B) BA, (C) PEA, (D) POEA, and (E) HPOPA. Also shown is the photoinitiator DMPA (F) which was used in the photopolymerization reactions.	96
Figure 5-2. Schematic of the mold used to produce the second set of photopolymerized samples with a reduced exposure area (Set 2 – Equivalent).	98
Figure 5-3. Depth/dose curve for EB polymerization, as predicted by Monte Carlo simulations. With a density of 1 g/cm^3 , the depth of penetration units become micrometers. A voltage of 250 kV was chosen to ensure a consistent dose through a film of 200 μm	100
Figure 5-4. Depth/irradiance curve for photopolymerizations, as predicted by the Kenning, <i>et al.</i> model, with decreasing concentrations of DMPA. A concentration of 0.1 wt% DMPA was chosen for the photopolymerization studies to reduce the irradiance gradient.	101
Figure 5-5. A comparison of the conversion EREs for 5 monomer/oligomer formulations initiated by EB and photo-radiation (Set 1) at 3 different doses (dose equivalents): 15 kGy (A), 30 kGy (B), and 60 kGy (C). In general, the ERE magnitude decreases with increasing energy and with increasing monomer size. The ERE magnitude is also larger for EB-cured films than photo-cured films.....	108
Figure 5-6. A comparison of the conversion EREs for five monomer/oligomer formulations initiated by EB and photo-radiation (Set 2) at three different doses (dose equivalents): 15 kGy (A), 30 kGy (B), and 60 kGy (C). In contrast to the EB EREs, there does not appear to be a trend in the photo ERE magnitude. Data columns marked with an asterisk have a lower conversion with 2 s exposure than a 0.2 s exposure.	114

Figure 5-7. A comparison of the T_g values for 5 monomer/oligomer formulations initiated by EB and photo-radiation (Set 1) at 60 kGy, 20 ft/min and 60 kGy equivalent, 100 s exposure, respectively. Polymerizing with EB radiation increases the T_g of a formulation, although only the EB-cured PA and HPOPA films are significantly different from the photo-cured films.	117
Figure 5-8. A comparison of the FWHM values of the $\tan \delta$ peak for five monomer/oligomer formulations initiated by EB and photo-radiation (Set 1) at 60 kGy, 20 ft/min and 60 kGy equivalent, 100 s exposure, respectively. Polymerizing with EB radiation decreases the FWHM of a formulation, although only the EB-cured PA films is significantly different from the photo-cured films.	118
Figure 5-9. A comparison of the maximum $\tan \delta$ peak height values for five monomer/oligomer formulations initiated by EB and photo-radiation (Set 1) at 60 kGy, 20 ft/min and 60 kGy equivalent, 100 s exposure, respectively. No consistent trend is observed across the formulations, and only PA and HPOPA have a significant difference.	119
Figure 6-1. Cationic ring-opening polymerizations include the active chain end (ACE) mechanism (A, propagation) and activated monomer (AM) mechanism (B, chain transfer). Figure adapted from Reference 19.	124
Figure 6-2. Semi-grafted network. Polymer A (dashed line) is grafted onto the cross-linked network of Polymer B (solid line). Adapted from Reference 22.	125
Figure 6-3. Monomers and photoinitiators used in this study: (A) EGMEA, (B) HEA, (C) EGMEMA, (D) HEMA, (E) EEC, (F) DAI, and (G) DMPA.	126
Figure 6-4. EGMEA conversion profiles, calculated from Raman spectra, as a function of EEC content. Each formulation was initiated using an effective irradiance of 140 mW/cm^2 for 5 minutes.	130
Figure 6-5. HEA conversion profiles, calculated from Raman spectra, as a function of EEC content. Each formulation was initiated using an effective irradiance of 140 mW/cm^2 for 5 minutes.	131
Figure 6-6. Epoxide conversion of EGMEA/EEC formulations, calculated from Raman spectra, as a function of EEC content. Each formulation was initiated using an effective irradiance of 140 mW/cm^2 for 5 minutes.	132
Figure 6-7. Epoxide conversion of HEA/EEC formulations, calculated from Raman spectra, as a function of EEC content. Each formulation was initiated using an effective irradiance of 140 mW/cm^2 for 5 minutes.	133
Figure 6-8. EGMEMA conversion profiles, calculated from Raman spectra, as a function of EEC content. Each formulation was initiated using an effective irradiance of 140 mW/cm^2 for 5 minutes.	136

Figure 6-9. HEMA conversion profiles, calculated from Raman spectra, as a function of EEC content. Each formulation was initiated using an effective irradiance of 140 mW/cm ² for 5 minutes.....	137
Figure 6-10. Epoxide conversion of EGMEMA/EEC formulations, calculated from Raman spectra, as a function of EEC content. Each formulation was initiated using an effective irradiance of 140 mW/cm ² for 5 minutes.....	139
Figure 6-11. Epoxide conversion of HEMA/EEC formulations, calculated from Raman spectra, as a function of EEC content. Each formulation was initiated using an effective irradiance of 140 mW/cm ² for 5 minutes.....	140
Figure 6-12. Hybrid monomer mixture viscosities (in centistokes) at 25°C as predicted by the Refutas equation.	142
Figure 6-13. Final conversion as a function of the weight fraction of EEC for the hybrid formulations EGMEA/EEC (A), HEA/EEC (B), EGMEMA/EEC (C), and HEMA/EEC (D). Viscosity increases with fractions of EEC; to the left of the vertical dotted line, this viscosity change is ~ 10 cSt.....	144
Figure 6-14. Conversion profiles of the four (meth)acrylate. EEC mixtures at the 20/80 EEC/(meth)acrylate weight fraction ratio: (A) (meth)acrylate conversion and (B) epoxide conversion. Although all starting viscosities were similar (± 10 cS), the conversion profiles and final conversions are quite different.	146
Figure 6-15. The glass transition temperature (T_g) of three of the hybrid formulations. Increases in T_g are not linear, and a formulation can remain at similar T_g ($\pm 10^\circ\text{C}$) for up to a 20 wt% increase in EEC.	148
Figure 6-16. The full width at half maximum of the $\tan \delta$ (FWHM) of three of the hybrid formulations. Formulations with a hydroxyl-containing (meth)acrylate have a smaller FWHM, and therefore experience less network heterogeneity.	149
Figure 7-1. Monomer (EEC, A) and photoinitiator (DAI, B) used in this study.....	156
Figure 7-2. Unmasked, 3-D schematic of a rectangular mold (A), and a photomasked, cutaway of the same rectangular mold (B).	157
Figure 7-3. Cutaway of a rectangular mold, post-illumination. Aliquots of liquid resin were collected from the three locations labeled with a black circle.	158
Figure 7-4. The polymer formed immediately post-illumination (0 hrs) is approximately 10 mm x 5 mm x 0.3 mm (A). After four hours, significant shadow cure has occurred (B). Maximum thickness and length of the polymer piece are 9 mm and 28 mm, respectively.	162
Figure 7-5. Polymer formed 8 hrs [(A) and (B)], 36 hrs [(C) and (D)], and 72 hrs [(E) and (F)] post-illumination. Shadow cure length remains constant during this time, however, conversion along the mold bottom increases noticeably between 8 and 36 hours. Shadow cure growth is seen laterally from the light-cured section, increasing by ~ 3 mm over 64 hrs. The cavity formed beneath the light-cured section does not diminish.	164

Figure 7-6. Shape of the mold well (above) and the resulting shadow-cured polymer (below). Examples (A) and (B) were initiated using a circular exposure area (0.28 cm ²) in the middle of the sample. Examples (C) and (D) were initiated using a 1 cm ² area at the end of the mold well.....	167
Figure 7-7. Side view of a shadow-cure polymer made in circular mold, initiated at the surface center. Although polymer strands connect surface and bottom cure, no polymer strands were produced directly beneath the light-cured section.	167
Figure 7-8. Schematics of one half of the crack mold (A) and of the two halves of the mold conjoined (B). The mold is shown at a 90° incline.	168
Figure 7-9. Shadow-cure sample polymerized at a 90° angle in the crack mold. Some uncured liquid resin was left in the sample to better illustrated the hollow cavity beneath the light-cured section (LCS).	169
Figure 7-10. Cutaway of the crevice mold. A monomer well (left) was added to facilitate improved shadow-cure growth in the crevice.	170
Figure 7-11. Shadow-cure polymer made in the crevice mold. Significant shadow-cure growth was achieved in the crevice (48 mm) by incorporating a monomer well at the end of the crevice.	170
Figure 7-12. Response surface depicting the influence of exposure area and exposure time on shadow cure length. Effective irradiance and sample depth were held constant at coded values of 1 and -0.95, respectively. Shadow cure length is maximized by decreasing exposure area and increasing exposure time.	174
Figure 7-13. Response surface depicting the influence of sample depth and effective irradiance on shadow cure length. Exposure time and exposure area were held constant at coded values of -0.51 and -0.84, respectively. Shadow cure length is maximized by increasing sample depth while decreasing effective irradiance.....	175
Figure 7-14. Response surface depicting the influence of exposure area and exposure time on gel fraction. Effective irradiance and sample depth were held constant at coded values of 0.49 and 1, respectively. The gel fraction is maximized by increasing both exposure area and exposure time.	177
Figure 7-15. Response surface depicting the influence of sample depth and effective irradiance on gel fraction. Exposure time and exposure area were held constant at coded values of 0.59 and -0.08, respectively. The gel fraction is maximized by decreasing sample depth and increasing effective irradiance.....	178
Figure 7-16. Gel fractions of two shadow-cured samples. Although the shadow-cure regions are made up of many small, cross-linked domains, each light-cured section and the shadow-cure formed in close proximity (inserts) remains completely intact after the sol fraction is removed, suggesting they are each one highly cross-linked domain. As this highly cross-linked domain increases in size, the lower cross-linked shadow-cure domains decrease.....	179

Figure 8-1. Monomer (EEC, A) and photoinitiators (DAI, B and MTB, C) used in this study.....	186
Figure 8-2. 3-D schematic of a rectangular mold with a spacer to control the monomer surface area to volume ratio (A), and a cross section of the same rectangular mold (B).....	187
Figure 8-3. Transferable shadow cure method. Step 1: The sample is illuminated, and, post-illumination, the light-cured section (LSC) is removed. Step 2: The active-center-containing monomer (AC monomer) is transferred to the desired location. Step 3: The AC monomer is allowed to polymerize.	189
Figure 8-4. Long-term kinetic comparison between light-cure samples (LC, with continued dark cure) and shadow-cure samples (SC) of EEC with two different photoacid generators (DAI and MTB). The reactions were monitored via Raman spectroscopy. Light-cure samples maintain a higher conversion (~15%) than shadow-cure samples even after 300+ days.	196
Figure 8-5. A comparison of the transferable shadow cure network (A) and light-cure network (B) of EEC after being dissolved in THF. The light cure network is a single cross-linked domain, whereas the shadow-cure network is composed of numerous smaller cross-linked domains. The inserts show the films before the sol extraction.	197
Figure 8-6. Comparison of the $\tan \delta$ curves of the first DMA temperature ramp sequence for EEC polymerized by transferable shadow cure (A) and light cure (B) at 8, 14, and 21 days post-illumination.	198
Figure 8-7. Comparison of the $\tan \delta$ curves of the second DMA temperature ramp sequence for EEC polymerized by transferable shadow cure (A) and light cure (B) at 8, 14, and 21 days post-illumination.	200
Figure 8-8. Comparison of the T_g (A), cross-link density (B), and maximum peak height of the $\tan \delta$ profile for EEC polymerized by transferable shadow cure and light cure at 8, 14, and 21 days post-illumination. T_g and cross-link density both decrease with increasing time post-illumination and polymerization by shadow cure. The $\tan \delta$ maximum increases with increasing time post-illumination and polymerization by shadow cure. Values were calculated from the second DMA temperature ramp sequence.	202
Figure 8-9. Polymer produced from transferable shadow cures samples, of the same size, with pigment added before illumination (A and C) and after illumination (B and D). When pigment was added after illumination, the entire volume of AC monomer polymerized.	203
Figure 8-10. Examples of using the transferable shadow cure method to produce pigmented polymers in complex geometries.	204

Figure 8-11. Thick polymers can be produced by layering the active-center-containing monomer. Shown is a 2-cm thick polymer made using the transferable shadow cure method, though even thicker polymers can be produced.	204
Figure 8-12. CCD 1 response surface depicting the influence of sample depth and effective irradiance on average shadow cure conversion. Exposure time and exposure area were held constant at coded values of 0.9 and -1, respectively. Shadow cure conversion is maximized by decreasing sample depth while increasing effective irradiance.....	207
Figure 8-13. CCD 1 response surface depicting the influence of exposure area and exposure time on average shadow cure conversion. Effective irradiance and sample depth were held constant at coded values of 0.4 and 1, respectively. Shadow cure conversion is maximized by decreasing exposure area and increasing exposure time.	208
Figure 8-14. CCD 1 response surface depicting the influence of sample depth and effective irradiance on LCS wt%. Exposure time and exposure area were held constant at coded values of 0.9 and -1, respectively. The LCS mass is maximized by decreasing sample depth while increasing effective irradiance.....	210
Figure 8-15. CCD 1 response surface depicting the influence of exposure area and exposure time on LCS wt%. Effective irradiance and sample depth were held constant at coded values of -0.2 and 1, respectively. LCS is maximized by increasing exposure area and exposure time.	211
Figure 8-16. CCD 2 response surface depicting the influence of exposure area and exposure time on average shadow cure conversion. Effective irradiance and sample depth were held constant at coded values of 1 and 0.6, respectively. Shadow cure conversion is maximized by increasing exposure time.	214
Figure 8-17. CCD 2 response surface depicting the influence of sample depth and effective irradiance on average shadow cure conversion. Exposure time and exposure area were held constant at coded values of -0.2 and 0.4, respectively. Shadow cure conversion is maximized by decreasing sample depth while increasing effective irradiance.....	215
Figure 9-1. Phenyl acrylate (A) and cyclohexyl acrylate (B).	228

LIST OF ABBREVIATIONS

General Abbreviations

2 FI Model	Two-factor interaction model
AC Monomer	Active-center-containing monomer
ACE Mechanism	Active chain end mechanism
AM Mechanism	Activated monomer mechanism
ANOVA	Analysis of variance
Avg.	Average
BA	Benzyl acrylate
BADGEDA	Bisphenol-A-diglycidylether diacrylate
CCD	Central Composite Design
Conv.	Conversion
CP	Checkpoint
DAI	4-(2-hydroxyl-1-tetradecyloxy)-phenyl] phenyliodonium hexafluoroantimonate
DE	Dose effect
DMA	Dynamic mechanical analysis
DMPA	2,2-dimethoxy-2-phenylacetophenone
DOE	Design of experiments
DRE	Dose rate effect
EB	Electron beam
EEC	3,4-epoxycyclohexane carboxylate
EGMEA	Ethylene glycol methyl ether acrylate
EGMEMA	Ethylene glycol methyl ether methacrylate
ERE	Energy rate effect
F-value	Fisher value
FTIR	Fourier transfer infrared
FWHM	Full width at half maximum
G_i	Radiation yield
GPC	Gel permeation chromatography
GPN	Grafted polymer network
h_v	Light
HEA	2-hydroxyethyl acrylate
HEMA	2-hydroxyethyl methacrylate
HPOPA	2-hydroxy-3-phenoxypropyl acrylate
ID	Inner diameter
IPN	Interpenetrating network
LC	Light cure
LCS	Light-cured section

Max	Maximum
MDEA	N-methyldiethanolamine
METHB	3,4-epoxy-cyclohexyl-methyl methacrylate
Min	Minimum
MTB	4-isopropyl-4'-methyldiphenyliodonium tetrakis(pentafluorophenyl)borate
NA	Not applicable
Obj	Objective
PA	Phenyl acrylate
PDMS	Polydimethylsiloxane
PEA	2-phenylethyl acrylate
PET	Polyethylene terephthalate
POEA	2-phenoxyethyl acrylate
R_{ct}	Rate of chain transfer
R_i	Rate of initiation
R_p	Rate of propagation
R_t	Rate of termination
RT-Raman	Real-time Raman
SC	Shadow cure
S/N	Signal-to-noise ratio
T_g	Glass transition temperature
THF	Tetrahydrofuran
TMPTA	Trimethylolpropane triacrylate
UV	Ultraviolet light
VOC	Volatile organic compounds

Unit Abbreviations

a.u.	Arbitrary units
Btu	British thermal unit
C	Celsius
ft	Feet
g	Gram
Gy	Gray
hrs	Hours
Hz	Hertz
J	Joule
K	Kelvin
L	Liter
m	Meter
min	Minute
mol	Mole
Pa	Pascal
s	Second
SCFM	Standard cubic feet per minute
St	Stokes
V	Volt
W	Watt
wks	Weeks
wt %	Weight percent

CHAPTER 1 INTRODUCTION AND BACKGROUND

1.1 Radiation Polymerization

In radiation polymerization, electromagnetic or electron beam radiation is used to initiate the covalent bonding of individual molecules (monomers) together into long chains (polymers).^A While there are many types of radiation, as illustrated in Figure 1-1, a minimum amount of energy is required to initiate polymerization.²

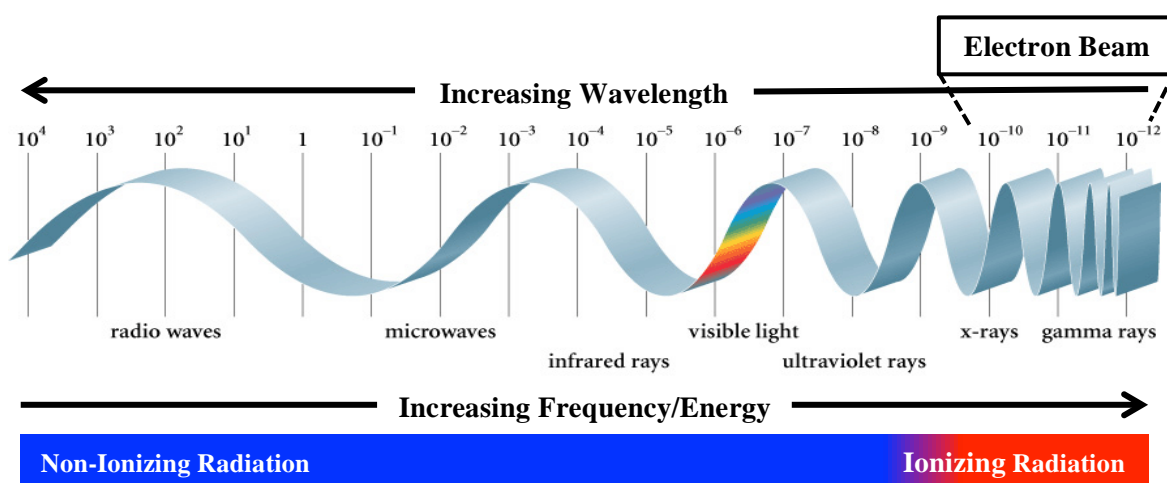


Figure 1-1. Electron beam radiation in comparison to the electromagnetic radiation spectrum. Wavelength is measured in meters. Adapted from Reference 2.

Since radiation energy increases as wavelength decreases, the longest electromagnetic waves with enough energy to make initiation of polymerization feasible are visible-light waves. Photopolymerization uses visible and ultraviolet (UV) light waves to effect polymerization; however, light at such wavelengths does not have enough energy to initiate most polymerization without the assistance of a photoinitiator. A common

^A The word polymer comes from the Greek roots $\pi\sigma\lambda\upsilon\varsigma$ (polus), meaning many, and $\mu\epsilon\rho\acute{o}\varsigma$ (meros), meaning parts; thus a polymer is thing of many parts.¹ Precursors to polymers share the same suffix, -mer, but change the prefix to reflect the length of the chain: monomer is a one-unit chain, dimer is a two-unit chain, trimer is a three-unit chain, etc. A short chain is referred to as an oligomer (from the Greek $\acute{o}\lambda\iota\gamma\omicron\varsigma$ (oligos), meaning a few) after numerical prefixes get too large and become cumbersome. As with the English *few*, the exact number of repeating units that constitutes an oligomer (or a polymer, for that matter) is ambiguous but is generally about 10 to 100 units.

application of visible-light polymerization is dental resins. UV polymerization^B is the most common type of radiation polymerization used on an industrial scale. It is used extensively in adhesive, coating, film, ink, and biomedical industries, creating products such as nail gels, floor coatings, and contact lenses.³⁻⁶ Since 1970, the radiation-cured polymer market in North America has grown consistently with 119,000 metric tons of polymers produced in 2011.⁵

UV polymerization has become a widely accepted process because it has many advantages over traditional, heat-initiated polymerization. The use of light instead of heat decreases energy consumption by as much as 6.81×10^7 Btu, annually.⁷ Photopolymer reactions often proceed faster and require less processing space than their thermal counterparts, saving time and reducing the equipment footprint in manufacturing facilities. UV reactions take place at room temperature, which allows for the curing of temperature-sensitive polymers, such as thermoresponsive shape-memory polymers, or for curing in temperature-sensitive environments. Photopolymerization is also solvent-free, eliminating the material and waste removal costs associated with environmentally-damaging volatile organic compounds (VOCs). Furthermore, thermal polymerizations lack the spatial and temporal control of photopolymerization, due to the need of solvents for heat dissipation and the inability to instantaneously heat and cool the reaction.

Certain limitations, however, prevent photopolymerization from being a pertinent choice in a wider range of industries. Photopolymerization is frequently restricted to the production of thin films or coatings because of the penetration constraints of the initiating UV light, which is governed by the Beer-Lambert law (Equation 1-14).^{8,9} Scattering and absorption cause little light to reach the bottom of thick samples, resulting in low to no polymer conversion.^C Similarly, the use of pigments and fillers is severely limited

^B UV polymerization is used synonymously with photopolymerization in this dissertation, and refers to polymerization initiated not only by UV light but also polymerization initiated by a combination of UV and visible light. In contrast, visible-light polymerization is only initiated by visible-light wavelengths (350-770 nm).

^C Generally, in industrial applications the thickness of photopolymerized coatings and films is restricted to <1 mm to ensure consistent cure throughout the coating/film.¹⁰ Polymer conversion is more fully defined in Section 1.3.1; however, broadly speaking, conversion is the percentage of monomer molecules that have been bonded together to form the polymer. For example, at 60% conversion, 60% of the monomer molecules form polymer chains and the remaining 40% are still individual monomer molecules.

because they impede light penetration. Other limitations of photopolymerization include oxygen inhibition and polymer shrinkage.

Similar to photopolymerization, electron-beam (EB) polymerization offers a fast, low-energy, and solvent-free means of polymerizing coatings, films, and adhesives (Table 1-1); however, EB polymerization uses accelerated electrons instead of photons as its initiation source.^{3,7}

Table 1-1. EB requires significantly less energy to dry/cure coatings compared to solvent-based and water-based systems. Adapted from Reference 3.

Property/Energy	System		
	Solvent	Water	EB Curable
Solid, weight %	40	40	100
Diluent	Toluene	Water	None
Boiling point, °C	111	100	N.A.
Vapor pressure, mmHg (20°C)	22	17	N.A.
Energy to dry/cure, 1 g dried coating, J/g	555	3,390	30

Because of its short wavelength and high frequency, the EB radiation has a greater penetration power than that of UV light (Figure 1-5); the thickness of EB-cured samples is only limited by the voltage potential that can be generated.^D EB free-radical polymerization also requires no photoinitiators, which reduces materials costs and has led to broad acceptance of EB in the food packaging industry where initiator fragments are of concern. Furthermore, electron penetration is not hindered by pigments and fillers, allowing widespread property-tuning through the use of additives for broader industrial applications.

Unlike photopolymerization, the greatest limitations of EB polymerization stem from lack of understanding and control rather than fundamental principles. For example, EB polymerization cannot produce high molecular weight polymers, which is a limiting factor since high molecular weight is often synonymous with high performance and durability. Instead, most EB-cured polymers are highly cross-linked as a result of the many side reactions caused by electron-induced free-radical formation. Greater

^D Increasing the voltage potential increases the acceleration of the electrons. The wavelength of the electrons can be derived from the voltage potential using DeBroglie's relationship.

understanding of EB kinetics and the influence of chemical structure and processing parameters would lead to better control over cross-linking density and other polymer properties.

Despite the development of both types of radiation polymerization occurring in the 1960's and the penetration advantages of using accelerated electrons, photopolymerization currently dominates the radiation-curing industrial market and its kinetics have been extensively studied.^{3,11,12} Reasons for the popularity of UV (over EB) polymerization range from cost to feasibility. On an industrial scale, the start-up cost for an electron beam accelerator is greater than that of a bank of UV lights. Furthermore, until the creation of the EB lab unit, EB polymerization research would have had to take place in an industrial setting or with industrial cooperation. Even now, EB lab units can be priced upwards of \$100,000; whereas lab-grade UV lights can be purchased for a few thousand dollars.¹² UV lights are also small, mobile, and easily paired with instruments, such as a Raman or Fourier Transfer Infrared (FTIR) spectrometer, to capture polymerization reactions in real time. Conversely, EB reactions cannot be monitored in real time due to the shielding in place to protect against X-rays and ability of accelerated electrons to damage sensitive equipment.^E Thus, EB polymerization technology has often outpaced fundamental, kinetic understanding, but it is ultimately limited until progress is made toward bridging the gap.

1.1.1 Radiation Kinetics

Most radiation polymerization is a type of chain polymerization, also known as addition polymerization.^F Chain polymerization differs from other polymerization mechanisms (namely step polymerization) in many ways.^{G,9,14} First, chain

^E When accelerated electrons hit metal, they produce X-rays in the form of bremsstrahlung or *braking* radiation.¹³

^F One exception would be photo-induced thiol-ene polymerization, which follows step polymerization kinetics.

^G Step polymerization is the other main polymer mechanism.⁹ It is characterized by the release of a small molecule, often water, and therefore is also called condensation polymerization. Step polymerization reactions can occur without release of a small molecule; the polyurethane reaction is an example of this type of step polymerization. However, these reactions are in the minority. The mechanism for step polymerization consists only of propagation and requires two reactive moieties to create a homopolymer. No active center is present in step polymerization; instead, monomers bond to each other, in a step-wise

polymerization only requires one type of reactive moiety to create a homopolymer.^H For example, a common reactive functional group in chain polymerization is the $-C=C-$; as monomer molecules are covalently bonded together, the double bond is transformed into the characteristic $-C-C-$ polymer backbone (Figure 1-2).^I

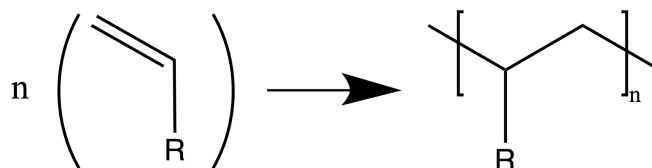


Figure 1-2. Chain polymerization of a reactive C=C bond.

Because this addition reaction is simply a rearrangement of bonds, there is no leaving group, and the molecular weight of the repeat unit is equal to that of the monomer. Moreover, in chain polymerization, a monomer molecule can only bond to the growing polymer chain at the active center (free radical, cation, or anion). The presence of an active center, perhaps more so than any other characteristic, makes chain polymerization reactions easily recognizable. Finally, the chain polymerization mechanism can be divided into four main steps: initiation – creation of the active center, propagation – growth of the polymer chain, chain transfer – transfer of the active center to a new polymer chain, and termination – death of the active center and end of chain growth.

Although the UV and EB polymerizations considered in this work both follow chain polymerization kinetics, they differ with respect to their initiation mechanisms, while the remaining reaction steps are the same for both systems. Comparing and contrasting free-radical UV and EB systems provides a unique opportunity to determine the effect of the EB initiation mechanism, since photopolymerization kinetics have been extensively studied. Understanding the impact of initiation will aid in predicting and

fashion, to first form dimers, then tetramers, octamers,...and eventually polymers. A common example of step polymerization is the reaction of a diol and a diacid to form a polyester.

^H A homopolymer is a polymer with a single repeat unit. Polymers containing more than one repeat unit are called copolymers.

^I Although the $-C-C-$ backbone is often considered one of the hallmarks of chain polymerization, deviations, such as the $-C-C-O-$ backbone, which results from the ring opening of an epoxide, do occur (Figure 1-14).

tuning physical properties of EB-cured polymers, as well as allowing further understanding of EB polymerization kinetics.

Visible/UV Light Initiation

For photopolymerization, initiation requires the presence of a photoinitiator and consists of two steps:



where I is the photoinitiator, R^* is the active center (whether free radical, cation, or anion), M is the monomer, M^* is the start of the growing polymer chain, $h\nu$ is the initiating light, and k_i is the initiation rate constant.⁹ A rate of initiation, R_i , can be derived from this initiation mechanism:

$$R_i = 2\phi I_a \quad (1-2)$$

where ϕ is the number of propagating polymer chains created per photon absorbed, also known as the quantum yield of the initiator, and I_a is the intensity of absorbed light. The 2 indicates the initiator forms two propagating active centers, which is common in the case of free-radical photopolymerization. In the cases of cationic and anionic photopolymerization, only one active center is formed per initiator molecule; therefore, the 2 is removed from the R_i equation. I_a can be further defined to illustrate its dependence on the photoinitiator concentration, $[A]$:

$$I_a = \alpha[A]I_0 10^3 e^{-\alpha[A]D} \quad (1-3)$$

where α is the absorption coefficient ($\text{L mol}^{-1} \text{cm}^{-1}$), I_0 is the incident effective irradiance at the sample surface ($\text{mol cm}^{-2} \text{s}^{-1}$), 10^3 is a conversion factor (mL L^{-1}), and D is the distance into the sample (cm).

EB Initiation

In contrast, EB initiation does not require a photoinitiator to produce radicals. At high energies, radiation is ionizing (Figure 1-1), which means it can separate electrons from atoms to create ions. EB radiation is of sufficient energy to be considered ionizing, and through an ionization process, it can create its own radicals from monomer molecules (Equation 1-4).¹⁵ One standard route to radical formation begins with the ionization of a monomer molecule (M) by an accelerated electron (β) into a cation (M^+) and a lone electron (e^-). The electron prefers to recombine with the parent cation to form an



excited monomer molecule (M^*), which then homolytically cleaves to form two radicals (R^\bullet).¹⁶ All possible routes to radical formation are summarized in the EB initiation steps:



where e^- now represents an accelerated electron.^K Unlike photopolymerization where a photon can only participate in the initiation mechanism once, in EB polymerization, this process of radical formation (Equation 1-5) can be repeated with the same accelerated electron multiple times, losing energy with each collision. As long as the energy of the accelerated electron is greater than the energy needed to cleave a bond in the monomer, the accelerated electron can instigate the initiation mechanism. The rate of initiation is derived from Equation 1-5 as:

^J Homolytic cleavage of a chemical bond results in both chemical species receiving one radical. For example, homolytic cleavage of a C–H bond leads to a C \cdot and a H \cdot . In contrast, heterolytic cleavage of the bond would leave one species with both radicals (a C: and a H).

^K Primary radicals (R^\bullet) differ between EB and photopolymerization since they are formed from a monomer molecule (Equation 1-5) and a photoinitiator (Equation 1-1), respectively; however, propagating radicals (M^\bullet) are expected to be the same for both initiation mechanisms.

$$R_i = G_i \rho \frac{dD}{dt} \quad (1-6)$$

where G_i is the radiation yield (number of molecules reacted per 100 eV absorbed^L), ρ is the monomer density, D is the electron dose,^M and t is time.^{3,6,15}

This initiation scheme has far-reaching effects. Though the lack of photoinitiator has its benefits, it also increases the difficulty of controlling key aspects of the polymerization reaction. In photopolymerization, the initiator concentration (in tandem with the quantum yield and absorbed light) controls how many radicals are created (Equations 1-2 and 1-3). Once a threshold light exposure is reached, increasing the exposure will not produce more free radicals.^N Contrastingly, in EB polymerization, radical concentration can, theoretically, only be capped by monomer concentration. Increasing the dose increases the number of free radicals produced (Equation 1-6). Photoinitiator concentration also determines free-radical concentration in light-initiated systems, which directly impacts chain length.^O In EB polymerization, free-radical spacing is, again, controlled by dose, since any monomer molecule colliding with an accelerated electron is equally likely to produce a free radical. Whether changing the number of free radicals or their spacing, photopolymerization can manipulate initiator concentration and exposure independently to affect initiation; EB polymerization can only change dose in the same scenarios. Nevertheless, though more challenging, choosing the correct dose could provide a balance between providing enough energy to adequately initiate the reaction while not over saturating the system with radicals.

^L G_i is sometimes also defined as the number of dissociation events per 100 eV. It is similar to the quantum yield of a photoinitiator. However, values of quantum yield range from 0 to 1 because it represents the probability of a photoinitiator molecule dissociating per photon absorbed, whereas values of radiation yield could range from 0 to ∞ . Additionally, the definition of G_i does not consider the number of electrons over which the energy is distributed. This lack of specificity may be problematic since 100 electrons, each of 1 eV, are not expected to be equivalent to 1 electron of 100 eV. The former would require 5 electrons to simultaneously collide with a single monomer molecule to break a C-C bond – an unlikely scenario. An electron volt (eV) is defined as amount of energy gained or lost by one electron as it travels through an electric potential difference of 1 volt.³ $1 \text{ eV} = 1.60218 \times 10^{-19} \text{ J}$.¹⁷

^M Dose is the term used for energy input in EB. It is further defined in Section 1.1.3, Equation 1-18.

^N Exposure is the term used for energy input in photopolymerization. It is further defined in Section 1.1.3, Equation 1-17.

^O Adequate mixing should space initiator molecules equally; therefore, decreasing or increasing the initiator concentration should decrease or increase the space between free radicals, respectively. If two radicals near each other, they will combine and terminate their chains. More propagation can occur, leading to increased chain length, if there is greater space between radicals.

However, the ability to produce radicals in EB systems without the aid of an initiator has further ramifications. Using EB, cross-linking can occur in what would be normally be considered linear systems. As a rule, monomers containing only one reactive functional group can only produce linear polymer chains.^P Monomers with two or more functional groups can create branched chains or cross-linked networks (Figure 1-3).

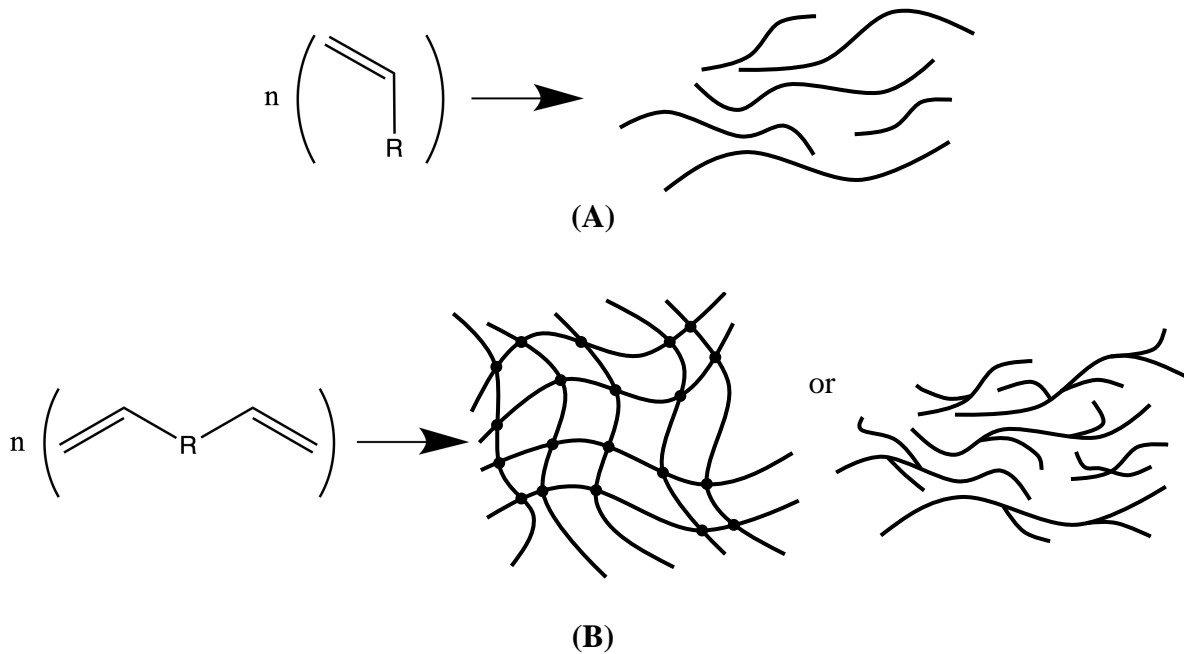


Figure 1-3. Monofunctional monomers for linear polymers (A) and multifunctional monomers form cross-linked or branched networks (B).

Yet, these statements assume a controlled reaction, which only takes place within the reactive moiety. A controlled reaction is a realistic assumption for photopolymerization, but it is directly contradicted by the EB-initiation scheme. Radicals can be formed anywhere on the monomer molecule using EB radiation, and these radicals do not necessarily all participate in the second initiation step to create an active center (Equation 1-5). Moreover, radical formation is not limited to monomer molecules; EB radiation can also create radicals on a polymer chain. If two of these radicals are near each other, they can combine to form a bond (*i.e.*, a cross-link) between polymer chains (Figure 1-4, A).

^P This statement is true in the absence of chain transfer or backbiting reactions.

Whether a radical is ultimately used to create an active center or a cross-link cannot be controlled. Controlling chain scission in EB is also of concern. Chain scission occurs when, instead of a side bond, a bond that makes up the polymer backbone is cleaved (Figure 1-4, B). If chain scission occurs at the same rate as polymer growth, effectively no polymer is formed. Previous work has demonstrated a connection between chemical structure and the promotion of cross-linking and/or chain scission in polymer systems that are irradiated, but this connection is not well developed in monomer systems.^{3,18}

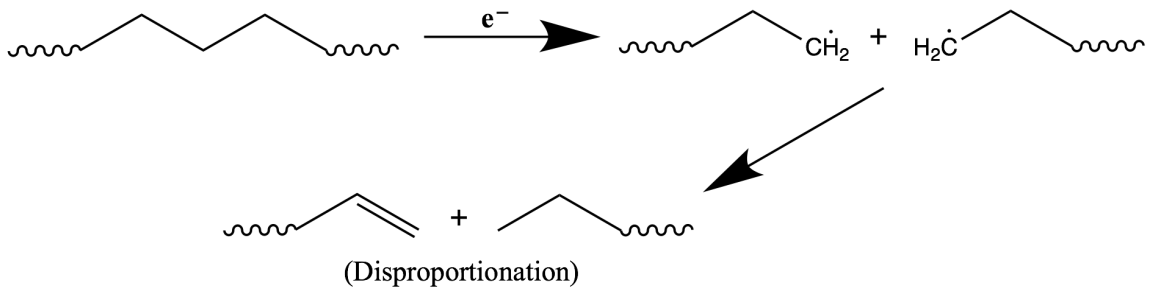
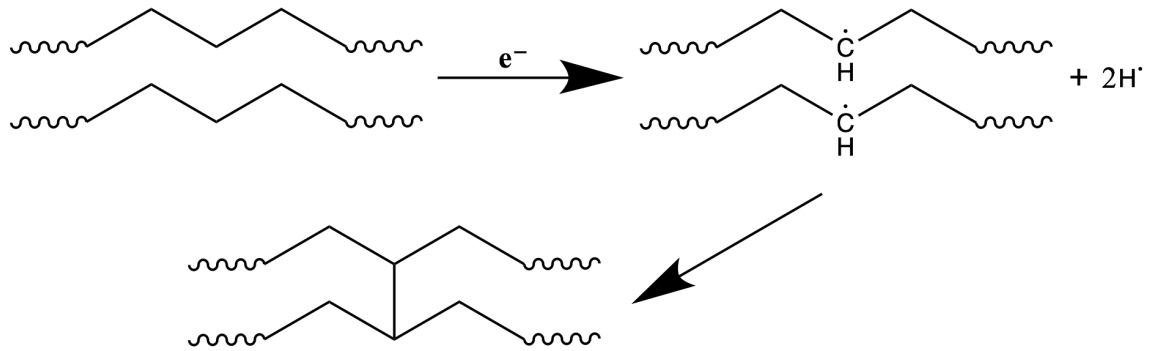


Figure 1-4. Cross-linking (A) and chain scission (B) of polymer chains by electron beam radiation. Adapted from Reference 18.

EB polymerization can also proceed via the cationic and anionic mechanisms; however, in these cases, an initiator is needed, and thus an initiation mechanism equivalent to Equation 1-1 results.¹⁹⁻²¹ Although free radicals will be formed by cleaving monomer molecules, these radicals should not lead to propagation if the cationic/anionic monomer cannot polymerize via the free-radical mechanism. Since the radicals can lead to cross-linking just as in the free-radical monomer system (Figure 1-4), the mode of initiation is presumed to impact cationic and anionic radiation polymerization as well.

Propagation

Once an active center is formed, the addition of monomer molecules (M) grow the polymer chain through propagation:



where M_n^* is a growing polymer chain with a length of n repeating units.^{9,14} In chain polymerization, this reaction only takes place at an active center. Rate of propagation (R_p) is defined as

$$R_p = k_p[M][M^*] \quad (1-8)$$

where k_p is the propagation rate constant, $[M]$ is the monomer concentration, and $[M^*]$ is the active center concentration.

Chain Transfer

Under certain conditions, a free-radical active center can abstract an atom, like a hydrogen, from another molecule in the system (RX), be it monomer, polymer, solvent, initiator, additive, or impurity (Equation 1-9).⁹



This abstracted atom terminates the current growing chain and leaves a free radical, which can go on to initiate a new polymer chain. This process is termed chain transfer. The rate of chain transfer (R_{ct}),

$$R_{ct} = k_{ct}[RX][M^*] \quad (1-10)$$

is dependent on the chain transfer rate constant (k_{ct}), the concentration of abstractable atoms ($[RX]$), and the active center concentration ($[M^*]$). Ionic polymerizations can also undergo chain transfer; however, the mechanism differs. Along with propagation, chain transfer can increase polymer conversion. Often long chains get mechanically entangled, limiting the movement of the active centers. If chain transfer occurs, new chains can be created that are free to diffuse throughout the system and react with the remaining monomer.

Termination

In a free-radical system, polymer chains can be terminated by either combination or disproportionation.⁹ In termination by combination, two active centers combine to form a covalent bond, and the length of terminated polymer is the sum of the lengths of the two chains bonded together (Equation 1-11).



In termination by disproportionation, a hydrogen is abstracted from a growing chain (M_m^*) to terminate another growing chain (M_n^*); removal of the hydrogen terminates the first growing chain (M_m^*) with an unsaturated bond. In this case, the terminated chains remain separate (Equation 1-12).



The rate of termination (R_t), for both combination and disproportionation is

$$R_t = k_t[M^*]^2 \quad (1-13)$$

where k_t is the rate constant of termination.

Termination in cationic or anionic chain polymerization is rare, which is why they are often considered *living* polymerizations. Because the active centers in these mechanisms are ions, they repel each other and, therefore, do not terminate by combination or disproportionation of two active centers. Termination can occur if the ionic active center recombines with its counterion, but most often the active centers simply become trapped in the polymer matrix (see Section 1.2.2).

1.1.2 Energy Deposition

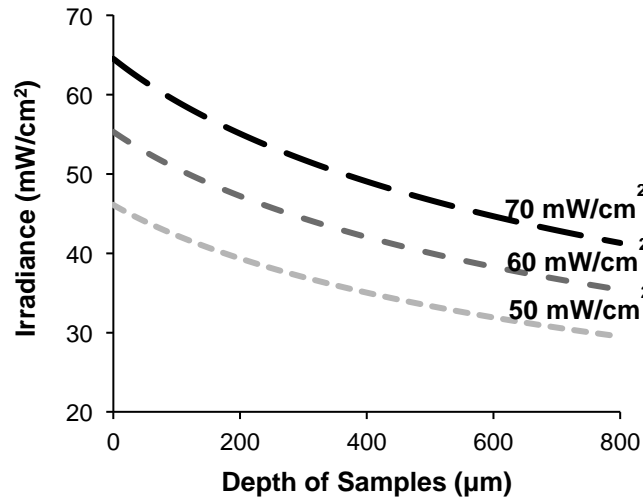
Electron-beam and UV polymerization also differ significantly in energy deposition (Figure 1-5). The energy penetration of UV light is governed by the Beer-Lambert law:

$$A = \varepsilon \ell c \quad (1-14)$$

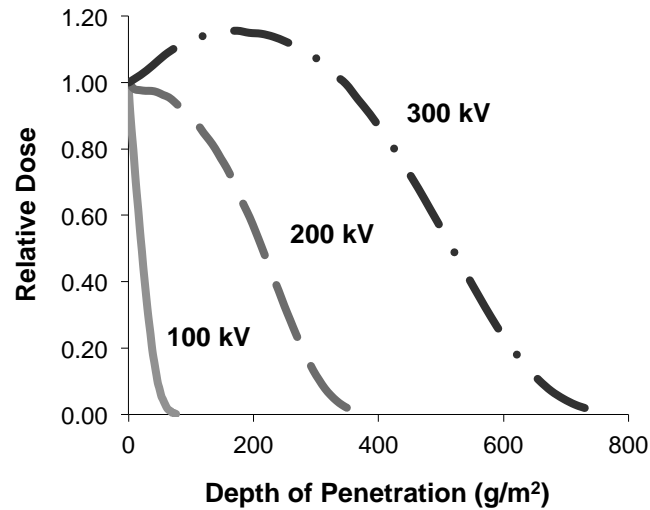
where A is absorbance, ε is the molar absorptivity of the material ($\text{L mol}^{-1} \text{cm}^{-1}$), ℓ is the path length (cm), and c is the concentration of the absorber (mol L^{-1}).⁸ If the law is expressed in terms of percent transmittance ($\%T$), where I_0 is the initial effective irradiance, the equation becomes a function of exponential decay:²²

$$\%T = \left(\frac{I}{I_0} \right) * 100 = e^{-\varepsilon \ell c} * 100 \quad (1-15)$$

Thus, the greatest energy deposition is at the sample surface where 100% of the photons are transmitted.



(A)



(B)

Figure 1-5. A comparison of the energy deposition of UV light (A) and electron beam (B) at an increasing energy and different voltages, respectively. The units of depth of penetration (B, x-axis) become micrometers if the film density is equal to 1 g/cm³.

Electrons, however, do not obey the Beer-Lambert law. Kanaya and Okayama determined the normalized fraction of electrons absorbed per unit mass-thickness is

$$\rho R \frac{d\eta_A}{d(\rho x)} = \frac{\gamma}{(1-\gamma)^2} e^{\frac{-\gamma y}{1-\gamma}} \left\{ 1 + \frac{6 * 1.9}{5} e^{\frac{-0.9\gamma y}{1-\gamma}} \left(\frac{1}{2^{5/6}} \right) - (1-\gamma)^{5/6} \right\} \quad (1-16)$$

where ρR is the mass range, ρx is the mass-thickness, η_A is absorbed electrons, y is the reduced depth, and γ is a parameter encompassing diffusion loss and energy retardation due to electronic collisions.²³ Because of its complexity, electron dose as a function of sample depth is often modeled using Monte Carlo simulations, which can be confirmed experimentally using dosimeters.¹³ These simulations show that, unlike UV, the maximum energy deposition is beneath the sample surface (Figure 1-5, B). The depth of energy maximum is dependent on the voltage used; at higher voltages, the maximum is deeper in the sample. Low energy deposition at the surface is a result of the high energy of the electrons. Most significantly, these differences in energy deposition lead to the necessity of nitrogen inerting in EB curing (see Section 1.2.1).

1.1.3 Exposure vs. Dose

These differences in energy deposition are further reflected in the units. In UV polymerization, energy input is termed *exposure*, which is a surface measurement with units of J/cm^2 . Exposure is the measure of effective irradiance (I) over time (t) (Equation 1-17).

$$\text{Exposure} = \int I dt \quad (1-17)$$

EB polymerization, however, is characterized by *dose* in J/kg , which measures energy input throughout the polymer, not just at the surface. Common units of dose include kilogray and megarad where $1 \text{ Mrad} = 10 \text{ kGy} = 10 \text{ kJ}/\text{kg}$. In terms of processing variables, dose is defined, for a sample moving at a set speed under the radiation source, as:

$$\text{Dose} = \frac{\text{Beam Current} * K}{\text{Line Speed}} \quad (1-18)$$

where K is a constant related to the efficiency of the electrons at a particular voltage.²⁴ By changing the beam current and line speed, the same dose can be given at various speeds. Thus, two samples can be polymerized with the same dose but with different *dose rates*.

1.1.4 Exposure Rate and Dose Rate

EB dose rate has its UV equivalent in *exposure rate*, where effective irradiance and time can be manipulated so that two samples can be polymerized with the same exposure but at different rates (Equation 1-19). It has long been believed that exposure rate has no consequence on the polymer properties due to the exposure reciprocity law, which states

$$It = \text{constant} \quad (1-19)$$

where I is the intensity of the exposing radiation (effective irradiance in the case of photopolymerization) and t is time.²⁵⁻²⁷ However, numerous reciprocity law failures have been reported in recent years, especially in the field of photopolymerized dental materials.²⁵⁻³¹ Wydra, *et al.* astutely highlight that the reciprocity law should only apply to processes that are first-order dependent on the exposing radiation; yet, the rate of propagation (R_p) of free-radical photopolymerization is dependent on effective irradiance (I_0) to the $1/2$ power.^{Q,27}

$$R_p \propto I_0^{1/2} \quad (1-20)$$

The exponent in Equation 1-20 is due to two assumptions: termination is bimolecular (includes both termination by combination and disproportionation) and the pseudo-steady state assumption (the rate of initiation equals the rate of termination) applies. These assumptions presume an ideal reaction with no impediments and are most often valid at the beginning of a reaction. However, most reactions depart from the ideal as vitrification or autoacceleration occur.^{R, 26} Increasing conversion, viscosity, and network stiffening all

^Q The complete R_p equation is

$$R_p = k_p [M] \left(\frac{\phi \alpha [A] I_0 10^3 e^{-\alpha [A] D}}{k_t} \right)^{1/2} \quad (1-20a)$$

where k_p is the propagation rate constant, $[M]$ is the monomer concentration, α is the absorption coefficient, I_0 is the incident effective irradiance at the sample surface, 10^3 is a conversion factor, D is the distance into the sample, and k_t is the termination rate constant. The derivation from Equation 1-8 to Equation 1-20a is demonstrated in Odian.⁹

^R A system is considered vitrified when the polymer chains become immobile and can no longer move to continue propagation or to terminate. Vitrification is caused when enough conversion has occurred that the glass transition temperature of the system is now above the curing temperature; the polymer chains are then

increase the probability of trapping radical active centers, or *monomolecular termination*. As monomolecular termination becomes dominant, the exponent in Equation 1-20 approaches the value of 1, which would validate the reciprocity law. This departure from an ideal reaction may explain the continued acceptance of the reciprocity law, especially when the law is not forced to extremes.

Similarly, EB polymerization is not expected to follow the reciprocity law. Increasing the dose rate increases the concentration of accelerated electrons at any given moment during an EB reaction, since the same amount of energy must be delivered over a shorter time period; in turn, the concentration of radicals ($[M^*]$) is also increased. Both the rate of propagation and the rate of termination are dependent on the radical concentration (Equations 1-8 and 1-13). However, the relationship between radical concentration and rate is first order for rate of propagation and second order for the rate of termination. Thus, increasing the radical concentration causes a larger increase in the termination rate than in the propagation rate, leading to shorter polymer chains and lower conversions. Increasing the exposure rate should have a similar effect in photopolymerization, but, due to the necessity of photoinitiator, there is a maximum achievable concentration of radicals. No such limit exists in EB polymerization.

Because dose rate has a strong kinetic foothold, one would expect to see changes in polymer properties as dose rate is varied, or *dose rate effects* (DRE). Yet, what little research has been done to investigate the impact of dose rate on EB polymerization has conflicting results.^{24,32-37} Perhaps even more perplexing, DREs are noticed in only a minority of materials polymerized in an industrial setting; but, when they do occur, DREs can be costly to circumvent, either by reformulation, increasing the dose, or decreasing the line speed. One possible explanation for why only catastrophic DREs are noticed is that most EB polymers are used as coatings, which need to meet minimal property requirements. As long as the conversion is sufficient, other DREs may not affect the performance of the coating; however, these DREs may be more apparent in free films or products, which must meet stricter property requirements. Additionally, the range in

in the glassy region where they are stiff and inflexible (see Section 1.3.2). Autoacceleration, or the Tromsdorff effect, is characterized by a sudden, sharp increase in the propagation rate and is a departure from the ideal kinetic scheme.¹⁴ It is a result of the exothermic polymerization reaction, which increases the rate of initiation through the kinetic rate constant's dependence on temperature, and vitrification, which limits termination.

magnitude of DREs suggests formulation chemistry (monomer and oligomer) plays a role. Some chemistries may be able to counteract DREs, in some fashion, more efficiently than others.

1.2 Polymerization Systems

1.2.1 Free-Radical Polymerization

Free-radical polymerization is a specific type of chain polymerization in which the active center propagating the reaction is a free radical. Free-radical photopolymerization is a common choice in current photopolymer industries for its quick reaction time, broad range of available monomers, and its insensitivity to moisture.^{9,38} However, free-radical polymerization also experiences oxygen inhibition, shrinkage, and shrinkage stress.³⁸⁻⁴⁰ These disadvantages limit the industrial applications of free-radical photopolymerization.

Oxygen inhibition occurs when oxygen reacts with primary (R^*) or propagating radicals (M_n^*) to form a peroxy radical ($M_nO_2^*$) (Equation 1-21).⁹



Peroxy radicals are much less reactive and effectively terminate chain growth; this premature termination leads to low surface conversions (tacky films) in the oxygen diffusion layer of the coating. Oxygen inhibition can be avoided by using an oxygen-free environment. While feasible in small-scale production, the requirement of such an environment to achieve the desired surface conversion on an industrial-scale is expensive and difficult to maintain.

To combat oxygen inhibition, industrial-scale UV curing typically uses increased effective irradiances and photoinitiator concentrations to increase radical formation.⁴¹ Increasing the radical concentration allows for the sacrifice of some radicals to oxygen consumption, while still retaining enough free radicals to effectively propagate polymerization to high conversions. However, this strategy is wasteful, increases costs, and the level of effective irradiance and photoinitiator concentration must be carefully

chosen. Increasing the radical concentration is helpful for overcoming oxygen inhibition, but if the radicals become too numerous, they can quickly vitrify the polymer network near the coating surface. The vitrified network traps the propagating active centers and reduces the optical clarity, preventing adequate light from penetrating and initiating new active centers deeper in the coating.^S Inadequate light penetration leaves the bottom of the coating wet and with low levels of conversion.

Additionally, this strategy does not work for EB polymerization for two reasons. First, although increasing the EB dose would increase radical concentration, it also increases the probability of chain scission.¹³ Chain scission cleaves –C–C– backbone bonds, reducing the polymer molecular weight and film properties. Second, unlike its UV counterpart, the maximum dose an EB-cured sample receives is not at the sample surface (Figure 1-5, B); thus, the concentration of radicals in the oxygen-inhibition layer is lower and not able to compete. Due to the larger impact oxygen inhibition has on EB polymerization, nitrogen-inerting is used in industrial curing. However, inerting is expensive and limits EB to thin films and coatings, much like UV systems. Other solutions for preventing oxygen from entering the system include shielding films and waxes, but these still require flat geometries, and there are the added processing steps of applying and removing the film/wax.^{4,41}

Shrinkage and shrinkage stress are also problematic for free-radical radiation polymerization. Shrinkage is caused by the shortening of bond length as monomer converts to polymer. The covalent bonds that regulate polymer bond length are shorter than the Van der Waals interactions that regulate monomer spacing.⁹ The volume of methacrylate monomers, for example, can decrease by as much as 25% during polymer cure. The fast conversion rate in free-radical polymerizations further exacerbates the problem by causing the shrinkage to occur rapidly.^{40,42,43} Rapid shrinkage creates areas of shrinkage stress within the polymer, which may later lead to material failure, such as buckling or wrinkling.

^S Examples that could result in a decrease in optical clarity include: increased light scattering of the polymer network versus the monomer formulation; photoinitiator absorption, causing the formation of radicals in the vitrified network that cannot defuse or propagate; or absorption of the photoinitiator fragments.

Monomers

Acrylates are the most commonly used monomers for both EB- and UV-initiated free-radical polymerization (Figure 1-6).

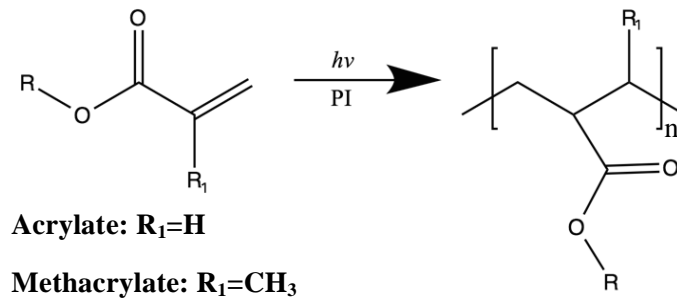


Figure 1-6. Free-radical polymerization of a (meth)acrylate.

They can be easily modified on the ester group to attain a variety of reactivities and physical properties and have high polymerization rates. In free-radical photopolymerization, methacrylates are also frequently used. As with acrylates, the methacrylate ester can be easily modified; however, due to the steric hindrance of the methyl group and the increased stability of the methacrylate radical, methacrylates can be three to seven times less reactive than their identical acrylate.⁴⁴ This decrease in reactivity results in slower polymerization rates in UV-initiated polymerization, and may be the reason methacrylates do not achieve any appreciable conversion in EB-initiated polymerization. Additionally, both acrylates and methacrylates are inexpensive and widely commercially available.

Initiators

Free-radical initiators for UV polymerization generally fall into two categories: Type I (cleavage initiators) and Type II.^{9,11} Type I initiators, when excited by a photon, undergo homolytic cleavage to form propagating radicals. Figure 1-7 shows the α -cleavage of Type I photoinitiator 2,2-dimethoxyphenyl acetophenone (DMPA).

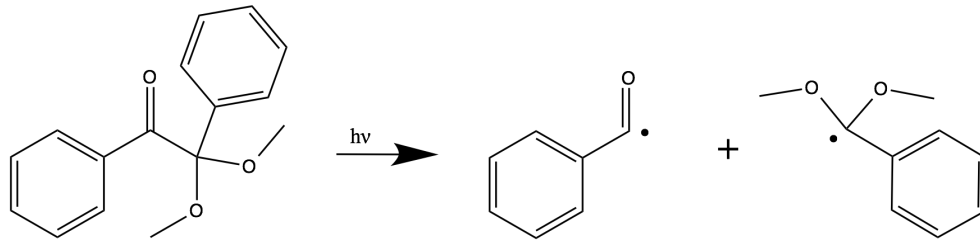


Figure 1-7. α -cleavage of DMPA to produce propagating free radicals.

Both radicals produced by the α -cleavage of DMPA can initiate polymerization.

Type II initiators require a co-initiator, with which they react when promoted to an excited state by the absorption of a photon. This reaction is either a hydrogen abstraction or a transfer of an electron. An example of hydrogen abstraction from N-methyldiethanolamine (MDEA) by benzophenone is shown in Figure 1-8.

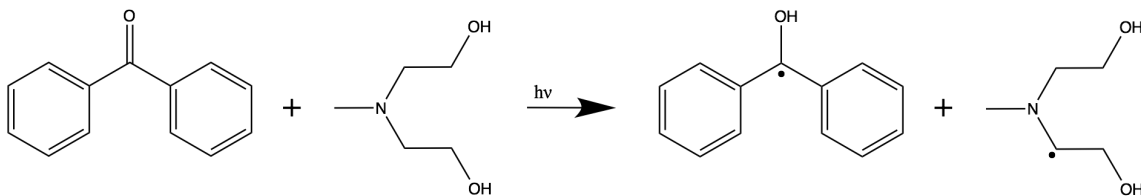


Figure 1-8. H-abstraction from MDEA by benzophenone to produce a propagating free radical

Here, the amine radical initiates polymerization.

Both the Type I and Type II photoinitiators shown above are examples of benzoyl-chromophore-based photoinitiators.¹¹ The benzoyl chromophore absorbs light in the UV and/or near-UV range and, as such, is the basis for many efficient photoinitiators developed for UV-curing applications. The X and Y groups on the chromophore affect how efficiently and at what wavelengths the photoinitiator absorbs (Figure 1-9).

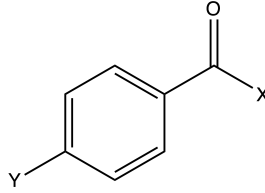


Figure 1-9. The X and Y groups on a benzoyl chromophore affect the wavelength range and efficiency of the photoinitiator.

EB free-radical polymerization does not require an initiator. As shown in the summary of the EB initiation mechanism (Section 1.1.1), the accelerated electrons have sufficient energy to cleave monomer molecules into initiating radicals, to which other monomer molecules add to create a propagating chain.

1.2.2 Cationic Polymerization

Cationic polymerization, like free-radical, is a type of chain polymerization.⁹ It is not as broadly used in photopolymer industries as free-radical polymerization because of its tendency toward a slow reaction speed.^T Where a free-radical reaction can achieve solid polymer in mere seconds, a cationic reaction might require minutes or hours. Additionally, the development of useable cationic photoinitiators is relatively recent and occurred after the establishment of free-radical polymerization. Cationic polymerization is also more susceptible to side reactions with impurities, such as bases, than its free-radical counterpart. However, cationic polymerization often excels in areas where free-radical polymerization falls short. Cationic polymerization suffers from less shrinkage (and consequently less shrinkage stress) than free-radical polymerization because the majority of cationic monomers undergo a ring-opening reaction (Figure 1-14). Unlike the single C–C bond incorporated into the polymer backbone in a free-radical system, the ring of the cationic reactive moiety contains multiple bonds, which are all incorporated into the polymer backbone as the ring opens, making the distance between repeat units similar to the Van der Waal's spacing of the monomers. Cationic active centers are also not hindered by oxygen, and, therefore the polymerization is not oxygen inhibited.

^T Vinyl ethers are an exception.

As previously discussed, termination of the cationic active centers is rare (Section 1.1.1). Without termination, the long-lived active centers can continue to propagate hours, days, or even weeks after the initiating UV light is removed. This continued polymerization in the absence of a light source is called post-polymerization or *dark cure*.^{10,45} In addition, these active centers possess mobility through reactive diffusion and may lead to polymerization in regions of the coating or film never exposed to light – a process termed *shadow cure* (Figure 1-10).

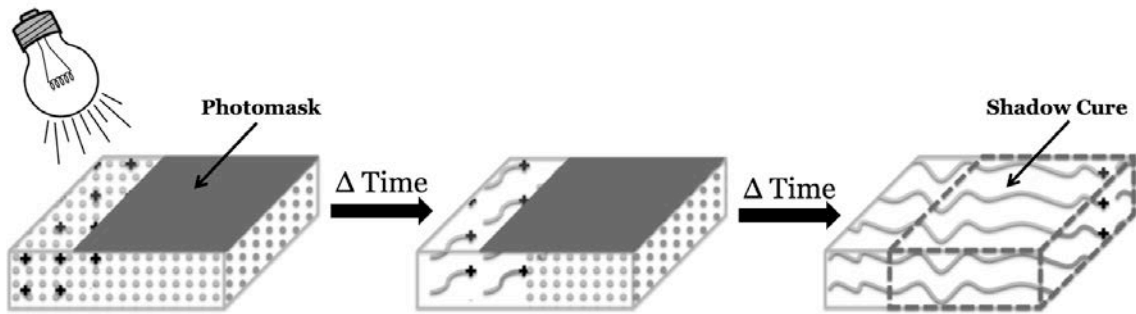


Figure 1-10. Over time, long-lived cationic active centers can diffuse into unilluminated areas and propagate. Polymer created in these unilluminated areas is called shadow cure.

Shadow cure, especially, has great potential to succeed in applications where traditional free-radical photopolymerization fails: optically thick systems; systems containing pigments, dyes, and/or fillers; systems with complex geometries, in which areas of the coating are effectively masked from the illuminated light source or do not receive equal exposure. In these light-challenged systems and in traditional systems, the ability of cationic polymerization to dark and shadow cure may also alleviate problems associated with cationic's slow rate of propagation. Because of dark/shadow cure, the film or coating does not need to remain exposed to light for the entire length of the reaction. And once a green strength is achieved, the cationic polymer could be rolled or stacked, packaged, and shipped, all the while continuing to polymerize until it reached its final properties, hopefully timed simultaneously with reaching its consumer destination.

Another challenge of cationic polymerization is its moisture sensitivity; a change in the humidity results in differences in the polymer network and, therefore, different physical properties in the resulting polymer.^{46,47} Without a moisture-controlled

environment, reproducibility of products following cationic polymerization would be impossible.

Cationic polymerization is moisture sensitive because water activates a second type of propagation mechanism. Propagation of cationically polymerizable monomers typically proceeds through the active chain end (ACE) mechanism.⁴⁸ An example of an epoxide monomer propagating by the ACE mechanism is shown in Figure 1-11.

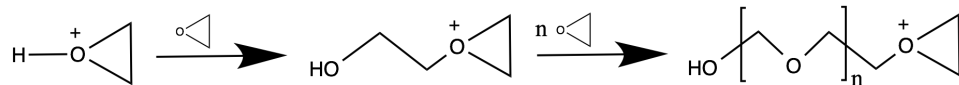


Figure 1-11. The cationic active chain end (ACE) propagation mechanism. Adapted from Reference 48.

However, a second mechanism, the activated monomer (AM) mechanism, occurs in the presence of a hydroxyl group, such as a water molecule or an alcohol moiety (Figure 1-12). In this chain transfer reaction, a hydroxyl group attacks a protonated monomer molecule at the carbon alpha to the oxygen, causing the epoxide ring to open and the release of a proton. This proton can then activate another epoxide monomer, which can proceed by the ACE mechanism to start a new polymer chain or by the AM mechanism to grow an existing polymer chain, depending on whether it is attacked by an epoxide monomer or hydroxyl group, respectively.⁴⁹

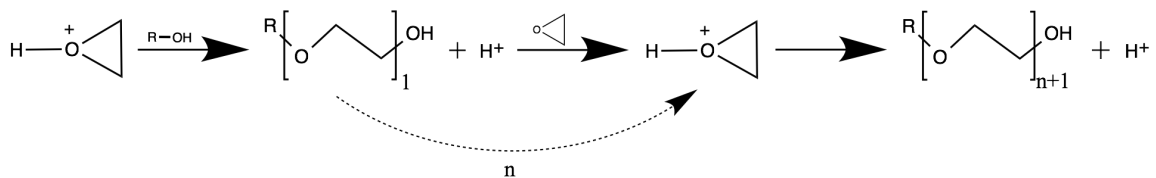


Figure 1-12. The cationic activated monomer (AM) propagation mechanism. This mechanism is promoting in the presence of hydroxyl groups. Adapted from Reference 48.

The ACE mechanism is known to result in slow propagation, which is evident by the low light-cured conversion of neat epoxides; however, previous research has found that the propagation rate constant for the AM mechanism can be approximately five times higher

than that of the ACE mechanism for a cyclic ether.⁵⁰ In addition to increasing the propagation rate, promoting the AM mechanism produces polymer networks that have higher conversions and are more branched (Figure 1-13).⁵¹ Establishing control over the balance of ACE and AM mechanisms should provide an additional pathway to tailoring polymer properties – a benefit that could outweigh the cost of humidity-controlled production lines.

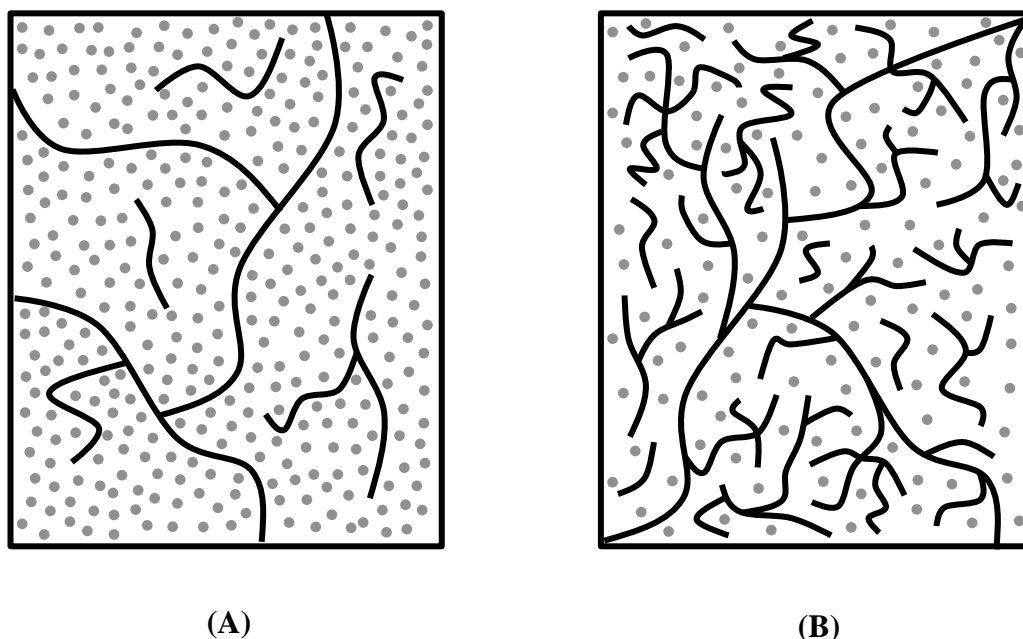


Figure 1-13. The architecture of the polymer network is influenced by whether the ACE mechanism (A) or the AM mechanism dominates (B). Adapted from Reference 51.

Monomers

Examples of monomers that can be photopolymerized via the cationic mechanism include some olefins, such as methoxyethene, and heterocyclic molecules, such as cyclic ethers, lactones, and lactams; of these, epoxides are the most widely used (Figure 1-14).⁵² Epoxides have good adhesion and mechanical properties and exhibit only 1-2% shrinkage.⁵³ Epoxides also have good heat and chemical resistance; however, they possess low reaction rates compared to acrylates. Epoxides have been shown to react using EB as well as UV.^{19,54}

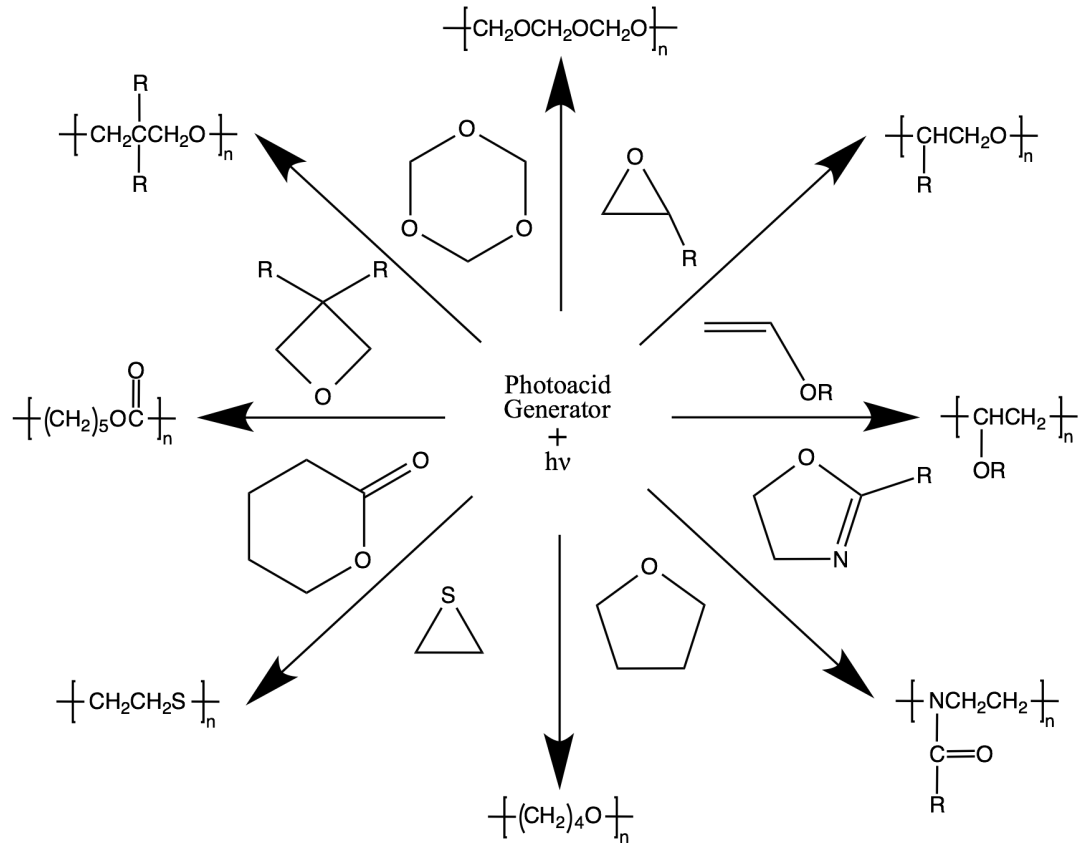


Figure 1-14. Examples of monomers that photopolymerize via the cationic mechanism. Adapted from Reference 52.

Initiators

Iodonium and triarylsulfonium salts comprise the majority of photoinitiators for cationic polymerization (Figure 1-15).^{11,55,56}

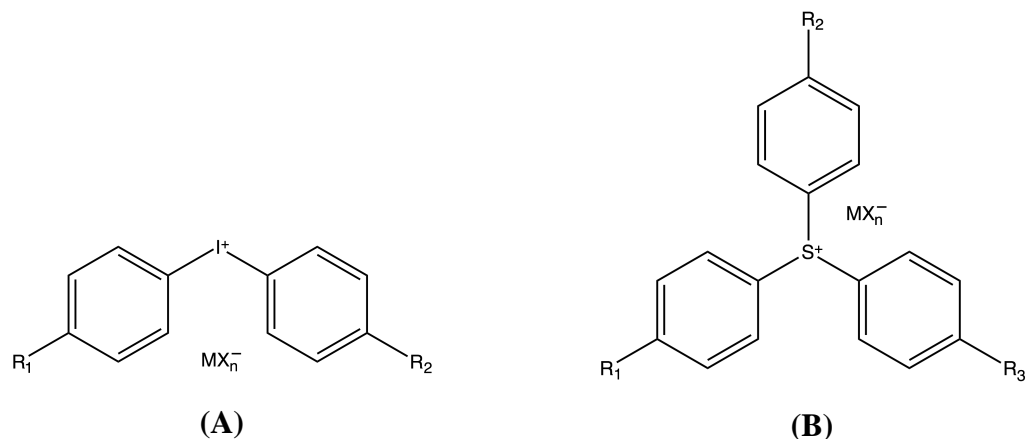


Figure 1-15. General structures of diaryliodonium (A) and triarylsulfonium salts (B).

Because these salts work by producing a highly acidic species upon exposure to light, they are often referred to as photoacid generators. Each onium salt contains an organic cation and an inorganic anion. As the light-absorbing portion, the structure of the cation governs the absorption spectrum and efficiency, the quantum yield, as well as the thermal stability of the photoinitiator.¹¹ The initiation efficiency and the strength of the acid formed are determined by the anionic structure. A simplified mechanism for the activation of a photoacid generator is shown for the case of 4-(2-hydroxyl-1-tetradecyloxy)-phenyl] phenyliodonium hexafluoroantimonate (DAI) in Figure 1-16. The absorption of light leads to the cleaving of the carbon-iodine bond. The cation formed is highly reactive and will abstract a hydrogen from a donor (monomer, impurity, or water) to form a neutral molecule, a radical, the cationic initiating species H^+ , and the counterion SbF_6^- . Throughout the polymerization reaction, the counterion remains near its cation (forming a propagating ion pair $H^+SbF_6^-$). In the rare cases of termination, the cation recombines with the counterion.

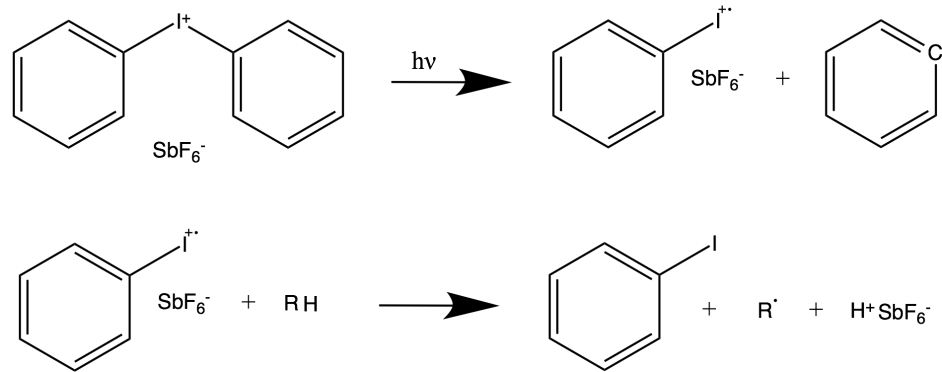


Figure 1-16. Photoactivation of a diaryliodonium hexafluoroantimonate photoacid generator (DAI).

Unlike free-radical polymerization, EB requires an initiator to commence cationic polymerization in all but the most extreme cases. Occasionally, some ultra pure monomers in moisture- and oxygen-free conditions can undergo *free cationic*, EB polymerization without initiator; however, such conditions are not practical, and, instead, cationic EB polymerization is typically initiated using the same onium salts used in photopolymerization.²⁰ Two mechanisms have been proposed for how EB radiation interacts with the onium salts to form a cationic active center. In the first mechanism, an accelerated electron cleaves a monomer bond, forming a radical on the monomer (Figure 1-17, A). Rearrangement of reactive moiety occurs until the radical is of sufficient strength to reduce the onium salt, creating an active center. In the second mechanism, the accelerated electron directly reduces the onium salt and then finds a cation to form the propagating ion pair (Figure 1-17, B).

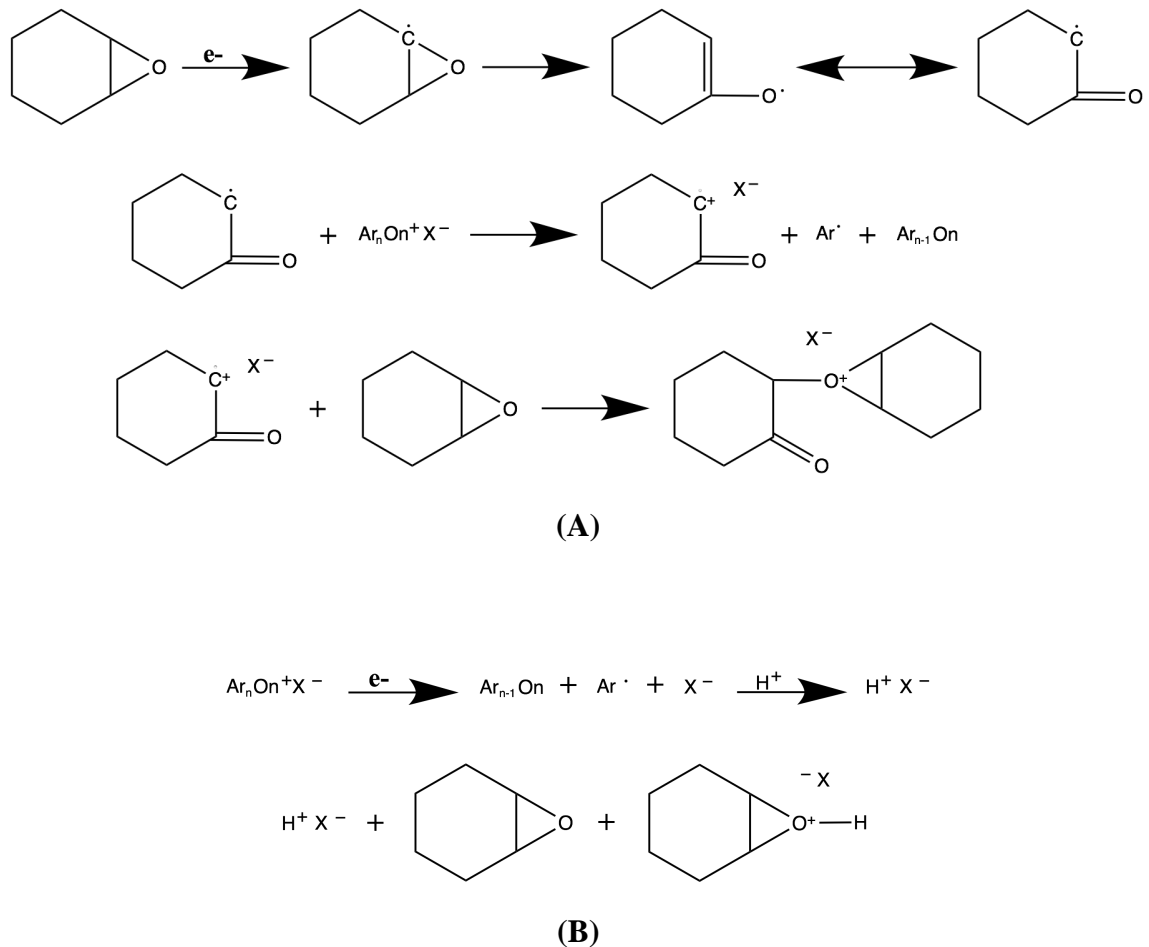


Figure 1-17. Two proposed mechanisms of EB-initiated cationic polymerization.

1.2.3 Hybrid Polymerization

Hybrid photopolymers use two (or more) mechanisms of polymerization in a single reaction system, such as the combination of free-radical and cationic polymerization. Previous research has demonstrated that free-radical/cationic hybrid systems can reduce the limitations of traditional polymer systems, including decreased sensitivity to moisture and oxygen.^{41,46,57} Other advantages can include reduction in shrinkage and shrinkage stress and continued conversion with dark and shadow cure for acrylate/epoxide systems. These advantages are the result of pairing polymerization mechanisms that are, in many ways, opposites. Oxygen inhibition is limited in the hybrid system because the cationic mechanism, unaffected by oxygen, simply takes over in oxygen-rich areas where the free-radical mechanism flounders. Adding any amount of a

moisture-insensitive, free-radical-pathway monomer reduces moisture sensitivity by just decreasing the fraction of the moisture-sensitive cationic monomer; the faster propagation rate of the free-radical monomer also restricts formation of the cationic network.^U

Similarly, any amount of a ring-opening, cationic monomer reduces shrinkage/stress by decreasing the fraction of free-radical monomer, and the mere presence of cationic monomer in a hybrid system allows for dark/shadow cure.

Along with many advantages in property development, hybrid systems also provide opportunities for better property control. Properties such as storage modulus, glass transition temperature, tensile strength, hardness, and cross-linking density can be tuned by adjusting the relative concentrations of reactive functional groups. Of course, changing the monomers and the number of functionalities on each monomer will also alter these physical and mechanical properties.

Functionality, for instance, determines the type of hybrid network produced. In an interpenetrating network (IPN), two monomers are polymerized and the two polymers produced are joined only through co-entanglement (Figure 1-18). A semi-IPN is the entanglement of one cross-linked polymer and one linear polymer. A full-IPN results when two difunctional monomers are polymerized, creating an entanglement of two, independently cross-linked polymers. Formation and alteration of polymer networks has long been known to vary the properties of the polymer.^{4,9} This statement is also true for hybrid polymer networks.

^U This statement is true in the bulk system. At the oxygen-rich surface, the free-radical mechanism is inhibited, and, therefore, does not impede the cationic network formation.

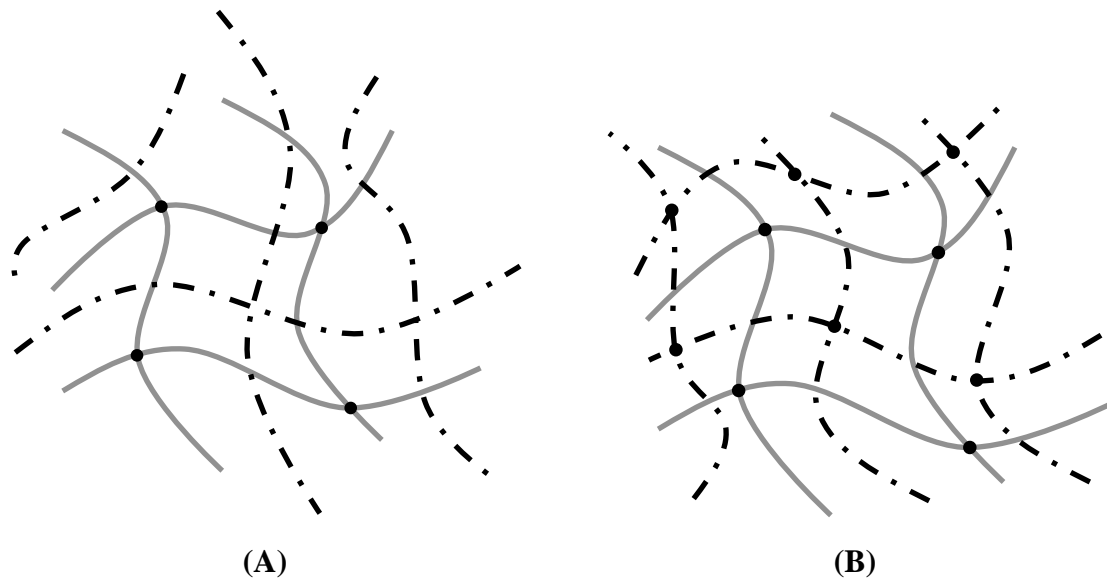


Figure 1-18. In an interpenetrating network (IPN), Polymer A (dashed line) is mechanically entangled to Polymer B (solid line), but each polymer is only covalently bonded (circles) to itself. In a semi-IPN (A), Polymer A is linear and Polymer B is cross-linked, and in a full-IPN (B), both polymers are cross-linked. Adapted from Reference 62.

Additionally, selecting photoinitiators that activate at different wavelengths of light can control the timing of the initiation of each polymerization mechanism. If the cationic photoinitiator only activated in the UV region and the free-radical photoinitiator only responded to visible light, the cationic mechanism, for example, could be given a head start by first illuminating with only UV light, followed by a combination of UV and visible light. Staggering the initiation will affect network formation and thus, the polymer properties; properties can be tailored by the order of the reactions, as well as the time difference between the two initiations.

One challenge with hybrid systems is phase separation. Phase separation is the formation of homopolymer domains due to a lack of mutual solubility (Figure 1-19).

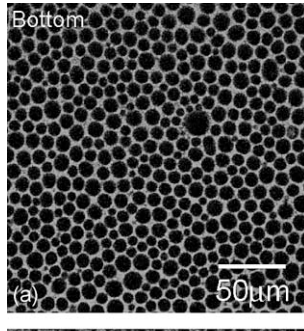


Figure 1-19. A laser scanning confocal microscopy image of phase separation

Factors that affect phase separation include the type of hybrid polymer network present, the order of the two monomer reactions, and the compatibility of secondary functional groups.⁵⁸⁻⁶⁰ The scale on which phase separation takes place governs its impact on polymer properties. Nanophase separation, for instance, results in toughening of the polymer; conversely, microphase separation has a negative effect on mechanical properties.⁶¹

Phase separation can be controlled by creating grafted polymer networks (GPNs). GPNs form when the two polymers are not only co-entangled but are covalently bonded together.⁶² In an acrylate/epoxide hybrid system, promoting the AM mechanism with a hydroxyl group located on the acrylate monomer will covalently bond the epoxide network to the acrylate chain through the hydroxide (Figure 1-20). GPNs can also be created using a hybrid monomer (see below).

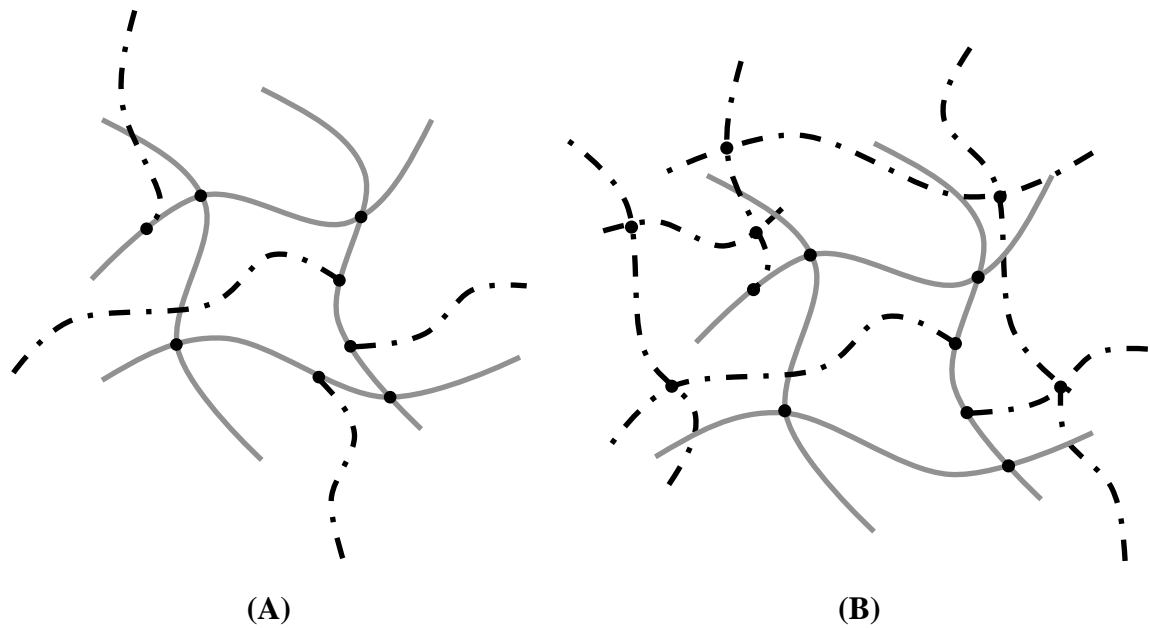


Figure 1-20. In a grafted network, Polymer A (dashed line) is covalently bonded (circles) to Polymer B (solid line). In a semi-grafted network (A), Polymer A is linear and Polymer B is cross-linked, and in a full-grafted network (B), both polymers are cross-linked. Adapted from Reference 62.

Monomers

Hybrid formulations can either consist of a single hybrid monomer, which contains two different reactive moieties, or a formulation comprised of a combination of traditional monomers, each containing one type of reactive moiety. One example of a hybrid monomer is 3,4-epoxy-cyclohexyl-methyl methacrylate (METHB, Figure 1-21, A). It contains both an epoxide functionality (which will proceed by cationic polymerization) and an acrylate functionality (which will proceed by free-radical polymerization) in a single molecule. An example of an acrylate/epoxide hybrid formulation containing traditional monomers would be a solution of 3,4-epoxycyclohexane carboxylate (EEC) and 2-hydroxyethyl methacrylate (HEMA, Figure 1-21, B).

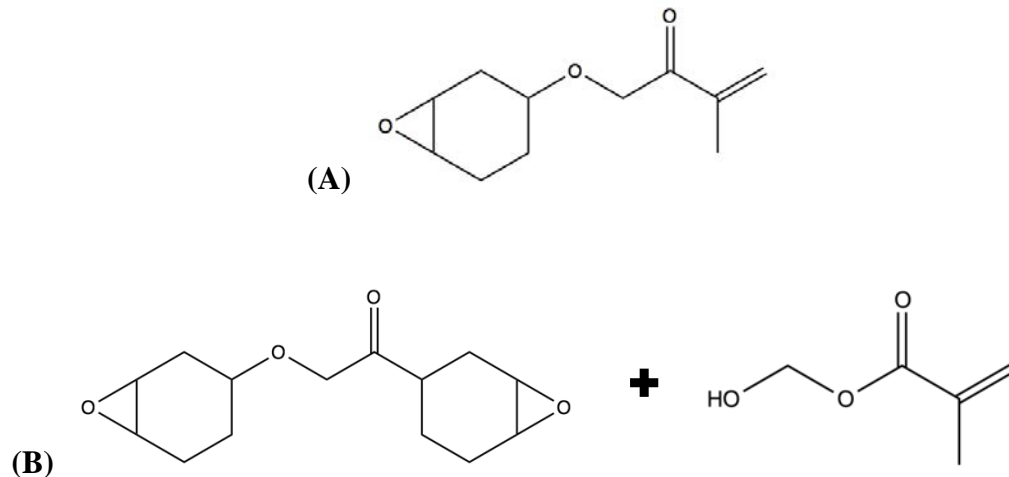


Figure 1-21. A hybrid resin can consist of a single hybrid monomer containing two different functional groups (A) or a solution of two or more monomers with different functional groups (B).

Initiators

Most hybrid formulations contain a dual-initiator system, consisting of both a free-radical and a cationic initiator. However, free-radical polymerization can be initiated by some cationic initiators.¹¹ The photoactivation of DAI, for example, produces a free radical in addition to the cation (Figure 1-16).

1.3 Analytical Methods

Raman spectroscopy and dynamic mechanical analysis are the principal analytical instruments used in this research. Together, these instruments provide complementary data to elucidate the influence of monomer chemistry and polymer development on the resulting physical and mechanical properties.

1.3.1 Raman Spectroscopy

Raman spectroscopy is a well-established technique for the characterization of polymers.^{46,57,63-65} It is commonly used for determining conversion, rate of polymerization, and polymer identification, but it is also capable of gathering information such as molecular orientation, degree of crystallinity, and presence/magnitude of internal

stresses. In this research, Raman is primarily used to calculate bulk conversion, as well as conversion as function of depth.

When molecular bonds interact with electromagnetic radiation, it causes a transition to occur between electronic states and/or vibrational and rotational levels, depending on the wavelength of the radiation.^{66,67} Microwaves, for example, only cause molecular rotation, whereas infrared light, with its increased energy, causes molecular vibration and rotation. Of interest is the type of scattering the photon undergoes during this interaction. There are three possible outcomes: elastic scattering, also known as Rayleigh scattering,^V in which the photon is released from the bond (or group of bonds) at the same frequency as it entered; Stokes scattering, in which part of the photon's energy is absorbed by the bond and the photon is released with a frequency of $\nu_o - \nu_m$, where ν_o is the incident frequency and ν_m is the scattered frequency; anti-Stokes scattering, in which the photon gains energy from the bond and is released with a frequency of $\nu_o + \nu_m$ (Figure 1-22).^{66,68} Rayleigh scattering is by far the most common outcome, with only one in a billion photons resulting in Stokes or anti-Stokes scattering.⁶⁹

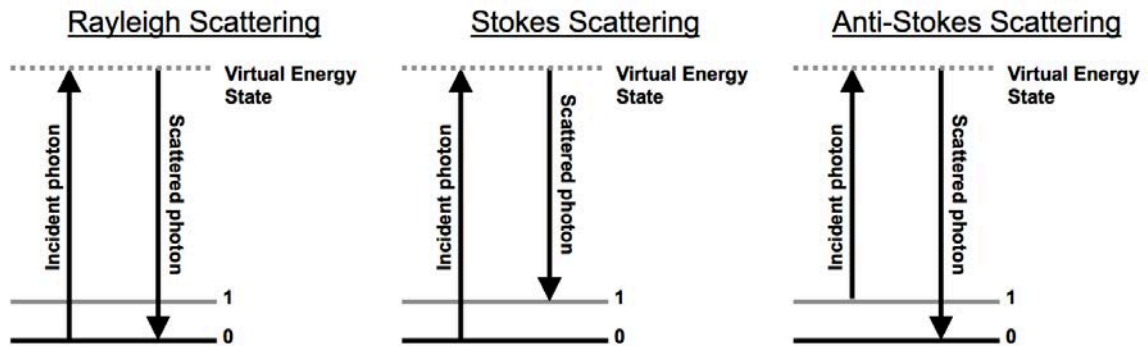


Figure 1-22. Raman spectroscopy relies on the inelastic scattering of photons by either Stokes or anti-Stokes scattering.

Raman spectroscopy is a finger-print technique based on the inelastic scattering of photons.⁷⁰ Both Stokes and anti-Stokes scattering can be used for Raman spectroscopy.

^V Elastic scattering is termed Rayleigh scattering when the wavelength of the incident light beam is much larger than the dimensions of the scatter (*e.g.*, atom or molecule). Debye and Mie scattering are types of elastic scattering that occurs when scatter dimensions are approximately equal to or greater than the wavelength of incident light, respectively.⁶⁶

However, Stokes scattering is generally preferred because more molecules populate the ground state, from which the Stokes signal is generated, than the excited states, from which the anti-Stokes signal is produced; thus, Stokes scattering provides higher intensities.

Because Raman spectroscopy is reliant on inelastic scattering, only those molecular bonds able to alter photon frequency are considered *Raman active*. These frequency changes are the result of a change in the bond's polarizability during a vibration.⁶⁶ Polarizability is the efficiency of a given incident frequency of electromagnetic radiation to induce a dipole in a particle. A bond with a large change in its polarizability will have a correspondingly more intense Raman band than a bond with a small change in polarizability.⁶⁷ Strongly polar bonds, which already contain a significant dipole in the ground state, are weak Raman scatterers because the efficiency of creating a dipole is not appreciably changed during a vibration. In contrast, relatively neutral or nonpolar bonds are excellent Raman scatterers because they have almost no dipole in their ground state, and, therefore, a large change in polarizability can occur during a vibration.

In Raman spectroscopy, a single incident wavelength (typically a laser) is used to excite a sample's molecular bonds, the scattered light is collected, and sophisticated filters are used to block the Rayleigh scattering. The changes in photon frequency as a result of Stokes scattering are recorded by the instrument and translated into Raman shift (cm^{-1}), defined in wavenumbers

$$\text{wavenumber} = \left(\frac{1}{\lambda_0} - \frac{1}{\lambda_1} \right) * 10^7 \quad (1-22)$$

where λ_0 is the source wavelength (nm) and λ_1 is the emission wavelength (nm). These wavenumbers are plotted as a function of Raman intensity (a.u.) to produce a Raman spectrum (Figure 1-23).

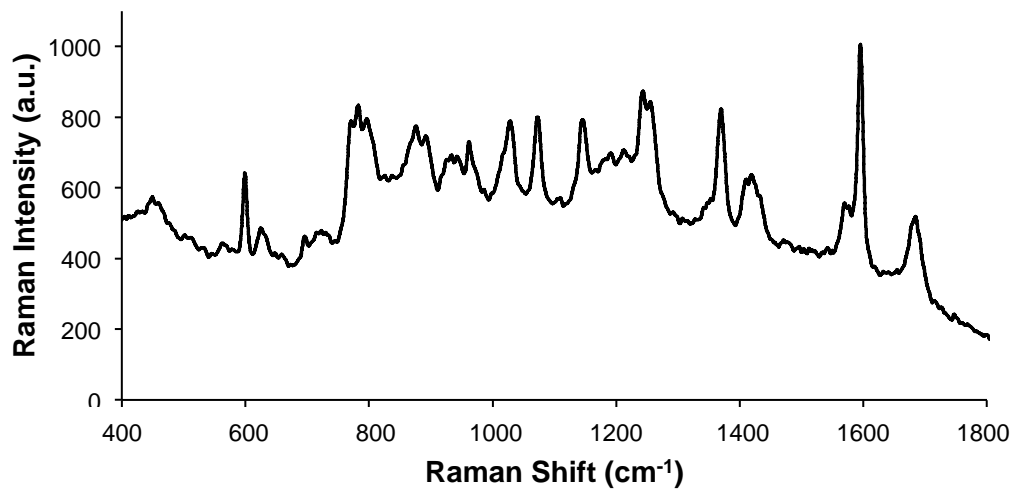


Figure 1-23. Example of a Raman spectrum of 2-hydroxy-3-phenoxypropyl acrylate.

Specific wavenumbers, or ranges of wavenumbers, correspond to specific Raman-active chemical bonds. Thus, it is possible to identify the Raman-active bonds in a molecule, as well as changes in those bonds. For example, during free-radical chain polymerization, the -C=C- bond of the monomer is consumed as propagation occurs. Initially, the presence of the -C=C- bond is characterized by a peak at 1640 cm^{-1} (for acrylates), but as the reaction proceeds and the bond is consumed, this peak diminishes (Figure 1-24).

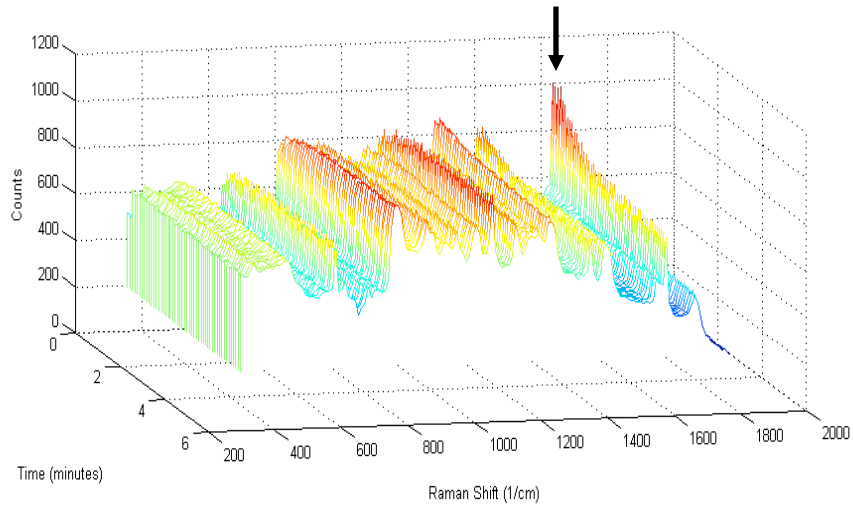


Figure 1-24. An example of the disappearance of the -C=C- acrylate bond, represented by the 1640 cm^{-1} peak (arrow), during photopolymerization.

The Raman spectra in this example not only demonstrate the qualitative change in the sample, but can be used for quantitative measurements of polymer conversion.

Conversion (α) is the fraction of reactive functional groups that have been incorporated into a polymer chain. Because peak intensity is directly proportional to the concentration of bonds characterized by that peak, the peak intensity of the reactive moiety in the monomer can be compared to that of the polymer to determine conversion. Additionally, a reference peak, stable throughout the reaction, is used to remove instrumental variations. Expressed mathematically, conversion is,

$$\alpha = 1 - \frac{I_{rxn}(P)/I_{ref}(P)}{I_{rxn}(M)/I_{ref}(M)} \quad (1-23)$$

where $I_{rxn}(P)$ and $I_{ref}(P)$ are the peak intensities of the reaction and reference peak of the polymer, respectively; $I_{rxn}(M)$ and $I_{ref}(M)$ are the peak intensities of the reaction and reference peak of the monomer.⁵⁷

Raman spectra can be collected on the order of milliseconds, allowing for real-time conversion analysis of UV-cured materials. Moreover, Raman spectra can be used to track multiple functional groups simultaneously. In hybrid systems, for example, both the epoxide and acrylate conversions can be calculated from a single Raman data set.

Raman measurements can also be taken without pretreatment or destruction of the sample, which allows for further testing on the same sample with dynamic mechanical analysis (DMA), gel permeation chromatography (GPC), and other analytical tools.

By routing the laser (incident light source) through a microscope and using a small diameter collection fiber ($\leq 20 \mu\text{m}$), confocal Raman measurements can be collected.^{64,71} Confocal Raman allows for depth analysis without sacrificing the sample. As seen in Figure 1-25, only the laser scattering from the focal plane reaches the detector; therefore, the resulting Raman spectrum is indicative of the chemistry at that point in the sample.⁷² The focal plane can be moved in the Z-direction by simply changing the height of the microscope stage. A compilation of these confocal Raman spectra shows bond changes, and subsequently conversion, as a function of depth.

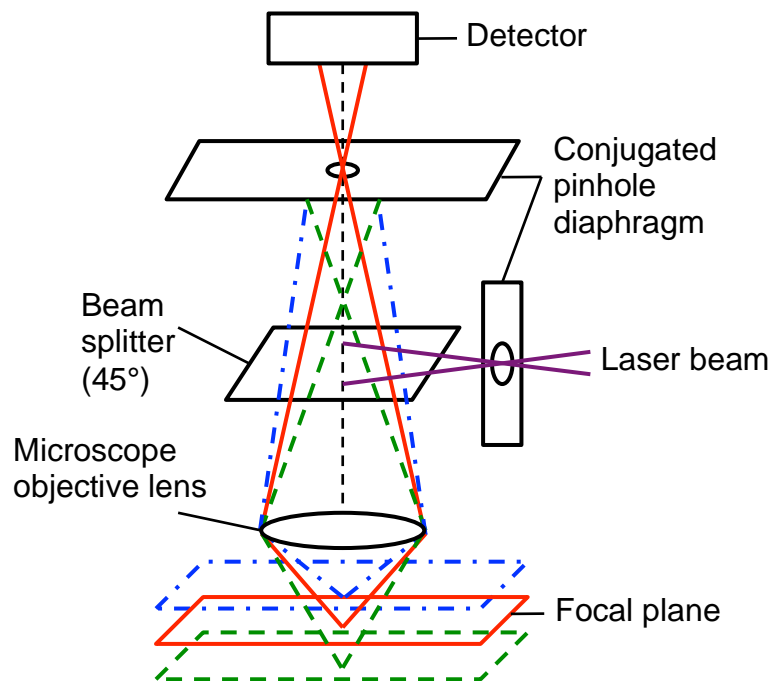


Figure 1-25. Schematic illustrating confocal Raman microscopy, adapted from Reference 72. The beam splitter is angled 45° to the incident laser beam. Only the laser scattered at the focal plane (red, solid line) reaches the detector.

1.3.2 Dynamic Mechanical Analysis

Dynamic mechanical analysis (DMA) is the use of sinusoidal deformation to determine the physical and mechanical properties of a material.⁷³ These material

properties include quantitative values such as the glass transition temperature (T_g), storage modulus, tensile strength, and cross-linking density, as well as qualitative estimations of network homogeneity. The variety of clamp types available allows materials to be tested in tension, shear, compression, *etc.* In this research, DMA is used to determine polymer T_g and estimate the cross-linking density.

Polymers exhibit viscoelastic behavior, meaning their response to deformation is neither wholly that of a viscous material (dependent on strain rate) or that of an elastic material (independent of strain rate) but some combination of the two responses.⁷³ This combination, termed the complex modulus, can be found using measurements of stress and strain. DMA applies a sinusoidal stress (σ) at a certain frequency or frequency sweep to a sample of known geometry, and the resulting strain (ε) is measured (or vice versa). Stress and strain are defined as

$$\sigma = \sigma_0 \sin(t\omega + \delta) \quad (1-24)$$

$$\varepsilon = \varepsilon_0 \sin(t\omega) \quad (1-25)$$

where t is time, ω is frequency, and δ is the phase lag between strain and stress. Since phase lag is only an artifact of viscous materials, δ is an important variable for determining polymer properties.

Once the value of δ is obtained, it is used to compute the storage modulus and the loss modulus, subcomponents of the complex modulus. Storage modulus (E') is representative of the material's elastic response and quantifies the energy stored in the material.

$$E' = \frac{\sigma_0}{\varepsilon_0} \cos \delta \quad (1-26)$$

Loss modulus (E'') is representative of the material's viscous response and quantifies energy lost as heat.

$$E'' = \frac{\sigma_0}{\varepsilon_0} \sin \delta \quad (1-27)$$

Ratioing the loss modulus to the storage modulus results in the phase angle, also known as $\tan \delta$.

$$\tan \delta = \frac{E''}{E'} \quad (1-28)$$

The $\tan \delta$, graphed as a function of temperature, elucidates the thermal transition states of the polymer. The temperature at which the maximum of the $\tan \delta$ appears is called the glass transition temperature (T_g) and is an important polymer property as it marks the temperature at which the polymer transforms from a brittle, glass-like material to a flexible, rubbery material (Figure 1-26).

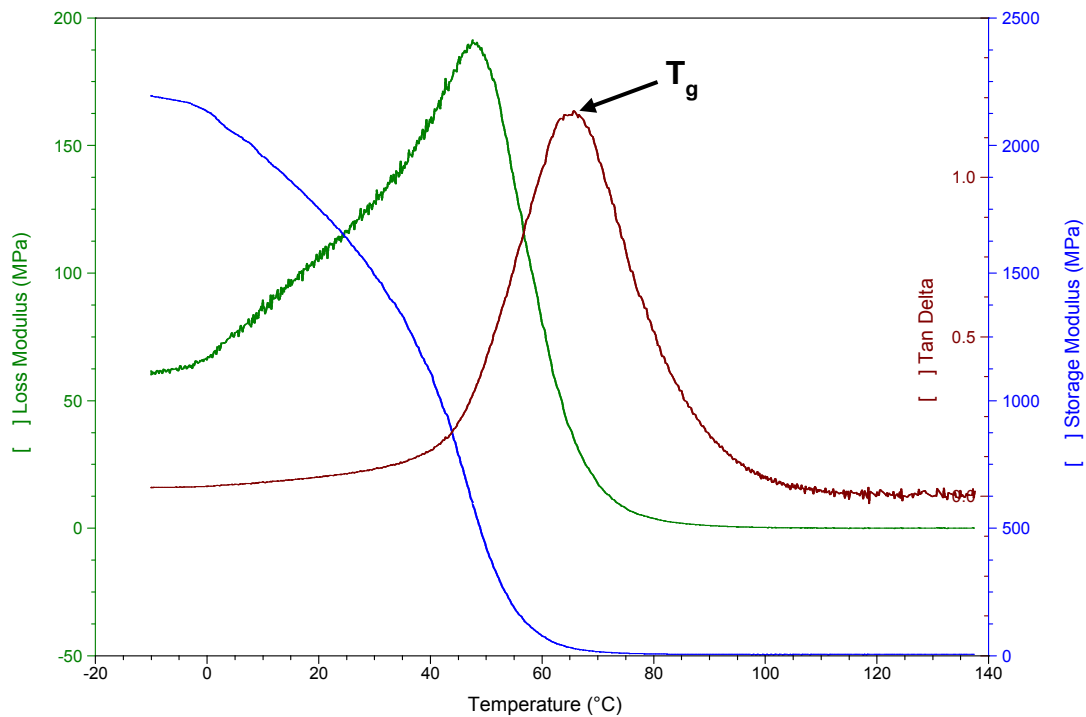


Figure 1-26. A DMA graph illustrating how the loss modulus (green), storage modulus (blue) and $\tan \delta$ (red) change with temperature. The temperature at which the maximum of the $\tan \delta$ peak occurs is taken as the glass transition temperature (T_g). Below the T_g , the polymer is in the glassy region, and above the T_g the polymer is in the rubbery region.

Cross-linking density (ν_e) can also be estimated by DMA using the storage modulus^W:

$$\nu_e = \frac{E'}{3RT} \quad (1-29)$$

where R is the ideal gas constant and T is absolute temperature. The cross-link density is a measure of the number of network chains per unit volume of polymer (mol/cm³). Increasing a material's cross-link density decreases its network flexibility and can increase the T_g. Additionally, Equation 1-30 is an alternative equation for materials expected to have a high cross-link density.⁷⁴

$$\nu_e = \frac{\log(E') - 7}{293} \quad (1-30)$$

^W Values of the storage modulus must be taken from the rubbery plateau region for use in this equation and in Equation 1-30.

1.4 References

- (1) Mounce, W. D. *Basics of Biblical Greek Grammar*; Zondervan, **2009**.
- (2) Houghton Mifflin Company. *The American Heritage Student Science Dictionary*, 1st ed.; Houghton Mifflin Harcourt: Boston, **2009**.
- (3) Drobny, J. G. *Radiation Technology for Polymers, Second Edition*, 2nd ed.; CRC Press, **2010**.
- (4) Fouassier, J.-P. *Photoinitiation, Photopolymerization, and Photocuring: Fundamentals and Applications*; Hanser/Gardner Publication Inc.: Cincinnati, **1995**.
- (5) Cohen, G. UV-EB Market Trends. *RadTech Report* **2012**, No. 2, 44–48.
- (6) *Radiation Curing: Science and Technology*, 1st ed.; Pappas, S. P., Ed.; Springer Science & Business Media: New York, **1992**.
- (7) Golden, R. What's the Score? A Method for Quantitative Estimation of Energy Use and Emission Reductions for UV/EB Curing. *RadTech Report* **2012**, 1–5.
- (8) Lykos, P. The Beer-Lambert Law Revisited. *Journal of Chemical Education* **1992**, 69 (9), 730–732.
- (9) Odian, G. *Principles of Polymerization*, 4 ed.; John Wiley and Sons, Inc., **2004**.
- (10) Ficek, B. A.; Thiesen, A. M.; Scranton, A. B. Cationic Photopolymerizations of Thick Polymer Systems: Active Center Lifetime and Mobility. *European Polymer Journal* **2008**, 44 (1), 98–105.
- (11) Fouassier, J.-P.; Lalevée, J. *Photoinitiators for Polymer Synthesis: Scope, Reactivity, and Efficiency*, 1st ed.; Wiley-VCH: Weinheim, Germany, **2012**.
- (12) Koleske, J. V. *Radiation Curing of Coatings*; West Conshohocken, Penn.: ASTM ; Bethesda, MD : Radtech International, North America, **2002**.
- (13) Makuuchi, K.; Cheng, S. *Radiation Processing of Polymer Materials and Its Industrial Applications*; John Wiley & Sons, Inc.: Hoboken, NJ, USA, **2012**.
- (14) Brazel, C. S.; Rosen, S. L. *Fundamental Principles of Polymeric Materials*, 3rd ed.; Hoboken, NJ, **2012**; pp 1–427.
- (15) Richter, K. B. Pulsed Electron Beam Curing of Polymer Coatings. **2007**, 1–246.
- (16) Weiss, D. E.; Dunn, D.; Richter, K. B.; Adler, R. Pulsed Electron Beam Polymerization. **2005**, 1–11.

- (17) Dowsett, D. *Radiological Sciences Dictionary: Keywords, Names and Definitions*; CRC Press, **2009**.
- (18) Drobny, J. G. *Ionizing Radiation and Polymers*; Elsevier Inc., **2013**.
- (19) Crivello, J. V.; Fan, M.; Bi, D. The Electron Beam-Induced Cationic Polymerization of Epoxy Resins. *J. Appl. Polym. Sci.* **1992**, *44* (1), 9–16.
- (20) Crivello, J. V. UV and Electron Beam-Induced Cationic Polymerization. *Nuclear Instruments and Methods in Physics Research Section B: Beam Interactions with Materials and Atoms* **1999**, 8–21.
- (21) Janke, C. J.; Dorsey, G. F.; Havens, S. J.; Lopata, V. J. Electron Beam Curing of Epoxy Resins by Cationic Polymerization. **1997**, 1–11.
- (22) Transmittance. *www.goldbook.iupac.org*. Accessed Jan. **2015**.
- (23) Kanaya, K.; Okayama, S. Penetration and Energy-Loss Theory of Electrons in Solid Targets. *Journal of Physics D Applied Physics* **2002**, *5* (1), 43–58.
- (24) Rangwalla, I.; Nablo, S. V. A Parametric Study of the Electron Curing of Inks and Coatings. *RadTech Report* **1990**, 18–28.
- (25) Martin, J. W.; Chin, J. W.; Nguyen, T. Reciprocity Law Experiments in Polymeric Photodegradation: a Critical Review. *Progress in Organic Coatings* **2003**, *47* (3-4), 292–311.
- (26) Feng, L.; Suh, B. I. Exposure Reciprocity Law in Photopolymerization of Multi-Functional Acrylates and Methacrylates. *Macromol. Chem. Phys.* **2007**, *208* (3), 295–306.
- (27) Wydra, J. W.; Cramer, N. B.; Stansbury, J. W.; Bowman, C. N. The Reciprocity Law Concerning Light Dose Relationships Applied to BisGMA/TEGDMA Photopolymers: Theoretical Analysis and Experimental Characterization. *Dental Materials* **2014**, *30* (6), 605–612.
- (28) Leprince, J. G.; Hadis, M.; Shortall, A. C.; Ferracane, J. L.; Devaux, J.; Leloup, G.; Palin, W. M. Photoinitiator Type and Applicability of Exposure Reciprocity Law in Filled and Unfilled Photoactive Resins. *Dental Materials* **2011**, *27* (2), 157–164.
- (29) Hadis, M.; Leprince, J. G.; Shortall, A. C.; Devaux, J.; Leloup, G.; Palin, W. M. High Irradiance Curing and Anomalies of Exposure Reciprocity Law in Resin-Based Materials. *Journal of Dentistry* **2011**, *39* (8), 549–557.

- (30) Emami, N.; Söderholm, K. J. M. How Light Irradiance and Curing Time Affect Monomer Conversion in Light-Cured Resin Composites. *European Journal of Oral Sciences* **2003**, *111* (6), 536–542.
- (31) Halvorson, R. H.; Erickson, R. L.; Davidson, C. L. Energy Dependent Polymerization of Resin-Based Composite. *Dental Materials* **2002**, *18* (6), 463–469.
- (32) Pedersen, W. B.; Singer, K. Electron Beam Curing of Organic Surface Coatings. **1971**, 1–10.
- (33) Xiancong, H.; Meiwu, S.; Guotai, Z.; Hong, Z. Investigation on the Electron-Beam Curing of Vinylester Resin. *Radiation Physics and Chemistry* **2008**.
- (34) Hoffman, A. S.; Jameson, J. T.; Salmon, W. A. Electron Radiation Curing of Styrene-Polyester Mixtures. Effect of Backbone Reactivity and Dose Rate. *Ind. Eng. Chem. Prod. Res. Develop.* **1970**, *9* (2), 158–167.
- (35) Squire, D. R.; Cleaveland, J. A.; Hossain, T. M. A.; Oraby, W.; Stahel, E. P.; Stannett, V. T. Studies in Radiation-Induced Polymerization of Vinyl Monomers at High Dose Rates. I. Styrene. *J. Appl. Polym. Sci.* **1972**, *16* (3), 645–661.
- (36) Labana, S. S. Kinetics of High-Intensity Electron-Beam Polymerization of a Divinyl Urethane. *Journal of Polymer Science Part A-1: Polymer Chemistry* **1968**, *6* (12), 3283–3293.
- (37) Burlant, W.; Hirsch, J. Divinyl Copolymerization Initiated by High Intensity, Low Energy Electrons. *Journal of Polymer Science Part A: General Papers* **1965**, *3* (10), 3587–3597.
- (38) Decker, C. Photoinitiated Crosslinking Polymerisation. *Progress in Polymer Science* **1996**, *21*, 593–650.
- (39) Anseth, K. S.; Bowman, C. N.; Peppas, N. A. Polymerization Kinetics and Volume Relaxation Behavior of Photopolymerized Multifunctional Monomers Producing Highly Crosslinked Networks. *Journal of Polymer Science Part A* **1994**, *32*, 139–147.
- (40) Davidson, C. L.; Feilzer, A. J. Polymerization Shrinkage and Polymerization Shrinkage Stress in Polymer-Based Restoratives. *Journal of Dentistry* **1997**, *25* (6), 435–440.
- (41) Decker, C.; Jenkins, A. D. Kinetic Approach of Oxygen Inhibition in Ultraviolet- and Laser-Induced Polymerizations. *Macromol. Symp.* **1985**, *18* (6), 1241–1244.

- (42) Lu, H.; Stansbury, J. W.; Bowman, C. N. Impact of Curing Protocol on Conversion and Shrinkage Stress. *Journal of Dental Research* **2005**, *84* (9), 822–826.
- (43) Lu, H.; Stansbury, J. W.; Dickens, S. H.; Eichmiller, F. C.; Bowman, C. N. Probing the Origins and Control of Shrinkage Stress in Dental Resin Composites. II. Novel Method of Simultaneous Measurement of Polymerization Shrinkage Stress and Conversion. *J. Biomed. Mater. Res.* **2004**, *71B* (1), 206–213.
- (44) Kurdikar, D. L.; Peppas, N. A. A Kinetic Study of Diacrylate Photopolymerizations. *Polymer* **1994**, *35* (5), 1004–1011.
- (45) Sipani, V.; Kirsch, A.; Scranton, A. B. Dark Cure Studies of Cationic Photopolymerizations of Epoxides: Characterization of Kinetic Rate Constants at High Conversions. *J. Polym. Sci. A Polym. Chem.* **2004**, *42* (17), 4409–4416.
- (46) Cai, Y.; Jessop, J. L. P. Effect of Water Concentration on Photopolymerized Acrylate/Epoxide Hybrid Polymer Coatings as Demonstrated by Raman Spectroscopy. *Polymer* **2009**, *50* (23), 5406–5413.
- (47) Hartwig, A.; Schneider, B.; Lühring, A. Influence of Moisture on the Photochemically Induced Polymerisation of Epoxy Groups in Different Chemical Environment. *Polymer* **2002**, *43* (15), 4243–4250.
- (48) Bednarek, M.; Kubisa, P.; Penczek, S. Coexistence of Activated Monomer and Active Chain End Mechanisms in Cationic Copolymerization of Tetrahydrofuran with Ethylene Oxide. *Macromol. Symp.* **1999**, *32* (16), 5257–5263.
- (49) Ghosh, N. N.; Palmese, G. R. Electron-Beam Curing of Epoxy Resins: Effect of Alcohols on Cationic Polymerization. *Bull Mater Sci* **2005**, *28* (6), 603–607.
- (50) Biedron, T.; Kubisa, P.; Szymanski, R.; Penczek, S. Kinetics of Polymerization by Activated Monomer Mechanism. *Makromol. Chem. Macromol. Symp.* **1990**, *32*, 155–168.
- (51) Vidil, T.; Tournilhac, F. Supramolecular Control of Propagation in Cationic Polymerization of Room Temperature Curable Epoxy Compositions. *Macromol. Symp.* **2013**, *46* (23), 9240–9248.
- (52) Matyjaszewski, K. *Cationic Polymerizations*; CRC Press, 1996.
- (53) Boey, F.; Rath, S. K.; Ng, A. K.; Abadie, M. J. M. Cationic UV Cure Kinetics for Multifunctional Epoxies. *J. Appl. Polym. Sci.* **2002**, *86* (2), 518–525.
- (54) Pascault, J.-P.; Williams, R. J. J. *Epoxy Polymers*; John Wiley & Sons, 2009.

- (55) Crivello, J. V.; Lam, J. H. W. Diaryliodonium Salts. a New Class of Photoinitiators for Cationic Polymerization. *Macromol. Symp.* **1977**, *10* (6), 1307–1315.
- (56) Crivello, J. V. Cationic Polymerization — Iodonium and Sulfonium Salt Photoinitiators. In *Initiators — Poly-Reactions — Optical Activity*; Advances in Polymer Science; Springer-Verlag: Berlin/Heidelberg, **1984**; Vol. 62, pp 1–48.
- (57) Cai, Y.; Jessop, J. L. P. Decreased Oxygen Inhibition in Photopolymerized Acrylate/Epoxy Hybrid Polymer Coatings as Demonstrated by Raman Spectroscopy. *Polymer* **2006**, *47* (19), 6560–6566.
- (58) Dean, K.; Cook, W. D.; Zipper, M. D.; Burchill, P. Curing Behaviour of IPNs Formed From Model VERs and Epoxy Systems I Amine Cured Epoxy. *Polymer* **2001**, 1345–1359.
- (59) Dean, K.; Cook, W. D. Effect of Curing Sequence on the Photopolymerization and Thermal Curing Kinetics of Dimethacrylate/Epoxy Interpenetrating Polymer Networks. *Macromol. Symp.* **2002**, *35* (21), 7942–7954.
- (60) Cook, W. D.; Chen, F.; Ooi, S. K.; Moorhoff, C.; Knott, R. Effect of Curing Order on the Curing Kinetics and Morphology of bisGMA/DGEBA Interpenetrating Polymer Networks. *Polym. Int.* **2006**, *55* (9), 1027–1039.
- (61) Sperling, L. H. Interpenetrating Polymer Networks: an Overview. In *Interpenetrating Polymer Networks*; Sperling, L. H., Klemmner, D., Utracki, L. A., Eds.; Advances in Chemistry; American Chemical Society: Washington, DC, **1994**; Vol. 239, pp 3–38.
- (62) Dillman, B.; Schissel, S.; Jessop, J. L. P. Epoxide-Acrylate Hybrid Photopolymers: Formation of Grafted Polymer Networks. In *Photopolymer Science and Applications*; Allonas, X., Ed.; Wiley, **2014**.
- (63) Dillman, B.; Kang, N. Y.; Jessop, J. L. P. Solventless Synthesis and Free-Radical Photopolymerization of a Castor Oil-Based Acrylate Oligomer. *Polymer* **2013**, *54* (7), 1768–1774.
- (64) Dieing, T.; Hollricher, O.; Toporski, J. *Confocal Raman Microscopy*; Springer Berlin Heidelberg: Berlin, **2011**.
- (65) Grasselli, J. G.; Snavely, M. K.; Bulkin, B. J. Applications of Raman Spectroscopy. *Physics Reports* **1980**, *65* (4), 231–344.
- (66) Ingle, J. D.; Crouch, S. R. *Spectrochemical Analysis*, 1st ed.; Prentice-Hall Inc.: Englewood Cliffs, NJ, **1988**.

- (67) Socrates, G. G. *Infrared and Raman Characteristic Group Frequencies: Tables and Charts*, 3rd ed.; John Wiley & Sons, LTD: Chichester, **2001**.
- (68) Mansour, H. M.; Hickey, A. J. Raman Characterization and Chemical Imaging of Biocolloidal Self-Assemblies, Drug Delivery Systems, and Pulmonary Inhalation Aerosols: a Review. *AAPS PharmSciTech* **2007**, 8 (4), 140–155.
- (69) *Comprehensive Materials Processing*, 1st ed.; Hashmi, S., Ed.; Elsevier: Oxford, **2014**.
- (70) Reichenbacher, M.; Popp, J. Vibrational Spectroscopy. In *Challenges in Molecular Structure Determination*; Springer Berlin Heidelberg: Berlin, Heidelberg, **2012**; pp 63–143.
- (71) Allahverdiev, K. R.; Lovera, D.; Altstadt, V.; Schreier, P.; Kador, L. Confocal Raman Microscopy: Non-Destructive Materials Analysis with Micrometer Resolution. *Review of Advance Material Science* **2009**, 20, 77–84.
- (72) Kaiser Optical Systems, Inc. *Confocal Raman Microscopy*; 1350; **2012**; pp 1–2.
- (73) Menard, K. P. *Dynamic Mechanical Analysis*, 2nd ed.; CRC Press: Boca Raton, FL, **2008**.
- (74) Shen, S. B.; Ishida, H. Dynamic Mechanical and Thermal Characterization of High-Performance Polybenzoxazines. *Journal of Polymer Science Part B Polymer Physics* **1999**, 37, 3257–3268.

CHAPTER 2 OBJECTIVES

Radiation polymerization provides a rapid, solvent-free, and energy-efficient means of curing films, coatings, inks, adhesives, and biomedical materials. Because of these inherent advantages, it has become an indispensable production method in the polymer industry and is used to manufacture a vast array of consumer goods that help stock our pantries, fill our homes, and connect us. However, as far as radiation polymerization has progressed, it still suffers from a lack of complete understanding. Problems have been recognized, and, in many cases, solutions have been identified; yet, these solutions often introduce new questions. This work focuses on three such scenarios.

Scenario 1: Photopolymerization is limited by the poor performance of light through thick and pigmented systems. Electron-beam (EB) polymerization is an obvious solution because it retains many of the advantages of photopolymerization and is not challenged by sample thickness or opaque films. Yet, how does changing the initiation source change polymer properties? How does changing the EB dose or dose rate impact glass transition temperature or conversion?

Scenario 2: Free-radical polymerization is inhibited by oxygen, while cationic polymerization is moisture sensitive. Previous research has shown these problems are mitigated by formulating free-radical/cationic hybrid systems. Still, what influence does the free-radical network have on the rate of formation of the cationic network? Does incorporating the two networks through the activated monomer (AM) mechanism prevent phase separation and/or stifle conversion?

Scenario 3: Both photo- and EB-polymerization are traditionally restricted to unobstructed, flat surfaces that can receive equal amounts of radiation. However, cationic polymerization, with its ability to dark and shadow cure, can cure in areas where light is impeded. Yet, can shadow cure be directed? What conditions best facilitate shadow-cured polymer growth?

The goal of this work is to address the known limitations of radiation curing in each of these three scenarios by developing kinetic- and property-control strategies for free-radical EB polymerization (Scenario 1), free-radical/cationic hybrid

photopolymerization (Scenario 2), and cationic shadow cure (Scenario 3). Through the development of control strategies, this work endeavors to answer fundamental questions about radiation polymerization, as well as to provide guidelines that aid in product design for each technology. The overarching goal was pursued through the following three objectives:

- 1. *Determine how monomer chemistry influences the magnitude of the dose rate effect in electron-beam polymerization and how these effects differ from photopolymerization.*** Raman spectroscopy was established as a reliable method of quantifying conversion in electron-beam polymerized samples (Chapter 3). A series of five acrylate monomers was polymerized at three different doses and three different line speeds. The conversion and glass transition temperature (T_g) of these samples was measured using Raman microscopy and dynamic mechanical analysis, respectively. Trends of the EB dose rate effect were established as a function of dose and monomer size (Chapter 4). A protocol for comparing equivalent initiation energies was developed, and it was used to compare EB and photopolymer trends across the five monomer series (Chapter 5).
- 2. *Characterize the impact of promotion of the activated monomer (AM) mechanism on the kinetics and mechanical properties of (meth)acrylate/epoxy hybrid formulations in UV photopolymerization.*** A series of two acrylates and two methacrylates, each with one control and one containing an AM-mechanism promoting alcohol group, were mixed with increasing concentrations of a dicycloaliphatic epoxide. Real-time Raman spectroscopy was used to simultaneously follow the (meth)acrylate and epoxide conversion. Mechanical properties were determined using DMA. The effect of the AM mechanism was determined by comparing the control system to the system containing alcohols. Comparisons were also made between the acrylate and methacrylate formulations to understand the influence of the free-radical moiety on polymer properties (Chapter 6).

3. Establish parameters for the optimization of shadow cure in cationic ring-opening photopolymerization. The limitations of shadow cure were probed using a variety of sample thicknesses and sample geometries. A central composite design (CCD) was constructed using design of experiments to determine the optimal combination of effective irradiance, sample thickness, exposure area, and exposure time (Chapter 7). An improvement on shadow cure was developed, termed transferrable shadow cure. This improvement allowed for the investigation of shadow cure kinetics and mechanical properties. A CCD was completed for transferrable shadow cure and compared to that of the traditional shadow-cure method (Chapter 8).

By accomplishing these objectives, this work strives to achieve an understanding of structure-processing parameters-properties relationships for EB (Obj 1) and to use the unique characteristics of cationic polymerization to control reaction rates and phase separation (Obj 2) and to circumvent light penetration limitations in photopolymerization (Obj 3). The ultimate aspiration of this work is to open up new avenues and applications for radiation polymerization and to push beyond the stereotypical 2-D, UV-cured, free-radical systems that dominate the commercial market.

CHAPTER 3

INTERNAL REFERENCE PEAK VALIDATION FOR EB-CURED POLYMER CONVERSIONS MEASURED VIA RAMAN SPECTROSCOPY^X

3.1 Introduction

Electron-beam (EB) curing offers a fast, low-energy, and solvent-free means of polymerizing inks, films, coatings, and adhesives.¹⁻³ This initiator-free technique is especially appealing for packaging applications where molecular migration would be problematic. In addition, unlike photopolymerization, additives such as pigments, fillers, fibers, and nanomaterials do not prevent penetration of the ionizing radiation, resulting in excellent product consistency.

Continued advancement of EB technologies requires an increased understanding of EB-induced polymerization to provide guidance for designing performance properties needed for targeted applications; however, there are very few published works on the kinetics of EB polymerizations.^{1,2,4,5} Several issues make characterization of EB kinetics particularly challenging. EB system design does not lend itself to on-line, real-time monitoring, and EB bombardment is a harsh environment for sensitive monitoring equipment. In addition, line speeds are faster than the time resolution of monitoring equipment suitable for an industrial environment.

Raman spectroscopy is a well-established technique for the characterization of photopolymerizations, facilitating conversion and rate of polymerization measurements and polymer identification.⁶⁻¹⁰ Raman confocal microscopy can also be used to probe polymer composition as a function of depth without destroying the sample. In order to obtain these quantitative measurements, significant peaks in the Raman spectrum must be identified and associated with specific bonds in the molecules comprising the sample. One of these peaks must serve as an internal reference and is typically determined by monitoring the photopolymerization in real time and noting peaks that do not change during the reaction.

Raman confocal microscopy could provide valuable data needed to gain a fundamental understanding of the EB polymerization process and how it affects the

^X This chapter is based on the article: Schissel, S. M.; Lapin, S. C.; Jessop, J. L. P. Internal Reference Validation for EB-Cured Polymer Conversions Measured via Raman Spectroscopy. *RadTech Report* 2014, No. 4, 46–50.

properties of the polymers that are formed. However, without the ability to monitor the EB reaction in real time, the reference peak stability cannot be directly confirmed for an EB-curing process, and quantitative measurements would be suspect. In this study, Raman confocal microscopy is demonstrated as a method of characterizing EB polymerizations by validating the stability of a reference peak through comparison with an UV-cured standard.

3.2 Experimental

3.2.1 Materials

Two formulations were used to validate spectroscopic-based conversion measurements for EB-polymerized coatings. The first formulation was neat trimethylolpropane triacrylate monomer (TMPTA, Cytec), and the second formulation was a 50/50 mixture (by weight) of TMPTA and bisphenol-A-diglycidylether diacrylate oligomer (BADGEDA, Ebecryl 3700, Cytec) (Figure 3-1). For corresponding UV studies, 0.5 wt% of the photoinitiator 2,2-dimethoxy-2-phenylacetophenone (DMPA, Aldrich) was added to each formulation. All chemicals were used as received.

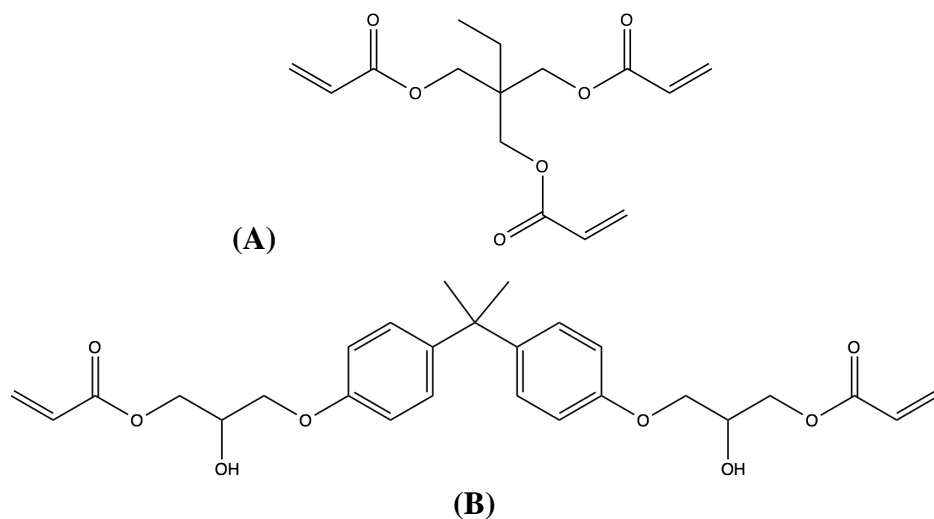


Figure 3-1. Chemical structures of acrylate monomers used in this study: (A) TMPTA and (B) BADGEDA.

3.2.2 Methods

EB Coatings

Coatings of each EB formulation were made on aluminum Q-panels using a 52-rod drawbar, resulting in ~100 micron films, measured using a micrometer. The coated panels were fed through an EB accelerator equipped with a variable-speed, fiberglass carrier web (BroadBeam EP Series, PCT Engineered Systems, Inc.). The coatings were EB-cured with a 30 kGy dose, and line speed, voltage, and N₂ flow rate were held constant at 50 ft/min, 200 kV, and 17 SCFM, respectively. The voltage level was selected because the Monte Carlo simulations (Integrated Tiger Series 3 from Oak Ridge National Labs) predicted a consistent energy deposition through the film.

UV Coatings

Coatings of each UV formulation were made on aluminum Q-panels using a drawbar, resulting in ~100 micron films. The coated panels were fed 3 times through a belt-driven curing system (Model No. P300MT, Fusion) equipped with an H-bulb (Model No. LC-6B). The coatings were UV-cured with an effective irradiance of 1.8 W/cm² (measured with a UVICURE® Plus radiometer), and the belt speed was held constant at 8 ft/min.

RT-Raman Spectroscopy

Real-time (RT) Raman spectroscopy was used to identify reference and reaction peaks for conversion calculations (Figure 3-2). Samples of the UV formulations were illuminated at ambient temperature in 1-mm ID quartz capillary tubes using a high-pressure 100-W mercury vapor short arc lamp with a 250 – 400 nm wavelength filter (Acticure® Ultraviolet/Visible Spot Cure system, EXFO Photonic Solutions, Inc.). The effective irradiance was 50 mW/cm² (measured with an OmniCure radiometer, Model No. R2000). Raman spectra were gathered using a holographic probehead (Mark II, Kaiser Optical Systems, Inc.) with a single-mode excitation fiber delivering ~220 mW of 785-nm near-infrared laser intensity to the sample through a 10x non-contact sampling objective. The probehead was connected to a modular research Raman spectrograph by a 100- μ m collection fiber (HoloLab 5000R, Kaiser Optical Systems, Inc.). Spectra were

collected continuously over 5 min with a 250-ms exposure time and 1 accumulation. Conversion, α , was calculated in real time as the photopolymerization proceeded:

$$\alpha = 1 - \frac{I_{rxn}(t)/I_{ref}(t)}{I_{rxn}(0)/I_{ref}(0)} \quad (3-1)$$

where $I_{rxn}(t)$ is the peak intensity of the reaction peak at time t and $I_{ref}(t)$ is the peak intensity of the reference peak at time t .¹⁰ This formula is useful for conversion measurements during real-time monitoring of reactions, as well as conversion measurements taken post-cure. The inclusion of a reference peak eliminates instrumental variation that occurs over time and signal-to-noise (S/N) changes that can occur at increasing sample depths during depth profiling.

RT-Raman spectroscopy assists in the selection of peaks used in Equation 3-1 (Figure 3-2): the reaction peak decreases as the reaction progresses, while the reference peak remains constant. For the TMPTA formulation, the reference peak was chosen at 1070 cm^{-1} (indicative of the $-\text{C}-\text{C}-\text{C}-\text{C}-$ bond in the backbone of the molecule), and the reaction peak was chosen at 1636 cm^{-1} (indicative of the $-\text{C}=\text{C}-$ bond in the acrylate moiety). For the TMPTA/BADGEDA formulation, the reference peak was chosen at 1613 cm^{-1} (indicative of the $-\text{C}=\text{C}-$ bond in the aromatic rings); however, the reaction peak remained at 1636 cm^{-1} .¹¹

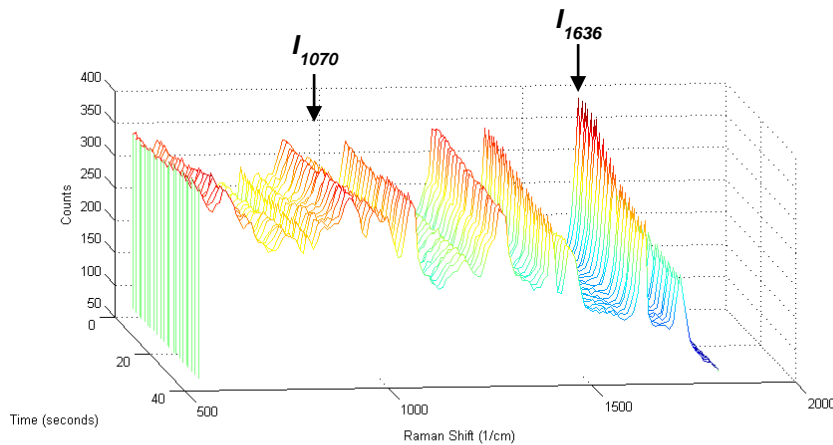


Figure 3-2. Real-time Raman spectra for photopolymerization of TMPTA. A reaction peak of 1636 cm^{-1} and a reference peak of 1070 cm^{-1} were identified.

Confocal Raman Microscopy

Confocal Raman microscopy was used to determine conversion and peak intensity as a function of depth in 100- μm thick coatings of the formulations on an aluminum substrate. Raman spectra of the samples were collected using an optical microscope (DMLP, Leica) connected to a modular research Raman spectrograph (HoloLab 5000R, Kaiser Optical Systems, Inc.) via a 10- μm confocal collection fiber. The beam from a 785-nm near-infrared laser was directed through a single-mode excitation fiber to the microscope with ~ 8 mW delivered to the sample through a 100x objective with a numerical aperture of 0.9 and a working distance of 0.27 mm. Monomer spectra were collected with an exposure time of 120 s and 3 accumulations. The peak height of both the reaction and reference peak were averaged over 5 monomer spectra to provide accurate values for $I_{rxn}(0)$ and $I_{ref}(0)$ to use in Equation 3-1. Spectra for depth-profiling studies were also collected with a 120 s exposure time and 3 accumulations, using a 1 to 3 μm step size.

Reference Peak Stability

Multiple Raman spectra were collected for both EB-cured and UV-cured coatings. The Raman microscope, detailed above, was used with an 100- μm collection fiber and 10x objective (numerical aperture of 0.25 and a working distance of 5.8 mm). Spectra were collected with a 15 s exposure time and 3 accumulations. For each sample, 20 spectra were collected at various points in the sample area (x and y axes) at constant sample depths (z axis). A ratio of $I_{rxn}:I_{ref}$ was calculated for each spectrum (HoloReact™ Revision 2.4.4, Kaiser Optical Systems, Inc.), and for each data set the standard deviation of these ratios was computed. The stability of the reference peak in the EB-cured coatings was evaluated by comparing the standard deviations of this ratio for EB-cured coatings to those for UV-cured coatings, for which a stable reference peak was demonstrated through RT-Raman measurements (Figure 3-2).

3.3 Results and Discussion

3.3.1 Reference Peak Stability

Although Raman microscopy has been shown to be useful in determining conversion as a function of depth in UV-cured samples, its efficacy in providing similar information for EB-cured samples must be established. In initial studies, conversion profiles were acquired as a function of depth for EB-cured TMPTA coatings. Based on the consistent energy deposition predicted by Monte Carlo simulations for the selected voltage level, the conversion was expected to be constant through the full depth of the coatings. The coatings were fully nitrogen-inerted to eliminate oxygen inhibition effects, and the irradiated coating surfaces were completely tack-free. However, as seen in Figure 3-3, Raman results indicated the opposite: the conversion increases with increasing depth, and the surface conversions are less than 50%. In addition, the standard deviation in the conversion profile is greater than can be attributed to the instrument, which is typically $\pm 3-4\%$.

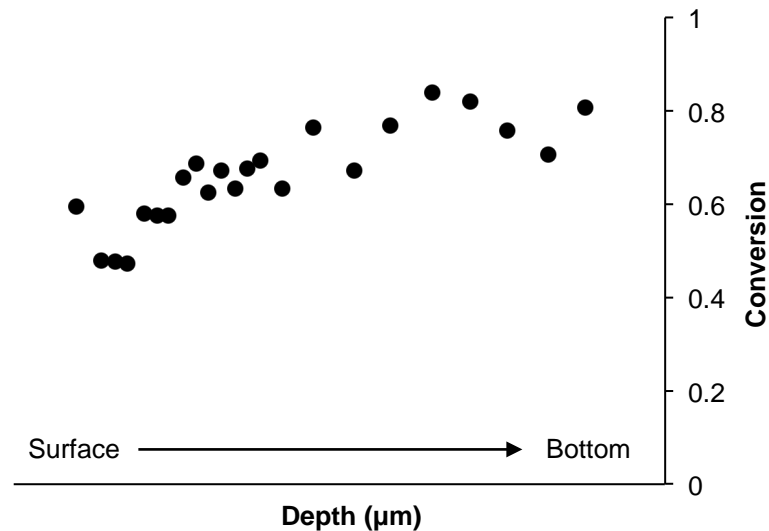


Figure 3-3. Depth profile of an EB-cured sample of TMPTA. Conversion was expected to be constant as a function of depth, but instead increases with sample depth.

Based on these contradictory results, it seemed improbable that the Raman measurements were providing a true picture of coating conversion for these EB-cured samples. Therefore, it was hypothesized that the chemical bond corresponding to the chosen reference peak was not stable during EB irradiation. To test this hypothesis, the standard deviation of the Raman peak intensity ratios, $I_{1636}:I_{1070}$, was compared for UV-cured and EB-cured TMPTA coatings in which the conversion as a function of depth was expected to be constant (Figure 3-4, A). If the reference peak, I_{1070} , is stable under both types of initiating radiation, the standard deviations for the two curing modes should be approximately equal. Instead, the standard deviation for the EB-cured coating is more than three times larger than that for the UV-cured coating.

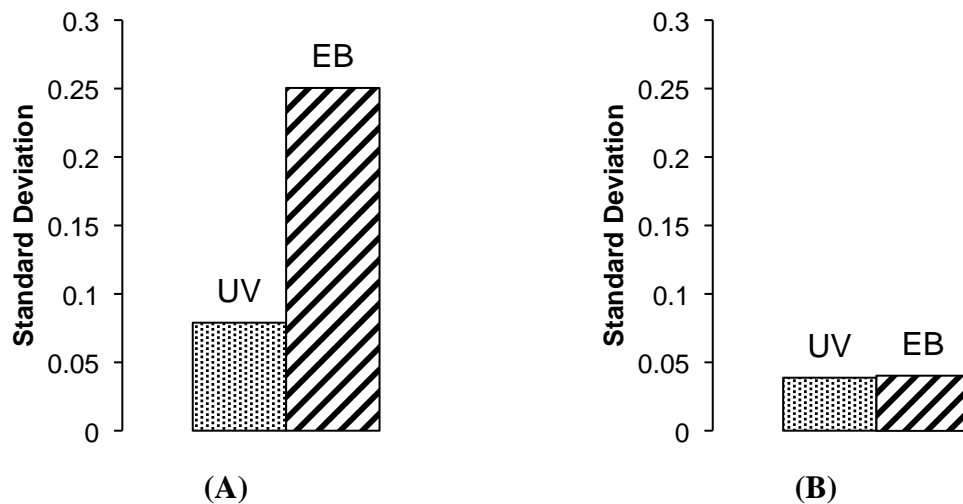


Figure 3-4. A comparison of the standard deviation of the Raman peak intensity ratios: (A) $I_{1636}:I_{1070}$ for UV-cured and EB-cured TMPTA coatings and (B) $I_{1636}:I_{1613}$ for UV-cured and EB-cured TMPTA/BADGEDA coatings. The small and equal standard deviations for the TMPTA/BADGEDA coatings suggest the reference peak I_{1613} is stable under EB radiation.

Since the chemical structure and Raman spectrum of TMPTA (Figures 3-1, A and 3-2, respectively) did not offer any suitable alternatives for a new reference peak, BADGEDA was added to the coating formulation. BADGEDA contains a phenyl ring, which should be stable even under EB irradiation. With this addition to the formulation, the standard deviation of the Raman peak intensity ratios, $I_{1636}:I_{1613}$, was compared for UV-cured and EB-cured coatings in which the conversion as a function of depth was

expected to be constant (Figure 3-4, B). The standard deviation for both curing modes was equal and within the range expected for the instrument.

Further confirmation of the stability of the new reference peak, I_{1613} , was accomplished by comparing the UV and EB Raman confocal depth profiles of the reference peak intensity. When using Raman confocal, the surface of a sample can be established by the peak intensity of a stable peak.¹² Light scattering is most intense at the sample surface, which, in turn, produces the maximum Raman peak intensity. This principle is demonstrated in a depth profile of a silicon wafer, where the peak intensity of the characteristic silicon peak (520 cm^{-1}) is monitored (Figure 3-5).

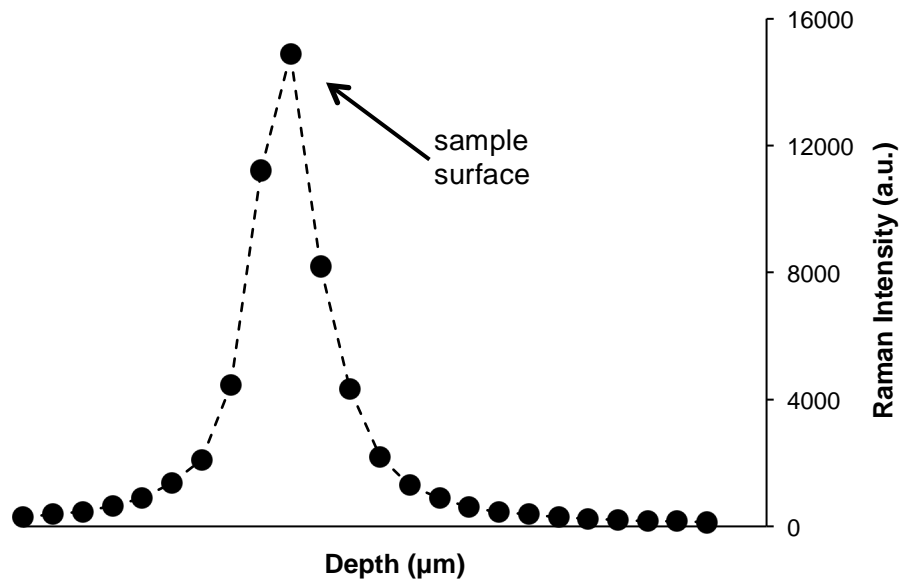


Figure 3-5. Raman confocal depth profile of a silicon wafer. The sample surface occurs at the maximum peak intensity of the characteristic silicon peak (520 cm^{-1}).

Therefore, if the I_{1613} reference peak is stable when exposed to EB radiation as it is for UV radiation, the depth profiles of the reference peak intensity should align for both radiation types. Figure 3-6 confirms the I_{1613} reference peak reaches a maximum peak intensity $\sim 3\text{ }\mu\text{m}$ (stage movement) after Raman peaks were first sighted for the EB-cured sample and $\sim 5\text{ }\mu\text{m}$ for the UV-cured sample, suggesting the reference peak is stable under EB radiation. The lack of a true Gaussian distribution, as demonstrated for the silicon wafer, is attributed to the aluminum substrate used during the confocal

experiments. Theoretically, the aluminum should increase light scattering, artificially increasing the peak intensity at the sample bottom.

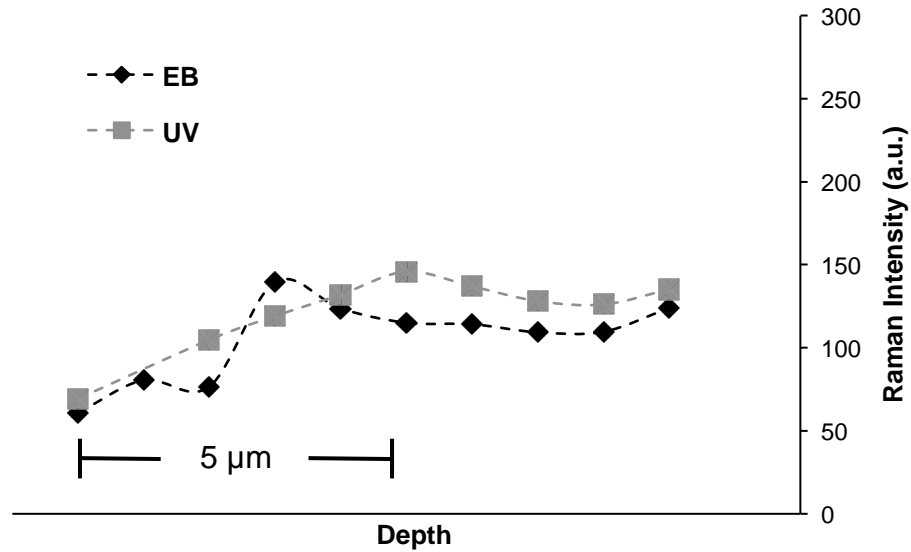


Figure 3-6. A comparison of UV and EB-cured Raman confocal depth profiles of the 1613 cm^{-1} peak intensity for the TMPTA/BADGEDA formulation. The UV and EB samples reach a maximum peak intensity within $2\text{ }\mu\text{m}$ of each other, suggesting the 1613 cm^{-1} peak is stable under EB radiation. Depth values refer to microscope stage movement, not actual sample depth.

In comparison, the depth profiles of the 1070 cm^{-1} peak intensity for UV- and EB-cured TMPTA do not align (Figure 3-7). Furthermore, the EB sample reaches a maximum $18\text{ }\mu\text{m}$ (stage movement) after Raman peaks were first spotted in the spectrum; it is highly improbable that spectra of the sample were collected so far above the sample surface, especially since sample spectra were only collected $4\text{ }\mu\text{m}$ above the surface of the UV-cured sample.

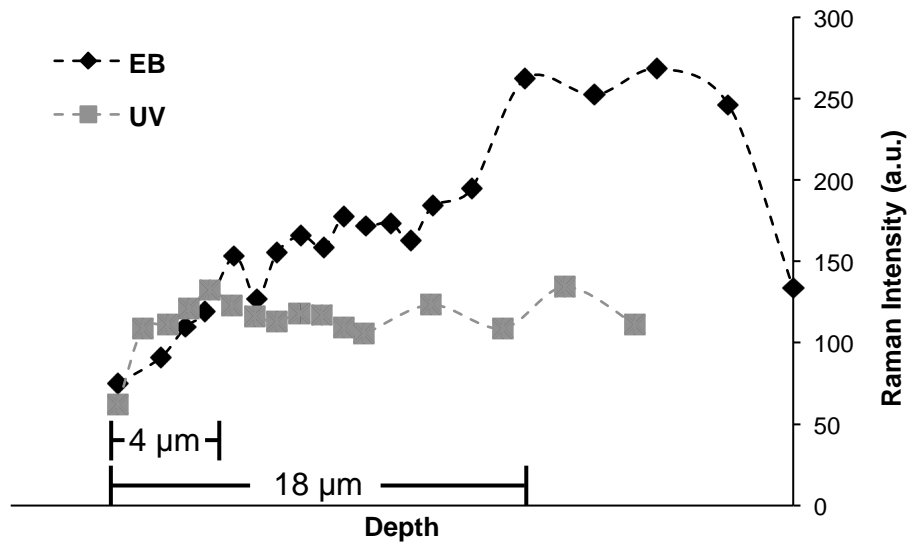


Figure 3-7. A comparison of UV and EB-cured Raman confocal depth profiles of the 1070 cm^{-1} peak intensity for the TMPTA formulation. The UV and EB samples reach a maximum peak intensity at very different depths, suggesting the 1070 cm^{-1} peak is unstable under EB radiation. Depth values refer to microscope stage movement, not actual sample depth.

For final validation of the new reference peak choice, conversion profiles were acquired as a function of depth for nitrogen-inerted, EB-cured TMPTA/BADGEDA coatings. As seen in Figure 3-8, Raman results confirmed consistent conversion throughout the coating, as predicted by Monte Carlo simulations for the selected voltage level. Thus, the new reference peak, I_{1613} , is stable under EB irradiation and can be used to obtain accurate conversion measurements of EB-cured samples using Raman microscopy.

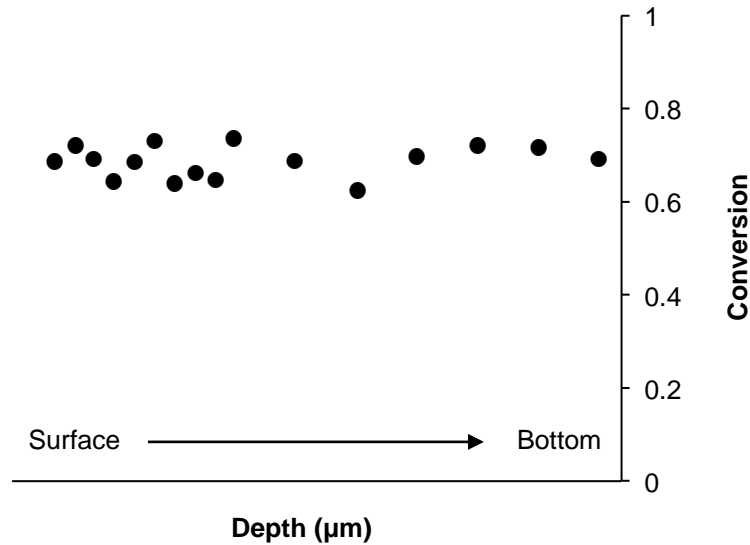


Figure 3-8. Depth profile of an EB-cured sample of TMPTA/BADGEDA. Conversion is constant as a function of depth considering the typical ± 3 to 4% instrumental deviation.

3.3.2 Peak Stability Comparison in UV and EB

By establishing a stable reference peak for EB polymerization, not only can the conversion of the polymer be accurately calculated, but the stability of bonds exposed to UV and EB radiation can be compared. For example, Figure 3-9 illustrates the identification of two other chemical bonds that are stable during a photopolymerization in addition to the aromatic C=C bond represented by the 1613 cm^{-1} peak.

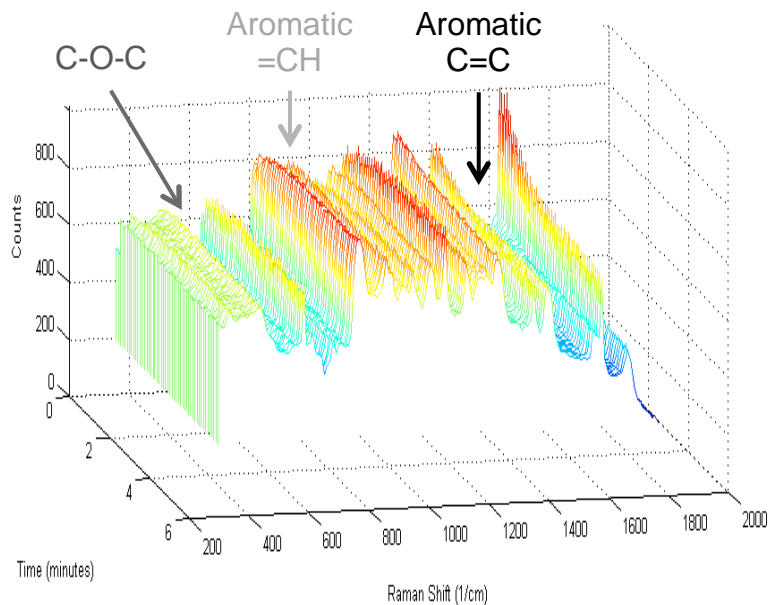


Figure 3-9. Real-time Raman profile of the TMPTA/BADGEDA photopolymerization. The C-O-C bending (665 cm^{-1}) and the aromatic =CH bond (1185 cm^{-1}) were determined to be unaltered during the reaction.

Using the stable reference peak, the percentage of the bond unaltered by EB radiation can be determined by the equation,

$$\text{Percent Unaltered} = \frac{I_{pk}(t)/I_{ref}(t)}{I_{pk}(0)/I_{ref}(0)} * 100 \quad (3-2)$$

where $I_{pk}(t)$ is the peak intensity of the peak of interest of the polymer, $I_{ref}(t)$ is the peak intensity of the reference peak of the polymer, and $I_{pk}(0)$ and $I_{ref}(0)$ are the monomer peak intensities. The response of the C-O-C bending (665 cm^{-1}) and the =CH bond (1185 cm^{-1}) to EB radiation is shown in Figure 3-10. Both bonds are unstable under EB radiation, though no trend is apparent as a function of sample depth.

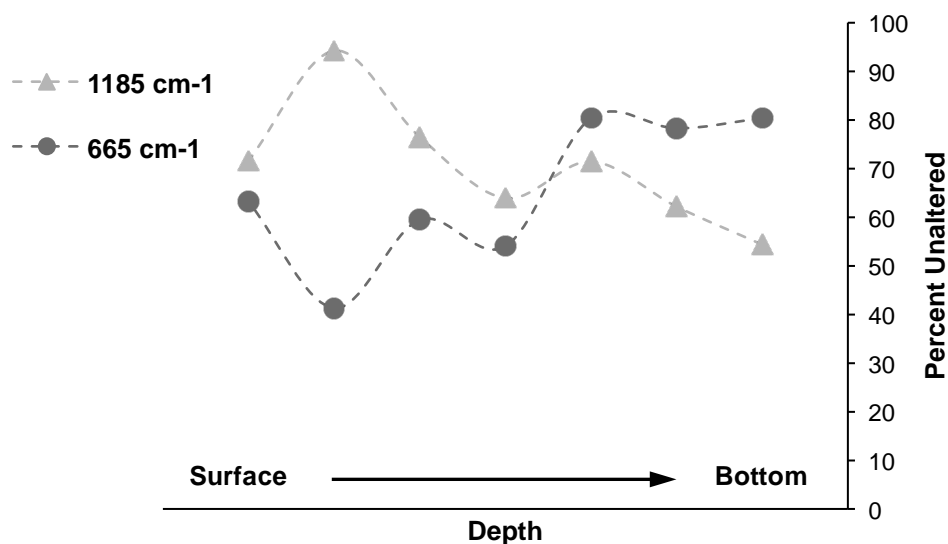


Figure 3-10. Depth profile of an EB-cured sample of TMPTA/BADGEDA. The 665 and 1185 cm^{-1} peaks, both stable in UV polymerization, are altered in EB polymerization.

Use of this technique may help elucidate how different chemical bonds respond to the two different radiation polymerization methods; however, the technique is limited to the comparison of Raman-active bonds (or groups of bonds) that are stable during the photopolymerization reaction.

3.4 Conclusions

Characterization of EB polymerization is difficult because real-time monitoring techniques are not well suited for use in the EB-curing environment. However, kinetic information is needed to develop a fundamental understanding of EB-induced polymerization in order to make future processing and material advancements. In this study, Raman confocal microscopy is demonstrated as a valid, quantitative technique to measure conversion as a function of depth in EB-cured samples provided the stability of the reference peak is verified. This preliminary investigation sets the stage for future work using Raman confocal microscopy to determine effects of critical processing factors, such as nitrogen inertion and energy deposition, on conversion of EB-cured monomers and oligomers. In addition, since the stability of Raman peaks from UV and EB cured samples can be compared, the chemical bonds most susceptible to EB radiation

can be identified, thereby providing further information about the kinetics during EB irradiation.

3.5 References

- (1) Datta, S. K.; Chaki, T. K.; Bhowmick, A. K. Electron Beam Processing of Polymers. **2000**, 1–30.
- (2) *Radiation Curing of Polymeric Materials*; Hoyle, C. E., Kinstle, J. F., Eds.; American Chemical Society, **1990**.
- (3) Drobny, J. G. *Ionizing Radiation and Polymers*; Elsevier Inc., **2013**.
- (4) Richter, K. B. Pulsed Electron Beam Curing of Polymer Coatings. **2007**, 1–246.
- (5) Weiss, D. E.; Dunn, D.; Richter, K. B.; Adler, R. Pulsed Electron Beam Polymerization. **2005**, 1–11.
- (6) Cai, Y.; Jessop, J. L. P. Effect of Water Concentration on Photopolymerized Acrylate/Epoxy Hybrid Polymer Coatings as Demonstrated by Raman Spectroscopy. *Polymer* **2009**, *50* (23), 5406–5413.
- (7) Dillman, B.; Jessop, J. L. P. Chain Transfer Agents in Cationic Photopolymerization of a Bis-Cycloaliphatic Epoxy Monomer: Kinetic and Physical Property Effects. *Journal of Polymer Science Part A* **2013**, *51* (9), 2058–2067.
- (8) Dieing, T.; Hollricher, O.; Toporski, J. *Confocal Raman Microscopy*; Springer Berlin Heidelberg: Berlin, **2011**.
- (9) Grasselli, J. G.; Snavely, M. K.; Bulkin, B. J. Applications of Raman Spectroscopy. *Physics Reports* **1980**, *65* (4), 231–344.
- (10) Cai, Y.; Jessop, J. L. P. Decreased Oxygen Inhibition in Photopolymerized Acrylate/Epoxy Hybrid Polymer Coatings as Demonstrated by Raman Spectroscopy. *Polymer* **2006**, *47* (19), 6560–6566.
- (11) Socrates, G. G. *Infrared and Raman Characteristic Group Frequencies: Tables and Charts*, 3rd ed.; John Wiley & Sons, LTD: Chichester, **2001**.
- (12) Ingle, J. D.; Crouch, S. R. *Spectrochemical Analysis*, 1st ed.; Prentice-Hall Inc.: Englewood Cliffs, NJ, **1988**.

CHAPTER 4 DOSE RATE EFFECTS IN ELECTRON-BEAM INITIATED POLYMERIZATION: THE EFFECTS OF MONOMER CHEMISTRY

4.1 Introduction

Electron-beam (EB) polymerization is used extensively to produce millions of tons of film, coating, ink, and adhesive products each year.¹ EB curing is a rapid, sustainable process, requiring no environmentally damaging solvents and less energy than thermal polymerization methods.²⁻⁴ Furthermore, in contrast to photopolymerization, EB polymerization is not hindered by fillers or pigments, allowing for widespread property tuning through the use of additives.

In spite of the established commercial use of EB-curing technology, published research describing the fundamental aspects of EB polymerization is limited.^{2,5-17} Large gaps exist in the understanding of EB kinetics and how EB-cured polymer properties are influenced by processing variables. One area where this knowledge gap is especially problematic is the application of dose rate and how dose rate affects polymer properties.

While the dose (*i.e.*, the energy imparted to the sample) can be held constant by adjusting the beam current and line speed (see Equation 4-1), the speed at which the dose is delivered – dose rate – changes.

$$Dose = \frac{Beam\ Current * K}{Line\ Speed} \quad (4-1)$$

Altering the dose rate can cause property changes in the cured polymer, known as dose rate effects.^{10,11,13,16}

Dose rate effects point to changes in the polymer network, and controlling these effects could be beneficial in advancing EB polymerization. Currently, EB polymerization is restricted to applications needing or allowing a highly cross-linked network, which is formed as a result of the many side reactions caused by electron-induced free-radical formation. If manipulating dose rate causes changes in the polymer network, it could be the additional variable needed to *control* network formation. However, as of yet, no fundamental understanding of how dose rate influences the EB polymerization reaction has been established.

Furthermore, avoiding dose rate effects, particularly in commercial applications, may be difficult. Many new formulations are tested on a slower pilot line or lab equipment, where the materials and required dose levels are optimized. Then, the beam current and line speed are scaled for commercial production requirements. If dose rate effects and their magnitude were consistent, adjustments could be made during this scale-up process; however, some formulations are more prone to dose rate effects than others, suggesting formulation chemistry has an impact on the magnitude of the dose rate effects.

In this study, a series of acrylate monomers was investigated, and a strong correlation was discovered between monomer chemical structure and the magnitude of the dose rate effect found in two, commonly reported polymer properties: conversion and glass transition temperature. From these data, a rudimentary structure/processing conditions/properties relationship was established, enabling predictions of a formulation's dose rate effect by comparing its response to different doses. This foundational research will allow more thorough investigations into the cause of dose rate effects in EB-cured polymers, providing a more reliable means of scaling to production modes.

4.2 Experimental

4.2.1 Materials

A series of five monomers was chosen to investigate the impact of monomer chemistry on the magnitude of the dose rate effect: phenyl acrylate (PA, MP Biomedicals), benzyl acrylate (BA, MP Biomedicals), 2-phenylethyl acrylate (PEA, Polysciences), 2-phenoxyethyl acrylate (POEA, TCI America), and 2-hydroxy-3-phenoxypropyl acrylate (HPOPA, Sartomer) (Figure 4-1).

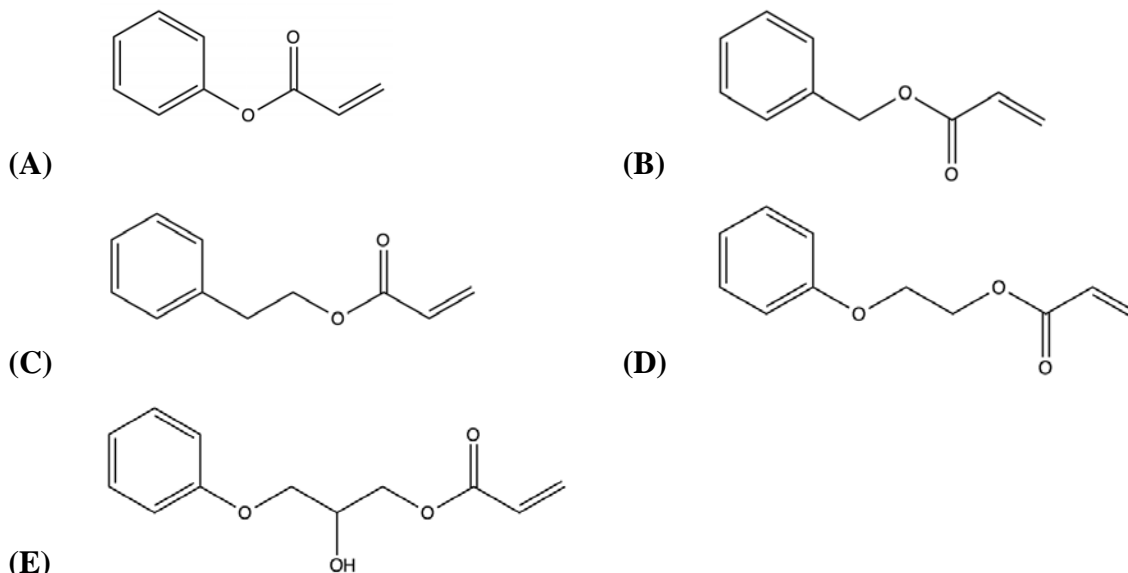


Figure 4-1. The chemical structures of the 5-monomer series: (A) PA, (B) BA, (C) PEA, (D) POEA, and (E) HPOPA.

To enable Raman conversion measurements, each monomer contains a phenyl group and an acrylate moiety.¹⁸ The number of chemical bonds separating the phenyl ring from the acrylate moiety differentiates the monomers and is incrementally increased across the series. An aliphatic urethane diacrylate oligomer, Ebecryl 8807 (proprietary structure, Allnex), was added to each monomer to improve the structural integrity of the samples and allowed for mechanical-property testing. All materials were used as received and stored at room temperature.

4.2.2 Methods

EB Film Preparation

Each formulation consisted of a 50/50, by weight, mixture of monomer and oligomer. Because of the high viscosity of the oligomer, the formulations were heated to approximately 60°C to allow mixing of the monomer and oligomer. Once heated, formulations were stirred using a drill with a paddle mixer attachment.

Samples for EB curing were prepared by first treating 4 x 3.25 inch glass slides (Ted Pella, Inc.) using two coats of Rain-X® 2-in-1 glass cleaner and rain repellent. Next, two layers of lab tape (VWR, total thickness ~180 μm) were placed on either side

of the glass to be used as spacers. A large droplet, approximately 1 mL, of a formulation was then placed near the top of the slide, between the pieces of tape, and covered with a piece of silicone-coated, 34- μm thick polyethylene terephthalate (PET). A straight edge was drawn across the PET to form a uniform film underneath.

The samples on the glass slides were polymerized by EB irradiation through the PET film using an EB accelerator equipped with a variable-speed, fiberglass carrier web (BroadBeam EP Series, PCT Engineered Systems, Inc.). Three different doses (15, 30, and 60 kGy) and three different line speeds (20, 100, and 200 ft/min) were used to cure the films. Accelerating voltage and N_2 flow rate were held constant at 250 kV and 17 SCFM, respectively. The voltage level was chosen because it produced a nearly uniform dose profile through the depth of the films. Once polymerized, the films were removed from the glass slides and cut into rectangles measuring 6.25 x 25 mm for characterization using a razor blade. The use of silanized (Rain-X®-treated) glass and silicone-coated PET assisted in the release of the polymer film. The PET cover was used to eliminate the effect of oxygen diffusion in the experiments.

Raman Spectroscopy

Polymer Conversion

Raman microscopy was used to determine conversion of the polymer films. In order to eliminate error from instrumental variations, a reference peak was used. Previous work has established the reaction peak at 1636 cm^{-1} (indicative of the $-\text{C}=\text{C}-$ bond in the acrylate moiety) and the reference peak at 1613 cm^{-1} (indicative of the $-\text{C}=\text{C}-$ bonds in the phenyl ring).¹⁸ Conversion, α , was calculated using the following equation:

$$\alpha = \left(1 - \frac{I_{rxn}(P)/I_{ref}(P)}{I_{rxn}(M)/I_{ref}(M)} \right) * 100 \quad (4-2)$$

where $I_{rxn}(P)$ and $I_{ref}(P)$ are the peak intensities of the reaction and reference peak of the polymer, respectively; $I_{rxn}(M)$ and $I_{ref}(M)$ are the peak intensities of the reaction and reference peak of the monomer.¹⁹

Raman spectra of the polymerized films were collected using an optical microscope (DMLP, Leica) connected to a modular research Raman spectrograph (HoloLab 5000R, Kaiser Optical Systems, Inc.) via a 100- μm collection fiber. A single-mode excitation fiber carried an incident beam of a 785-nm near-infrared laser to the sample through a 10x objective with a numerical aperture of 0.25 and a working distance of 5.8 mm. Laser power at the sample was ~ 10 mW. Spectra were collected with an exposure time of 15 seconds and 3 accumulations. Fifteen monomer spectra were collected and averaged to provide accurate values for $I_{rxn}(M)$ and $I_{ref}(M)$ to use in Equation 4-2. Three spectra were collected from different areas of each polymer film and averaged to report conversion. The majority of samples had a standard deviation within ± 5 percent conversion. Exceptions to this standard deviation: BA 15 kGy-200 ft/min (7%), PA 15 kGy-200 ft/min (27%), PA 30 kGy-100 ft/min (11%), PA 30 kGy-200 ft/min (14%), and PA 60 kGy-100 ft/min (7%).

Rate of Polymerization

To determine the impact of polymerization rate (R_p) on dose rate effects, bulk conversion versus time profiles and propagation rate data were collected using real-time Raman spectroscopy. Because EB is not conducive to real-time measurements, photo-initiated reactions were monitored to measure the polymerization rate. It is assumed, based on the identical UV and EB propagation mechanisms, that R_p trends observed for UV reactions are valid for EB reactions, as well.

To each monomer/oligomer formulation, 0.1 wt% of 2,2-dimethoxy-2-phenylacetophenone (DMPA, Sigma Aldrich) was added to initiate a photopolymerization reaction. Neat monomer formulations contained 0.5 wt% DMPA. An Omnicure® S1000 Ultraviolet/Visible Spot Cure System (Excelitas, 250-450 nm band pass filter) with a 3 mm liquid lightguide was used to polymerize the formulations at ambient temperature in 1-mm ID quartz capillary tubes. The effective irradiance, measured by a radiometer (OmniCure, Model No. R2000), was 100 mW/cm^2 . Raman spectra were collected continuously throughout the reaction using a holographic probehead (Mark II, Kaiser Optical Systems, Inc.) with a single-mode excitation fiber and 10x non-contact sampling objective. The incident beam was a 785-nm near-infrared laser

with an intensity of ~220 mW at the sample, and the Raman scattering was analyzed using a modular research Raman spectrograph (HoloLab 5000R, Kaiser Optical Systems, Inc.). Each spectrum had an exposure time of 250 ms and 1 accumulation.

Conversion values were calculated using Equation 4-2. $R_{p,max}$ was calculated for each reaction by differentiating the conversion vs. time curve, then smoothing the data using a five-point moving average to minimize noise. $R_{p,max}$ was calculated for each monomer/oligomer formulation in triplicate and those values averaged. The standard deviation was approximately ± 6 (1/s), with the exception of BA (12), and HPOPA (21).

Dynamic Mechanical Analysis

A dynamic mechanical analyzer (DMA, Q800 TA Instruments) equipped with a film tension clamp was used to find the glass transition temperature (T_g) of the same polymer films used to determine conversion. A mono-frequency strain, temperature ramp sequence was used to collect $\tan \delta$ values as a function of temperature. Temperature was increased at a rate of 3°C/min over a broad temperature range at a constant oscillating frequency of 1 Hz and a sinusoidal strain of 0.05%. The polymer T_g was taken as the maximum of the $\tan \delta$ peak. Using established manufacturer calibration techniques, an instrumental error of $\leq 5^\circ\text{C}$ is acceptable for T_g measurements; however, previous research with similar polymer films demonstrated that the standard deviation on three, averaged T_g values was within $\pm 2.2^\circ\text{C}$.

Viscosity

To investigate the influence of formulation viscosity on dose rate effects, viscosities were determined for each of the five-monomer series. Monomer viscosity was measured using a rotational cup and bob viscometer (Brookfield, Model No. DV-I+) equipped with a small sample adapter and S18 spindle. A rotation speed of 60 RPM was used for all monomers, except HPOPA. HPOPA required a reduced rotation speed of 12 RPM because of its higher viscosity. All samples were allowed to equilibrate to a temperature of 25°C over 30 minutes before the viscosity was recorded. The manufacturer-provided value (at 25°C) was used for the oligomer viscosity.²⁰

Because some viscosity values were outside the viscometer range, the viscosities of the monomer/oligomer formulations were predicted using the Refutas equation (Equation 4-3).²¹

$$\nu_{mixture} = e^{e^{\left(\frac{VBI_{mixture}-10.975}{14.534}\right)}} - 0.8 \quad (4-3)$$

where

$$VBI_{mixture} = [W_{comp,1} * VBI_{comp,1}] + [W_{comp,2} * VBI_{comp,2}] \quad (4-4)$$

and

$$VBI_{comp} = 14.534 * \ln[\ln(\nu_{comp} + 0.8)] + 10.975 \quad (4-5)$$

$VBI_{mixture}$ and VBI_{comp} represent the viscosity blending index (VBI) for the mixture and components, respectively. Mixture and component viscosity (cStokes) are represented by $\nu_{mixture}$ and ν_{comp} , respectively. Weight fraction of monomer and oligomer in the formulation is represented by $W_{comp,1}$ and $W_{comp,2}$, respectively.

4.3 Results and Discussion

This study investigated the impact of chemical structure on the magnitude of the dose rate effect. Dose rate effects were monitored by acrylate conversion and the polymer T_g , measured by Raman spectroscopy and DMA, respectively. Using the results of this study, a relationship to predict the dose rate effect for a given formulation was developed for industrial scale-up.

4.3.1 Influence of Dose on Dose Rate Effects

Conversion

The conversion of the polymer films was measured after exposure to EB radiation. Both dose and line speed were systematically varied to determine the effect of dose on dose rate effects. As expected, due to the increased number of electrons, conversion increases with increasing EB dose for all five monomer/oligomer

formulations (Table 4-1). Conversion also increases, generally, with increasing monomer size; the PEA, POEA, and HPOPA formulations have approximately 10 to 25 % greater conversion than the PA and BA formulations at 15 kGy, 20 ft/min. Because a similar trend is demonstrated in photo-initiated reactions of the same formulations (Chapter 5), the trend is broadly attributed to characteristics of the monomer structures that would affect both types of radiation initiation, such as viscosity, steric hindrance, and/or the propagation rate constant (k_p).

Table 4-1. Acrylate conversion (%) for five monomer/oligomer formulations at three different doses and line speeds. Conversion was measured using Raman spectroscopy and calculated using Equation 4-2. Conversion increases with increasing dose (at a constant line speed), but decreases with increasing line speed (at a constant dose).

	20 ft/min			100 ft/min			200 ft/min		
	15 kGy	30 kGy	60 kGy	15 kGy	30 kGy	60 kGy	15 kGy	30 kGy	60 kGy
PA	74	94	98	45	78	90	41	52	76
BA	86	95	97	53	76	86	36	57	74
PEA	96	98	99	62	87	97	55	87	89
POEA	100	96	98	74	95	97	68	92	97
HPOPA	96	98	99	96	97	98	93	96	97

Additionally, conversion decreases with increasing the line speed at a given dose. PEA polymerized at 15 kGy, for example, achieved 96% conversion at 20 ft/min but only reached 55% conversion at 200 ft/min. To better evaluate this dose rate effect (DRE) and its trends, a conversion DRE was defined as the change in conversion, at a single dose, as the line speed is increased from 20 ft/min to 200 ft/min, or

$$Conv. DRE(dose) = |Conversion_{20ft/min} - Conversion_{200ft/min}| \quad (4-6)$$

The conversion DRE for the five formulations, at each of the three doses, is shown in Figure 4-2.

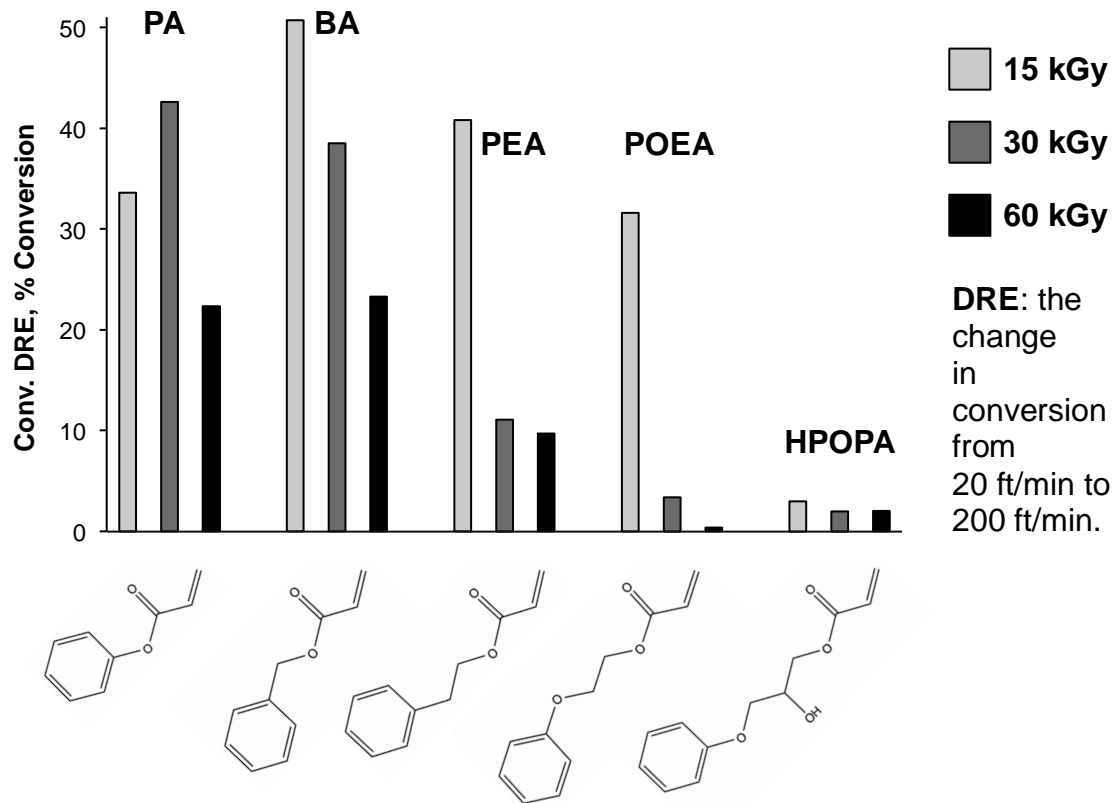


Figure 4-2. The conversion DREs, at three different doses, for three monomer/oligomer formulations. In general, the DRE magnitude decreases with increasing dose and with increasing monomer size.

With the exception of PA at 15 kGy, the magnitude of the conversion DRE decreases as dose increases for all five monomers. PA at 15 kGy is most likely anomalous due to its low conversion value at 20 ft/min (74%) relative to the other formulations. Large decreases in the DRE are observed for the first four monomers in the series (up to ~30%) across increasing dose. In contrast, HPOPA shows a very small (< 4%) change in conversion DRE at all three dose levels. The changes in monomer structure may provide an explanation for this trend and will be considered in the following section.

The dependence of DREs on dose has been previously studied with mixed results. Although the EB-curing conditions and formulations vary, a few studies substantiate the results of this research and show DREs decrease with increasing dose.^{10,11,17} One study

was found to be in contradiction with these results;¹⁵ however, the formulation included styrene, which is known to EB-polymerize via both the free-radical and cationic mechanisms and may, therefore, not be comparable to a solely free-radical system.²² In other studies, dose and line speed are not clearly specified, so it is not possible to compare DREs unambiguously.^{13,16} Because an alteration of either dose or line speed results in a dose rate change, both must be reported, especially since the work reported here indicates opposite DRE trends whether increasing the dose rate by dose or by line speed (Table 4-1).

A possible kinetic explanation for this dose/DRE relationship resides in the relative dependence of the propagation and termination mechanisms on radical concentration. The main process resulting from EB irradiation is the generation of free radicals from ionization (Figure 4-3).

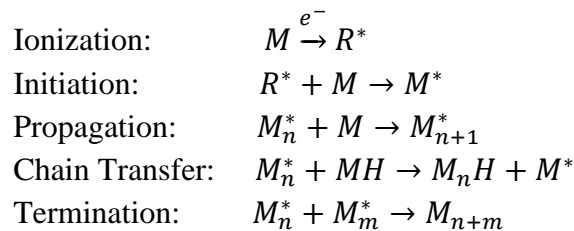


Figure 4-3. The EB polymerization reaction mechanism.

In EB polymerization, these radicals are used to initiate the reaction, propagate the growing polymer chain, and eventually terminate the reaction. In the presence of abstractable hydrogens, chain transfer can also occur due to the low bond dissociation energy of C-H and O-H bonds. Each of these kinetic steps is dependent on the concentration of free radicals in the system. Increasing the dose rate (dD/dt) increases the concentration of accelerated electrons at any given instant in time during an EB reaction, since the same amount of energy must be delivered over a shorter time period; in turn, the concentration of radicals ($[M^*]$) is also increased. Increasing the concentration of radicals increases the rate of propagation, R_p ,

$$R_p = k_p[M][M^*] \quad (4-7)$$

where k_p is the propagation rate constant and $[M]$ is the concentration of monomer. The rate of termination, R_t , also increases when the radical concentration is increased,

$$R_t = k_t [M^*]^2 \quad (4-8)$$

where k_t is the termination rate constant. However, the relationship between radical concentration and rate is first order with respect to the rate of propagation and second order with respect to the rate of termination. Thus, increasing the radical concentration causes a larger increase in the termination rate than in the propagation rate, leading to shorter polymer chains and lower conversions. Kinetically, dose rate effects are expected assuming traditional, bimolecular termination. Yet, if monomolecular termination is dominant, then the rate of termination becomes first-order dependent on radical concentration (Equation 4-9).

$$R_t = k_t [M^*] \quad (4-9)$$

If both R_p and R_t are directly proportional to $[M^*]$, dose rate effects are no longer anticipated. Conditions that promote monomolecular termination are those that decrease active center diffusion, including increased viscosity and conversion. At high doses (60 kGy), not only is high conversion reached (Table 4-1), but higher conversions are expected at earlier reaction times than for lower doses due to the increase in R_p . Thus, by increasing the dose, monomolecular termination should become dominant at increasingly shorter reaction times, limiting dose rate effects.

Glass Transition Temperature

The trends observed with polymer T_g are similar to those of conversion: as the dose was increased, a corresponding increase was seen in the T_g (Table 4-2). The T_g also decreased with increasing line speeds (at a constant dose).

Table 4-2. Glass transition temperature (T_g , °C) of the EB-cured films for five monomer/oligomer formulations at three different doses and line speeds. T_g was measured using DMA. T_g increases with increasing dose (at a constant line speed), but decreases with increasing line speed (at a constant dose).

	20 ft/min			100 ft/min			200 ft/min		
	15 kGy	30 kGy	60 kGy	15 kGy	30 kGy	60 kGy	15 kGy	30 kGy	60 kGy
PA	26	49	57	3	31	50	-21	6	19
BA	21	24	27	-3	2	14	-26	-19	14
PEA	17	21	24	-8	10	24	-17	9	18
POEA	28	31	30	3	30	27	-4	23	27
HPOPA	28	29	30	26	30	30	24	27	28

Parallel to the conversion DRE equation (Equation 4-6) and definition, a T_g DRE equation was established to investigate T_g DREs (Equation 4-10).

$$T_g \text{ DRE}(dose) = |T_{g,20ft/min} - T_{g,200ft/min}| \quad (4-10)$$

For each formulation, the magnitude of the T_g DRE decreases as dose is increased from 15 to 60 kGy (Figure 4-4).

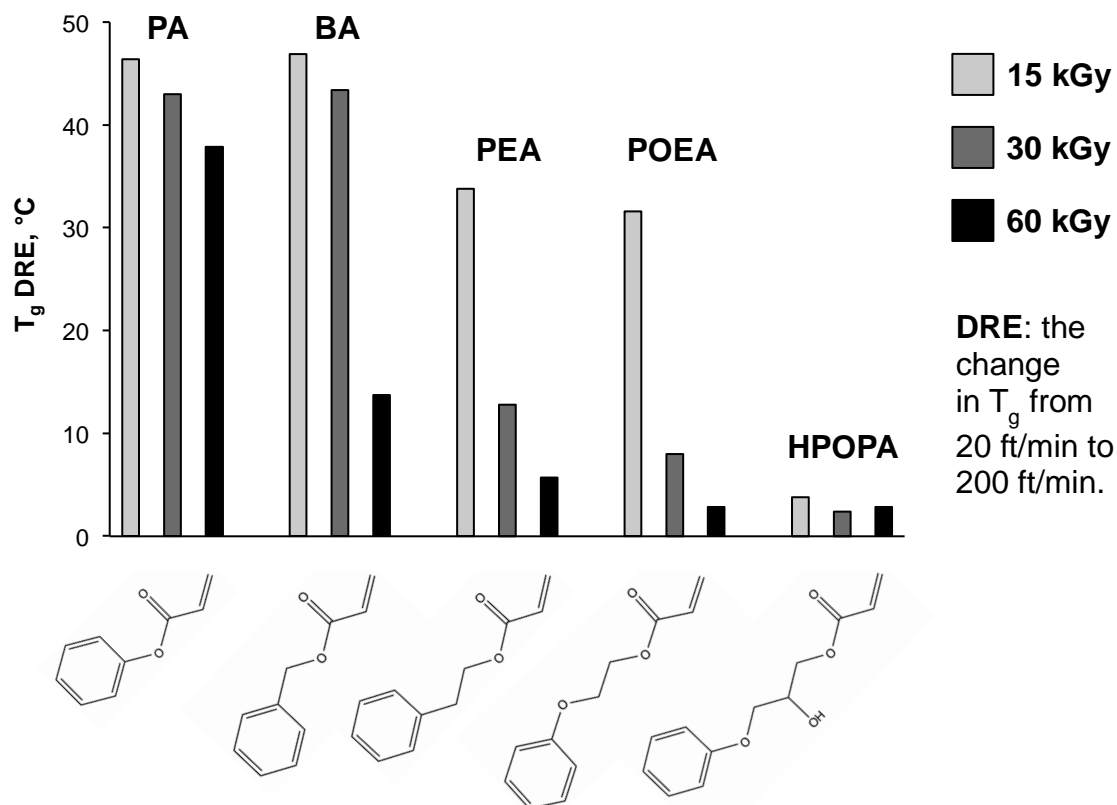


Figure 4-4. The T_g DREs, at three different doses, for five monomer/oligomer formulations. In general, the DRE magnitude decreases with increasing dose and with increasing monomer size.

However, this decrease in DRE is not necessarily linear. The PEA formulation, for example, experiences a relatively large change ($\sim 20^\circ\text{C}$) in its T_g DRE from 15 to 30 kGy but a relatively smaller DRE shift ($\sim 5^\circ\text{C}$) from 30 to 60 kGy. BA and POEA experience similar trends in T_g DRE as dose is increased. This noted difference suggests that a minimum amount of energy, unique to each monomer chemistry, is required to form the majority of the polymer network. Once this majority network is reached, the T_g is more stable and changes less with increasing dose.

This theory that extent of polymer network formation influences the DRE as dose is increased is corroborated by the DRE conversion trends (Figure 4-2) and the conversion values (Table 4-1). Since the majority of films achieved high conversions (typically $\geq 90\%$) at 20 ft/min (Table 4-1), regardless of dose, Equation 4-10 shows a

decrease in DRE must be due to an increase in polymer conversion at 200 ft/min. Therefore, small conversion DREs indicate a more fully formed polymer network.

This connection between conversion and T_g is well known: the T_g will increase with increasing polymer molecular weight, which in turn increases with conversion, until it reaches a threshold molecular weight where a maximum T_g is achieved.²³ Furthermore, monomer is known to plasticize the polymer film. At lower conversions, more monomer remains and suppresses the T_g .

4.3.2 Influence of Monomer Structure on Dose Rate Effects

As monomer size decreases across the series, the magnitudes of both the conversion and T_g DREs increase significantly (Figures 4-2 and 4-4). The formulation containing HPOPA, the largest molecule in the five-monomer series, shows the lowest DREs in the series in both T_g (4°C) and conversion (3%) at a constant dose of 15 kGy. At the same dose, the smallest molecules (PA and BA) have the largest DREs (51% and 47°C, respectively). This trend may not actually be reflective of the size of the monomer molecule, but rather properties intrinsic to the monomer chemistry such as viscosity, T_g , and R_p , which will affect the transition from bimolecular to monomolecular termination, and/or the number of abstractable hydrogens, which influences chain transfer.

High formulation viscosities can limit active center mobility from the onset of the reaction, and, as propagation occurs and polymer is produced, the system viscosity only increases, promoting monomolecular termination and limiting DREs. As predicted by this theory, HPOPA, having the lowest DREs in the series, does have the highest viscosity by an order of magnitude (Table 4-3).

Table 4-3. Component viscosities of the five monomers were measured experimentally at 25°C, while the viscosity of the oligomer was reported by the manufacturer. Formulation viscosities were calculated using the Refutas equation (Equation 4-3) assuming a 50/50, by weight, mixture of monomer and oligomer.

	Component Viscosity (cStokes)	Formulation Viscosity (cStokes)
PA	3.6	72.4
BA	2.3	40.8
PEA	3.5	70.4
POEA	7.5	167.9
HPOPA	173.0	2,986.2
Oligomer	246,285.7	

Yet, the influence of viscosity falls short when applied to the remaining monomers of the series. Viscosity does not increase incrementally with monomer size as the DRE trends would suggest. PA and PEA have almost identical viscosities, but their DREs differ substantially (Figures 4-2 and 4-4). The POEA formulation viscosity is a full order of magnitude greater than that of PEA, but the two formulations have similar T_g DREs (Figure 4-4). While viscosity may be a contributing factor in the influence of monomer structure on DREs, it does not appear to be the overriding cause.

Another property expected to contribute to the monomer structure/DRE relationship is T_g . Once the reaction has proceeded far enough to establish a polymer T_g greater than the curing temperature, vitrification occurs and the reaction becomes diffusion controlled due to the stiffened polymer network. If the polymer T_g is at or below room temperature, vitrification should not occur, making monomolecular termination less likely. Using reported T_g values,^{20,24-27} the formulation T_g 's were estimated using the Flory-Fox equation,

$$\frac{1}{T_g} = \frac{w_1}{T_{g,1}} + \frac{w_2}{T_{g,2}} \quad (4-11)$$

where w_1 and w_2 are the weight fractions of the two components in the formulation (here, a monomer and the oligomer) and $T_{g,1}$ and $T_{g,2}$ are their respective, homopolymer, glass

transition temperatures (in K). This method of estimation was used because of the wide range of T_g values in Table 4-2. Figure 4-5 demonstrates the lack of correlation between the estimated T_g value and the DRE magnitude.

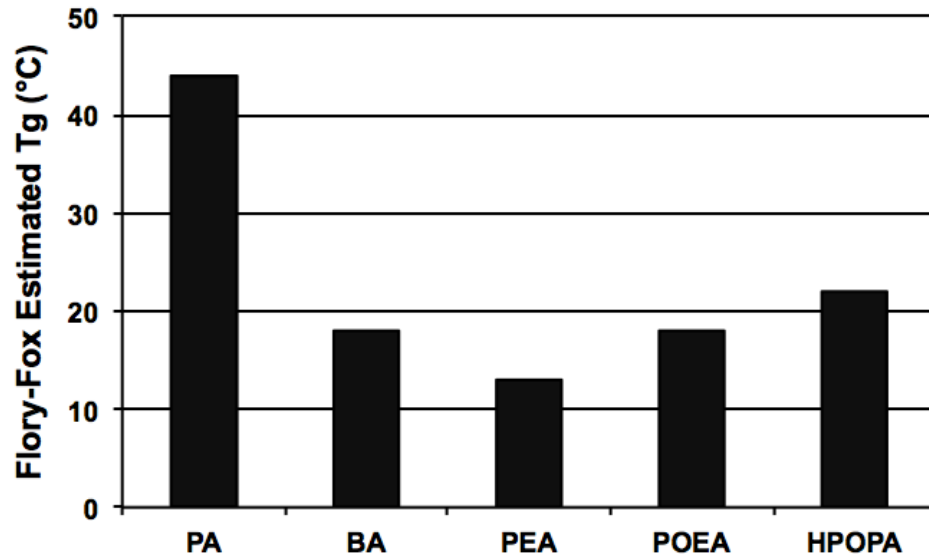


Figure 4-5. The monomer/oligomer formulation T_g values, as estimated by the Flory-Fox equation (Equation 4-8), presented in order of decreasing DRE magnitude (PA > HPOPA). T_g and DRE magnitude do not correlate.

PA, with the highest T_g (well above room temperature), should have the smallest DREs; in fact, PA has some of the largest DREs (Figures 4-2 and 4-4). Additionally, PEA, with the lowest T_g (below room temperature), should have the largest DREs; yet, as previously observed, its DRE magnitude falls in the middle of the five monomer series. Note, of the experimental T_g values, those of the films polymerized at 30 kGy and 20 ft/min best correspond to the estimated values. These experimental values deviate from the estimated values by 5 to 13°C, though PA and PEA remain the high and low T_g 's, respectively (Table 4-2).

In addition to viscosity and T_g , R_p is another property expected to influence the DRE trends. As previously discussed, when R_p is increased, higher conversions are reached earlier in the reaction, promoting monomolecular termination. Therefore, as the magnitude of the DREs decreases across the five-monomer series (PA to HPOPA), the magnitude of R_p should increase. This relationship between DREs and R_p is clearly

illustrated for UV-initiated reactions of the five monomers in Figure 4-6, where R_p is the slope of the conversion profile.

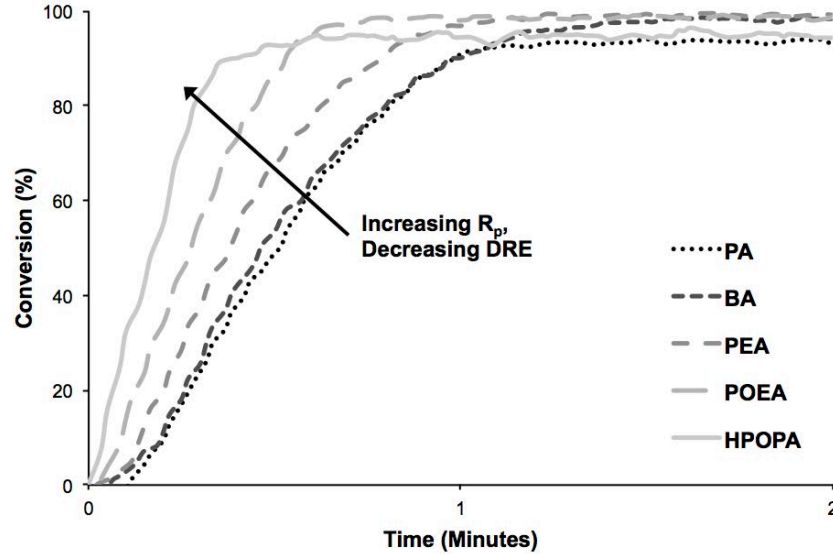


Figure 4-6. Real-time conversions from UV-initiated reactions of neat monomer collected using Raman spectroscopy. The R_p increases and the DRE decreases with increasing monomer size.

Additionally, numerical values of $R_{p,max}$ are listed in Table 4-4. The magnitude of $R_{p,max}$ increases and the reaction time at which it occurs decreases with increasing monomer size, with the exception of the timing of PA's $R_{p,max}$. Although PA's $R_{p,max}$ occurs a few seconds before BA's, BA retains a slightly higher conversion than PA through most of the reaction (Figure 4-6).

Table 4-4. The maximum R_p value and the reaction time at which it occurred for the six components and five monomer/oligomer formulations. R_p values were calculated using the conversion vs. time profiles (Figures 4-6 and 4-7). Decreasing DRE magnitude (PA > HPOPA) correlates with increasing monomer and formulation R_p values, with the exception of the HPOPA formulation.

	Component		Formulation	
	$R_{p, \max}$	Time (min)	$R_{p, \max}$	Time (min)
PA	173	0.24	92	1.01
BA	183	0.35	150	0.63
PEA	217	0.20	159	0.51
POEA	316	0.15	217	0.51
HPOPA	349	0.08	163	0.55
Oligomer	141	0.36		

Although a clear relationship between DREs and R_p is seen for the five monomers, this trend becomes obscured when considering the five monomer/oligomer formulations. Unlike the neat monomer, the HPOPA/oligomer formulation violates the trend by not having the largest value of R_p (Table 4-4). A possible explanation for HPOPA's violation may be due to its formulation viscosity, which is an order of magnitude (or two) above the other formulations (Table 4-3). While it could not be proven that viscosity is a majority cause of DREs, the substantial magnitude of HPOPA's formulation viscosity may be more than enough to compensate for its low R_p . The high viscosity could cause HPOPA to begin the reaction in the monomolecular termination regime, in which case, a high R_p would not be required to maintain little to no DREs.

In both cases (*i.e.*, neat monomer and monomer/oligomer formulations), there are indications that R_p , while certainly a contributing factor, is not the sole cause of DREs. If R_p was the singular source of DREs, similarities in DRE magnitude for two different formulations should be the result of similar R_p values; however, a comparison of DRE and R_p values does not follow this logic. For example, the BA and PEA formulations have near identical conversion profiles (Figure 4-7), yet differ in their respective DRE magnitudes (Figures 4-2 and 4-4). In fact, the magnitude of the BA formulation's DREs more closely resembles that of PA rather than PEA, even though the PA formulation's conversion profile (and thus R_p) is quite different from BA's.

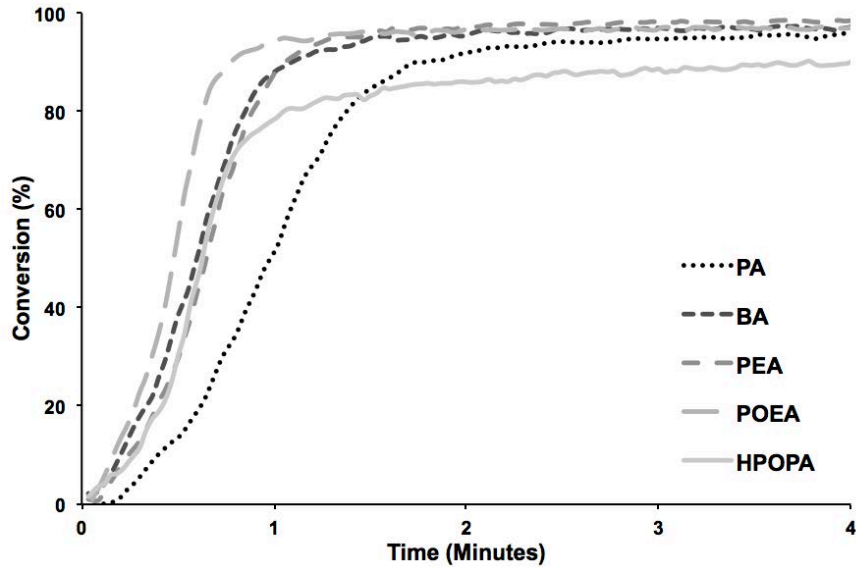


Figure 4-7. UV-initiated reactions of monomer/oligomer formulations collected using Raman spectroscopy.

In addition to maximizing R_p , promoting chain transfer may also reduce DREs. A notable difference among the five monomers investigated is the quantity of abstractable hydrogens (Figure 4-1). Setting aside the hydrogen atoms the monomers have in common (on the phenyl ring and acrylate moiety), PA, for example, does not contain any additional hydrogen atoms, while HPOPA has five potentially abstractable hydrogen atoms, including a tertiary hydrogen atom alpha to an oxygen atom that should be easily abstracted due to the low bond energy (4.4 eV).²⁸ Increasing the concentration of abstractable hydrogens ($[MH]$) increases the rate of chain transfer (R_{ct}):

$$R_{ct} = k_{ct}[M^*][MH] \quad (4-12)$$

where k_{ct} is the chain transfer rate constant. Chain transfer provides a route to conversion by effectively untethering the propagating radical from an entangled polymer chain, increasing the radical's ability to diffuse through the system and reach unreacted monomer molecules. Therefore, if the monomer structure is conducive to a higher rate of chain transfer, the combined propagation and chain transfer mechanisms can compete more effectively with termination, leading to higher conversion. At low dose rates, where high conversions (>90%) are achievable, the aid of the chain transfer mechanism may go

unnoticed. However, when the dose rate is increased, R_t is increased exponentially faster than R_p (assuming bimolecular termination). Thus, it is possible that promoting chain transfer restores the balance between termination and conversion, lessening or eliminating dose rate effects. This explanation is consistent with the relative order of DREs for the monomers in this study.

4.3.3 Predicting Dose-Rate-Effect Magnitude

The results discussed above demonstrate that the T_g of a polymer produced via EB initiation can be increased by increasing the dose or by decreasing the dose rate (Table 4-2 and Figure 4-4). These results were used to develop a predictive correlation between the magnitude of the T_g DRE and the T_g shift caused by a formulation's response to different doses. The latter is defined as the T_g dose effect (DE, Equation 4-13).

$$T_g DE(\text{line speed}) = |T_{g,60kGy} - T_{g,15kGy}| \quad (4-13)$$

Specifically, in this five-monomer series, the change in polymer properties caused by a 4-fold increase in dose (15 to 60 kGy) was found to be equivalent to the property change caused by a 10-fold increase in line speed (20 to 200 ft/min).

To demonstrate this relationship between dose and line speed, Figure 4-8 compares the change in T_g caused by the increase in dose (15 to 60 kGy) at 20 ft/min [T_g DE (20 ft/min)] to the change in T_g caused by the increase in line speed (20 to 200 ft/min) at 60 kGy [T_g DRE (60 kGy)].

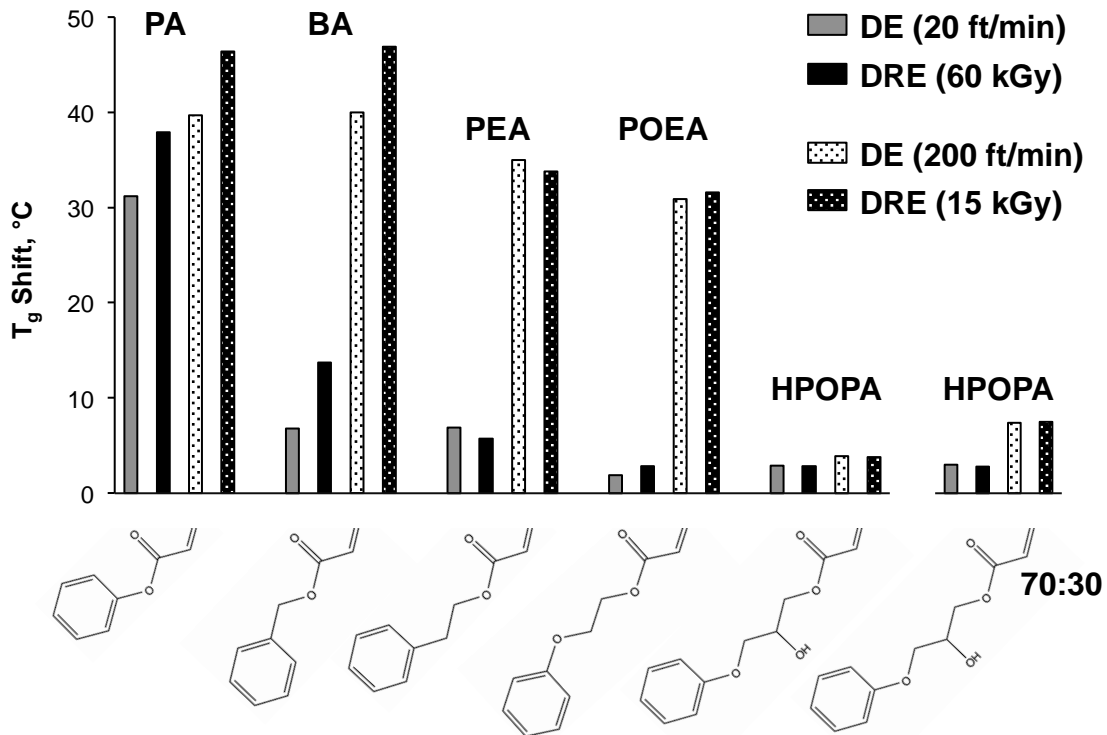


Figure 4-8. Using T_g -shift comparisons, a demonstration of the relationship between increasing dose 4-fold and line speed 10-fold. DE (20 ft/min) is the magnitude of the T_g shift from 15 kGy to 60 kGy at a constant line speed of 20 ft/min. DRE (60 kGy) is the magnitude of the T_g shift from 20 ft/min to 200 ft/min at a constant dose of 60 kGy. To be perfectly predictive, the bar values in gray should be equal to those in black, and light-textured bar values should equal dark-textured bar values.

The same relationship is also shown for an increase in dose at 200 ft/min [T_g DE (200 ft/min)] and an increase in line speed at 15 kGy [T_g DRE (15 kGy)] (Figure 4-8, textured bars). To be accurately predictive, the T_g shift of the corresponding DE and DRE should be equal. The DE magnitude is within 2°C of that of the DRE for the PEA, POEA, and HPOPA formulations. The largest difference between T_g shifts is approximately 7°C for the PA and BA formulations. This error in prediction is expected to decrease with replication of the results. Even with the current level of error, the T_g of the final BA film was predicted to within 4°C of the actual experimental value using this DE-DRE relationship. The kinetic significance of a 4-fold increase in dose being equivalent to a 10-fold increase in line speed is not yet fully understood.

This predictive correlation holds for the conversion DE-DRE relationship as well, though with less accuracy (Figure 4-9), where the conversion dose effect (DE) is defined as

$$\text{Conv. DE}(\text{line speed}) = |\text{Conversion}_{60\text{kGy}} - \text{Conversion}_{15\text{kGy}}| \quad (4-14)$$

BA and PEA have the largest difference between conversion shifts of 13 and 7% conversion, respectively. The other three formulations are accurately predictive with differences in conversion shifts of less than 3% conversion.

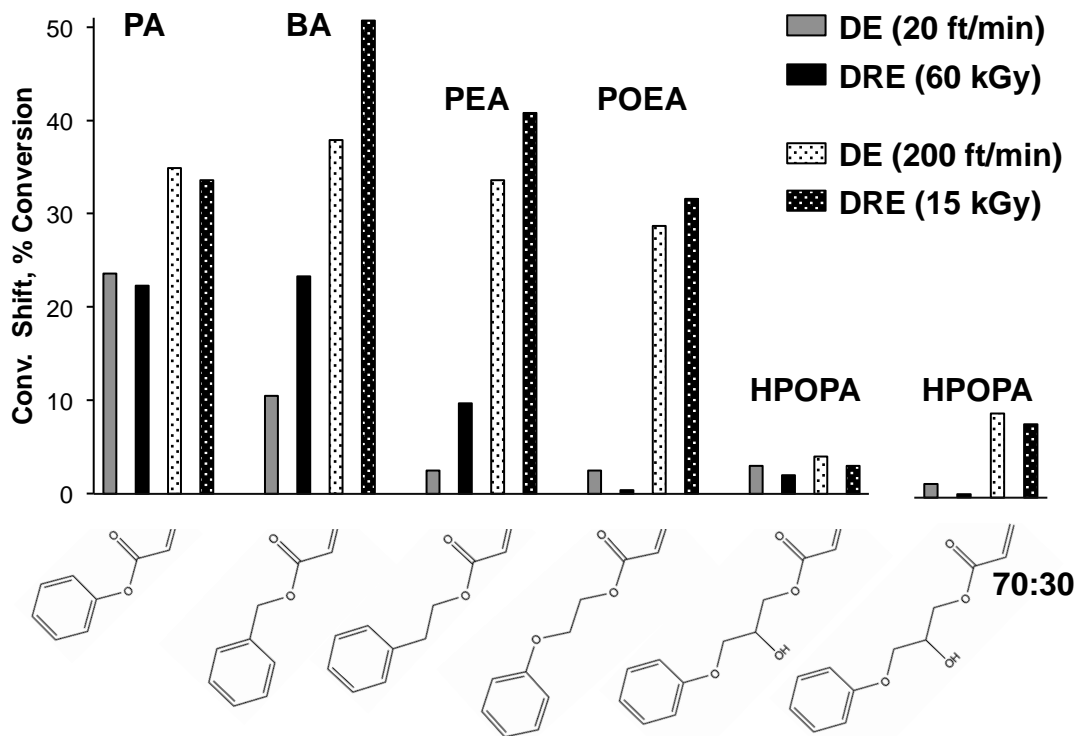


Figure 4-9. Using conversion-shift comparisons, a demonstration of the relationship between increasing dose 4-fold and line speed 10-fold. DE (20 ft/min) is the magnitude of the conversion shift from 15 kGy to 60 kGy at a constant line speed of 20 ft/min. DRE (60 kGy) is the magnitude of the conversion shift from 20 ft/min to 200 ft/min at a constant dose of 60 kGy. To be perfectly predictive, the bar values in gray should be equal to those in black, and light-textured bar values should equal dark-textured bar values.

The correlation between DE and DRE for EB-polymer properties (in this case, T_g), is significant because it allows for the prediction of DREs by simply changing the dose. DREs often may only be observed at high processing speeds, which are difficult to achieve in a lab or pilot-line setting; however, dose is easily adjusted in either situation.

4.4 Conclusions

This study has demonstrated clear DRE trends, as measured by shifts in the conversion and T_g of EB-polymerized films. It was established DREs are dependent on dose: as dose was increased, the magnitude of the dose rate effect decreased. The size of the DRE was also shown to be highly dependent on the chemical structure of the monomer: the magnitude of the DRE increased across the five-monomer series, having the largest effects on the smallest molecules, PA and BA. This influence of monomer structure on the DRE trend was consistent with the expected differences in the rate of chain transfer contributed by the relative number of abstractable hydrogens. Furthermore, this work has shown that predictions can be made about the magnitude of a formulation's DRE by comparing its response to different doses (DE). These DRE predictions are useful for industrial scale-up, as well as the establishment of a fundamental kinetic foundation that EB polymerization currently lacks. Future studies will determine the efficacy of this predictive relationship for a broad range of monomers and will explore how reaction kinetics support the 4-to-10 ratio of dose to line speed.

Confirming DREs in both conversion and T_g and establishing similar DRE trends in both polymer properties are integral steps for future investigations. This study examined DREs on monomer/oligomer formulations because the inclusion of oligomers was necessary to achieve films with enough structural integrity for DMA measurements. Although the oligomer chemistry remained constant, it would be preferable to study DREs on pure monomers. Similarly, the presence of a phenyl ring in the monomer structure was needed for Raman measurements, yet few acrylate monomers contain a phenyl ring. By comparing conversion and T_g results in a formulation series that could withstand both Raman spectroscopy and DMA, series can now be developed that can only be explored using one method or the other with reasonable certainty that the presence of conversion DREs will indicate T_g DREs and vice versa. Structural integrity

is not needed for Raman, thus the effect of oligomers can be studied by comparing current conversion results with those of pure monomer formulations. A phenyl monomer is not needed for DMA experiments, thus widening the field of acrylates that can be investigated.

Taken collectively, the results of this study have established a rudimentary structure/processing conditions/properties relationship. Albeit preliminary and only confirmed for this 5-monomer acrylate series, understanding how the chemical structure of the starting materials and the processing conditions they undergo collectively influence the final properties of the polymer produced is vital to understanding the fundamental aspects of EB polymerization and furthering the development of EB technology. As future studies strengthen this structure/processing conditions/properties relationship, this knowledge can be used to expand EB technology to create high-performance EB materials at high production speeds.

4.5 References

- (1) Cohen, G. UV-EB Market Trends. *RadTech Report* **2012**, No. 2, 44–48.
- (2) Datta, S. K.; Chaki, T. K.; Bhowmick, A. K. Electron Beam Processing of Polymers. **2000**, 1–30.
- (3) *Radiation Curing of Polymeric Materials*; Hoyle, C. E., Kinstle, J. F., Eds.; American Chemical Society, **1990**.
- (4) Drobny, J. G. *Ionizing Radiation and Polymers*; Elsevier Inc., **2013**.
- (5) Kinstle, J. F. Electron-Beam Curing of Polymeric Materials. In *Radiation Curing of Polymeric Materials*; Hoyle, C. E., Kinstle, J. F., Eds.; ACS Symposium Series; American Chemical Society: Washington, DC, **1990**; Vol. 417, pp 17–23.
- (6) Richter, K. B. Pulsed Electron Beam Curing of Polymer Coatings. **2007**, 1–246.
- (7) Burth, D.; Lechner, V.; Krebs, F. Electron Beam Dose Rate Effects. *RadTech Report* **2010**, 34–41.
- (8) Davidson, R. S.; Ellis, R. J.; Wilkinson, S. A.; Summersgill, C. A. A Study of the Polymerization of Acrylates Using Electron-Beam Radiation. *European Polymer Journal* **1987**, 23 (2), 105–108.
- (9) Patacz, C.; Defoort, B.; Coqueret, X. Electron-Beam Initiated Polymerization of Acrylate Compositions 1: FTIR Monitoring of Incremental Irradiation. *Radiation Physics and Chemistry* **2000**, 59 (3), 329–337.
- (10) Pedersen, W. B.; Singer, K. Electron Beam Curing of Organic Surface Coatings. **1971**, 1–10.
- (11) Rangwalla, I.; Nablo, S. V. A Parametric Study of the Electron Curing of Inks and Coatings. *RadTech Report* **1990**, 18–28.
- (12) Defoort, B.; Lopitiaux, G.; Dupillier, J.-M.; Larnac, G.; Coqueret, X. Electron-Beam Initiated Polymerization of Acrylate Compositions, 6. *Macromol. Chem. Phys.* **2001**, 202, 3149–3156.
- (13) Labana, S. S. Kinetics of High-Intensity Electron-Beam Polymerization of a Divinyl Urethane. *Journal of Polymer Science Part A-1: Polymer Chemistry* **1968**, 6 (12), 3283–3293.
- (14) Seto, J.; Nagai, T.; Noguchi, T.; Arakawa, S.; Shibata, A.; Ishimoto, C.; Miyashita, M. Electron Beam Curing of Acrylic Oligomers. *Radiation Physics and Chemistry* **1985**, 25, 567–579.

- (15) Hoffman, A. S.; Jameson, J. T.; Salmon, W. A. Electron Radiation Curing of Styrene-Polyester Mixtures. Effect of Backbone Reactivity and Dose Rate. *Ind. Eng. Chem. Prod. Res. Develop.* **1970**, 9 (2), 158–167.
- (16) Burlant, W.; Hinsch, J. Divinyl Copolymerization Initiated by High Intensity, Low Energy Electrons. *Journal of Polymer Science Part A: General Papers* **1965**, 3 (10), 3587–3597.
- (17) Xiancong, H.; Meiwu, S.; Guotai, Z.; Hong, Z. Investigation on the Electron-Beam Curing of Vinylester Resin. *Radiation Physics and Chemistry* **2008**.
- (18) Schissel, S. M.; Lapin, S. C.; Jessop, J. L. P. Internal Reference Validation for EB-Cured Polymer Conversions Measured via Raman Spectroscopy. *RadTech Report* **2014**, No. 4, 46–50.
- (19) Cai, Y.; Jessop, J. L. P. Decreased Oxygen Inhibition in Photopolymerized Acrylate/Epoxy Hybrid Polymer Coatings as Demonstrated by Raman Spectroscopy. *Polymer* **2006**, 47 (19), 6560–6566.
- (20) *RadCure Energy Curable Resins Product Guide*; **2006**; pp 1–28.
- (21) Eom, H. S.; Jessop, J. L. P.; Scranton, A. B. Photoinitiated Cationic Copolymerizations: Effects of the Oligomer Structure and Composition. *Polymer* **2013**, 54, 4134–4142.
- (22) Squire, D. R.; Cleaveland, J. A.; Hossain, T. M. A.; Oraby, W.; Stahel, E. P.; Stannett, V. T. Studies in Radiation-Induced Polymerization of Vinyl Monomers at High Dose Rates. I. Styrene. *J. Appl. Polym. Sci.* **1972**, 16 (3), 645–661.
- (23) Odian, G. *Principles of Polymerization*, 4 ed.; John Wiley and Sons, Inc., **2004**.
- (24) 2-Phenylethyl Acrylate, Min. 92%. www.polysciences.com. Accessed Jun. **2015**.
- (25) Benzyl Acrylate, ~99%. www.polysciences.com. Accessed Jun. **2015**.
- (26) Phenyl Acrylate, Min. 95%. www.polysciences.com. Accessed Jun. **2015**.
- (27) Cn131b. americas.sartomer.com. Accessed Jun. **2015**.
- (28) Darwent, B. D. *Bond Dissociation Energies in Simple Molecules*; U.S. Government Printing Office: Washington, D.C., **1970**; pp 1–58.

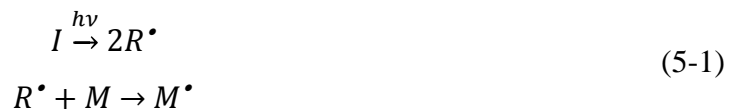
CHAPTER 5 EQUIVALENT INITIATION ENERGY COMPARISON OF PHOTO- AND ELECTRON-BEAM-INITIATED POLYMERIZATION: KINETIC AND PHYSICAL PROPERTIES

5.1 Introduction

Both photo- and electron beam-initiated (EB) reactions, belonging to the category of radiation polymerization, have become widely accepted *green* methods for producing adhesives, inks, coatings, and films.¹⁻⁵ Switching from the traditional, thermal-initiated polymerization method reduces the use of volatile organic compounds, saves processing space, and significantly reduces energy consumption. Moreover, radiation polymerization generally benefits from increased reaction speeds and improved temporal and spatial control.

Because of the similarity in applications and advantages of these forms of radiation polymerization, the distinction between EB polymerization and photopolymerization is often blurred. Consequently, it is assumed that the polymers produced by each of the two methods are also indistinguishable. Yet, EB polymerization and photopolymerization differ in multiple ways, and previous studies have demonstrated so do their respective polymers.⁶⁻⁸

One of the main ways in which the two radiation reactions differ is the initiation mechanism. In photopolymerization, specifically free-radical photopolymerization, a photoinitiator (I) decomposes upon exposure to light ($h\nu$) into radicals, which can then, through the addition of a monomer (M), form the beginning of a propagating polymer chain (M^*) (Equation 5-1).⁹



In contrast, EB free-radical polymerization does not require an initiator. The accelerated electrons (e^-) are more energetic than the photons of visible/ultraviolet light, and as such, are able to homolytically cleave the bonds of monomer molecules to create the necessary radicals (Equation 5-2).^{4,10}



This alteration in the initiation mechanism can have far-reaching effects; prominent among them is the increase in cross-linking, due to the indiscriminate nature of the electrons. Formation of radicals is a controlled process in photopolymerization, but in EB polymerization, an accelerated electron can theoretically break any bond it encounters, as long as its energy is greater than that required to break the bond.

By comparing EB- and photo-cured polymers, the impact of the initiation mechanism on the polymerization and resulting polymer can be distinguished, due to the remaining polymer mechanisms (propagation and termination) being identical. In addition, through this comparison, photopolymerization can serve as a benchmark for EB studies. EB polymerization is difficult to characterize because of the harsh nature of the accelerated electrons and need for radiation shielding; comparison to the well-developed field of photopolymerization would give insight into such aspects as reaction kinetics, which can only be indirectly measured in EB polymerization.

Such a comparison would also help elucidate kinetic phenomena like dose rate effects, or, as it is more commonly known in the photopolymerization literature, reciprocity failure. To achieve reciprocity, the resulting polymer film must be identical despite changing the rate at which the energy (dose or exposure) is delivered. In many cases, reciprocity is assumed for both EB and photopolymerization, especially if the extremes are ignored: very high energy, short delivery time vs. very low energy, long delivery time. However, as discussed in Chapter 4, when reciprocity is not attained in EB polymerization, dose rate effects can be problematic during industrial scale-up. In photopolymerization, reciprocity failure is studied extensively in dentistry, where even minute changes in conversion, adhesion, or shrinkage could cause dental fillings to fail.¹¹⁻

17

However, complicating a direct comparison between photo- and EB-initiated polymerization is another difference between the two – energy units. EB dose is measured in kilogray or megarads, with base units of J/g. In contrast, light exposure is measured in J/cm². These units are a reflection of energy deposition for each method of

radiation. Light through a film is governed by the Beer-Lambert law: its greatest energy is always at the film surface, and therefore its energy unit is a surface measurement. EB dose as a function of film depth is more complex. It is modeled using Monte Carlo simulations, is affected by film density, and, as such, its energy unit is three-dimensional in nature. In order to obtain a quantitative comparison of the two polymerization methods, the initiation energies must be equal.

In this study, a protocol was developed to investigate photo- and EB-polymerized films of equivalent initiation energies. This protocol was then applied to a series of five monomers, chosen to characterize the impact of the initiation mechanism on reciprocity failure or energy rate effects. Raman spectroscopy and dynamic mechanical analysis (DMA) were used to determine differences in polymer conversion and physical properties, respectively.

5.2 Experimental

5.2.1 Materials

A series of five monomers was chosen to investigate the impact of initiation mechanism and monomer chemistry on the magnitude of the energy rate effect: phenyl acrylate (PA, MP Biomedicals), benzyl acrylate (BA, MP Biomedicals), 2-phenylethyl acrylate (PEA, Polysciences), 2-phenoxyethyl acrylate (POEA, TCI America), and 2-hydroxy-3-phenoxypropyl acrylate (HPOPA, Sartomer) (Figure 5-1).

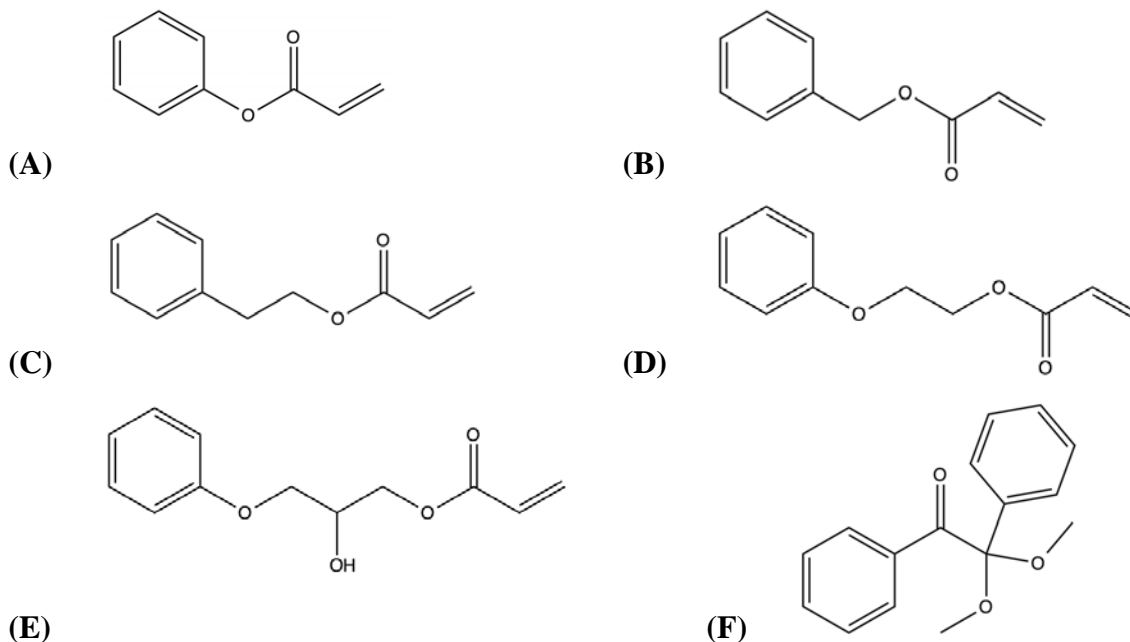


Figure 5-1. The chemical structures of the 5-monomer series: (A) PA, (B) BA, (C) PEA, (D) POEA, and (E) HPOPA. Also shown is the photoinitiator DMPA (F) which was used in the photopolymerization reactions.

This series was first conceived to study dose rate effects in EB polymerization (Chapter 4). An aliphatic urethane diacrylate oligomer, Ebecryl 8807 (proprietary structure, Allnex), was added to each monomer to improve the film properties of the samples and allowed for mechanical-property testing. To each monomer/oligomer formulation, the Type 1 photoinitiator 2,2-dimethoxy-2-phenylacetophenone (DMPA, Sigma Aldrich, Figure 5-1) was added for the photopolymerization reactions. No initiator was used in EB-initiated polymerizations. All materials were used as received and stored at room temperature.

5.2.2 Methods

EB Film Preparation

Each formulation consisted of a 50/50, by weight, mixture of monomer and oligomer. Because of the high viscosity of the oligomer, the formulations were heated to approximately 60°C to allow mixing of the monomer and oligomer. Once heated, formulations were stirred using a drill with a paddle mixer attachment.

Samples for EB curing were prepared by first treating 4 x 3.25 inch glass slides using two coats of Rain-X® 2-in-1 glass cleaner and rain repellent. Next, two layers of lab tape (total thickness ~180 µm) were placed on either side of the glass to be used as spacers. A large droplet, approximately 1 mL, of a formulation was then placed near the top of the slide, between the pieces of tape, and covered with a piece of silicone-coated, 34-µm thick polyethylene terephthalate (PET). A straight edge was drawn across the PET to form a uniform film underneath. The PET cover was used to eliminate the effect of oxygen diffusion in the experiments.

The samples on the glass slides were polymerized by EB irradiation through the PET film using an EB accelerator equipped with a variable-speed, fiberglass carrier web (BroadBeam EP Series, PCT Engineered Systems, Inc.). Three different doses (15, 30, and 60 kGy) and three different line speeds (20, 100, and 200 ft/min) were used to cure the films. Accelerating voltage and N₂ flow rate were held constant at 250 kV and 17 SCFM, respectively. Once polymerized, the films were removed from the glass slides and cut into rectangles measuring 6.25 x 25 mm for characterization. The use of silanized (Rain-X®-treated) glass and silicone-coated PET assisted in the release of the polymer film.

UV Film Preparation

Photo-curable formulations were prepared identical to the EB-curable formulations, with the addition of 0.1 wt% DMPA to the homogenous monomer/oligomer mixture. The formulations were sonicated for 60 minutes to dissolve the photoinitiator.

Two sets of samples were prepared for photopolymerization. The first set (Set 1-Initial) was prepared by forming a mold consisting of two silanized (Rain-X® washed) glass microscope slides separated by 200 µm spacers, then injecting the formulation into the mold via syringe. An Omnicure® S1000 Ultraviolet/Visible Spot Cure System (Excelitas, 250-450 nm band pass filter) with a 3 mm liquid lightguide and adjustable collimating lens attachment (Lumen Dynamics, Model No. 810-00041) was used to polymerize the formulations at ambient temperature. A 20 cm distance was set between the collimating lens and the sample surface to ensure a consistent irradiance profile over the entire exposure area. The effective irradiance was measured by a radiometer

(Versaprobe Pro, Con-Trol Cure). Once polymerized, samples were removed from the glass molds and cut into 6.25 mm x 25 mm films to be characterized by both Raman spectroscopy and DMA.

The second set of photopolymerized samples (Set 2 – Equivalent) required increased effective irradiances, and therefore the exposure area was reduced. Two pieces of tape (total thickness ~200 μm) were layered, and then a 3 mm diameter hole was punched into the layered tape. The edge of the hole was placed on the edge of a silanized glass microscope slide, and another silanized slide was used to sandwich the tape and create a mold (Figure 5-2). The formulation was injected into the mold, and Critoseal was used to seal the exposed edge, preventing oxygen diffusion.

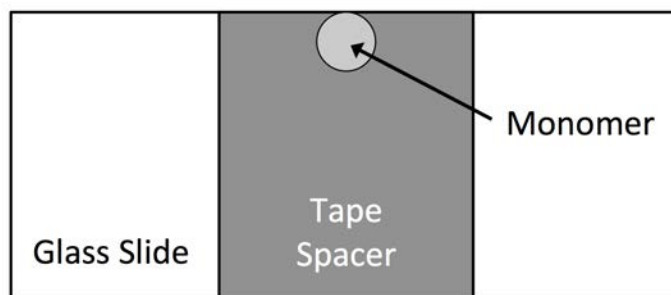


Figure 5-2. Schematic of the mold used to produce the second set of photopolymerized samples with a reduced exposure area (Set 2 – Equivalent).

Polymerization was initiated using the same light source, but without the collimating lens attachment. The end of the lightguide was placed directly over the monomer area. Whenever possible, the end of the lightguide was in contact with the glass slide; however, in some instances, the distance was increased to no more than 1 cm to adjust the effective irradiance when the lamp adjustment did not have enough resolution to match the needed value. The effective irradiance was measured by a radiometer (OmniCure, Model No. R2000). After polymerization, samples were removed from the mold and placed on an aluminum Q-panel for Raman characterization. Due to the small size of the films, they were not used for physical property testing.

UV/EB Initiation Energy Comparison

In order to estimate equivalent initiation energies, the energy units of either photopolymerization or EB polymerization needed to be transformed. In this case, the photopolymerization energy units were manipulated to match those of EB polymerization. As illustrated in Equation 5-3, the units of effective irradiance ($\frac{mW}{cm^2}$) were multiplied by the surface area of the film (cm^2).

$$\frac{mW}{cm^2} * cm^2 * \frac{mJ/s}{mW} * s * \frac{J}{1000 mJ} * \frac{1}{g} = \frac{J}{g} = kGy \quad (5-3)$$

Then, a conversion factor ($\frac{mJ/s}{mW}$) was used to reduce mW to its base units. Next, the value was multiplied by the exposure time (s) and another conversion factor ($\frac{J}{1000 mJ}$). Finally, the value was divided by the film mass (g), which transformed the units into J/g , or kGy .

Another important aspect to achieving equivalent initiation energies was establishing a consistent energy level throughout the film depth. For the EB-cured films, a voltage of 250 kV was chosen, based on Monte Carlo simulations (Integrated Tiger Series 3 from Oak Ridge National Labs), to ensure a consistent absorbed dose through a 200- μm film (Figure 5-3).

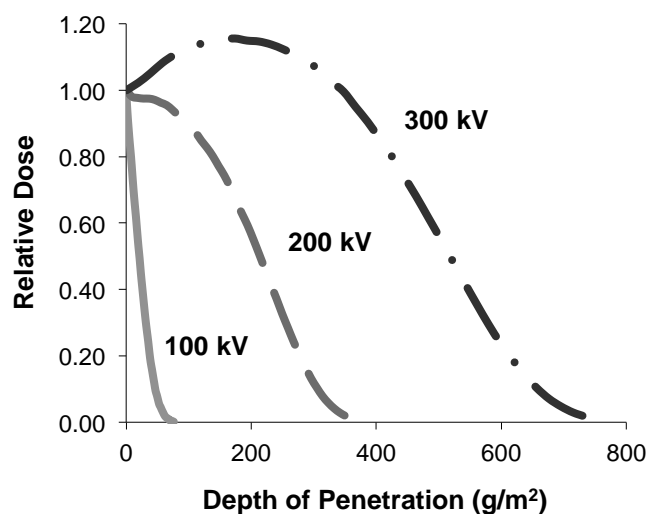


Figure 5-3. Depth/dose curve for EB polymerization, as predicted by Monte Carlo simulations. With a density of 1 g/cm^3 , the depth of penetration units become micrometers. A voltage of 250 kV was chosen to ensure a consistent dose through a film of $200 \text{ }\mu\text{m}$.

Similarly, a depth/effective irradiance curve was estimated for the photo-cured films using the model created by Kenning, *et al.*, which uses the differential equations governing polychromatic illumination.¹⁸ The spectral output of the lamp was obtained using an Ocean Optics USB 4000 fiber optic spectrometer. The molar absorptivity of DMPA was collected using an Agilent UV-Visible spectrometer in 1 nm increments.¹⁹ The photoinitiator concentration was varied to reduce the irradiance gradient through the film depth, and a concentration of 0.1 wt% DMPA was chosen for the photopolymerization studies (Figure 5-4). By selecting 0.1 wt% as the photoinitiator concentration, the Kenning, *et al.* model predicted less than a 10% variance in energy across the film depth for the initial photo-cured films (Set 1) and less than a 15% variance for the equivalent photo-cured films (Set 2).

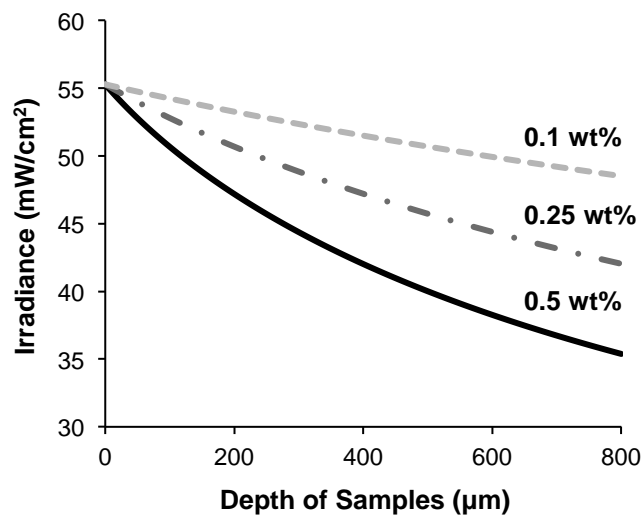


Figure 5-4. Depth/irradiance curve for photopolymerizations, as predicted by the Kenning, *et al.* model, with decreasing concentrations of DMPA. A concentration of 0.1 wt% DMPA was chosen for the photopolymerization studies to reduce the irradiance gradient.

In order to calculate exposure time and effective irradiance, a value of $\left(\frac{cm^2}{g}\right)$ was determined for each monomer/oligomer formulation by photopolymerizing three films, then taking the average of the surface area and mass. Using Equation 5-3, the effective irradiance equivalent to 60 kGy, the highest EB dose, was calculated for various exposure times. Based on the limiting lamp output with the collimating lens attachment, the exposure times for the first photopolymerized sample set (Set 1) were established as 10, 20, and 100 seconds. These times correspond to the 10-fold increase in magnitude seen in the EB line speeds chosen (20, 100, and 200 ft/min), but do not match the exposure time of each line speed (2, 0.4, and 0.2 seconds, respectively). The effective irradiance needed at the film for each equivalent dose and exposure time was calculated, and then the Kenning, *et al.* model was used to determine the effective irradiance setting of the lamp (Table 5-1, see Appendix A for set of values).

Table 5-1. Effective irradiances needed, at three exposure times, to equal the initiation energies of 15, 30, and 60 kGy for the PA formulation. The irradiances were estimated using Equation 5-3 and the Kenning, *et al.* model.

Exposure time (s)	Effective Irradiance (mW/cm ²)		
	10	37.8	75.6
20	18.9	37.8	75.6
100	3.8	7.6	15.1



15 kGy
30 kGy
60 kGy

An acknowledged weakness of the first photo-cured sample set (Set 1 – Initial) is the discrepancy between the photopolymerization and EB polymerization exposure times. The collimating lens was necessary to achieve a broader spot size to produce films for DMA characterization; however, it greatly reduced the maximum irradiance output of the lamp. Therefore, a second set of photo-cured films (Set 2 – Equivalent) were produced with equivalent initiation energies and exposure times (2, 0.4, and 0.2 seconds) that were only characterized by Raman spectroscopy. Due to the small size and irregular shape of the films, the value of $\left(\frac{cm^2}{g}\right)$ calculated for the first sample set was used.

Conversion studies using Raman Spectroscopy

Raman spectroscopy was used to determine conversion of the polymer films. In order to eliminate error from instrumental variations, a reference peak was used. Previous work has established the reaction peak at 1636 cm⁻¹ (indicative of the –C=C– bond in the acrylate moiety) and the reference peak at 1613 cm⁻¹ (indicative of the –C=C– bonds in the phenyl ring) for both photo- and EB polymerization.²⁰ Conversion, α , was calculated using the following equation:

$$\alpha = \left(1 - \frac{I_{rxn}(P)/I_{ref}(P)}{I_{rxn}(M)/I_{ref}(M)} \right) * 100 \quad (5-4)$$

where $I_{rxn}(P)$ and $I_{ref}(P)$ are the peak intensities of the reaction and reference peak of the polymer, respectively; $I_{rxn}(M)$ and $I_{ref}(M)$ are the peak intensities of the reaction and reference peak of the monomer.²¹

Raman spectra of the EB-polymerized films and the first set of photopolymerized films were collected using an optical microscope (DMLP, Leica) connected to a modular research Raman spectrograph (HoloLab 5000R, Kaiser Optical Systems, Inc.) via a 100- μ m collection fiber. A single-mode excitation fiber carried an incident beam of a 785-nm near-infrared laser to the sample through a 10x objective with a numerical aperture of 0.25 and a working distance of 5.8 mm. Laser power at the sample was \sim 10 mW. Spectra were collected with an exposure time of 15 seconds and 3 accumulations. Fifteen monomer spectra were collected and averaged to provide accurate values for $I_{rxn}(M)$ and $I_{ref}(M)$ to use in Equation 5-4. Three spectra were collected from different areas of each polymer film and averaged to report conversion. The photopolymerized films had a standard deviation within \pm 1 percent conversion. The majority of EB-polymerized films had a standard deviation within \pm 5 percent conversion. Exceptions include: BA 15 kGy-200 ft/min (7%), PA 15 kGy-200 ft/min (27%), PA 30 kGy-100 ft/min (11%), PA 30 kGy-200 ft/min (14%), and PA 60 kGy-100 ft/min (7%).

Raman spectra of the second set of photopolymerized films (Set 2 – Equivalent) were collected using a holographic probehead (Mark II, Kaiser Optical Systems, Inc.) with a single-mode excitation fiber and 10x non-contact sampling objective. The incident beam was a 785-nm near-infrared laser with an intensity of \sim 200 mW at the sample. Spectra were collected with an exposure time of 1 second and 3 accumulations. The use of the Raman probehead instead of the microscope for this set of films was the result of the microscope being unavailable during the time period these data were collected; however, the data collected by either attachment are interchangeable. The standard deviation on this second set of photopolymerized films was within \pm 5 percent conversion, with only two exceptions: PA 30 kGy-20 ft/min equivalent (7%) and PEA 30 kGy-200 ft/min equivalent (6%).

Physical Property Studies using Dynamic Mechanical Analysis

A dynamic mechanical analyzer (DMA, Q800 TA Instruments) equipped with a film tension clamp was used to find the glass transition temperature (T_g), the full width at half maximum (FWHM) of the $\tan \delta$ peak, and the maximum height of the $\tan \delta$ peak. DMA characterization was performed on the 60 kGy, 20 ft/min EB-polymerized films and the equivalent energy samples of the first set of photopolymerized films (Set 1 – Initial) after they were subjected to Raman characterization. A mono-frequency strain, temperature ramp sequence was used to collect $\tan \delta$ values as a function of temperature. Temperature was increased at a rate of $3^\circ\text{C}/\text{min}$ from -30°C to 100°C at a constant oscillating frequency of 1 Hz and a sinusoidal strain of 0.05%. The polymer T_g was taken as the maximum of the $\tan \delta$ peak. For each formulation, films were run in triplicate for both initiation mechanisms. All films had a standard deviation equal to or within 3°C for T_g , 1.5°C for FWHM, and 0.3 (dimensionless) for maximum height of the $\tan \delta$ peak.

5.3 Results and Discussion

In this study, the effects of the initiation mechanism, energy rate, and monomer chemistry of acrylate formulations on kinetic and physical properties were investigated. Both EB and photopolymerization reactions were studied by Raman spectroscopy to determine the acrylate conversion, and the physical properties of the films were investigated by dynamic mechanical analysis.

5.3.1 Conversion Studies and Energy Rate Effects

EB-initiated

The acrylate conversion of the EB-initiated polymer films was measured for 5 monomer/oligomer formulations at 3 different doses and 3 increasing line speeds. Systematic variation of both dose and line speed was used to determine the effect of dose on dose rate effects. Increasing the EB dose causes an increase in conversion for all 5 monomer/oligomer formulations due to the increase in initiation energy (Table 5-2). In addition, increasing the line speed at a given dose causes decreases in conversion. BA polymerized at 60 kGy, for example, achieved 97% conversion at 20 ft/min but only

reached 74% conversion at 200 ft/min. These data have been previously presented in Chapter 4 and are repeated here for comparison to the equivalent photo-initiated data.

Table 5-2. Average values of EB-initiated acrylate conversion (%) for five monomer/oligomer formulations at three different doses and line speeds. Conversion increases with increasing dose (at a constant line speed), but decreases at increasing line speed (at a constant dose).

	EB-Cured								
	20 ft/min (2 s)			100 ft/min (0.4 s)			200 ft/min (0.2 s)		
	15 kGy	30 kGy	60 kGy	15 kGy	30 kGy	60 kGy	15 kGy	30 kGy	60 kGy
PA	74	94	98	45	78	90	41	52	76
BA	86	95	97	53	76	86	36	57	74
PEA	96	98	99	62	87	97	55	87	89
POEA	100	96	98	74	95	97	68	92	97
HPOPA	96	98	99	96	97	98	93	96	97

Photo-initiated, Set 1 - Initial

Similar trends in conversion were seen in the first set of photo-initiated films (Set 1- Initial). Although most monomer/oligomer formulations achieved high conversion (> 95%) at the 15 kGy initiation energy equivalent, increases in conversion were still observed as the initiation energy was increased (Table 5-3). Furthermore, decreasing the exposure time caused small (3%) changes in conversion; this trend is also consistent with that seen in the EB-initiated films (Table 5-2), albeit on a smaller scale.

Table 5-3. Average values of photo-initiated acrylate conversion (%) for five monomer/oligomer formulations at three equivalent doses and three different exposure times. Conversion increases with increasing energy (at a constant exposure time), but decreases with decreasing exposure time (at a constant dose).

Photo-Cured : Set 1 - Initial											
	100 s				20 s				10 s		
	15 kGy	30 kGy	60 kGy		15 kGy	30 kGy	60 kGy		15 kGy	30 kGy	60 kGy
PA	98	98	99		96	98	98		95	97	98
BA	98	99	99		96	98	98		95	97	98
PEA	98	99	99		97	98	99		97	99	99
POEA	96	96	97		96	96	97		96	97	97
HPOPA	89	92	94		89	92	94		90	92	94

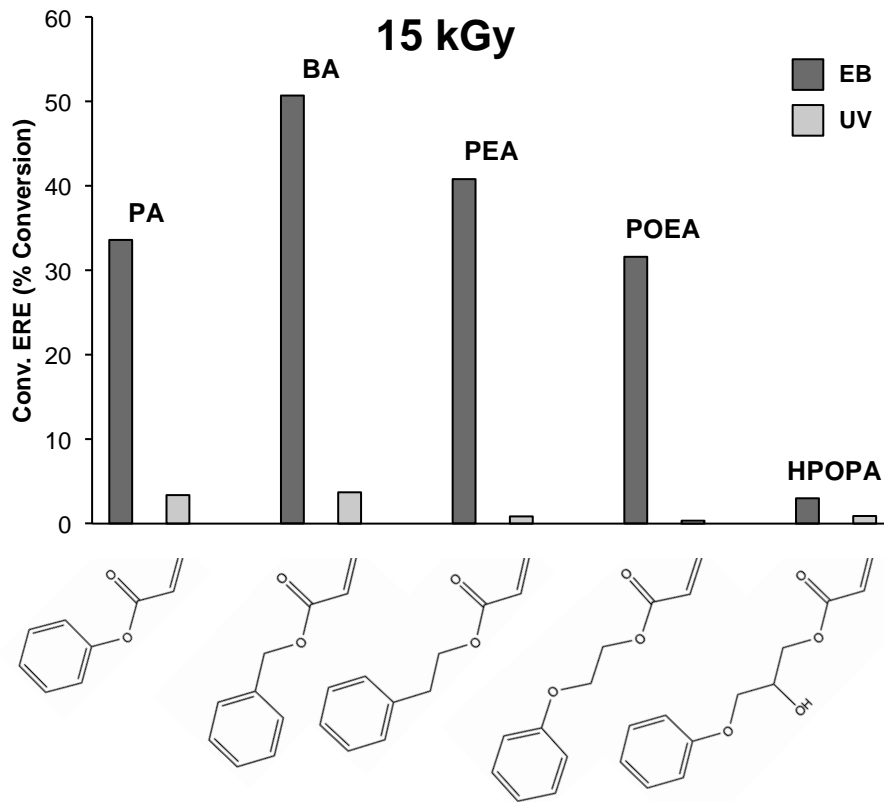
Comparing the magnitude of conversion between EB-initiated and photo-initiated films, some monomer chemistries appear to favor one type of initiating radiation. For example, both PA and BA achieve mediocre conversion (74 and 86%, respectively) at 15 kGy and 20 ft/min when exposed to EB radiation; yet, both reach 98% conversion when initiated by light of an equivalent energy. HPOPA, in contrast, fares better when polymerized via EB across all studied energies.

To better visualize the affect of the energy rate and its trends, a variable, ERE, was created. The ERE, or energy rate effect, is equivalent to the dose rate effect (DRE) discussed in Chapter 4 with a change in nomenclature to reflect its application to both EB and photopolymerization. The ERE is defined as the change in conversion, at a single energy (dose or exposure), as the exposure time is decreased from level *A* to level *B*, or

$$ERE(energy) = |Conversion_A - Conversion_B| \quad (5-5)$$

where level *A* refers to a 20 ft/min (2 s) line speed in EB (100-second exposure time in photopolymerization) and level *B* refers to a 200 ft/min (0.2 s) line speed in EB (10-second exposure time in photopolymerization). The conversion EREs for the 5 formulations, at each of the 3 energies (dose and dose equivalents), are shown in Figure 5-5.

In general, the ERE magnitude decreases with increasing energy and with increasing monomer size for both initiation mechanisms. This trend is more easily observed in the EB-initiated films because the magnitude of the EREs is as much as 45% conversion greater than of that seen in the photo-initiated films. One noticeable exception to this trend is the EB-cured PA at 15 kGy. Although both PA and BA reach similar conversions at 200 ft/min, PA does not cure as well at 20 ft/min; thus, it has a lower ERE despite its smaller size (Table 5-2).



(A)

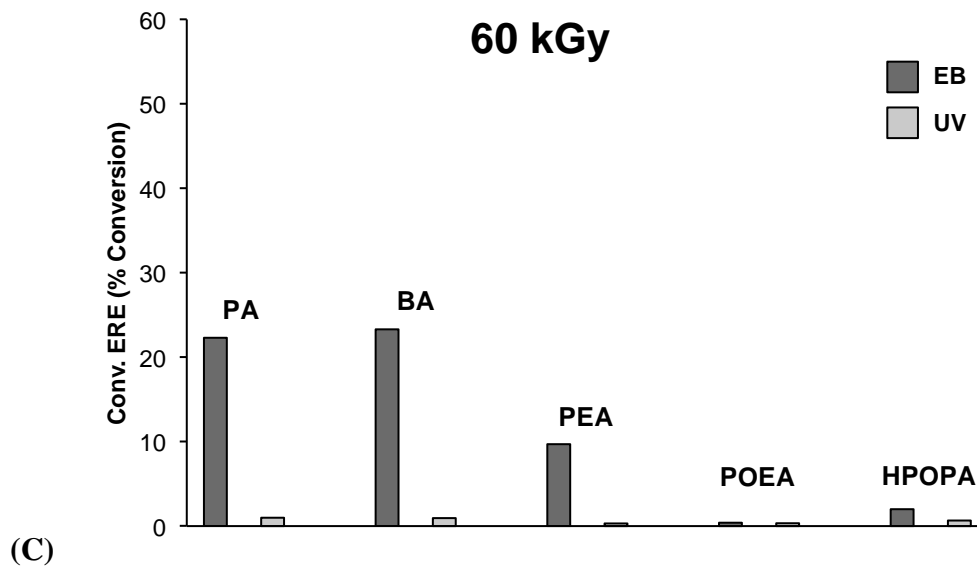
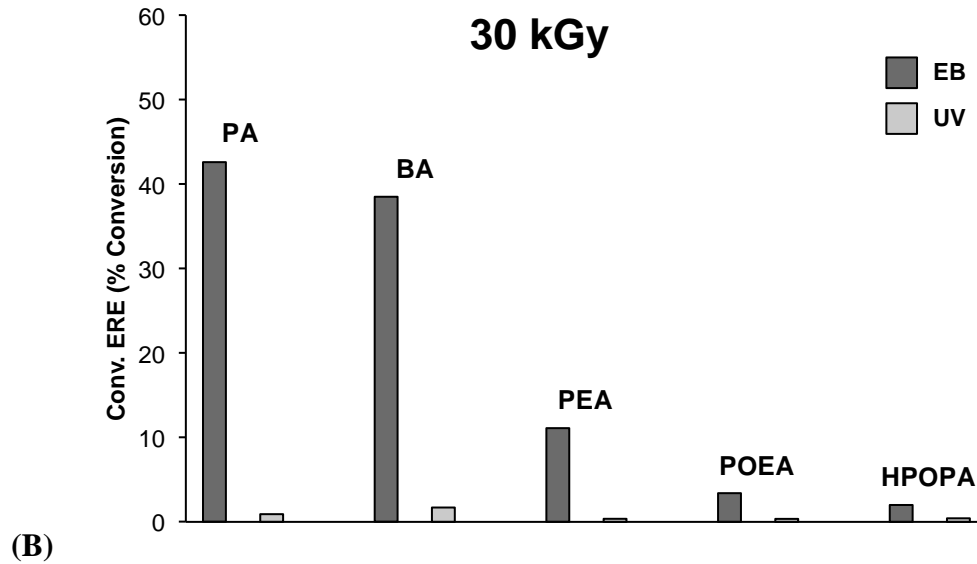


Figure 5-5. A comparison of the conversion EREs for 5 monomer/oligomer formulations initiated by EB and photo-radiation (Set 1) at 3 different doses (dose equivalents): 15 kGy (A), 30 kGy (B), and 60 kGy (C). In general, the ERE magnitude decreases with increasing energy and with increasing monomer size. The ERE magnitude is also larger for EB-cured films than photo-cured films.

However, it is difficult to attribute these differences in response to the change in initiating radiation when the time scale of exposure differs by two orders of magnitude. As discussed at length in Chapter 4, the cause of EREs is hypothesized to be the increased

concentration of free-radicals at earlier moments in the reaction, a result of the same amount of energy delivered over a shorter period. This increase in free-radical concentration, and thus active center concentration ($[M^*]$), increases the rate of termination (R_t) and the rate of propagation (R_p)

$$R_t = k_t[M^*]^2 \quad (5-6)$$

$$R_p = k_p[M][M^*] \quad (5-7)$$

where k_t is the termination rate constant, k_p is the propagation rate constant, and $[M]$ is the concentration of monomer. Yet, the dependence of R_t on $[M^*]$ is to the second order; thus, increasing the energy rate disproportionately increases termination over propagation, causing shorter chain lengths and low conversions. Because exposure time is central to this theory, it is no surprise that the initial photo-cured samples in Set 1 have significantly smaller EREs. Although the change in energy rate was 10-fold for both the EB polymerized (2 s to 0.2 s) and photopolymerized (100 s to 10 s) films, the energy rates of the two radiation methods differed by a factor of 50 (Table 5-4).

Table 5-4. Example energy rates for the EB- and photo-cured (Set 1) exposure times, assuming 10 J of energy delivered.

Exposure Time (s)	Energy Rate (J/s)
0.2	50
2	5
10	1
100	0.1

Photo-initiated, Set 2 - Equivalent

To better compare the EREs of each initiation mechanism, a second set of photo-initiated films was produced with equivalent exposure times to those of the EB-initiated films. Although Set 2 provided a more direct comparison with the EB data, resolution of the irradiance measurement for this second set of films was less than that of the first set. Above 1 W, the radiometer only reports irradiance with 0.1 W resolution, so while the

time scales for EB and photopolymerization are matched in this second set, there is more variation in the initiation energies. Nevertheless, significant trends in the ERE were observed. Reducing the exposure times had a negative impact on the conversion, the magnitude of which was dependent on the monomer chemistry and the dose equivalent (Table 5-5). For example, comparing 30 kGy at 100 s (Set 1) and at 2 s (Set 2), the PA and BA formulations experience a drop in conversion of 24 and 37 %, respectively, but the conversions of PEA, POEA, and HPOPA remain steady ($\leq 3\%$ conversion change, Tables 5-3 and 5-5). At the 60 kGy equivalent for the same exposure times, conversion changes across the 5 monomer series are all $\leq 7\%$.

Table 5-5. Average values of photo-initiated acrylate conversion (%) for five monomer/oligomer formulations at three equivalent doses and three different exposure times. Conversion increases with increasing energy (at a constant exposure time), but decreases with decreasing exposure time (at a constant dose).

Photo-Cured: Set 2 - Equivalent									
	2 s			0.4 s			0.2 s		
	15 kGy	30 kGy	60 kGy	15 kGy	30 kGy	60 kGy	15 kGy	30 kGy	60 kGy
PA	*9	74	93	30	49	66	28	42	52
BA	10	62	93	27	43	54	25	35	44
PEA	41	97	97	33	63	77	36	45	62
POEA	41	96	94	58	91	94	58	84	92
HPOPA	48	89	91	89	92	92	88	92	93

*The conversion of PA at 15 kGy equivalent dose and 2 s exposure is collected from only one sample. The conversion of the other samples was too low to be transferred for characterization.

Comparing EB- and photo-cured films with equivalent exposure times, the EB initiation mechanism produces equal or higher conversions at all studied energy levels (Tables 5-2 and 5-5). The greatest differences between the two mechanisms being PA and BA with a 63 and 76 % conversion increase, respectively (15 kGy, 2 s). These conversion differences between the EB and photopolymerized films may be attributed to differences in the number of propagating radicals, network formation, or both.

Despite having equivalent initiation energies, the EB- and photo-systems do not necessarily have equivalent concentrations of propagating radicals. The Kenning, *et al.* model used to estimate the photo-initiation energy accounts for the quantum yield of the

photoinitiator; however, the quantum yield is defined as the fraction of absorbed photons leading to initiator fragmentation, or primary radicals (R^{\bullet}).¹⁸ While it is generally assumed that primary radicals react with monomer to become propagating radicals (M^{\bullet} , Equation 5-2), at least some primary radicals are quenched by dissolved oxygen, introducing error in the estimation. In EB, not even primary radical concentration is known since the radiation yield G_i , defined as the number of molecules reacted per 100 eV absorbed, is unknown.⁴ Even if G_i was known for each of the monomers, the number of side reactions in EB would increase the error in estimating what fraction of primary radicals become propagating radicals. If the concentration of propagating radicals is not equivalent for each radiation, the rate of propagation and termination will be affected and could cause changes in the conversion (Equations 5-6 and 5-7).

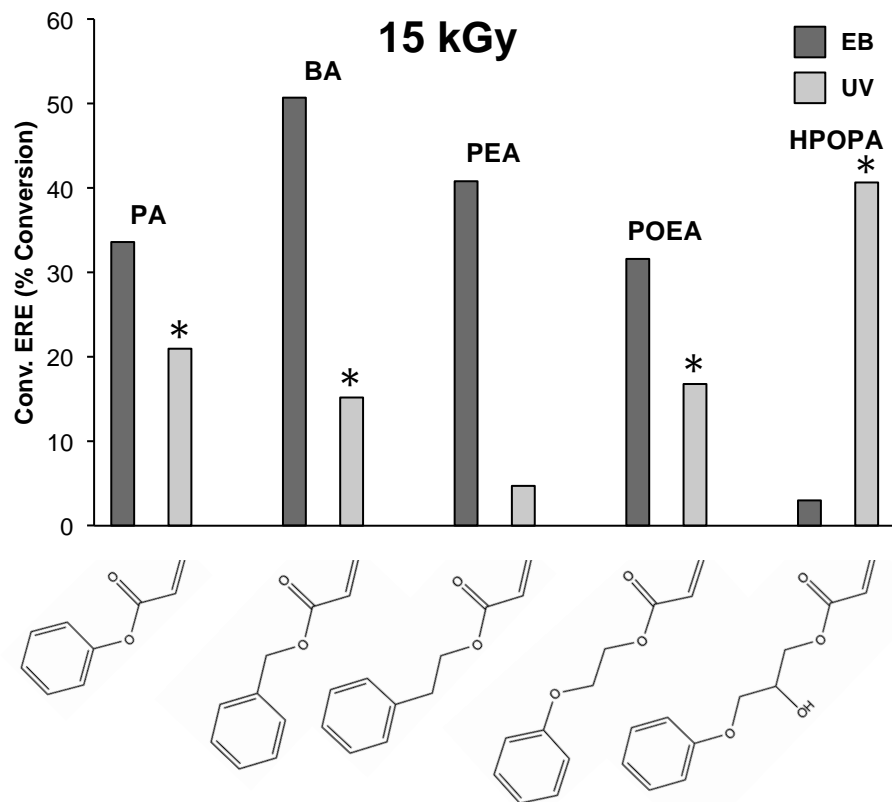
Differences in network formation may also contribute to the discrepancies in conversion for the two initiation mechanisms. In photopolymerization, network formation is relatively controlled. In the absence of chain transfer, monofunctional acrylates form linear polymers and multifunctional acrylates form branched or cross-linked networks. EB polymerization, in contrast, is known for its side reactions, which can produce a cross-linked network even with monofunctional monomers. If the EB-cured films produce a more heavily cross-linked network, especially earlier in the reaction, termination by trapping (monomolecular termination) may become dominant. Monomolecular termination changes the rate of termination's dependence on radical concentration to first order, therefore reducing the rate of termination relative to the rate of propagation and promoting conversion (Equation 6).

Another difference between the photo-initiated films in Set 2 and the EB-initiated films is the ERE trend at 15 kGy. At the 30 and 60 kGy energy equivalents for the second set of photo-initiated films, for the same initiation energy, conversion decreases as the exposure time decreases, as is the trend for the EB-initiated films (Tables 5-5 and 5-2). The one exception to this trend is the HPOPA formulation, which increases in conversion by $\leq 3\%$, but this change is within the standard deviation. At the 15 kGy equivalent, however, the direct opposite trend occurs: conversion increases as the exposure time decreases from 2 s to 0.4 s for the photo-cured films, with the exception of PEA (Table 5-5). Conversion at the 15 kGy equivalent from 0.4 s to 0.2 s remains stable

($\pm 2\%$ conversion). These increases in conversion are greater than the standard deviation ($\pm 5\%$ conversion) and range from 17 (BA) to 41% conversion (HPOPA). Explanation for this discrepancy in the ERE trend is difficult. Because this discrepancy did not occur in Set 1 of the photo-initiated samples, it must be dependent on both the magnitude of the initiation energy and the exposure time. One theory is that this discrepancy is caused by oxygen inhibition from dissolved oxygen. At the 15 kGy energy equivalent, it is estimated that the primary radical concentration is similar to the dissolved oxygen concentration. Using the Kenning, *et al.* model, the concentration of primary radicals in the photo-initiated, 15 kGy, 0.2 s films was found to be $\sim 1.79 \times 10^{-3}$ mol/L. Gou, *et al.* has estimated the dissolved oxygen concentration for seven different (meth)acrylates ranging from ~ 0.80 to 2.07×10^{-3} mol/L.²² In addition to simply being at a lower initiation energy level, this overlap in concentrations may explain the low conversions observed at 15 kGy, regardless of exposure time (Table 5-5). Moreover, the concentration of primary radicals in the 15 kGy, 2 s films at the same time point (0.2 s) is only 0.16×10^{-3} mol/L. Although over full course of the reaction (2 s) the primary radical concentration should be equal to that of the 15 kGy, 0.2s films, the lower concentration of free radicals at any given moment in the reaction may make them more susceptible to reaction with the dissolved oxygen, consequently lowering the conversion. Conversion for the 30 kGy energy equivalent films fares better because the radical concentration is doubled and firmly outside the range presented by Gou, *et al.* Further supporting this theory, film conversion at the 15 kGy equivalent increases with increasing monomer size (Table 5-5). The size of the monomer molecule should limit oxygen solubility, and the increased viscosity, which also generally increases across the monomer series (Chapter 4, Table 4-3), will limit diffusion of the oxygen during the reaction according to the Stokes-Einstein equation.²³ Also, EB-initiated films would not be expected to be as affected by dissolved oxygen as photo-initiated films because the radical concentration is expected to be greater at equivalent absorbed energies.

Comparing the magnitude of the conversion EREs of the EB- and photopolymerized films (Set 2 – Equivalent), it is apparent that the response to the energy rate is affected by the initiation mechanism (Figure 5-6). Excluding the 15 kGy data, the photopolymer EREs are greater than those observed in the EB films for all monomers

except PA and BA at 30 kGy. These two exceptions may be a remnant of the oxygen inhibition hypothesized to occur at 15 kGy. As the two smallest molecules, PA and BA would be most likely to experience a continued inhibition even at the higher energy level. The PA and BA conversions at 30 kGy, 2 s (74 and 62 %, respectively) are ~ 25% lower than the equivalent EB films (Tables 5-2 and 5-5); yet, the other three formulations have similar EB- and photo-initiated conversion values, possibly suggesting a discrepancy that could be attributed to the dissolved oxygen.



(A)

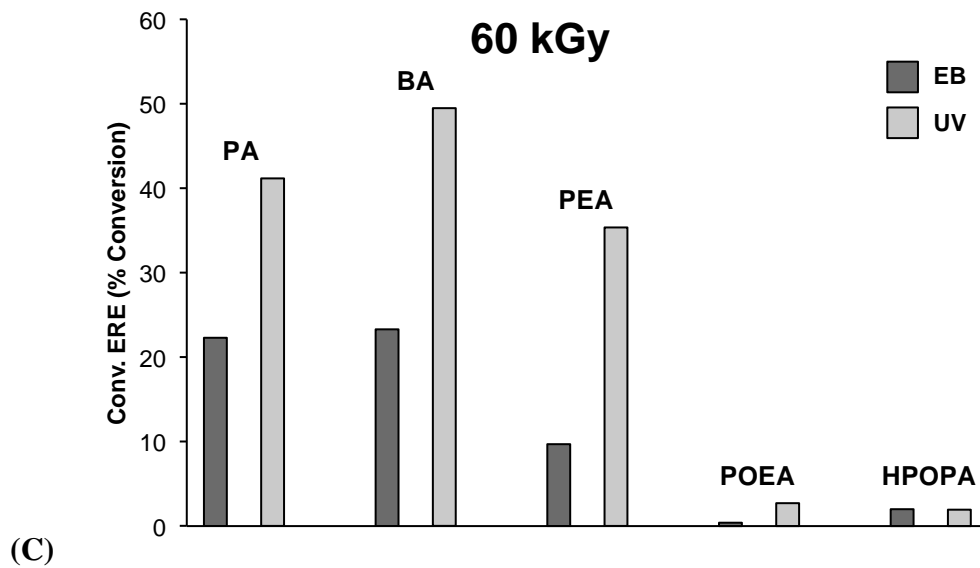
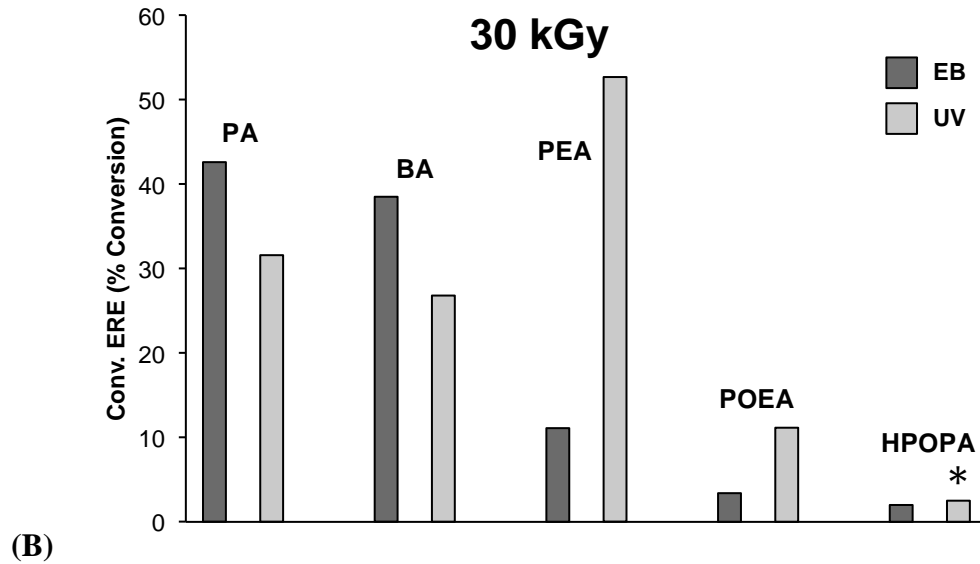


Figure 5-6. A comparison of the conversion EREs for five monomer/oligomer formulations initiated by EB and photo-radiation (Set 2) at three different doses (dose equivalents): 15 kGy (A), 30 kGy (B), and 60 kGy (C). In contrast to the EB EREs, there does not appear to be a trend in the photo ERE magnitude. Data columns marked with an asterisk have a lower conversion with 2 s exposure than a 0.2 s exposure.

As EREs are simply a mathematical manipulation of the conversion values, the arguments of differing propagating radical concentration and network formation between the two initiation energies can also be applied as explanation of the difference in ERE

magnitude. In Chapter 4, it is argued that the presence of chain transfer restores the balance between the rate of propagation and termination as the radical concentration is increased, minimizing the EB ERE for those monomer formulations that can readily participate in chain transfer – those with abstractable hydrogens. In EB polymerization, this process is likely exaggerated because the primary radicals are formed on the monomer molecules. In photopolymerization, chain transfer is expected to be more controlled and thus possibly less effective at lower energies (15 kGy equivalent). It is also argued in Chapter 4 that EREs should be limited at high EB doses (60 kGy) because higher conversions are expected at earlier reaction times than for lower doses due to the increase in the rate of propagation, and therefore, by increasing the dose, monomolecular termination should become dominant at increasingly shorter reaction times. The photopolymerized PA and BA formulations violate this logic. The magnitude of their ERE increases from the 30 to 60 kGy energy equivalent (the reverse ERE trends of 15 kGy [marked with an asterisk] make it difficult to compare). However, this violation may, too, be justified by oxygen inhibition. If oxygen inhibition is the cause of the reduced conversion seen at 30 kGy, consider the ERE magnitude at full conversion (that is, 100% conversion): PA would have an ERE of 58 at 30 kGy and BA would have a ERE of 65. These ERE magnitudes are higher than those of PA and BA at 60 kGy, restoring the trend of decreasing EREs with increasing initiation energy.

If the oxygen inhibition theory is again relied upon, the monomer chemistry/ERE trend of the photopolymer films is also consistent with that of the EB polymer trend: increasing monomer size decreases EREs. This consistency supports the theory presented in Chapter 4, since the probability of a monomer participating in chain transfer should increase with the concentration of abstractable hydrogens in both EB- and photopolymerization.

5.3.2 Physical Property Studies

As some differences in conversion between initiation mechanisms were attributed to changes in the network formation, the physical properties of select films were tested to determine if those network differences could be detected. DMA was used to collect the glass transition temperature (T_g), full width at half maximum (FWHM) of the $\tan \delta$ peak,

and the maximum height of the $\tan \delta$ peak for the 60 kGy, 20 ft/min EB-polymerized films and the 60 kGy equivalent, 100 s exposure photopolymerized films (Set 1). These films were chosen for comparison because of the similarity in their conversions (Tables 5-2 and 5-3). All films were $\leq 2\%$ conversion from their counterpart, with the exception of the HPOPA formulation (5% conversion).

The average T_g of each of the five monomer/oligomer formulations was higher when initiated by EB radiation (Figure 5-7); however, only the PA and HPOPA formulations demonstrated an increase outside the standard deviation of the instrument. Because of the slightly lower conversion (94 vs. 99% conversion) of the photo-cured HPOPA films, the 7°C decrease in T_g between the two initiation mechanisms could be the result of plasticization by monomer in the photo-cured films. Yet, the 16°C T_g difference observed in the EB and photopolymerized PA films cannot be attributed to a difference in conversion. This increase in the PA formulation T_g is ascribed to an increased cross-link density, which increases the rigidity of the polymer. Larger differences in T_g might be expected when comparing initiation mechanisms if the exposure times were equivalent, based on the differences seen in conversion between Sets 1 and 2 of the photopolymerized samples. However, photopolymerized films with equivalent initiation energies and exposure times that were large enough for DMA characterization could not be produced.

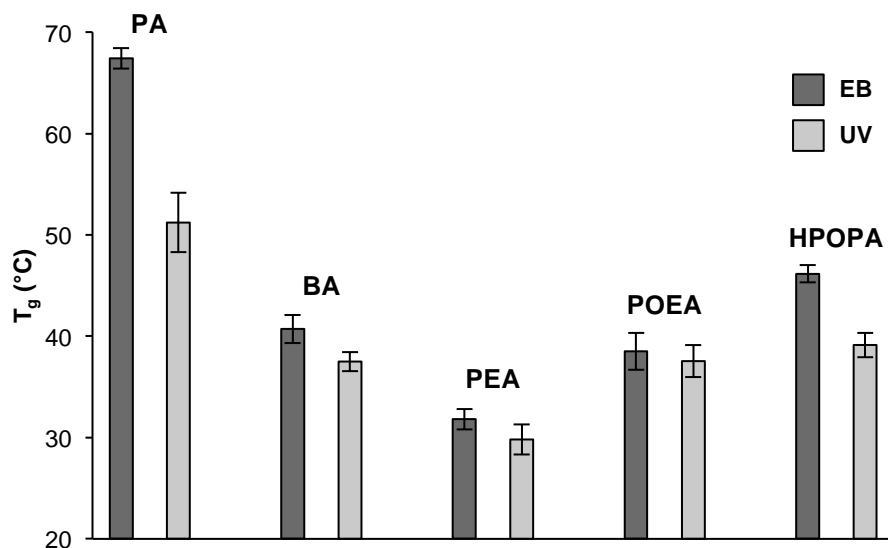


Figure 5-7. A comparison of the T_g values for 5 monomer/oligomer formulations initiated by EB and photo-radiation (Set 1) at 60 kGy, 20 ft/min and 60 kGy equivalent, 100 s exposure, respectively. Polymerizing with EB radiation increases the T_g of a formulation, although only the EB-cured PA and HPOPA films are significantly different from the photo-cured films.

Where polymerizing with EB radiation increases the T_g of the formulation, it decreases the FWHM of the $\tan \delta$ peak, albeit slightly (Figure 5-8). This decrease is also consistent with EB forming a more cross-linked network, or, at least, a more homogenous network. A broad $\tan \delta$ peak is indicative of a more diverse network. The magnitude of the changes in FWHM caused by initiation energy mirror those observed in the T_g values (Figure 5-7). The PA formulation has the largest difference (4°C), followed by HPOPA (1.3°C) and the rest of the formulations. Again, magnification of the trend would be expected if both initiation mechanisms had identical exposure times.

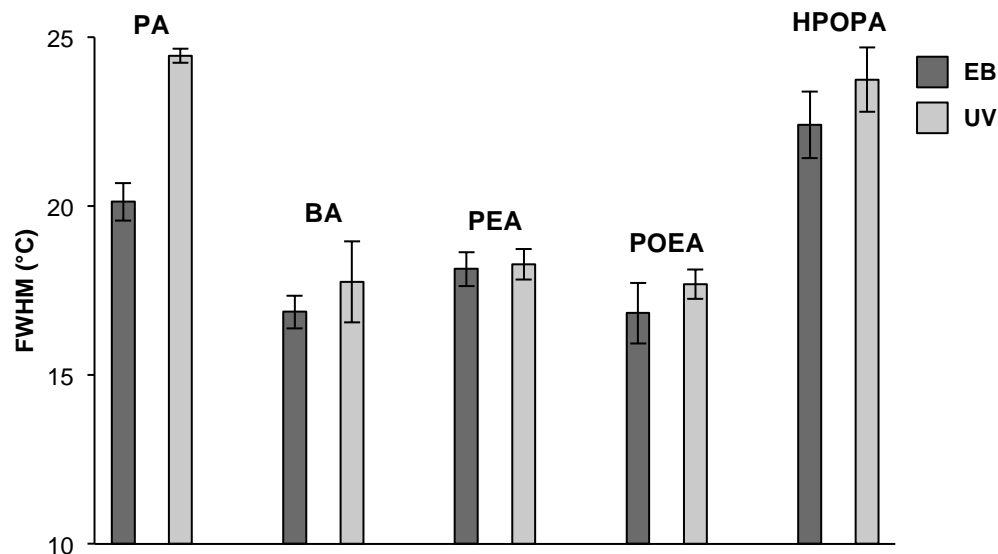


Figure 5-8. A comparison of the FWHM values of the $\tan \delta$ peak for five monomer/oligomer formulations initiated by EB and photo-radiation (Set 1) at 60 kGy, 20 ft/min and 60 kGy equivalent, 100 s exposure, respectively. Polymerizing with EB radiation decreases the FWHM of a formulation, although only the EB-cured PA films is significantly different from the photo-cured films.

The maximum height of the $\tan \delta$ peak, indicative of the dampening properties of the films, shows no consistent trend between the EB- and photo-cured samples (Figure 5-9). The PA formulation, for example, has a lower peak height when photo-initiated, but the peak height of the HPOPA formulation is greater when the film is photo-initiated. It is difficult to draw conclusions from this data because of these opposing trends; however, it is clear that the initiation mechanism can alter the dampening properties of a material. Furthermore, the magnitude of the difference between initiation mechanisms is consistent with that of the T_g and FWHM values; the PA formulation has the largest difference (0.16), followed by the HPOPA formulation (0.12).

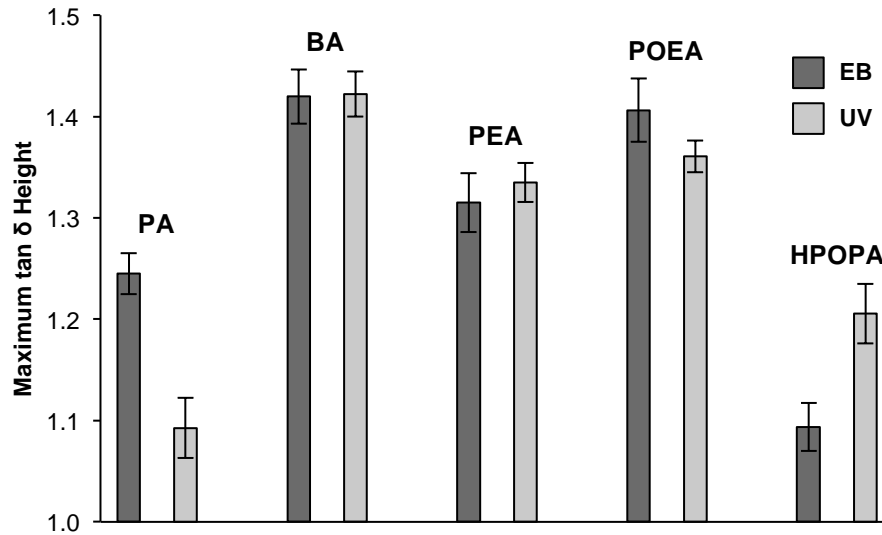


Figure 5-9. A comparison of the maximum tan δ peak height values for five monomer/oligomer formulations initiated by EB and photo-radiation (Set 1) at 60 kGy, 20 ft/min and 60 kGy equivalent, 100 s exposure, respectively. No consistent trend is observed across the formulations, and only PA and HPOPA have a significant difference.

5.4 Conclusions

A protocol was developed to estimate equivalent initiation energies between EB and photopolymerization. This protocol was then used to compare EB-initiated films to two sets of photo-initiated films of the same initiation energy. The first set had a longer exposure time, and the second set had an equivalent exposure time. In addition, compared against the EB polymerized films, the photopolymerized films with equivalent exposure times had equal or lower conversions and did not follow the ERE or monomer chemistry trends established in the EB films. However, monomer chemistry is a key variable in photopolymerization EREs, as changes in ERE magnitude were demonstrated across the five monomer series.

Furthermore, the importance of formulation chemistry is also visible in the comparison of the physical properties produced by the two initiation mechanisms. The largest differences in T_g FWHM of the tan δ peak, and the maximum height of the tan δ peak, were all observed in the PA formulation. The HPOPA formulation experienced the second largest differences across all three physical property measures. In contrast, the physical properties differences produced by the two initiation mechanisms for the BA,

PEA, and POEA formulations were all within the standard deviation. It is expected, however, that these differences would be magnified if the photo-cured films used for comparison had an equivalent exposure time to the EB-cured films.

5.5 References

- (1) Drobny, J. G. *Radiation Technology for Polymers, Second Edition*, 2nd ed.; CRC Press, **2010**.
- (2) Fouassier, J.-P. *Photoinitiation, Photopolymerization, and Photocuring: Fundamentals and Applications*; Hanser/Gardner Publication Inc.: Cincinnati, **1995**.
- (3) Cohen, G. UV-EB Market Trends. *RadTech Report* **2012**, No. 2, 44–48.
- (4) *Radiation Curing: Science and Technology*, 1st ed.; Pappas, S. P., Ed.; Springer Science & Business Media: New York, **1992**.
- (5) Golden, R. What's the Score? a Method for Quantitative Estimation of Energy Use and Emission Reductions for UV/EB Curing. *RadTech Report* **2012**, 1–5.
- (6) Patacz, C.; Coqueret, X.; Decker, C. Electron-Beam Initiated Polymerization of Acrylate Compositions 3: Compared Reactivity of Hexanediol and Tripropyleneglycol Diarylates Under UV or EB Initiation. *Radiation Physics and Chemistry* **2001**, 62, 403–410.
- (7) Glauser, T.; Johansson, M.; Hult, A. A Comparison of Radiation and Thermal Curing of Thick Composites. *Macromolecular Materials and Engineering* **2000**, 274, 25–30.
- (8) Batten, R. J.; Davidson, R. S.; Wilkinson, S. A. Radiation Curing of an Epoxy-Acrylate-6,7-Epoxy-3,7-Dimethyloctyl Acrylate. *Journal of Photochemistry and Photobiology A: Chemistry* **1991**, 58 (1), 115–122.
- (9) Odian, G. *Principles of Polymerization*, 4 ed.; John Wiley and Sons, Inc., **2004**.
- (10) Richter, K. B. Pulsed Electron Beam Curing of Polymer Coatings. **2007**, 1–246.
- (11) Martin, J. W.; Chin, J. W.; Nguyen, T. Reciprocity Law Experiments in Polymeric Photodegradation: a Critical Review. *Progress in Organic Coatings* **2003**, 47 (3-4), 292–311.
- (12) Feng, L.; Suh, B. I. Exposure Reciprocity Law in Photopolymerization of Multi-Functional Acrylates and Methacrylates. *Macromol. Chem. Phys.* **2007**, 208 (3), 295–306.
- (13) Wydra, J. W.; Cramer, N. B.; Stansbury, J. W.; Bowman, C. N. The Reciprocity Law Concerning Light Dose Relationships Applied to BisGMA/TEGDMA Photopolymers: Theoretical Analysis and Experimental Characterization. *Dental Materials* **2014**, 30 (6), 605–612.

- (14) Leprince, J. G.; Hadis, M.; Shortall, A. C.; Ferracane, J. L.; Devaux, J.; Leloup, G.; Palin, W. M. Photoinitiator Type and Applicability of Exposure Reciprocity Law in Filled and Unfilled Photoactive Resins. *Dental Materials* **2011**, *27* (2), 157–164.
- (15) Hadis, M.; Leprince, J. G.; Shortall, A. C.; Devaux, J.; Leloup, G.; Palin, W. M. High Irradiance Curing and Anomalies of Exposure Reciprocity Law in Resin-Based Materials. *Journal of Dentistry* **2011**, *39* (8), 549–557.
- (16) Emami, N.; Söderholm, K. J. M. How Light Irradiance and Curing Time Affect Monomer Conversion in Light-Cured Resin Composites. *European Journal of Oral Sciences* **2003**, *111* (6), 536–542.
- (17) Halvorson, R. H.; Erickson, R. L.; Davidson, C. L. Energy Dependent Polymerization of Resin-Based Composite. *Dental Materials* **2002**, *18* (6), 463–469.
- (18) Kenning, N. S.; Kriks, D.; El-Maazawi, M.; Scranton, A. Spatial and Temporal Evolution of the Photoinitiation Rate for Thick Polymer Systems Illuminated with Polychromatic Light. *Polym. Int.* **2006**, *55* (9), 994–1006.
- (19) Kenning, N. L. Spatial and Temporal Evolution of the Photoinitiation Rate in Thick Polymer Systems, **2006**, pp 1–163.
- (20) Schissel, S. M.; Lapin, S. C.; Jessop, J. L. P. Internal Reference Validation for EB-Cured Polymer Conversions Measured via Raman Spectroscopy. *RadTech Report* **2014**, No. 4, 46–50.
- (21) Cai, Y.; Jessop, J. L. P. Decreased Oxygen Inhibition in Photopolymerized Acrylate/Epoxy Hybrid Polymer Coatings as Demonstrated by Raman Spectroscopy. *Polymer* **2006**, *47* (19), 6560–6566.
- (22) Gou, L.; Scranton, A. B.; Coretsopoulos, C. N. Measurement of the Dissolved Oxygen Concentration in Acrylate Monomers with a Novel Photochemical Method. *Journal of Polymer Science Part A* **2004**, *42* (5), 1285–1292.
- (23) Sharma, K. R. *Polymer Thermodynamics*; CRC Press, **2011**.

CHAPTER 6

EPOXIDE-(METH)ACRYLATE HYBRID PHOTOPOLYMERIZATIONS WITH HYDROXYL-CONTAINING (METH)ACRYLATES: ENHANCED KINETICS AND PHYSICAL PROPERTY TUNING

6.1 Introduction

Previous research of hybrid photopolymers, which use two (or more) independent mechanisms of polymerization in a single reaction system, has demonstrated their ability to reduce the limitations of traditional polymer systems. Combining the free-radical and cationic mechanisms in an (meth)acrylate/epoxide hybrid system, for example, decreases sensitivity to ambient moisture and oxygen.^{1,2} The ring-opening reaction of the epoxide reduces the shrinkage and shrinkage stress inherent in the (meth)acrylate network.³⁻⁵ Furthermore, sequential cure of the two networks can be accomplished by choice of photoinitiators and their regions of absorption.⁶ Reported examples of free-radical/cationic hybrid systems include (meth)acrylate/vinyl ether⁷⁻⁹, thiol-ene/vinyl ether¹⁰, and (meth)acrylate/cyclic ether.^{6,11,12}

Yet, as certain limitations are overcome through the use of hybrid photopolymers, others are introduced. Hybrid reaction systems that consist of a single hybrid monomer, which contains both functional groups, are highly cross-linked, as is typical with any multifunctional monomer, and often produce rigid, brittle polymers. Hybrid monomers also have limited commercial availability. Alternatively, a hybrid mixture of two monomers can be used, each with a different functional group. Using a hybrid mixture significantly increases monomer options; however, these mixtures are prone to phase separation, since mechanical entanglement is the only force joining the two networks.¹³⁻¹⁵ Phase separation in (meth)acrylate/epoxide systems is exacerbated by the slow network formation and low conversion of the epoxide.¹¹

One avenue for increasing epoxide conversion and propagation rate is by promotion of the activated monomer (AM) mechanism. Previous research has explored promoting the AM mechanism and its effects in both UV- and visible-light initiated systems.¹⁶⁻¹⁸ Propagation of cationically polymerizable epoxides typically proceeds through the active chain end (ACE) mechanism,¹⁹ shown in Figure 6-2, A. However, a

second mechanism, the AM mechanism, occurs in the presence of a hydroxyl group, such as a water molecule or an alcohol moiety, on a comonomer (Figure 6-2, B).

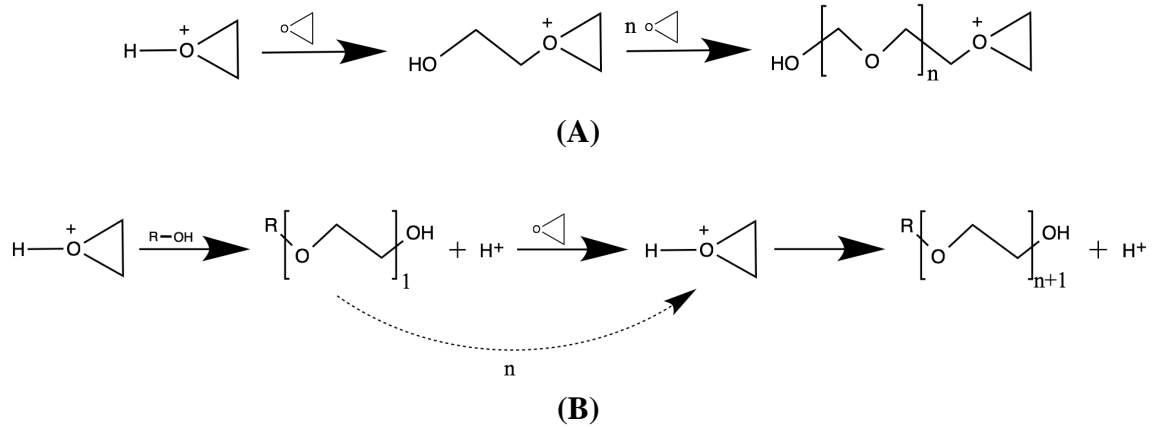


Figure 6-1. Cationic ring-opening polymerizations include the active chain end (ACE) mechanism (A, propagation) and activated monomer (AM) mechanism (B, chain transfer). Figure adapted from Reference 19.

In this chain transfer reaction, a hydroxyl group attacks a protonated monomer molecule at the carbon alpha to the oxygen, causing the epoxide ring to open and the release of a proton. This proton can then activate another epoxide monomer, which can proceed by the ACE mechanism to start a new polymer chain or by the AM mechanism to grow an existing polymer chain, depending on whether it is attacked by an epoxide monomer or hydroxyl group, respectively.²⁰ The ACE mechanism is known to result in slow propagation, which is evident by the low light-cured conversion of neat epoxides; however, the propagation rate constant for the AM mechanism can be approximately five times higher than that of the ACE mechanism for a cyclic ether.²¹ Furthermore, promoting the AM mechanism with a hydroxyl group located on the acrylate monomer, in a hybrid system, will covalently bond the epoxide network to the acrylate chain through the hydroxide and produce a semi-grafted polymer network, reducing phase separation (Figure 6-3).²²



Figure 6-2. Semi-grafted network. Polymer A (dashed line) is grafted onto the cross-linked network of Polymer B (solid line). Adapted from Reference 22.

In this study, the AM mechanism is promoted through incorporation of hydroxyl-containing (meth)acrylates in epoxy-acrylate hybrid formulations. Facilitation of the AM mechanism will increase epoxide polymerization rate and conversion, reduce phase separation, and modulate the glass transition temperature (T_g) of the resulting hybrid films. By varying acrylate content in the hybrid formulations, the extent and impact of these effects on the kinetics and polymer properties are characterized for improved control.

6.2 Experimental

6.2.1 Materials

Epoxide-acrylate hybrid formulations were made by varying the content of (meth)acrylate in increments of 10 wt% in 3,4-epoxycyclohexane carboxylate (EEC, Sigma Aldrich). The AM mechanism was promoted through 2-hydroxyethyl acrylate (HEA, Sigma Aldrich), while the non-hydroxyl-containing ethylene glycol methyl ether acrylate (EGMEA, Sigma Aldrich) served as a control. A similar set of epoxide-methacrylate formulations was made using hydroxyethyl methacrylate (HEMA, Sigma Aldrich) and the control ethylene glycol methyl ether methacrylate (EGMEMA, Sigma Aldrich) to compare the effects of the methacrylate moiety to that of the acrylate. Formulations contained 0.5 wt% of the photoacid generator 4-(2-hydroxyl-1-

tetradecyloxy)- phenyl] phenyliodonium hexafluoroantimonate (DAI, Polysciences) and 0.2 wt% of the α -cleavable free-radical photoinitiator 2,2-dimethoxy-2-phenylacetophenone (DMPA, Sigma Aldrich). All materials were used as received (Figure 6-3).

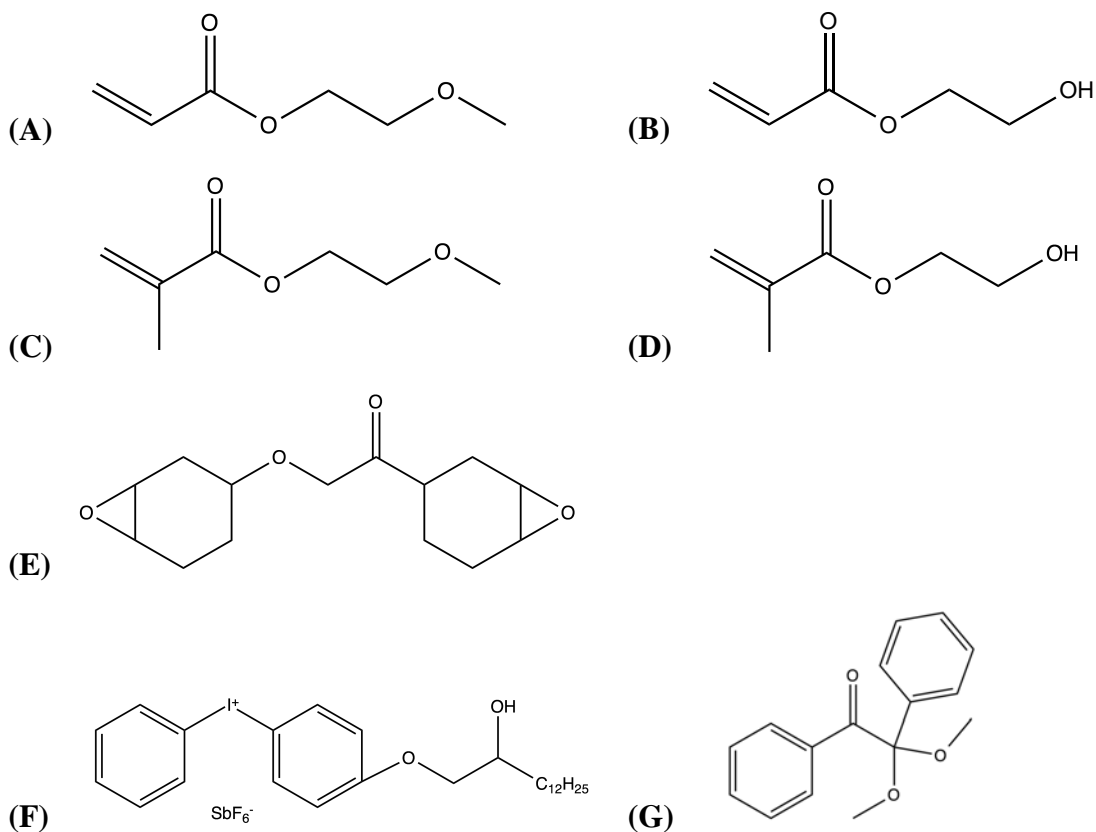


Figure 6-3. Monomers and photoinitiators used in this study: (A) EGMEA, (B) HEA, (C) EGMEMA, (D) HEMA, (E) EEC, (F) DAI, and (G) DMPA.

6.2.2 Methods

Kinetic studies using Raman spectroscopy

Real-time Raman spectroscopy was used to measure conversion of epoxide and acrylate moieties during photopolymerization. Epoxide-acrylate hybrid formulations were cured at ambient temperature in 1-mm ID quartz capillary tubes using an Acticure® Ultraviolet/Visible Spot Cure System (EFOS, 250-450 nm band pass filter) with an effective irradiance of 140 mW/cm^2 as measured by a radiometer (OmniCure, Model No. R2000). Raman spectra were gathered before and during the photopolymerization using

a holographic probehead (Mark II, Kaiser Optical Systems, Inc.) with a single-mode excitation fiber delivering ~220 mW of 785-nm near-infrared laser intensity to the sample through a 10x non-contact sampling objective. The probehead was connected to a modular research Raman spectrograph (HoloLab 5000R, Kaiser Optical Systems, Inc.). Spectra were collected continuously for 5 minutes with an exposure time of 250 ms. The conversion (α) of each reactive moiety was calculated separately using the collected Raman spectra using Equation 6-1:

$$\alpha = 1 - \frac{I_{rxn}(t)}{I_{rxn}(0)} \quad (6-1)$$

where $I_{rxn}(t)$ is the peak intensity of the reactive band at a given time, t , in the reaction and $I_{rxn}(0)$ is the peak intensity of the reactive band before the reaction at time zero. The reactive bands representing the acrylate C=C double bond and epoxide ring are located at 1640 and 790 cm^{-1} , respectively.² Since the spectral baselines were constant throughout the experiments containing HEA and EGMEA, a reference band was not needed. However, baseline fluctuations in the methacrylate experiments (HEMA and EGMEMA) required the use of a reference peak. The nonreactive, stable peak at 1445 cm^{-1} , representative of the $-\text{CH}_2-$ vibration, was used as a reference for these experiments and Equation 6-1 was adapted as follows

$$\alpha = 1 - \frac{I_{rxn}(t)/I_{ref}(t)}{I_{rxn}(0)/I_{ref}(0)} \quad (6-2)$$

where $I_{ref}(t)$ is the peak intensity of the reference band at a given time, t , in the reaction and $I_{ref}(0)$ is the peak intensity of the reference band before the reaction at time zero.²³ Because the lower concentrations have small peak intensities, which introduce noise in the conversion data, the data presented have been smoothed using a 5-point moving average in Microsoft Excel.

Physical property studies using dynamic mechanical analysis

Polymer films were tested using dynamic mechanical analysis (DMA) to obtain the glass transition temperature (T_g) and full width at half maximum (FWHM) of the $\tan \delta$. Molds consisting of two silanized (Rain-X treated) glass slides sandwiched with 300 μm glass cover slip spacers were used to prepare the epoxide-acrylate hybrid films. Formulations in the glass molds were irradiated using an Omnicure® S1000 Ultraviolet/Visible Spot Cure System (Excelitas, 250-450 nm band pass filter) with an adjustable collimating lens attachment (Lumen Dynamics, Model No. 810-00041) and an effective irradiance of 140 mW/cm^2 as measured by a radiometer (Versaprobe Pro, Control Cure). Samples were irradiated immediately before testing to minimize dark cure (continued polymerization after the initiating light source is removed) of the epoxide, with the exception of neat EEC. Neat EEC only formed a usable film approximately 5 hours post illumination. After removal from the molds, samples were cut to approximately $6.25 \text{ mm} \times 25 \text{ mm}$ and tested in a dynamic mechanical analyzer (Q800, TA Instruments) equipped with a film tension clamp. A mono-frequency strain, temperature ramp sequence was used to collect storage modulus and T_g values as a function of temperature. Temperature was increased at a rate of 3°C/min over a broad temperature range at a constant oscillating frequency of 1 Hz and a sinusoidal strain of 0.05%. The temperature ramp was repeated twice for each sample since annealing occurs at elevated temperatures in the first sequence. All DMA data were reported from the second temperature ramp.

6.3 Results and Discussion

In this study, the effect of promoting the AM mechanism in epoxide-(meth)acrylate hybrid formulations on reaction kinetics and physical properties was examined by comparing a hydroxyl-containing acrylate and methacrylate to non-hydroxyl-containing controls. The photopolymerization reactions were monitored by real-time Raman spectroscopy, and the physical properties of the films were investigated by dynamic mechanical analysis. The impact of viscosity on the reaction kinetics was investigated using the Refutas equation, which predicted the viscosity of the hybrid mixtures.

6.3.1 Free-radical Photopolymerization of Epoxy-Acrylate Hybrid Formulations

Conversion profiles for acrylate polymerization were obtained via Raman spectroscopy as the epoxide concentration was increased in the hybrid formulations. In Figure 6-4, the acrylate conversion of neat EGMEA, the non-hydroxyl-containing control, begins with an induction period of approximately 30 s, then steadily increases until EGMEA has reached its maximum conversion, nearly 100%, after 3 minutes of illumination. The induction period of neat EGMEA is attributed to dissolved oxygen in the system, which inactivates the free-radical active centers. As EEC is introduced into the system, the induction period shortens for all but the 20% EEC formulation. This decreased induction period is likely due to the increased formulation viscosity, which decreases the rate of oxygen diffusion. Moreover, adding up to 60 wt% EEC either matches or increases the rate of propagation (taken as the slope of the line), and maximum acrylate conversion, still nearly 100%, is reached after approximately 2 minutes of illumination. At high concentrations of EEC (70-90 wt%), maximum acrylate conversion occurs after about 4 minutes of illumination and is reduced to ~ 95%. However, this trend does not appear consistent: increasing concentrations of EEC do not necessarily increase the propagation rate or vice versa; rather an intermediate concentration of EEC (30 and 60 wt%) best improves the acrylate kinetics. This inconsistent trend may be the result of the interplay between multiple factors, such as viscosity, dilution, increased temperature (due to autoacceleration or the exotherm of the epoxide reaction), and/or network rigidity. At different concentrations of epoxide, or epoxide concentration regimes, different parameter(s) may dominate. The impact of viscosity will be discussed in detail in the next section.

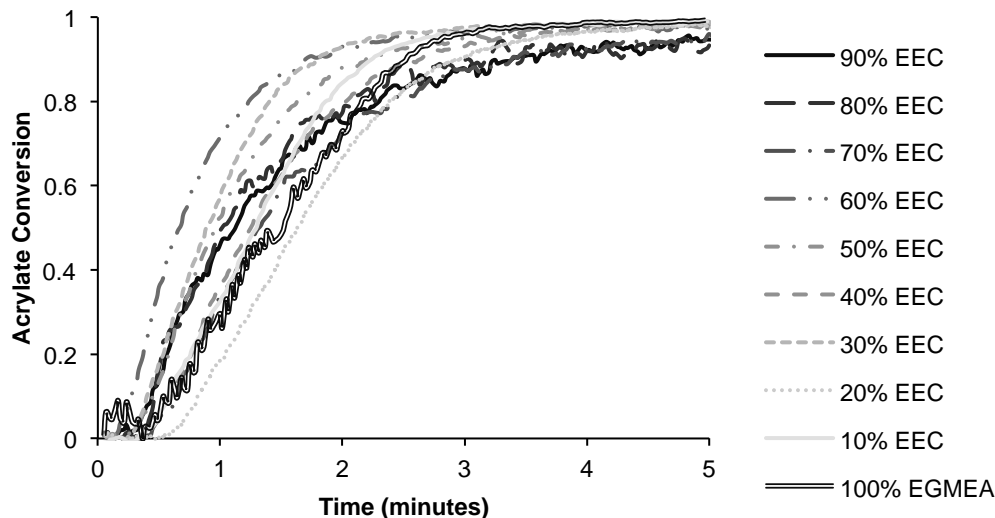


Figure 6-4. EGMEA conversion profiles, calculated from Raman spectra, as a function of EEC content. Each formulation was initiated using an effective irradiance of 140 mW/cm^2 for 5 minutes.

In the HEA/EEC series (Figure 6-5), neat HEA performs best, achieving maximum conversion in under a minute of illumination. However, many of the EEC/HEA formulations perform equally as well; some reduce HEA's short induction period by ~ 10 seconds. In contrast to EGMEA, the addition of intermediate amounts of EEC (20 to 60 wt%, with the exception of 30 wt%) retard the rate of acrylate conversion after the first 30 seconds, albeit only slightly. The largest weight percent of EEC (90%) also had a negative effect on the acrylate rate and conversion.

In comparing the overall effects of EEC on the two different acrylates, it is initially surprising that HEA, which is expected to interact with EEC through the AM mechanism, is the acrylate less affected. Although there are noticeable changes, all of the HEA/EEC conversion profiles fit together compactly (Figure 6-5). The EGMEA/EEC conversion profiles, in contrast, are more dispersed, suggesting the presence of EEC has a greater impact on EGMEA (Figure 6-4). These different responses to EEC are attributed to the differences in propagation rate between the two acrylates. Neat EGMEA requires a little more than 3 minutes illumination to reach full conversion, whereas neat HEA only needs 1 minute. While still faster than EEC's propagation rate (Figure 6-6), EGMEA's

extended propagation time means it must contend with a more developed epoxide network than HEA, and, as a result, the acrylate propagation is more greatly affected.

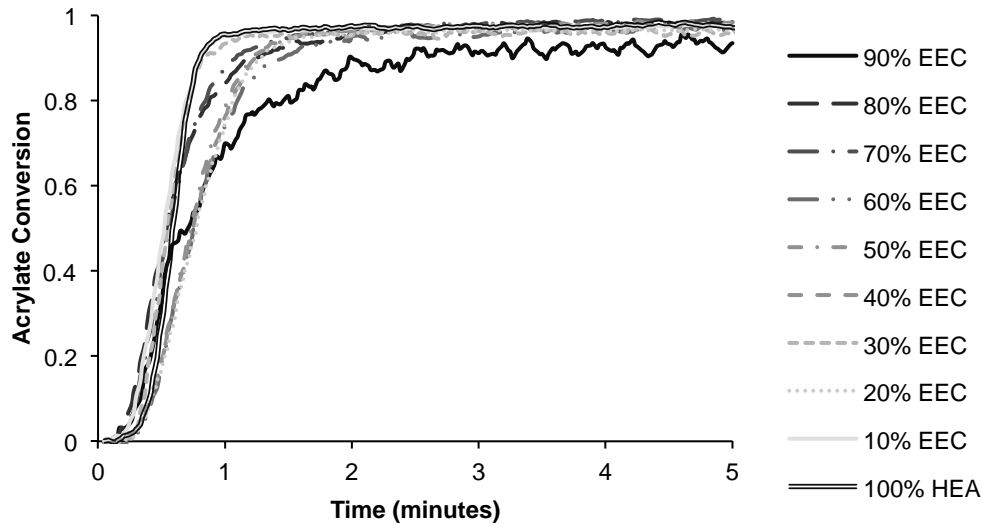


Figure 6-5. HEA conversion profiles, calculated from Raman spectra, as a function of EEC content. Each formulation was initiated using an effective irradiance of 140 mW/cm^2 for 5 minutes.

6.3.2 Cationic Ring-Opening Photopolymerization of Epoxy-Acrylate Hybrid Formulations

Conversion profiles for epoxide polymerization were obtained via Raman spectroscopy as the epoxide concentration was increased in the hybrid formulations. The cationic photopolymerization was monitored simultaneously with the free-radical reaction, and the conversion results as a function of time are presented in Figures 6-6 and 6-7 for EGMEA/EEC and HEA/EEC formulations, respectively.

In Figure 6-6, the ring-opening polymerization of EEC primarily proceeds through the active chain end (ACE) mechanism due to the lack of added hydroxyl groups. As a result, the neat EEC and EGMEA/EEC formulations exhibit low conversion and low polymerization rates. Neat EEC reaches a maximum light-cure conversion of only 10% after approximately 2 minutes of illumination. The addition of EGMEA suppresses the epoxide conversion in all but the 10/90 EGMEA/EEC formulation. This suppression is

likely due to EGMEA's faster polymerization rate, which facilitates the formation of the acrylate network, inhibiting the growth of the epoxide network. Although difficult to see in all of the formulations because of the low conversion values, there is a distinct extension of neat EEC's induction period (~20 sec) in the 80 and 90 wt% EEC formulations to ~1.5 minutes. This is a trend that was repeated, albeit more clearly, in all of the epoxide formulations containing (meth)acrylate to various extents. Also noticeable is the absence of any thermal enhancement of the epoxide polymerization rate by the exotherm of the acrylate reaction, with the possible exception of the 10/90 EEC/EGMEA formulation, despite the acrylate conversion reaching over 90% for all formulations.

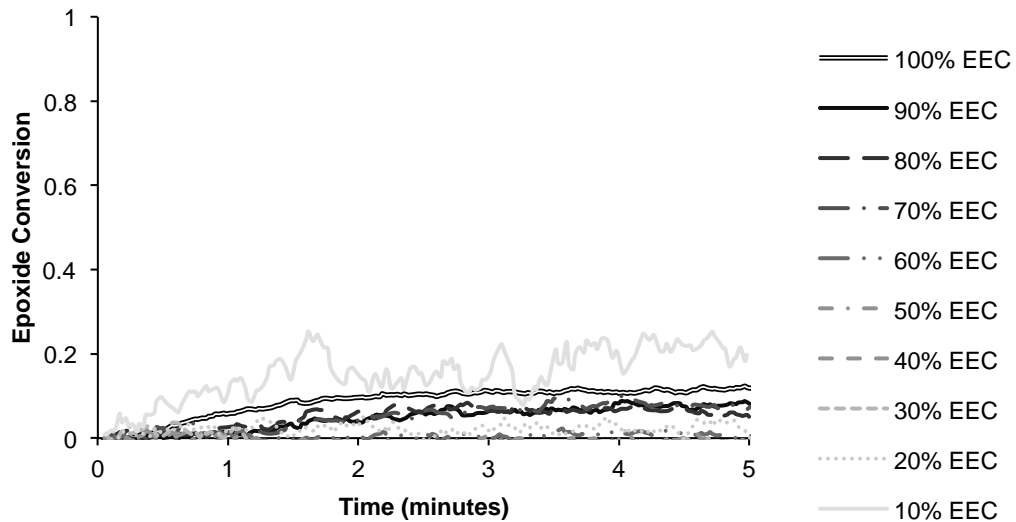


Figure 6-6. Epoxide conversion of EGMEA/EEC formulations, calculated from Raman spectra, as a function of EEC content. Each formulation was initiated using an effective irradiance of 140 mW/cm² for 5 minutes.

The promotion of the AM mechanism, through the addition of a hydroxyl group on the acrylate monomer (HEA), is apparent in the dramatic increase in epoxide conversion in comparison to that of the EGMEA/EEC system (Figure 6-7). HEA/EEC formulations containing 50 wt% or more of EEC all respond similarly. There is no decrease in conversion, as seen with the EGMEA/EEC formulations, but neither is there an increase in polymerization rate or conversion. Yet, when the majority of the

HEA/EEC formulation is HEA, final epoxide conversion is increased as much as 60%. By promoting the AM mechanism, the epoxide not only has another avenue to achieve conversion, but, perhaps more importantly, the chain transfer nature of the mechanism allows for greater mobility of the active center. These active centers, unhindered by the propagating chain they are attached to in the ACE mechanism, are free to diffuse as only small, secondary oxonium ions and, thus, are less likely to be trapped by either the acrylate or epoxide network. Based on these results and past work by Biedroń and Kubisa, a critical concentration of hydroxyl groups may be necessary for the AM mechanism to effectively increase both the polymerization rate and final conversion.^{21,24}

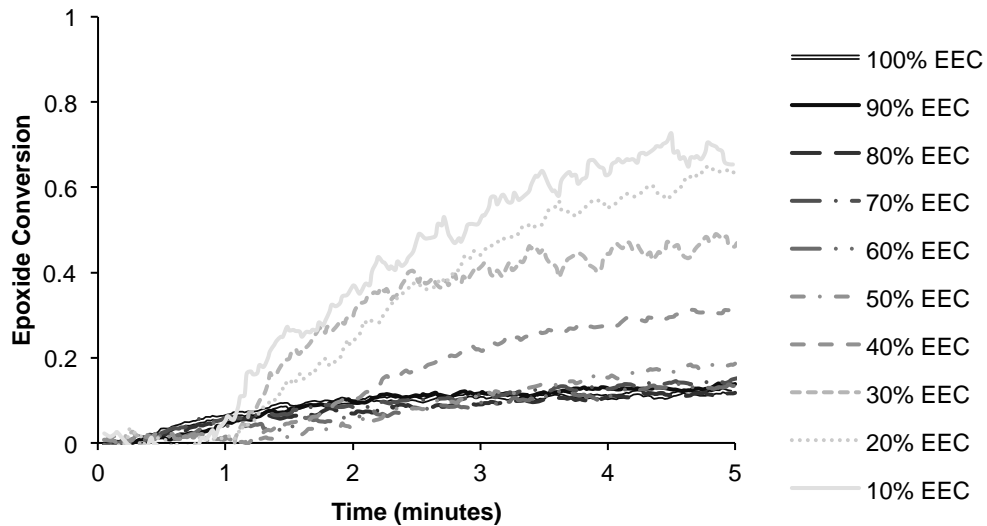


Figure 6-7. Epoxide conversion of HEA/EEC formulations, calculated from Raman spectra, as a function of EEC content. Each formulation was initiated using an effective irradiance of 140 mW/cm² for 5 minutes.

In order to better understand the importance of the hydroxyl concentration, consider the kinetics of the ACE and AM mechanisms. The rate of propagation of the ACE mechanism ($R_{p,ACE}$) can be defined as

$$R_{p,ACE} = k_{p,ACE} [M^*][M] \quad (6-3)$$

where $k_{p,ACE}$ is the ACE mechanism propagation rate constant, $[M^*]$ is the concentration of cationic active centers, and $[M]$ is the concentration of monomer.²⁴ In contrast, the AM mechanism rate of propagation ($R_{p,AM}$) is not dependent on the concentrations of monomer or active centers, but rather is defined as

$$R_{p,AM} = k_{p,AM}[+HOCH_2CH_2][OH] \quad (6-4)$$

where $k_{p,AM}$ is the AM mechanism propagation rate constant, $[+HOCH_2CH_2]$ is the concentration of secondary oxonium ions, and $[OH]$ is the hydroxyl concentration. By taking the ratio of Equations 6-3 and 6-4

$$\frac{R_{p,AM}}{R_{p,ACE}} = \frac{[OH]}{[M]} * \frac{k_{p,AM}[+HOCH_2CH_2]}{k_{p,ACE}[M^*]} \quad (6-5)$$

Equation 6-5 demonstrates that, all other variables being constant, increasing the hydroxyl concentration increases the proportion of the epoxide conversion accomplished by the AM mechanism. Furthermore, the ratio of AM to ACE propagation can be tuned by adjusting the hydroxyl to monomer concentration. Referencing Equation 6-5 and the data in Figure 6-7, it is estimated that the AM mechanism becomes dominant in the HEA/EEC reaction at approximately 50/50 wt% (2.7/1.1 mol/L by molecule, or 2.7/2.1 mol/L by functional group $[OH/OCH_2CH_2]$). The 50/50 wt% formulation is the first to increase the final epoxide conversion. Moreover, the rate and final epoxide conversion for formulations containing greater than 50 wt% EEC increase dramatically.

In addition, as with the EGMEA/EEC formulations, there is an increase in the induction period at the beginning of the epoxide reaction. This elongation of the induction period has been demonstrated in previous work and attributed to the presence of hydroxyl groups and thus the AM mechanism.^{2,25} However, in this study, the increase in the epoxide induction period is shown in both the hydroxyl-containing and control formulations, suggesting its presence is a result of the (meth)acrylate. Nonetheless, HEA/EEC formulations overcome the induction period more quickly than the non-hydroxyl-containing acrylate formulation. High concentrations of HEA (≤ 50 wt% EEC),

lengthen the induction period to ~1 minute, but 90 wt% EEC only experiences an induction period a few seconds longer than neat EEC. Even though the AM mechanism is not thought to be dominant at 90 wt% EEC, the chain transfer mechanism appears to help alleviate the induction time.

6.3.3 Free-Radical Photopolymerizations of Epoxy-Methacrylate Hybrid Formulations

Because of their commercial availability and industrial importance, methacrylates were also studied. The addition of a methyl group often increases the brittleness (and correspondingly, the T_g) of a material, when compared to the polyacrylate. The methyl group also tends to decrease the rate of polymerization, due to the added steric hindrance and the increased stability of the radical active center.²⁶ In these formulations, this slower rate of the free-radical reaction provides a more competitive edge to the cationic polymerization.

Neat EGMEMA (seen in Figure 6-8) polymerizes more slowly than EGMEA and has a final conversion of ~5%. Unlike the equivalent acrylate hybrid formulation (EGMEA/EEC, Figure 6-4), both the polymerization rate and final methacrylate conversion increase with increasing amounts of EEC. At 90 wt% EEC, a 55% increase in methacrylate conversion is seen compared to neat EGMEMA. Such drastic enhancement of the methacrylate conversion, in a system where the epoxide conversion is dominated by the ACE mechanism, is unexpected. Instead, perturbations in the (meth)acrylate conversion, such as seen in the EGMEA conversion profiles (Figure 6-4), would be more appropriate based on the factors considered. Increasing viscosity and dilution by increasing the percentage of EEC, should decrease conversion by simultaneously making diffusion more difficult and more necessary; however, the opposite trend is demonstrated in Figure 6-8. Inspection of the corresponding epoxide conversion profiles (Figure 6-10) shows that the epoxide network provides no impediments for at least the first 1.5 minutes of the reaction. Moreover, thermal enhancement of the methacrylate reaction due to the epoxide exotherm is unlikely because of the low epoxide conversion. Thermal enhancement by autoacceleration also does not appear plausible, as the propagation rates for each formulation are quite constant.

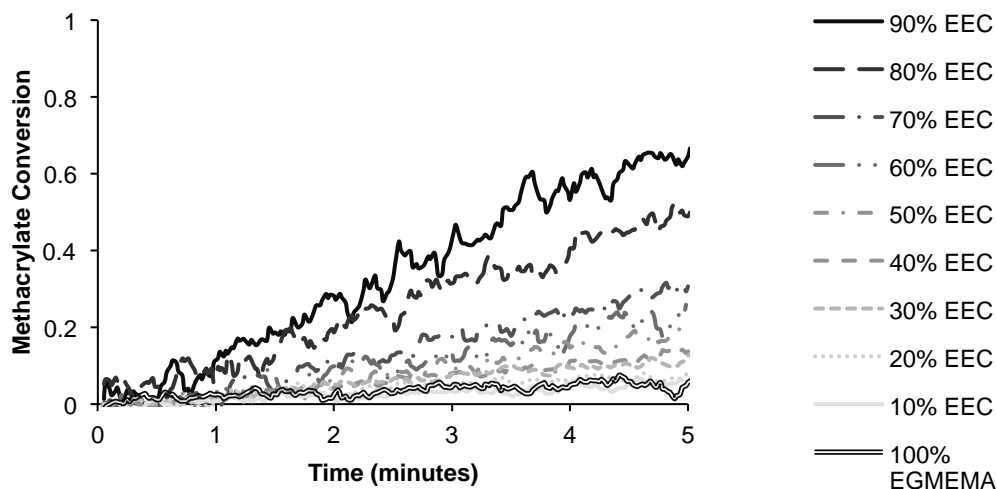


Figure 6-8. EGMEMA conversion profiles, calculated from Raman spectra, as a function of EEC content. Each formulation was initiated using an effective irradiance of 140 mW/cm^2 for 5 minutes.

Therefore, it is concluded that the rate and conversion of EGMEMA is increased by some synergistic effect between the free-radical active center and either a cationic active center or by the EEC monomer chemistry. This chemical interaction could be the result of the addition of the methyl group on the acrylate, or, as previously discussed, the interaction could simply be more visible due to the slow propagation kinetics. Further Raman studies confirmed that the effect is not a result of interaction with cationic active centers by performing identical trials without the cationic photoinitiator DAI (see Appendix B). Kilambi, *et al.* has attributed similar increases in the reactivity of (meth)acrylates with increasing dilution to intramolecular conformational effects, which may affect the (meth)acrylate active centers or the reactive (meth)acrylate moiety.²⁷ Additionally, while reduced with increasing amounts of EEC, an induction period of ~ 30 seconds still remains at 90% EEC. Because of neat EGMEMA's extremely low rate of propagation, it is difficult to decipher the cause of this induction period. It could be the result of oxygen inhibition, with which an induction period should be present in the neat methacrylate formulation, or it could be the result of the interaction between the methacrylate and epoxide, in which case an induction period would not be expected in the neat EGMEMA formulation.

In contrast to EGMEMA, neat HEMA photopolymerizes well under the set conditions, reaching a maximum methacrylate conversion of just under 80% after approximately 2 minutes of illumination (Figure 6-9). This increase in reactivity is the result of the hydrogen bonding possible through the hydroxyl group and was similarly observed between neat EGMEMA and HEA.^{27,28} Analogous to EGMEMA's response, HEMA's reaction kinetics are greatly affected by the addition of EEC. Adding high concentrations of EEC (80 to 90 wt%) increases the methacrylate conversion to ~95%. Indeed, adding any concentration of EEC increases the final methacrylate conversion, but lower concentrations (≤ 70 wt% EEC) also decrease the rate of polymerization and increase the induction period (~ 1 min with 10% EEC), requiring over 4 minutes of illumination to reach final conversion. This decrease in rate from neat HEMA is attributed to EEC acting as both a diluent and a heat sink, preventing autoacceleration. HEMA is known to undergo autoacceleration, and in Figure 6-9, it exhibits two regimes, with distinct polymerizations rates before leveling off, which is indicative of autoacceleration.^{26,29} However, adding 10 wt% EEC reduces the sharp distinction between the two regimes, and with the addition of 20 wt% EEC, evidence of autoacceleration is no longer visible.

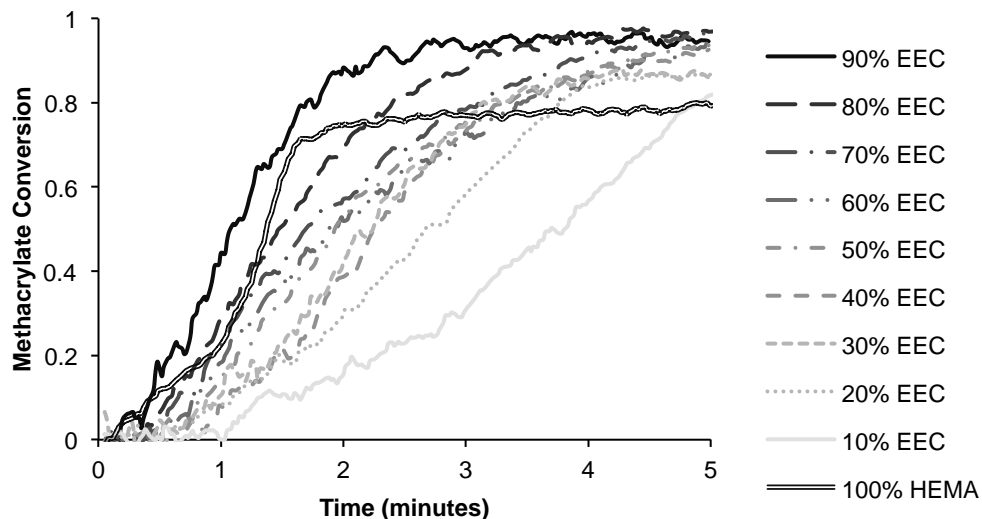


Figure 6-9. HEMA conversion profiles, calculated from Raman spectra, as a function of EEC content. Each formulation was initiated using an effective irradiance of 140 mW/cm^2 for 5 minutes.

Adding EEC also creates an induction period in all but the 90% EEC formulation. Because neat HEMA does not experience an induction period, it is unlikely that it is the result of oxygen inhibition as was the case for the EGMEA/EEC formulations. If the induction period seen on the EGMEMA/EEC formulation is a result of a methacrylate/epoxide interaction, a similar interaction could be demonstrated in the HEMA/EEC formulations, made more visible by neat HEMA's higher propagation rate (relative to that of EGMEMA). Alternatively, this induction period could be due to the presence of the AM mechanism. The induction period is at its longest at 10 wt% EEC, where the ratio of hydroxyl groups to epoxides is greatest, and thus $R_{p,AM} : R_{p,ACE}$ is also maximized (Equation 6-5). The length of the induction period for the epoxide conversion of the same formulations also correlates well (Figure 6-11). Moreover, the induction period of the epoxide in the HEA/EEC formulations also has a similar length. The acrylate conversion of the HEA/ECC formulations does not exhibit a similar induction period (Figure 6-5). In fact, HEA's induction period is slightly reduced. Yet, HEA's propagation rate is greater than that of HEMA. As much as 40% acrylate conversion has occurred during EEC's shortest induction periods (≤ 40 wt % EEC), when the ACE mechanism dominates (Figure 6-5). HEA's quick network formation likely precedes the majority of any draw on the hydroxyl groups to participate in the epoxide mechanism; therefore, the effects on the acrylate network are limited. In comparison, HEMA's conversion is only 5 to 10% under similar conditions; thus, when the AM mechanism dominates, the participation of the hydroxyl groups in the epoxide mechanism may inhibit methacrylate conversion by limiting diffusion. In addition, the synergistic effects seen with the EGMEMA/EEC formulations may also contribute (Figure 6-8).

6.3.4 Cationic Photopolymerizations of Epoxy-Methacrylate Hybrid Formulations

The epoxide conversion for the EGMEMA/EEC formulations tracks well with the methacrylate conversion of the same formulations (Figure 6-10). Analogous to the EGMEA/ECC formulations, the addition of methacrylate also appears to lengthen the epoxide induction period, though to a lesser extent. After overcoming the induction period, low concentrations of EEC achieve approximately double the epoxide conversion of neat EEC, most likely due to a combination of formulation viscosity reduction (see

section below) and the low methacrylate conversions (and thus the absence of an obstructive methacrylate network) (Figure 6-8). As the concentration of EEC increases, methacrylate conversion also increases, simultaneously depressing the epoxide conversion. For the 10/90 EGMEMA/EEC weight fraction ratio, the methacrylate conversion depresses the epoxide conversion to below that for neat EEC. This interplay between methacrylate and epoxide conversion is probably more visible than in the epoxide/acrylate systems because of the similar rate of network formation.

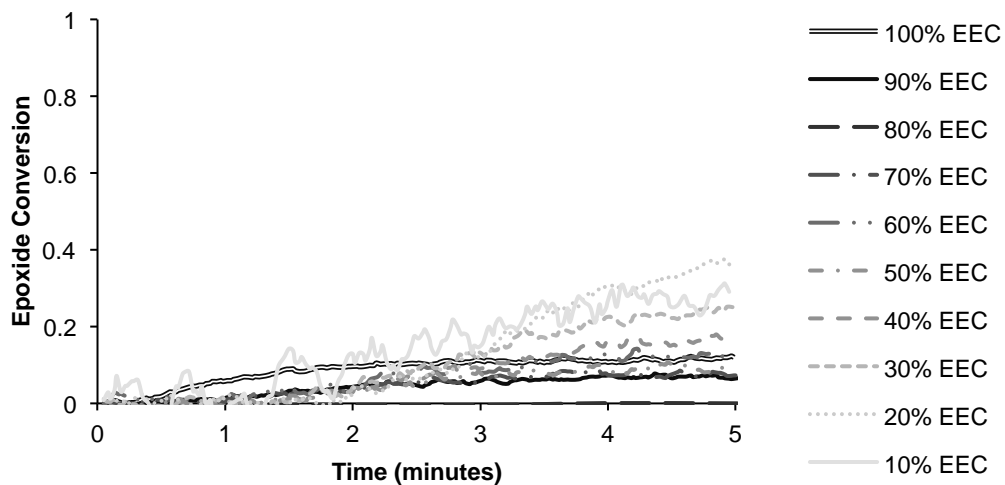


Figure 6-10. Epoxide conversion of EGMEMA/EEC formulations, calculated from Raman spectra, as a function of EEC content. Each formulation was initiated using an effective irradiance of 140 mW/cm^2 for 5 minutes.

EEC responded to the addition of a hydroxyl group to the methacrylate in much the same way as in the HEA/EEC formulations: the final epoxide conversion increased by as much as 20% (Figure 6-11). However, in contrast to the trends demonstrated in the epoxide conversion of the HEA/EEC formulations, at high concentrations of methacrylate ($\leq 30 \text{ wt\% EEC}$), the initial rate decreases. Yet, an overall conversion of $\sim 60\%$ is reached for all three concentrations. This overall epoxide conversion is 10% less than that of the HEA/EEC system (Figure 6-7). Both the change in trend and lower epoxide conversion are attributed to the simultaneous methacrylate/epoxide network formation. To a lesser extent, the increased brittleness of the methacrylate (due to the higher T_g) may

also impact the epoxide network; although by a concentration of 80% EEC, the HEA/EEC and HEMA/EEC formulation T_g values converge (Figure 6-15).

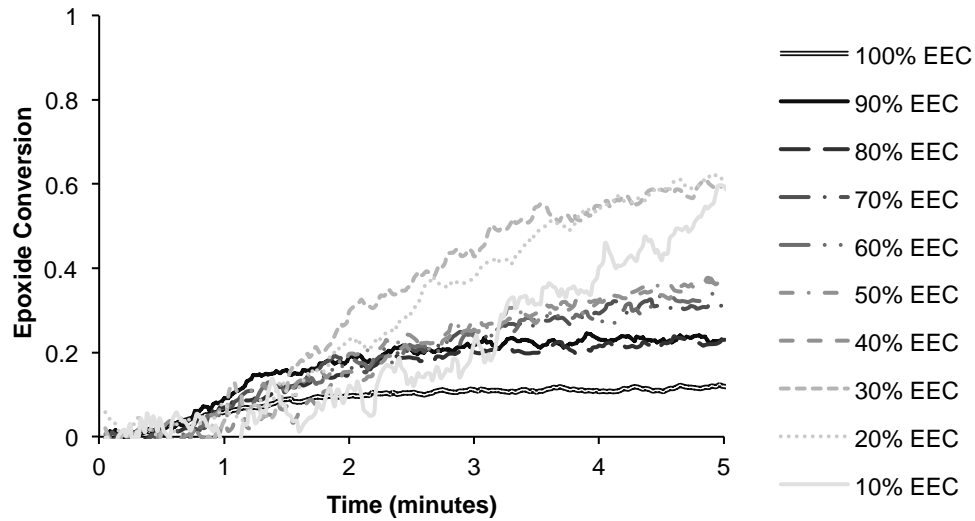


Figure 6-11. Epoxide conversion of HEMA/EEC formulations, calculated from Raman spectra, as a function of EEC content. Each formulation was initiated using an effective irradiance of 140 mW/cm² for 5 minutes.

The methacrylate (OH) concentration at which the AM mechanism becomes dominant is also more difficult to distinguish than in its acrylate counterpart. An increase in rate is seen with as little as 10 wt% methacrylate (90 wt% EEC); however, this increase could be due to the synergistic effects experienced by the non-hydroxyl-containing control (EGMEMA), as well as the AM mechanism. Kinetically, since the same epoxide is used, the concentration of OH at which the AM mechanism dominates should be approximately the same as with the HEA/EEC formulations (*i.e.*, 53/47 wt% HEMA/EEC). Both 50 and 40 wt% EEC formulations fall into a range of concentrations (40 to 70 wt% EEC) with similar rates and final conversions and are not distinguishable as AM dominant. However, if the increase in rate at 90 wt% EEC is ascribed to the dominance of the AM mechanism, one explanation for this concentration discrepancy rests again on the rate of network formation. As previously discussed, it is proposed that a significant portion of the HEA network was formed before the acrylate's hydroxyl

groups participated heavily in the epoxide mechanism. In this case, some hydroxyl groups may be inaccessible to the epoxides, requiring an overall increase in the acrylate concentration to compensate. The HEMA network, in contrast, is not as fully developed, and therefore does not require any additional methacrylate.

6.3.5 Impact of Viscosity on Hybrid Kinetics

Because of the large discrepancy in viscosity between neat EEC and the neat (meth)acrylate monomers (~ 450 cSt), the effect of viscosity was investigated. First, the viscosities of each of the four (meth)acrylate/EEC monomer mixtures were predicted using the Refutas equation (Equation 6-6),³⁰ and the results are shown in Figure 6-12.

$$\nu_{mixture} = e^{\left(\frac{VBI_{mixture}-10.975}{14.534}\right)} - 0.8 \quad (6-6)$$

where

$$VBI_{mixture} = [W_{comp,1} * VBI_{comp,1}] + [W_{comp,2} * VBI_{comp,2}] \quad (6-7)$$

and

$$VBI_{comp} = 14.534 * \ln[\ln(\nu_{comp} + 0.8)] + 10.975 \quad (6-8)$$

The viscosity blending index (*VBI*) for mixture and components is represented by $VBI_{mixture}$ and VBI_{comp} , respectively. The viscosity of mixture and components in centistokes is represented by $\nu_{mixture}$ and ν_{comp} . Weight fraction of monomers in the mixture is represented by $W_{comp,1}$ and $W_{comp,2}$.

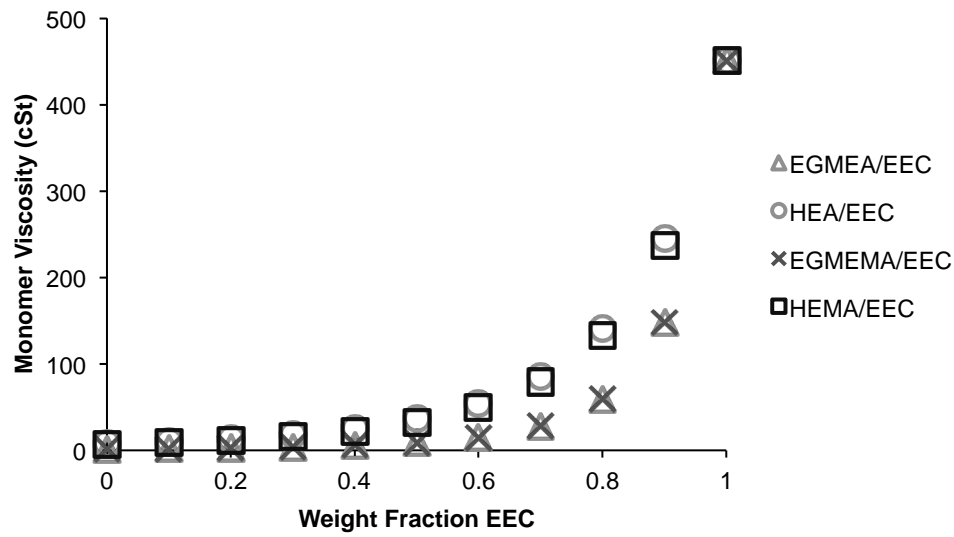
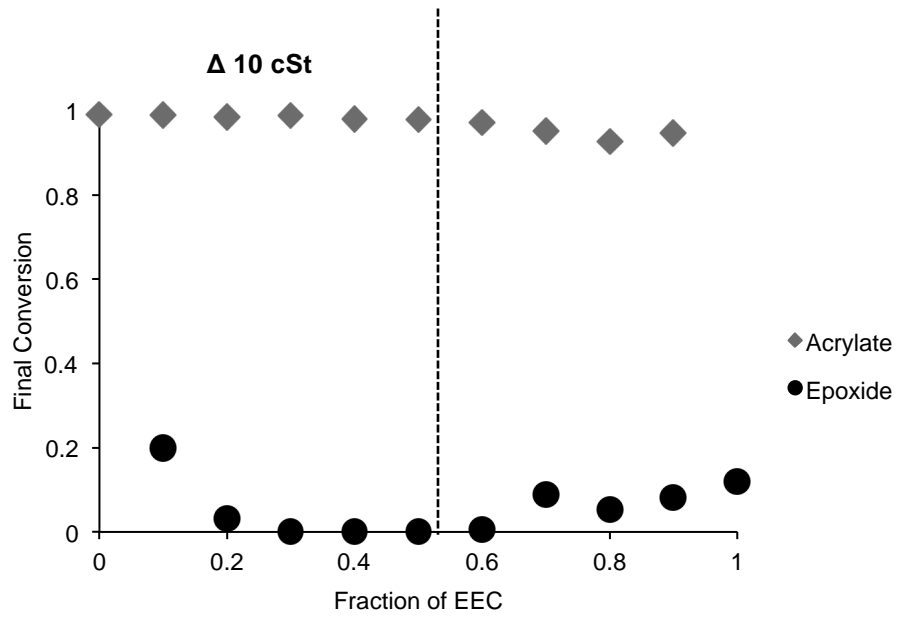
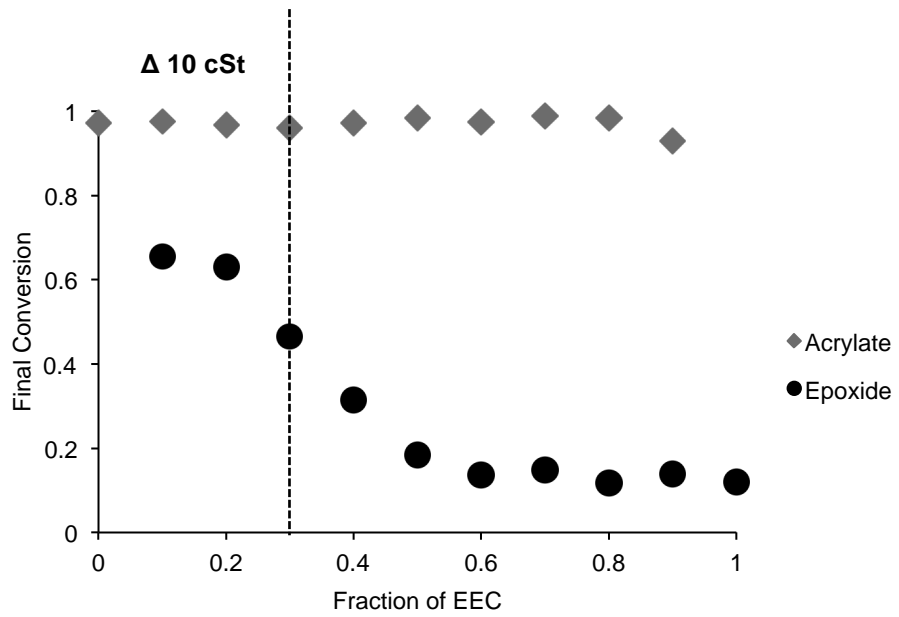


Figure 6-12. Hybrid monomer mixture viscosities (in centistokes) at 25°C as predicted by the Refutas equation.

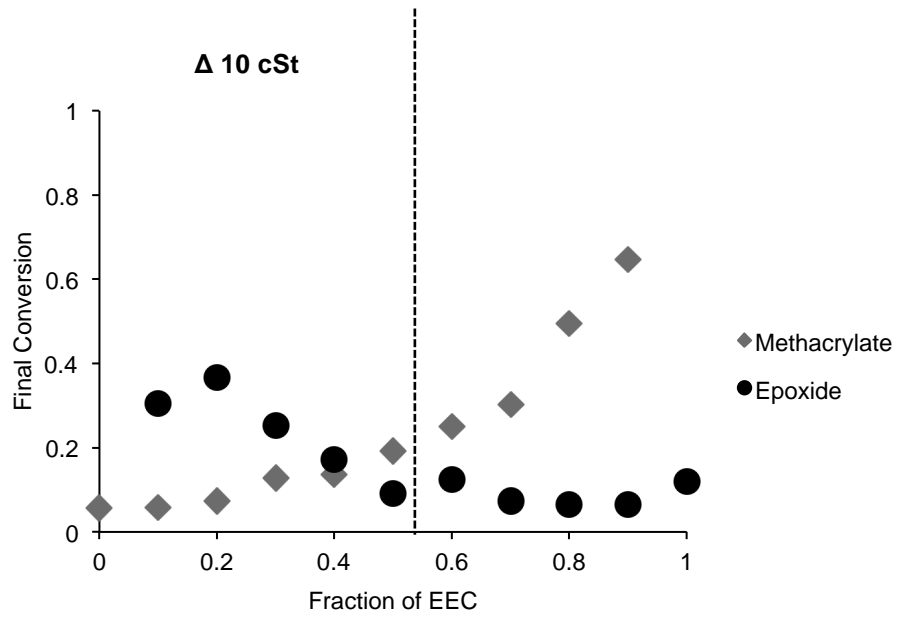
The Refutas equation predicts that all four mixture formulations have similar viscosities at low weight fractions of EEC; however, at approximately 40 wt% EEC, the mixtures diverge into two curves – the hydroxy-(meth)acrylates and the ethylene glycol-(meth)acrylates. Although the viscosity of the formulation will increase with conversion, previous work has made correlations between the initial monomer mixture viscosity and its effect on the final conversion values for epoxide mixtures.³⁰ In theory, a decrease in viscosity should improve the mobility of the active centers by increasing the rate of diffusion and, therefore, increase conversion. However, comparing initial viscosity and final conversion for each of the studied formulations demonstrates that decreasing viscosity does not always result in increased conversion (Figure 6-13). The acrylate conversion does decrease slightly with increasing viscosity for both EGMEA/EEC and HEA/EEC formulations (A and B in Figure 6-13).



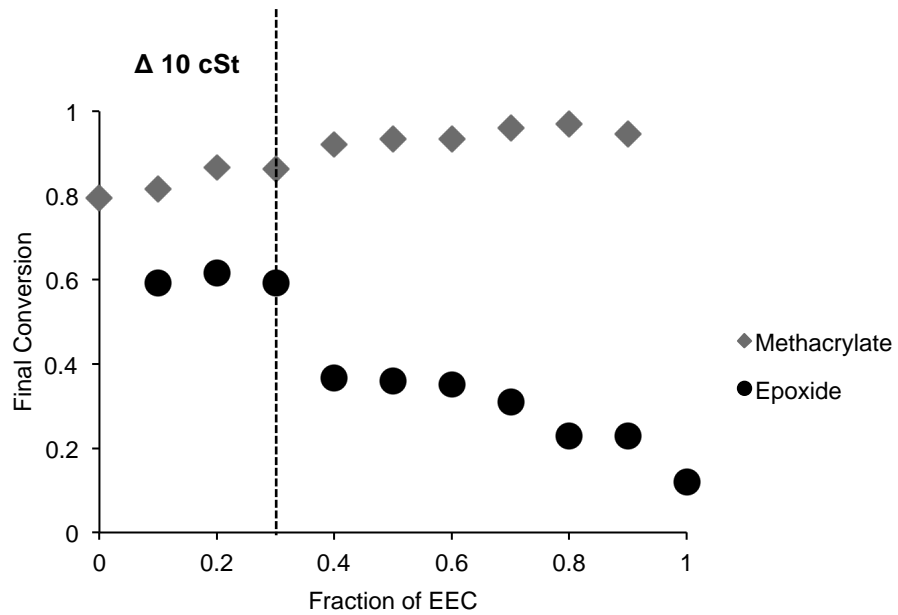
(A)



(B)



(C)



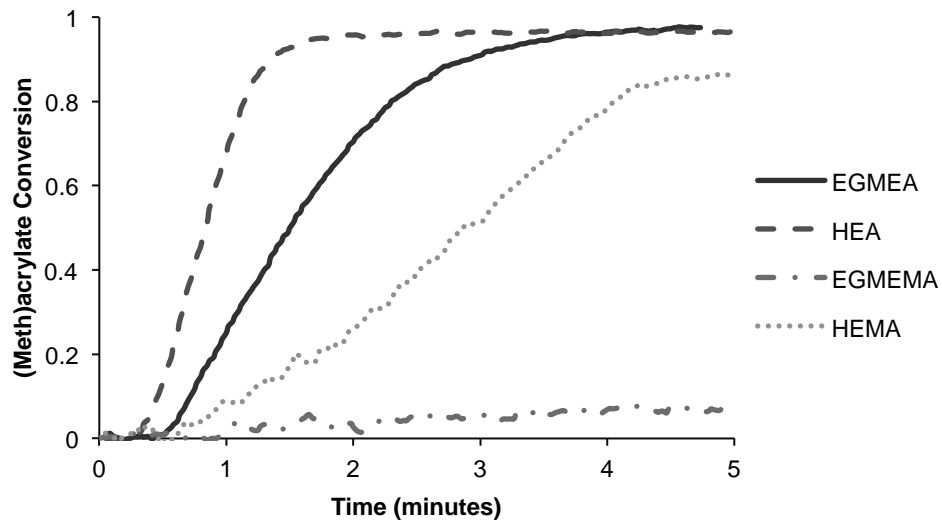
(D)

Figure 6-13. Final conversion as a function of the weight fraction of EEC for the hybrid formulations EGMEMA/EEC (A), HEA/EEC (B), EGMEMA/EEC (C), and HEMA/EEC (D). Viscosity increases with fractions of EEC; to the left of the vertical dotted line, this viscosity change is ~ 10 cSt.

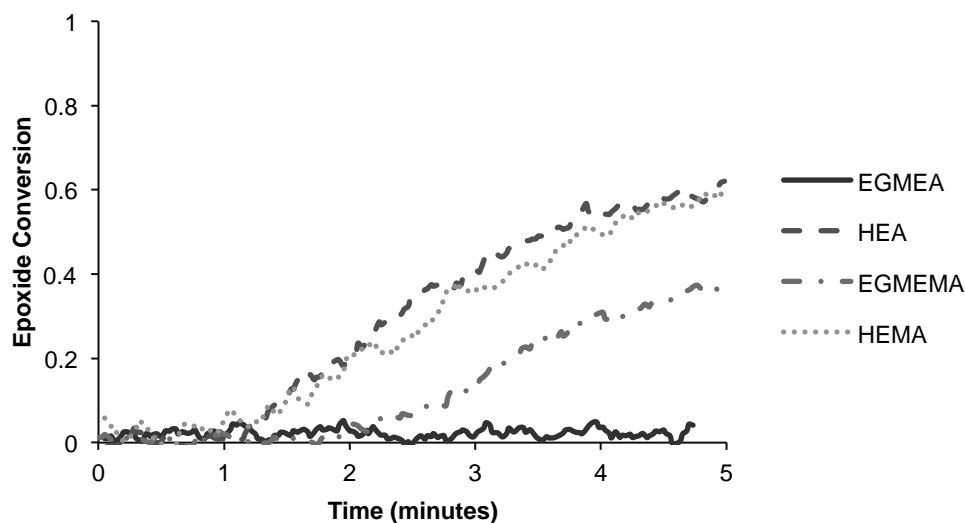
In contrast, the methacrylate conversion increases with increasing viscosity for both EGMEMA/EEC and HEMA/EEC (C and D in Figure 6-13). Larger increases in the HEMA conversion occur at lower weight fractions of EEC (≤ 0.4), where the viscosity change is minimal ($\Delta 15$ cSt), yet the enhancement of EGMEMA conversion is actually greater when the viscosity increase is more drastic (right side of dotted line), suggesting viscosity is not the discriminating variable for determining final conversion.

The epoxide conversions appear partially subject to the influence of viscosity. In both the HEA/EEC and HEMA/EEC formulation series the epoxide conversion decreases with increasing viscosity (B and D in Figure 6-13). However, EEC conversion increases, albeit slightly (5 to 10 %), at high concentrations of EEC (and thus, higher viscosities) for both the EGMEA/EEC and EGMEMA/EEC formulations (A and C in Figure 6-13).

Viscosity's lack of influence over these hybrid reactions is further illustrated by comparing the conversion profiles of the four different formulations with similar (± 10 cSt) initial viscosities (Figure 6-14). The four hybrid formulations chosen for comparison also contain the same 20 wt% EEC (if converted to mol% calculated by functional group, 16.8 to 22.2 mol%, Appendix B). A marked difference is exhibited in the conversion profiles of the four different (meth)acrylates in formulations of the same viscosity (Figure 6-14, A). At their final conversion, they range from 6% conversion (EGMEMA/EEC) to 96% conversion (HEA/EEC and EGMEA/EEC). Similarly, and perhaps most notably, the conversion profile of EEC changes with the (meth)acrylate included in the formulation, despite the nearly identical viscosities of the four formulations (Figure 6-14, B). The impact of the AM mechanism is also clearly shown on the HEA/EEC and HEMA/EEC conversion profiles, compared to their non-hydroxyl-containing controls (EGMEA/EEC and EGMEMA/EEC, respectively).



(A)



(B)

Figure 6-14. Conversion profiles of the four (meth)acrylate. EEC mixtures at the 20/80 EEC/(meth)acrylate weight fraction ratio: (A) (meth)acrylate conversion and (B) epoxide conversion. Although all starting viscosities were similar (± 10 cS), the conversion profiles and final conversions are quite different.

6.3.6. Physical Properties of Epoxide-Acrylate Hybrid Photopolymers

In addition to kinetics, promotion of the AM mechanism through hydroxyl-containing acrylates is also expected to influence the physical properties of the resulting hybrid polymers. Not only does increasing propagation through the AM mechanism increase epoxide conversion, it also covalently bonds the epoxide and (meth)acrylate

networks to form a semi-grafted network, which is expected to increase network homogeneity (Figure 6-2). Furthermore, the chain transfer-like AM mechanism changes the epoxide network structure by increasing branching and creating more, shorter polymer chains.³¹ Changes to the polymer network, as well as control over physical properties were studied using dynamic mechanical analysis.

The EGMEMA/EEC formulations were characterized by low conversion, and as a result, the physical properties of the polymers were too poor to collect DMA samples. However, DMA samples were tested for the other three hybrid formulations. From the second DMA temperature cycle, the $\tan \delta$ trace as a function of temperature was analyzed to determine the glass transition temperature (T_g) and full width at half maximum (FWHM) for each sample.

The T_g is a well-established polymer property that is an important determiner of relevant applications. Usually the T_g is well outside the temperature range of the application to avoid unexpected property changes. Additionally, T_g is a good predictor of brittleness, with high T_g polymers, such as EEC ($T_g \sim 230^\circ\text{C}$), being more brittle than those with T_g values near or below room temperature. Figure 6-15 demonstrates that the T_g , and thus the brittleness, of EEC can be controlled by adjusting the (meth)acrylate and its concentration. (Meth)acrylates with a lower homopolymer T_g , such as EGMEA ($T_g = -50^\circ\text{C}$, manufacturer value³²) and HEA ($T_g = 32^\circ\text{C}$), are more effective at reducing the formulation T_g , as is consistent with the Flory-Fox equation.³³ Beyond the magnitude change, no noticeable difference is seen between the T_g trend for EGMEA/EEC and that of HEA/EEC and HEMA/EEC, suggesting that the impact of the AM mechanism on the T_g is minimal. The T_g 's of all three formulations increase non-linearly with increasing EEC concentration. At low concentrations of epoxide (10 to 20 or 30 wt%) the formulations remain at a fairly constant T_g ($\pm 10^\circ\text{C}$), but by 80 wt% EEC, the T_g values of the three formulations converge.

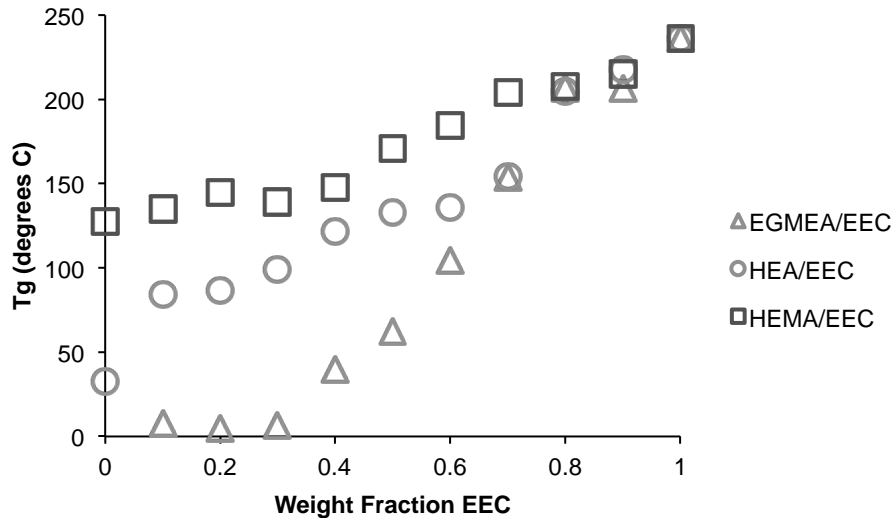


Figure 6-15. The glass transition temperature (T_g) of three of the hybrid formulations. Increases in T_g are not linear, and a formulation can remain at similar T_g ($\pm 10^\circ\text{C}$) for up to a 20 wt% increase in EEC.

The FWHM of the $\tan \delta$ peak is a qualitative estimation of the network heterogeneity. Samples with greater network heterogeneity have a broad $\tan \delta$ peak because differences in polymer chain segments, such as chain length, cross-link density, *etc.*, will alter the temperature at which that segment transitions from the glassy state to the rubbery state. Samples with phase separation or a large amount of unreacted monomer can even experience two distinct $\tan \delta$ peaks. Of the three formulations for which DMA data were collected, the two hydroxyl-containing formulations (HEA/EEC and HEMA/EEC) displayed better network homogeneity overall than the non-hydroxyl-containing control (EGMEA/EEC), though low FWHM values were still achievable without covalently bonding the (meth)acrylate and epoxide networks (Figure 6-16). Approximately half of the EGMEA/EEC formulations have a FWHM value less than 90°C , within the range of the two hydroxyl-containing formulations. Yet, between 50 and 80 wt% EEC, the EGMEA/EEC FWHM values increase significantly, up to 166°C at 70 wt% EEC. At the same epoxide concentration, the hydroxyl-acrylate HEA reduced this FWHM from 166°C to 83°C . With the exception of neat HEMA, the HEMA/EEC formulations retained a fairly constant FWHM across the increasing EEC concentrations. This consistency suggests that the AM mechanism does not necessarily need to be

dominant for better network homogeneity to occur; however, the FWHM of the HEA/EEC formulations does increase by up to 30°C at some higher concentrations of EEC (60 to 80 wt% EEC) where the ACE mechanism is thought to be dominant.

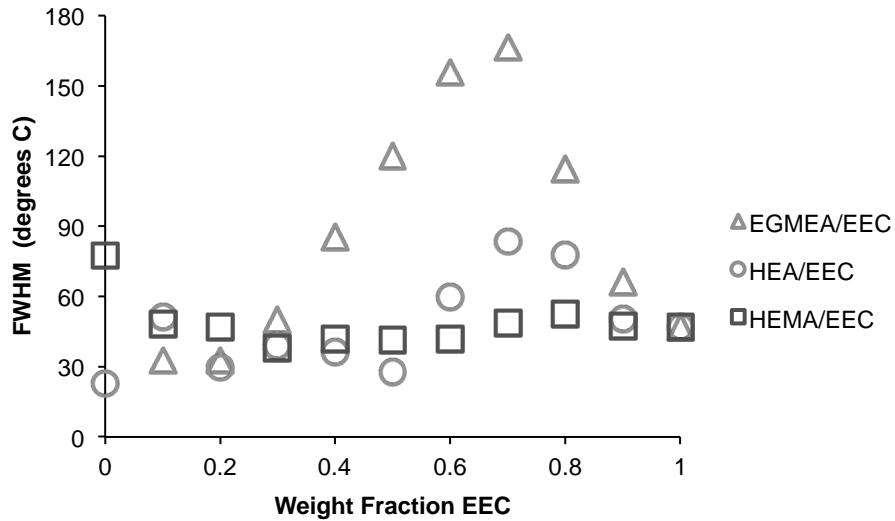


Figure 6-16. The full width at half maximum of the $\tan \delta$ (FWHM) of three of the hybrid formulations. Formulations with a hydroxyl-containing (meth)acrylate have a smaller FWHM, and therefore experience less network heterogeneity.

6.4 Conclusions

Using real-time Raman spectroscopy, it was demonstrated for both an acrylate/epoxide and a methacrylate/epoxide system that promotion of the AM mechanism through a hydroxyl-containing (meth)acrylate increases the epoxide conversion in comparison to the non-hydroxyl-containing control. Even though the majority of the acrylate network was formed by the time the epoxide began to react in earnest, high epoxide conversion (~70%) was achievable. The effect on the (meth)acrylate network by the epoxide is dependent on the rate of (meth)acrylate conversion. If the rate of (meth)acrylate network formation is comparable to that of the epoxide, greater changes in rate and final conversion are exhibited with increasing epoxide concentrations.

The initial formulation viscosity was found to have minimal impact on the final conversion, despite increasing approximately 450 cSt over the range of epoxide concentration. Different formulations with the same initial viscosity (± 10 cSt) and sample epoxide content were shown to have significantly different reaction profiles. The epoxide conversion profiles in the presence of the hydroxyl-containing (meth)acrylates was noticeably higher than those of the control due to the presence of the AM mechanism.

Control over the T_g was achieved by adjusting the (meth)acrylate and its concentration. No significant difference between the hydroxyl-containing (meth)acrylates and the non-hydroxyl-containing control was found for the T_g trends; however, the addition of a hydroxyl group, allowing covalent bonding between the (meth)acrylate and epoxide networks, resulted in more homogenous networks. Comparing the hydroxyl-acrylate and its control, the FWHM was halved for the same epoxide concentration.

6.5 References

- (1) Cai, Y.; Jessop, J. L. P. Decreased Oxygen Inhibition in Photopolymerized Acrylate/Epoxy Hybrid Polymer Coatings as Demonstrated by Raman Spectroscopy. *Polymer* **2006**, *47* (19), 6560–6566.
- (2) Cai, Y.; Jessop, J. L. P. Effect of Water Concentration on Photopolymerized Acrylate/Epoxy Hybrid Polymer Coatings as Demonstrated by Raman Spectroscopy. *Polymer* **2009**, *50* (23), 5406–5413.
- (3) Bailey, W. J.; Endo, T. Radical Ring-Opening Polymerization and Copolymerization with Expansion in Volume. *Journal of Polymer Science: Polymer Symposia* **1978**, *64* (1), 17–26.
- (4) Leung, D.; Bowman, C. N. Reducing Shrinkage Stress of Dimethacrylate Networks by Reversible Addition–Fragmentation Chain Transfer. *Macromolecular Chemistry and Physics* **2012**, *213*, 198–204.
- (5) Sangermano, M.; Carbonaro, W. UV-Cured Interpenetrating Acrylic-Epoxy Polymer Networks: Preparation and Characterization. *Macromol. Symp.* **2008**, *293*, 515–520.
- (6) Oxman, J. D.; Jacobs, D. W.; Trom, M. C. Evaluation of Initiator Systems for Controlled and Sequentially Curable Free-Radical/Cationic Hybrid Photopolymerizations. *Journal of Polymer Science Part A* **2005**, *43*, 1747–1756.
- (7) Rajaraman, S. K.; Mowers, W. A.; Crivello, J. V. Interaction of Epoxy and Vinyl Ethers During Photoinitiated Cationic Polymerization. *Journal of Polymer Science Part A* **1999**, *37* (21), 4007–4018.
- (8) Lin, Y.; Stansbury, J. W. Kinetics Studies of Hybrid Structure Formation by Controlled Photopolymerization. *Polymer* **2003**, *44*, 4781–4789.
- (9) Cho, J.-D.; Hong, J.-W. UV-Initiated Free Radical and Cationic Photopolymerizations of Acrylate/Epoxy and Acrylate/Vinyl Ether Hybrid Systems with and Without Photosensitizer. *J. Appl. Polym. Sci.* **2004**, *93*, 1473–1483.
- (10) Wei, H.; Li, Q.; Ojelade, M.; Madbouly, S.; Otaigbe, J. U. Thiol-Ene Free-Radical and Vinyl Ether Cationic Hybrid Photopolymerization. *Macromol. Symp.* **2007**, *40* (24), 8788–8793.
- (11) Decker, C.; Viet, T.; Decker, D.; Weber-Koehl, E. UV-Radiation Curing of Acrylate/Epoxy Systems. *Polymer* **2001**, *42*, 5531–5541.

- (12) Crivello, J. V. Synergistic Effects in Hybrid Free Radical/Cationic Photopolymerizations. *Journal of Polymer Science Part A: Polymer Chemistry* **2007**, *45*, 3759–3769.
- (13) Russell, B.; Chartoff, R. The Influence of Cure Conditions on the Morphology and Phase Distribution in a Rubber-Modified Epoxy Resin Using Scanning Electron Microscopy and Atomic Force Microscopy *Polymer* **2005**, *46*, 785–798.
- (14) Duan, J.; Kim, C.; Jiang, P. On-Line Monitoring of Cycloaliphatic Epoxy/Acrylate Interpenetrating Polymer Networks Formation and Characterization of Their Mechanical Properties. *Journal of polymer research* **2009**, *16*, 45–54.
- (15) Rocco, C.; Karasu, F.; Croutxé-Barghorn, C.; Allonas, X.; Lecompère, M.; Riess, G.; Zhang, Y.; Esteves, A. C. C.; van der Ven, L. G. J.; van Benthem, R. A. T. M.; et al. Highly-Interpenetrated and Phase-Separated UV-Cured Interpenetrating Methacrylate–Epoxy Polymer Networks: Influence of the Composition on Properties and Microstructure. *Materials Today Communications* **2016**, *6*, 17–27.
- (16) Ajiboye, G.; Jessop, J. L. P. Synergistic Effect of Hydroxyl-Containing Acrylates in Epoxide-Acrylate Hybrid Photopolymerizations; **2012**; pp 1–6.
- (17) Ge, X.; Ye, Q.; Song, L.; Misra, A.; Spencer, P. Visible-Light Initiated Free-Radical/Cationic Ring-Opening Hybrid Photopolymerization of Methacrylate/Epoxy: Polymerization Kinetics, Crosslinking Structure, and Dynamic Mechanical Properties. *Macromol. Chem. Phys.* **2015**, *216* (8), 856–872.
- (18) Crivello, J. V.; Liu, S. Photoinitiated Cationic Polymerization of Epoxy Alcohol Monomers. *Journal of Polymer Science Part A* **2000**, *38* (3), 389–401.
- (19) Bednarek, M.; Kubisa, P.; Penczek, S. Coexistence of Activated Monomer and Active Chain End Mechanisms in Cationic Copolymerization of Tetrahydrofuran with Ethylene Oxide. *Macromol. Symp.* **1999**, *32* (16), 5257–5263.
- (20) Ghosh, N. N.; Palmese, G. R. Electron-Beam Curing of Epoxy Resins: Effect of Alcohols on Cationic Polymerization. *Bull Mater Sci* **2005**, *28* (6), 603–607.
- (21) Biedron, T.; Kubisa, P.; Szymanski, R.; Penczek, S. Kinetics of Polymerization by Activated Monomer Mechanism. *Makromol. Chem. Macromol. Symp.* **1990**, *32*, 155–168.
- (22) Dillman, B.; Schissel, S.; Jessop, J. L. P. Epoxide-Acrylate Hybrid Photopolymers: Formation of Grafted Polymer Networks. In *Photopolymer Science and Applications*; Allonas, X., Ed.; Wiley, **2014**.

- (23) Socrates, G. G. *Infrared and Raman Characteristic Group Frequencies: Tables and Charts*, 3rd ed.; John Wiley & Sons, LTD: Chichester, **2001**.
- (24) Kubisa, P.; Bednarek, M.; Biedron, T.; Biela, T.; Penczek, S. Progress in Activated Monomer Polymerization. Kinetics of AM Polymerization. *Macromol. Symp.* **2000**, *153*, 217–226.
- (25) Dillman, B.; Jessop, J. L. P. Chain Transfer Agents in Cationic Photopolymerization of a Bis-Cycloaliphatic Epoxide Monomer: Kinetic and Physical Property Effects. *Journal of Polymer Science Part A* **2013**, *51* (9), 2058–2067.
- (26) Odian, G. *Principles of Polymerization*, 4 ed.; John Wiley and Sons, Inc., **2004**.
- (27) Kilambi, H.; Stansbury, J. W.; Bowman, C. N. Deconvoluting the Impact of Intermolecular and Intramolecular Interactions on the Polymerization Kinetics of Ultrarapid Mono(Meth)Acrylates. *Macromol. Symp.* **2007**, *40* (1), 47–54.
- (28) Lee, T. Y.; Roper, T. M.; Jonsson, E. S.; Guymon, C. A.; Hoyle, C. E. Influence of Hydrogen Bonding on Photopolymerization Rate of Hydroxyalkyl Acrylates. *Macromol. Symp.* **2004**, *37* (10), 3659–3665.
- (29) Tuft, B. W.; Xu, L.; Hangartner, A.; White, S.; Hansen, M.; Guymon, C. A. Photopolymerized Patterning and Materials to Enhance Neural Prosthetic Performance; **2014**.
- (30) Eom, H. S.; Jessop, J. L. P.; Scranton, A. B. Photoinitiated Cationic Copolymerizations: Effects of the Oligomer Structure and Composition. *Polymer* **2013**, *54*, 4134–4142.
- (31) Vidil, T.; Tournilhac, F. Supramolecular Control of Propagation in Cationic Polymerization of Room Temperature Curable Epoxy Compositions. *Macromol. Symp.* **2013**, *46* (23), 9240–9248.
- (32) *Monomers Product Guide*; **2011**; pp 1–20.
- (33) Menard, K. P. *Dynamic Mechanical Analysis: a Practical Introduction*, 2nd ed.; CRC Press: Boca Raton, FL, **2008**.

CHAPTER 7

CONTROLLING CATIONIC SHADOW CURE USING PHYSICAL CUES AND PROCESSING VARIABLES

7.1 Introduction

Photopolymerization holds many key advantages over its more traditional thermal counterpart, including improved spatial and temporal control, reduced energy consumption, and reduced use (or elimination) of environmentally harmful organic solvents.¹⁻⁴ Yet, photopolymerization remains a technique largely relegated to thin (< 1mm) film, coating, ink, and adhesive applications due to its need for light.⁵ While advantageous when polymerizing nano-scale features, light attenuation, governed by the Beer-Lambert law, greatly limits the film thickness to which photopolymerization can be applied. In addition to physically thick systems, photopolymerization is also hindered by optically thick systems, such as translucent or opaque films. Limiting optical thickness limits the addition or concentration of pigments, dyes, and fillers; the latter of which is often used to improve or tune polymer properties. Complex geometries, in which areas of the coating are effectively masked from the illuminated light source or do not receive equal exposure, also are traditionally poor applications for photopolymerization; however, exploitation and control of cationic polymerization's long-lived active centers may allow for photopolymerization to be used effectively in light-restricted applications.

Although poor light penetration is problematic in terms of initiation, the termination mechanism can also play a significant role in limiting photopolymerization to thin films and coatings. In free-radical polymerization, because nature prefers balance, free-radical active centers are attracted to one another, and termination occurs either when two free radicals form a covalent bond (termination by combination) or when that balance is achieved through the donation of a hydrogen atom (termination by disproportionation).² This attraction between free-radical active centers causes termination to occur rapidly, to the extent that it is assumed the moment the initiating light source is removed, the entire polymerization reaction ceases because no new active centers are generated, and all existing active centers are instantaneously terminated.

In contrast to free-radical photopolymerization, cationic photopolymerization rarely participates in chain termination because the cationic active centers repel each

other.^{6,7} Without termination, these long-lived cationic active centers can continue to propagate hours, days, or even weeks after the initiating light is removed. This continued polymerization in the absence of a light source is called post-polymerization or *dark cure*.^{5,8,9} In addition, these active centers possess mobility through reactive diffusion and may lead to polymerization in regions of the coating or film never exposed to light; a process termed *shadow cure*. Shadow cure, especially, has great potential to succeed in light-limited applications where free-radical photopolymerization fails, thus providing new opportunities for photopolymerization.

Investigation of cationic photopolymerization has been cursory in comparison to free-radical photopolymerization due, in part, to the relatively recent discovery of onium salt cationic photoinitiators and to free-radical polymerization's overwhelming majority of the industrial photopolymerization market.¹ Of this research, only a few studies refer to cationic shadow cure.^{5,9} The purpose of this study is to explore the potential of photo-initiated cationic shadow cure by determining how cationic active centers respond to physical cues and processing variables. Molds of various shapes were used to qualitatively test active center mobility in different geometries. A central composite design (CCD) was used to ascertain the impact of effective irradiance, exposure time, exposure area, sample depth, and their interactions on the distance active centers can travel and the amount of cross-linked polymer mass produced.

7.2 Experimental

7.2.1 Materials

The cationic dicycloaliphatic epoxide monomer 3,4-epoxy-cyclohexylmethanyl 3,4-epoxycyclohexane carboxylate (EEC, Sigma Aldrich, Figure 7-1) was chosen for its industrial relevance and high reactivity. The photoacid generator 4-(2-hydroxyl-1-tetradecyloxy)-phenyl] phenyliodonium hexafluoroantimonate (DAI, trade name PC-2506, Polyset), was used to initiate the cationic ring-opening polymerization of EEC.

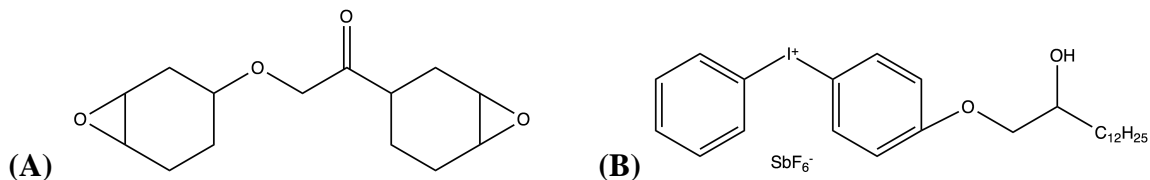


Figure 7-1. Monomer (EEC, A) and photoinitiator (DAI, B) used in this study.

7.2.2 Methods

Molds

Molds were created using polydimethylsiloxane (PDMS, Alumilite Quick Set RTV Silicone Rubber) and were allowed to set for at least 24 hours before first use. PDMS was chosen as a mold material for several reasons. It has an inert surface chemistry, which prevents bonding between the newly formed polymer and the mold, avoids favorable or adverse influence on the polymerization reaction, and allows for easy removal of the polymer sample. The flexibility PDMS provides also eases sample removal and mold cleaning, allowing for repeated use. Additionally, the PDMS used in these studies has been shown to be a very poor transmitter of light, which ensures the shadow cure reported is the result of active center diffusion (see Appendix C).

Different geometries of mold wells were made to explore the active center diffusion during shadow cure (Figures 7-2, 7-6, 7-8, and 7-10). The dimensions of these wells are summarized in Table 7-1. For both the L- and t-shaped molds, the width dimension is reported as the channel width, not the width of the entire shape. The dimensions of the crevice mold are reported for the side well and the crevice, respectively.

Table 7-1. The different geometries of mold wells used and their dimensions (in mm).

	Length	Width	Diameter	Depth
Circle			25	11
Star			25	5
Rectangle	40	10		Various
L-shaped	30	10		6
t- shaped	40	10		6
Crack	25	2		36
Crevice	10 / 63	20		14 / 2

Photopolymerizations

All shadow cure samples referenced in this work contained 0.5 wt% DAI and were initiated using an Omnicure S1000 mercury arc lamp (Excelitas, 250-450 nm band pass filter) with an adjustable collimating lens attachment (Lumen Dynamics, Model No. 810-00041). The distance between the collimating lens and the sample surface was set at 20 cm to ensure a consistent irradiance profile over the entire exposure area. The effective irradiance was measured by a radiometer (Versaprobe Pro, Con-Trol Cure). The size of the exposure area was controlled using a photomask, and all samples were irradiated at the surface (Figure 7-2). Both illumination and shadow cure occurred at ambient temperature (~21°C).

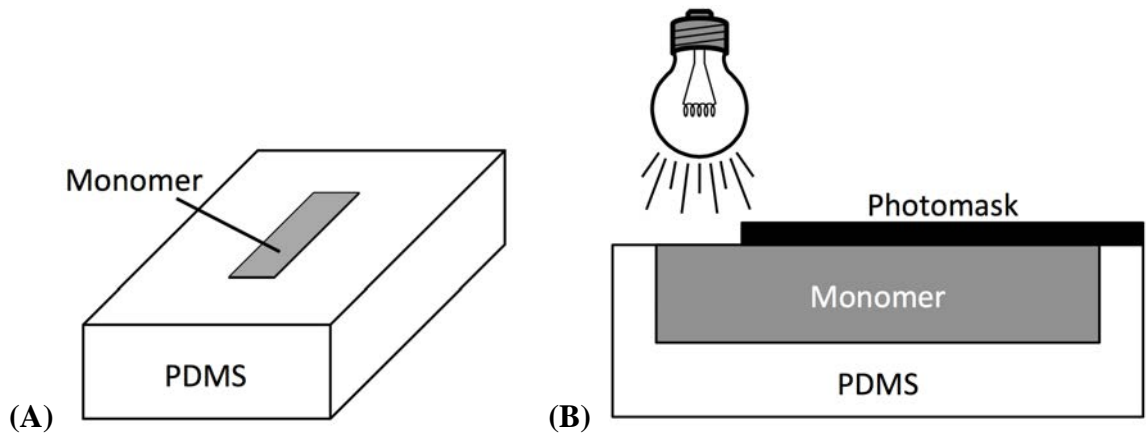


Figure 7-2. Unmasked, 3-D schematic of a rectangular mold (A), and a photomasked, cutaway of the same rectangular mold (B).

Sacrificial Trials

Samples were made in a rectangular mold with a depth of 9 mm and were initiated using 30 mW/cm^2 delivered over an exposure area of 0.5 cm^2 . These samples were removed from the molds after a set length of time, ranging from 4 hours to 2 weeks, and observations were made as to the extent each sample shadow cured. For 3 of the samples (48 hrs, 72 hrs, and 2 wks post-illumination), aliquots of the remaining liquid resin were removed from three sample locations (Figure 7-3): at the surface of the mold well, approximately 1.75 cm from the edge of the light-cured section; at the liquid-solid interface at near the bottom of the mold well, approximately 1.75 cm from the edge of the light-cured section; and from the pocket of liquid directly beneath the light-cured section.

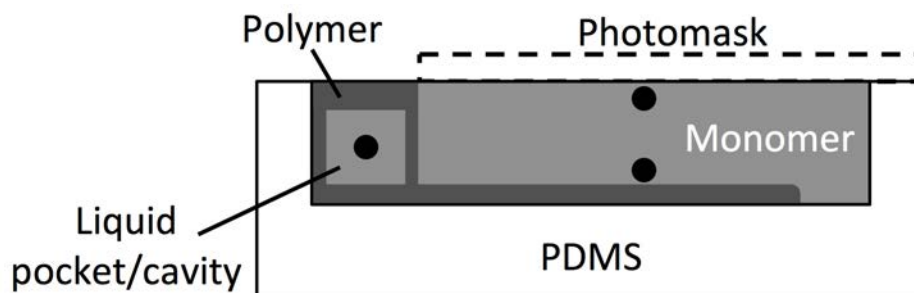


Figure 7-3. Cutaway of a rectangular mold, post-illumination. Aliquots of liquid resin were collected from the three locations labeled with a black circle.

The surface aliquot was collected first, then that from the bottom of the mold. To avoid contamination, the polymer piece was removed from the mold, lightly dried, and then the polymer enclosure was broken open and the third aliquot collected. Three aliquots were collected from each location. Each aliquot was placed in a 1-mm ID quartz capillary tube, where conversion was measured using Raman spectroscopy.

Raman spectra were collected using a holographic probehead (Mark II, Kaiser Optical Systems, Inc.) equipped with a single-mode excitation fiber, 785-nm near-infrared laser, and a 10x non-contact sampling objective. The probehead was connected to a modular research Raman spectrograph (HoloLab 5000R, Kaiser Optical Systems, Inc.). Three spectra were gathered for each sample with an exposure time of 1 second and 3 accumulations. Laser power was recorded at $\sim 220 \text{ mW}$.

The epoxide conversion (α) was calculated from the collected Raman spectra using Equation 7-1:

$$\alpha = \left(1 - \frac{I_{rxn}(P)/I_{ref}(P)}{I_{rxn}(M)/I_{ref}(M)} \right) * 100 \quad (7-1)$$

where $I_{rxn}(M)$ and $I_{rxn}(P)$ are the peak intensities of the reactive band for the monomer and polymer, respectively. Similarly, $I_{ref}(M)$ and $I_{ref}(P)$ are the peak intensities of the reference band for the monomer and polymer, respectively. The reactive band, representing the epoxide ring, is located at 790 cm^{-1} , and the reference band, representative of the $-\text{CH}_2-$ vibration, is located at 1445 cm^{-1} .¹⁰

Complex Geometry Experiments

The samples cured in the circle- and star-shaped molds were both initiated at the center of the surface with a 6 mm-diameter, circular exposure area. The L-shaped mold sample had an exposure area of 0.5 cm^2 . Both the sample in the t-shaped mold and the sample in the crevice mold had an exposure area of 1 cm^2 . The effective irradiance was 30 mW/cm^2 and the exposure time was 5 minutes for all samples.

Central Composite Design

In an effort to control and predict shadow cure, a central composite design (CCD) was constructed using the software Design Expert® (Version 9.0.6.2, State-Ease, Inc.). A CCD is a design constructed on the principles of design of experiments (DOE), which strategically adjusts the levels of the experiment variables (factors) in order to reduce the number of samples needed to effectively demonstrate how these variables, and their interactions, influence measurable outcomes (responses) over the tested variable range (design space). A CCD was chosen because of its ability to include multiple factors and factor interactions for five levels.

The factors varied in the design were effective irradiance, exposure area (area of the sample exposed to UV light), exposure time, and sample depth (Table 7-2). Preliminary studies have shown these factors to be important in controlling shadow cure (see Appendix C). The design space was also chosen based on the results of preliminary

work. Effective irradiance, for example, was varied from 10 to 100 mW/cm² because the length of shadow cure was seen to increase, achieve a maximum, and decrease within that range (all other factors held constant).

Table 7-2. Coded factor levels for the four factors used in the central composite design.

Factor Level:	-2	-1	0	+1	+2
Eff. Irradiance (mW/cm ²)	10	32.5	55	77.5	100
Sample Depth (mm)	3	4.5	6	7.5	9
Exposure Time (min)	1	3.25	5.5	7.75	10
Exposure Area (cm ²)	0.3	0.4	0.5	0.6	0.7

In order to account for the different ranges for each factor in the design, coded space is used (Table 7-2). All factors have the same range in coded space. Additionally, coded space allows factors to be weighed equally in the design. For example, an exposure area of 0.7 cm² is as influential to the design as effective irradiance of 100 mW/cm², because both are assigned a coded value of +2. In a five level CCD, the coded space ranges from -2 to +2.

The CCD was calculated using 30 samples, 6 of which were replicates of the center point (all factors set to coded level 0) used to estimate the experimental error. Samples were stored in the mold in the dark for 6 days before being removed for testing. Extra checkpoint samples, cured using variable values within the design space, were made to check the validity of the design (see Appendix C). These samples were not included in the calculation of the design, but rather the design was used to predict the responses of these samples. Then the predicted and experimental values were compared. All samples, including checkpoint samples, were polymerized over the same 6-day period to reduce any variation as a result of humidity fluctuations in the lab.

Two responses were measured for the design: shadow cure length and gel fraction. The first response is defined as the length of solid polymer, formed along the bottom of the mold, past the exposure area. Thus, the vertical lengths of shadow cure along the mold walls, the length of shadow cure extending from the light-cured section along the surface, nor the length of shadow cure formed at the bottom of the mold in the

exposure area are not included in this measurement. The length was measured using a digital micrometer.

The second response, the gel fraction, was measured by first collecting the mass of the initial monomer sample. After the six days of shadow cure, the residual monomer was removed from the sample. The sample was covered in tetrahydrofuran (THF) for 24 hours to dissolve the remaining monomer. The THF solution was filtered through grade 1 filter paper (Whatman) to separate the gel fraction, which was further rinsed with clean THF. The gel fraction was then placed in the oven at 80°C for an hour to evaporate any remaining solvent, weighed, and then compared to the initial sample mass in Equation 7-2.

$$Gel\ Fraction = \left(\frac{Crosslinked\ Mass\ (g)}{Sample\ Mass\ (g)} \right) * 100 \quad (7-2)$$

7.3 Results and Discussion

This study investigated the effect of physical cues and processing variables on the cationic shadow cure active center mobility. Qualitative tracking of the cationic active centers was investigated using a sacrificial time study. Molds of complex geometries, including corners, angles, and crevices, were used to determine the active centers' response to physical cues. A central composite design was used to model the influence of effective irradiance, exposure time, exposure area, sample depth, and their interactions on shadow cure length and gel fraction.

7.3.1 Active Center Mobility

Sacrificial Study

A sacrificial study was completed to track the growth of shadow cure over time. Samples were removed from rectangular molds 4, 8, 12, 24, 36, 48 and 72 hours post-illumination to assess the extent of observable shadow cure. One sample was also removed 2 weeks post-illumination. Previous work by Ficek, *et al.* examined shadow cure growth in a similar manner; however, samples were illuminated from the bottom, through a clear cuvette, in which active center diffusion and shadow cure growth was

strictly vertical.⁵ In contrast, the work presented here is surface-illuminated and shadow cure growth occurred both vertically and laterally. These changes in experimental set-up result in substantially different growth profiles and give new insight into active center mobility.

Immediately post-illumination (0 hrs), only a thin film (~ 0.3 mm) of polymer was formed on the sample surface in the area exposed to the initiating light (Figure 7-4, A). The polymer edge flanking the photomask is well defined, which indicates light was effectively blocked at that juncture and did not penetrate beneath the photomask. There is also no noticeable increase in viscosity in the resin beneath this light-cured section, suggesting little to no polymer formed.

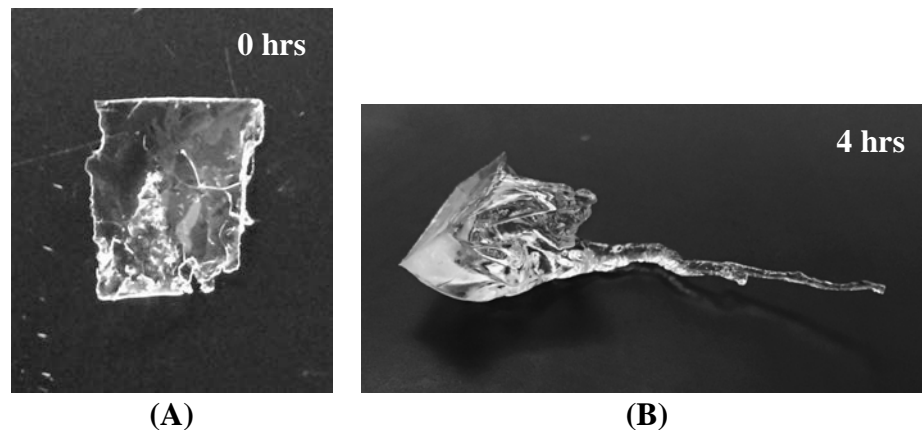


Figure 7-4. The polymer formed immediately post-illumination (0 hrs) is approximately 10 mm x 5 mm x 0.3 mm (A). After four hours, significant shadow cure has occurred (B). Maximum thickness and length of the polymer piece are 9 mm and 28 mm, respectively.

After 4 hours, significant shadow cure has taken place (Figure 7-4, B). At the surface, shadow cure has extended the thickness and length of the light cured section by ~ 1 mm and ~ 4 mm, respectively. Beneath the light-cured section, polymer has formed along the walls and the bottom of the mold; however, a pocket of liquid resin still remains between the light-cured section and the polymer at the bottom of the mold (Figure 7-3). The polymer formed at the bottom of the mold continues for ~28 mm past the light exposure area. This polymer has a very low conversion, most likely <20%, based on its physical properties. EEC forms a solid at as little as 20-25% conversion, but the polymer

formed along the bottom of the mold is only a semi-solid, viscous liquid after 4 hours of shadow cure. The majority of this section was not structurally sound enough to remove from the mold. Above this bottom piece of shadow cure, the resin remains liquid, again with no noticeable difference in viscosity.

Surprisingly, there is very little difference in shadow cure growth between 4 and 8 hours post-illumination. The length of shadow cure along the bottom of the mold has not grown, nor has the liquid resin in the cavity beneath the light-cured section become solid polymer. The most noticeable change over these four hours is the increase in conversion in the shadow-cure areas formed in the first four hours. Although still quite flexible, the bottom length of shadow cure was more easily removed from the mold (Figure 7-5, A and B).

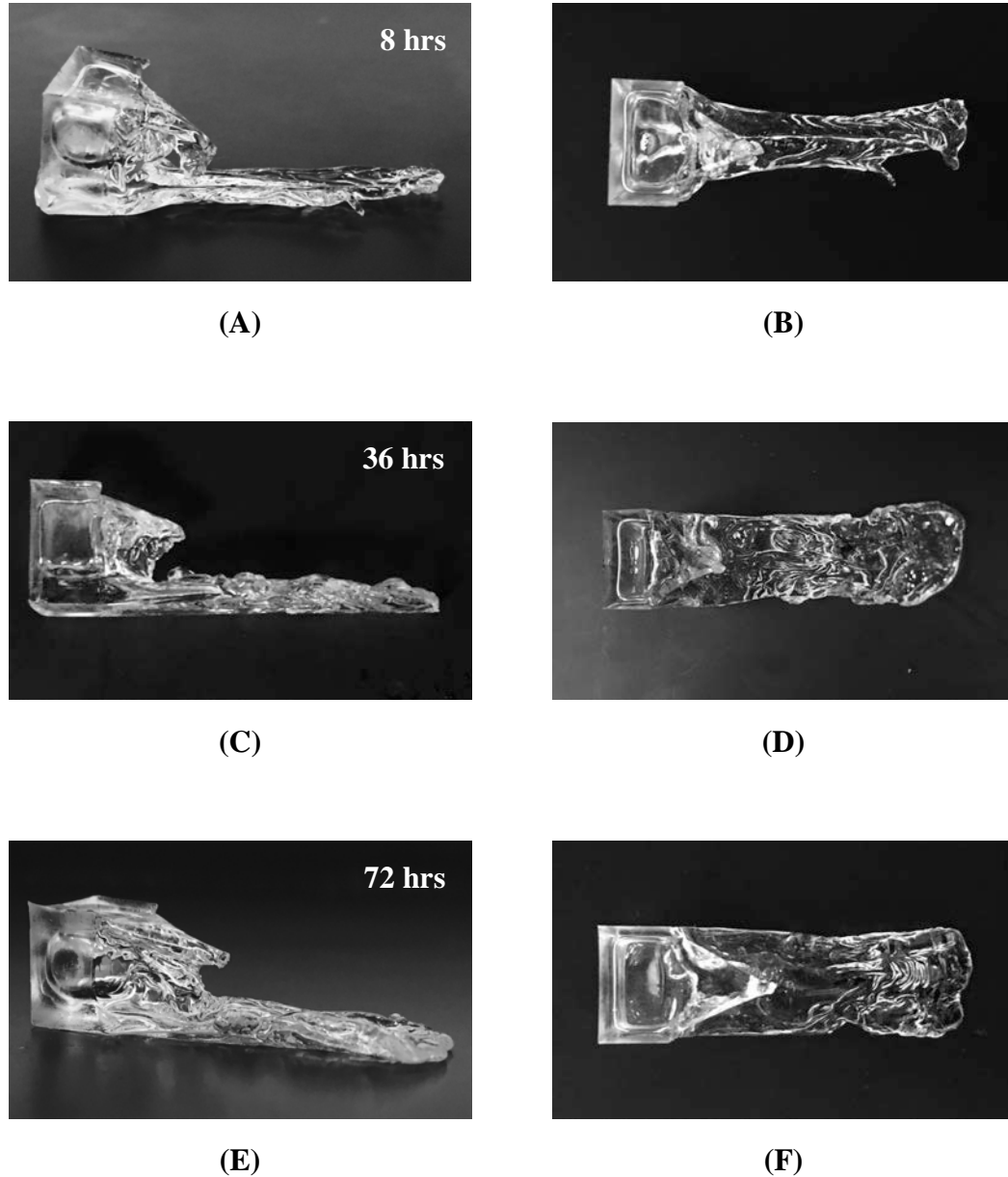


Figure 7-5. Polymer formed 8 hrs [(A) and (B)], 36 hrs [(C) and (D)], and 72 hrs [(E) and (F)] post-illumination. Shadow cure length remains constant during this time, however, conversion along the mold bottom increases noticeably between 8 and 36 hours. Shadow cure growth is seen laterally from the light-cured section, increasing by ~ 3 mm over 64 hrs. The cavity formed beneath the light-cured section does not diminish.

Similarly, samples examined at 12 to 72 hours post-illumination show almost no shadow-cure growth, only hardening of the solid polymer produced in the first 4 hours, suggesting increased conversion in those areas (Figure 7-5, C-F). The one area that does experience shadow cure growth during this time is beneath the polymer edge, at the

juncture of the light-exposed area and the photomask. Here, the shadow cure forms a vertical wall between the edge of the light-cured section on the surface and the shadow cure growth along the bottom of the mold. No visible increase in polymerization takes place directly below the light-cured section during this time interval, so the formation of this shadow-cure wall seals in the pocket of liquid resin.

Attempts were made to measure conversion of the shadow cure polymer using Raman spectroscopy with limited success. Because the shadow polymerization takes place over hours/days, there is ample time for monomer to diffuse into the polymer matrix, which skews conversion values. Additionally, the surface of the shadow cure is quite coarse and irregular, which increases light scattering and makes spectral collection difficult. However, conversion of the remaining liquid resin was measured to determine if low levels of polymerization had taken place outside the areas where solid polymer had formed. Samples of the liquid resin were collected from three locations: at the surface of the mold well; at the liquid-solid interface at near the bottom of the mold well; and from the pocket of liquid directly beneath the light-cured section (Figure 7-3). Of these locations, the resin beneath the light-cured section was found to have the highest conversion, increasing from ~5 % to ~13 % conversion over 12 days. (Table 7-3). Considering the initial rate of active center diffusion and propagation in the first 8 hours post-illumination, this minimal conversion increase suggests only a small number of active centers are present. Conversion of the liquid resin collected from the surface and the bottom of the mold is < 3% and does not increase over the 2-week time period.

Table 7-3. Conversion (%), measured by Raman spectroscopy, of the remaining liquid resin from three locations after 48 hrs, 72 hrs, and 2 wks of shadow cure. Only the conversion of the liquid resin in the cavity beneath the light-cured section (LCS) increases.

	48 hrs	72 hrs	2 wks
Surface	1.8 ± 0.4	0.6 ± 0.3	2.4 ± 0.4
Bottom	2.0 ± 0.5	0.6 ± 0.4	2.8 ± 1.2
Beneath LCS	5.6 ± 1.3	4.0 ± 1.2	12.6 ± 1.2

Although the cationic active centers were not directly tracked, aspects of their mobility can be inferred from the shape of the resulting polymers. For example, it is

likely the solid polymer of the light-cured section restricts the movement of the active centers, since the cavity between the light-cured section and the bottom polymer section remains liquid resin. Active center movement at the edges of the light-cured section appears less restricted, because considerable polymer growth occurs along the walls of the mold and at the photomask edge. Because no strands of solid polymer, directly beneath the light-exposure area, connect the light-cured section and the bottom polymer section, active centers must have either diffused downward from the light-cure section before their propagating tails became entangled to continue polymerization along the bottom of the mold or simply continued the polymerization front laterally after reaching the bottom of the mold wall. Since no appreciable propagation occurs in the liquid-resin regions that remain after the initial shadow cure formation during the first four hours, with the exception of the pocket beneath the light-cured section, it can be assumed the vast majority of active centers are contained within the polymer matrix, and that either gravity, mechanical entanglement, or a combination of the two restrict these active centers.

7.3.2 Complex Geometries

Other molds of various shapes, including circle-, star-, t-, and L-shaped molds, were used to further investigate active center mobility (Figure 7-6). These more complex shapes demonstrate that active centers can be directed using physical cues. They do not simply propagate in a path of least resistance, but follow the mold walls around corners and curves. Active centers also diffuse fairly symmetrically.

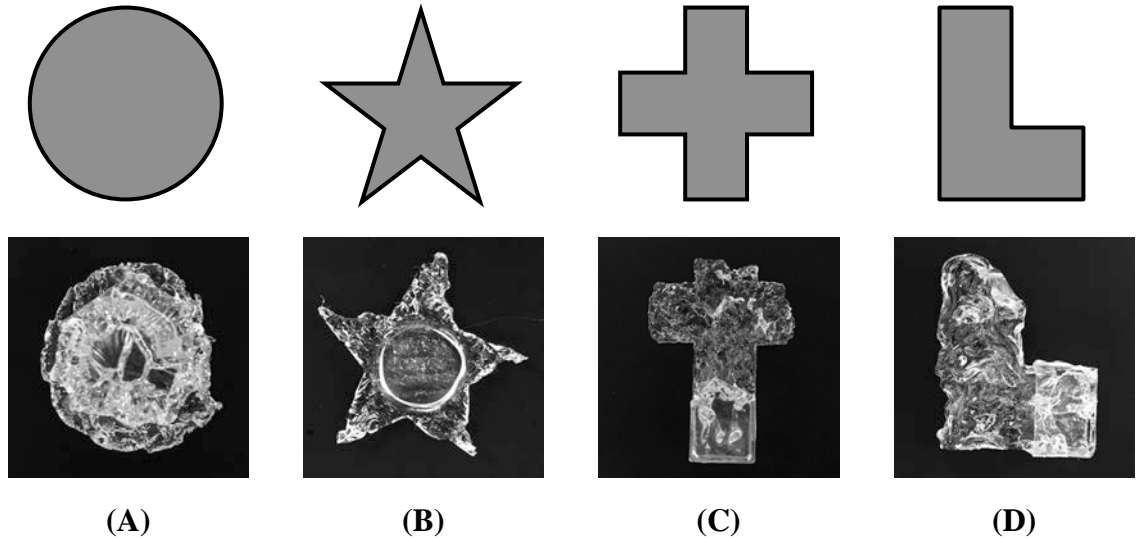


Figure 7-6. Shape of the mold well (above) and the resulting shadow-cured polymer (below). Examples (A) and (B) were initiated using a circular exposure area (0.28 cm^2) in the middle of the sample. Examples (C) and (D) were initiated using a 1 cm^2 area at the end of the mold well.

Furthermore, examination of the shadow cure produced in the circular mold reaffirms the theories of active center mobility that were established during inspection of the sacrificial samples polymerized in the rectangular mold. As observed in the sacrificial samples, no polymer is produced directly beneath the light-cured section except at the sample bottom (Figure 7-7). The strands of polymer connecting the surface cure to the polymer produced at the bottom of the mold all originate from surface cure outside of the light-cured section.

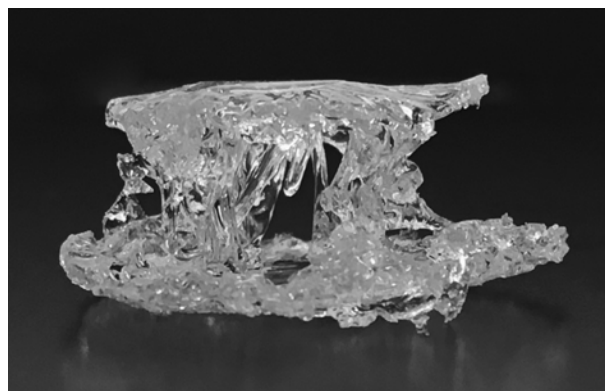


Figure 7-7. Side view of a shadow-cure polymer made in circular mold, initiated at the surface center. Although polymer strands connect surface and bottom cure, no polymer strands were produced directly beneath the light-cured section.

In addition, because the light-exposure area was located in the center of the circular mold, active center mobility was not influenced by the mold walls, as was the case for the rectangular molds. Lateral propagation, across the sample surface, radiates out from the light-cured section in all directions for 3 to 7 mm.

7.3.3 Crack and Crevice Molds

One of the intended applications of shadow cure is to photopolymerize in light-restricted areas, such as cracks and crevices, where traditional free-radical photopolymerization fails. To this end, attempts were made to polymerize in a PDMS mold designed to simulate a crack (Figure 7-8).

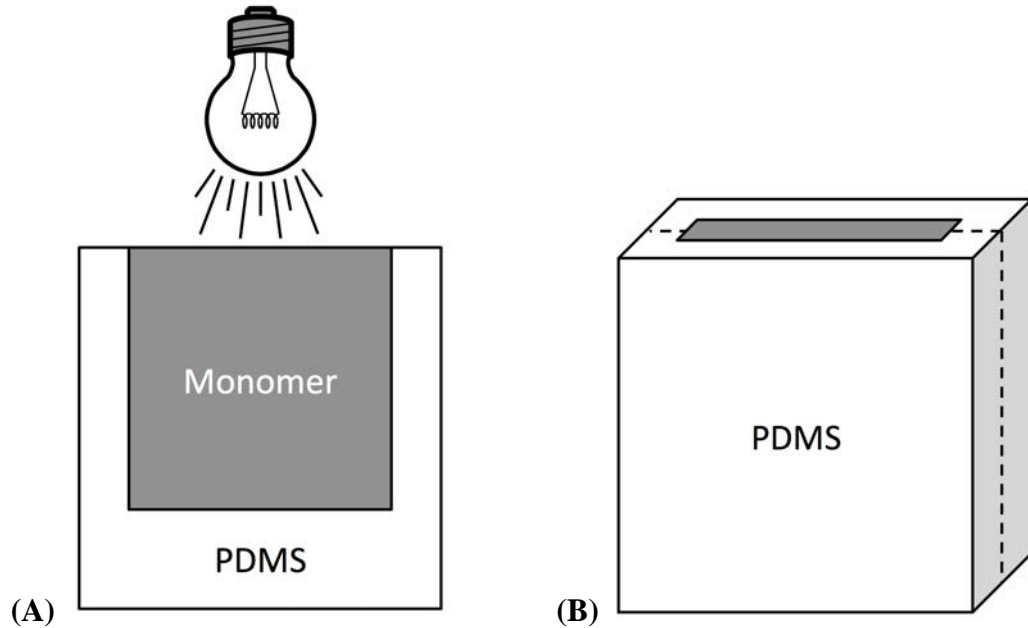


Figure 7-8. Schematics of one half of the crack mold (A) and of the two halves of the mold conjoined (B). The mold is shown at a 90° incline.

However, despite changing the effective irradiance and the incline angle of the mold (20°, 45°, and 90°, the light source was angled to match the mold), the crack was never fully polymerized. Large fractions of monomer remained, and the shadow cure growth that did occur was less than expected based on experiments performed in other mold geometries

(Figure 7-9). Moreover, even though the width was only 2 mm, a region of uncured resin was still found directly beneath the light-cured section.

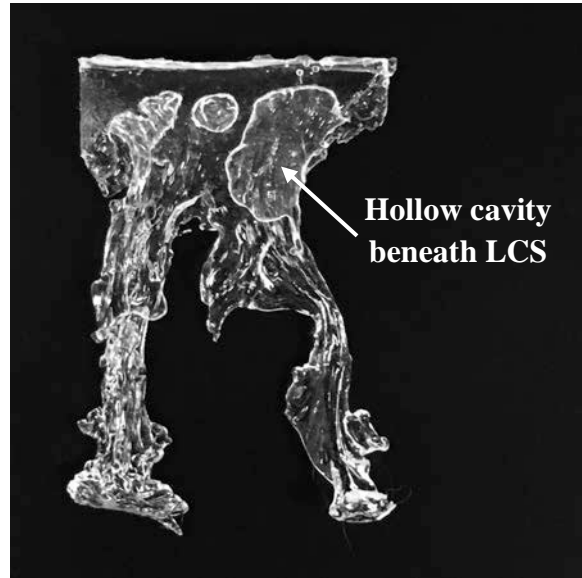


Figure 7-9. Shadow-cure sample polymerized at a 90° angle in the crack mold. Some uncured liquid resin was left in the sample to better illustrate the hollow cavity beneath the light-cured section (LCS).

These results further illustrate the restrictions the light-cured section imposes on the system's active centers. No photomasks were used in these experiments; thus, the entire sample surface was light-cured. Additionally, shadow cure growth could only occur vertically as no space was allowed for lateral growth. In comparison to the results demonstrated in other geometries, it is not surprising limited shadow cure was observed due to the entrapment of the majority of active centers in the light-cured section.

To overcome this limitation, a new crevice mold was designed to support and exploit the natural proclivity of the active centers to propagate more effectively after descending from the light-cured section (Figure 7-10). The crevice mold makes use of a monomer well, which allows for this active center descent before diffusion into the crack/crevice.

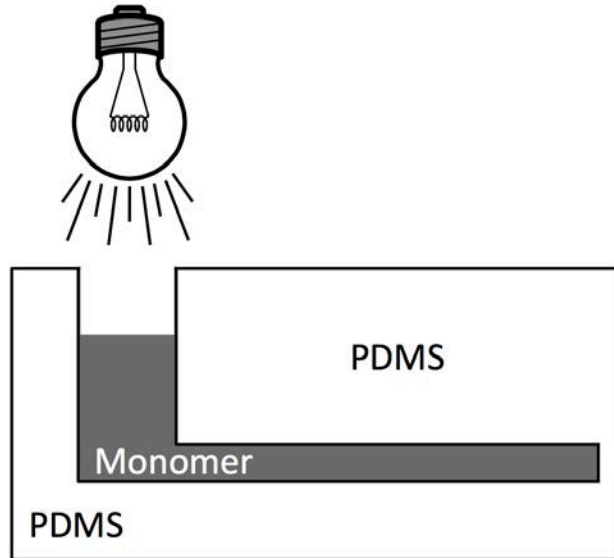


Figure 7-10. Cutaway of the crevice mold. A monomer well (left) was added to facilitate improved shadow-cure growth in the crevice.

The crevice mold produces a sample similarly shaped to one produced in the rectangular mold (Figure 7-11), but it conserves monomer and demonstrates that the cationic active centers are not hindered by confined areas (here, crevice depth is 2 mm).

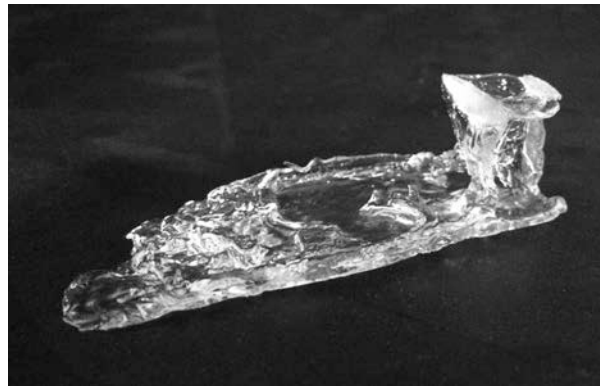


Figure 7-11. Shadow-cure polymer made in the crevice mold. Significant shadow-cure growth was achieved in the crevice (48 mm) by incorporating a monomer well at the end of the crevice.

Using this mold geometry, a 48 mm length of shadow cure was achieved, measuring from the beginning of the crevice. Furthermore, the shadow-cured polymer formed in the crevice filled the thickness and breadth of the space better than in the crack mold. Only

in the far reaches of the crevice, where the shadow cure had reached its maximum distance, was liquid resin found.

7.3.4 Central Composite Design (CCD)

One important aspect of characterizing shadow cure is determining the factors, and possible factor interactions, that influence its growth. Here, a statistical analysis is applied to determine the relative impact of each factor and factor interaction through the use of a central composite design. For each response, the CCD produces a model equation. This equation can be used to predict that response for a given set of variable conditions, but, more importantly, the model equation can be used to produce a response surface – a visual representation of the model that depicts factor influences and enables better observation of response trends. In addition, because the variables in the model equation are in coded space, the magnitude of the coefficients associated with each variable or interaction is representative of the relative importance of that variable/interaction, allowing for straightforward recognition of key factors.

The CCD was used to model two responses: shadow cure length and gel fraction. The shadow cure length response was chosen because of its relevance to active center mobility and measures how far the active centers were able to travel. Understanding which factors promote active center mobility should provide insight as to the fundamental nature of the polymerization reaction. Also, maximizing shadow cure length is relevant to the expected applications of shadow cure, such as polymerizing in cracks and crevices. Simply recording the shadow cure length, however, fails to account for differences in how effective the active centers are in developing the polymer network. To this end, the second response, gel fraction, was included in the study.

Shadow Cure Length

The relationship between the four factors and the first response, shadow cure length, determined was best fit to a two-factor interaction (2FI) model, defined by the equation,

Shadow Cure Length

$$= 21.71 + 0.36(I) + 2.32(D) + 1.20(T) + 0.14(A) - 2.01(ID) \quad (7-3) \\ + 0.97(IT) - 0.19(IA) - 1.80(DT) - 0.62(DA) - 0.85(TA)$$

where I is effective irradiance, D is sample depth, T is exposure time, and A is exposure area. The statistical significance of the model and its factors were determined using the analysis of variance (ANOVA) technique, which employs the Fisher statistical test (F-test). The model has an F-value of 6.33. An F-value of that magnitude translates to a 0.03% chance that the model is a result of noise. Variables and interactions that have a statistically significant effect on the response include: D , T , ID , and DT (see Appendix C). To be statistically significant, the probability that the magnitude of the F-value associated with each variable/interaction did not affect the response must be less than 5%.

With a coefficient of 2.32, sample depth (D) is the most influential factor in determining shadow cure length, closely followed by the interaction of effective irradiance and sample depth (ID , Equation 7-3). Recalling earlier theories of active center movement (Section 7.3.1), the influence of sample depth and its presence in three of the four statistically significant variables is not surprising. Increasing sample depth increases the distance from the restrictive light-cured section before the active center is forced to turn and propagate lengthwise along the mold bottom. The longer the distance, the longer the polymer chain that tethers the active center, and with length comes increased flexibility. The importance the model credits sample depth also supports the theory that active centers, assisted by gravity and reaction diffusion, simply drop from the light-cured section untethered, to form the section of shadow cure along the mold bottom. In this case, increased depth would give active centers at the bottom of the mold more time to propagate out from beneath the light-cured section before being hampered by the polymer formation descending from the light-cured section.

Exposure area (A) is the only factor that is not statistically significant and also not represented in a statistically significant interaction for the shadow cure length response. The lack of statistical significance, as well as the small coefficients associated with the factor and its interactions, suggests shadow cure length is only minimally affected by exposure area (Equation 7-3). This result is contradictory to the established knowledge that, within reason, increasing the energy delivered to the system increases

polymerization by increasing the active center concentration.⁶ A range of 0.3 cm² to 0.7 cm² was tested in the design space, indicating that even doubling the energy delivered to a sample (constant effective irradiance and exposure time) does not affect shadow cure length. However, consider the implications to increasing the length of the light-cured section. Based on the growth pattern, it appears most of the active centers that produce shadow cure propagate from the edges of the light-cured section because it is heavily cross-linked. Increasing the exposure area from 0.3 cm² to 0.7 cm² (130% increase) only increases the perimeter from 0.26 cm to 0.34 cm (30% increase). While still considerable, the active center concentration increase would be greatly reduced if diffusion only occurs at the perimeter. Additionally, because the measurement of shadow cure length does not account for increases elsewhere in the sample, any increase in active center concentration could be contributing to polymer growth in other areas. This result does not well support the theory of untethered active centers diffusing from the light-cured section early in the reaction. In that case, a change in the exposure area would be expected to have the same effect as with a typical photopolymer system.

Better visualization of variable influence on shadow cure length is accomplished by response surfaces. Figure 7-12 shows, to maximize shadow cure length, exposure area should be decreased and exposure time increased to the edges of the design space. Additionally, larger exposure areas (≥ 0 [coded value], *i.e.* ≥ 0.5 cm² [actual value]) are shown to have little impact, and exposure time can be varied with less consequence. Exposure time becomes more important as exposure area is minimized. Based on these trends, exploring the influence of exposure area over a wider value range might increase the likelihood of it being recognized as a statistically significant factor.

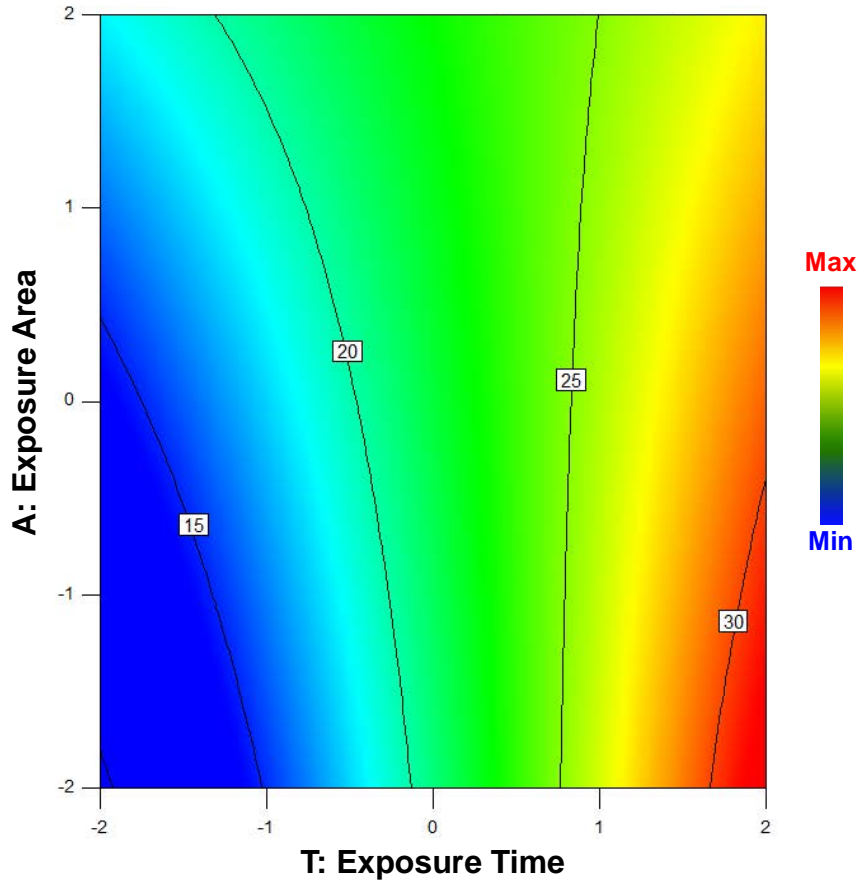


Figure 7-12. Response surface depicting the influence of exposure area and exposure time on shadow cure length. Effective irradiance and sample depth were held constant at coded values of 1 and -0.95, respectively. Shadow cure length is maximized by decreasing exposure area and increasing exposure time.

Contrastingly, the response surface in Figure 7-13 illustrates the strong influence of both sample depth and effective irradiance. Though difficult to discern from its small coefficient in the response equation, the response surface shows effective irradiance is, in fact, an important factor due to its interaction with sample depth. At greater values of sample depth (≥ 1 , *i.e.* ≥ 7.5 mm), effective irradiance must be minimized in order to maximize shadow cure length; yet, as sample depth is decreased, the opposite trend is true: effective irradiance must be increased to increase shadow cure length. Decreasing effective irradiance would decrease the initial light cure in the system by reducing the rate of initiation and therefore the active center concentration upon which the rate of propagation is dependent (Equations 1-2 and 1-8). Reducing the initial light cure would

potentially make it less restrictive to active center diffusion, thus the trend illustrated at increased sample depths supports the theories noted above. Increasing effective irradiance at shallow sample depths, however, lies counter to the above theories. Though perhaps when the mobility of the active centers is compromised, shadow cure length can be accomplished by drastically increasing active center concentration to increase the probability of some fraction diffusing out of the light-cured section. Note, when sample depth is at a coded value of -2 (3 mm), no change in shadow cure length is predicted until the effective irradiance is ≥ 0.5 ($\sim 66 \text{ mW/cm}^2$), suggesting a large concentration of active centers is needed to overcome the restrictions imposed by a shallow sample depth.

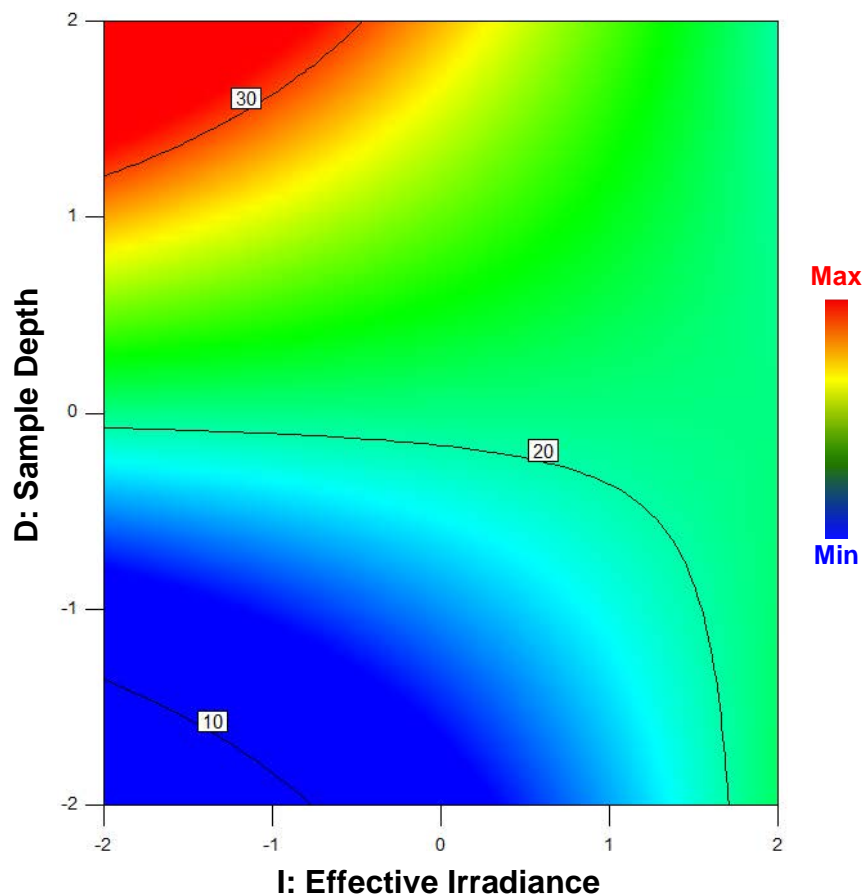


Figure 7-13. Response surface depicting the influence of sample depth and effective irradiance on shadow cure length. Exposure time and exposure area were held constant at coded values of -0.51 and -0.84, respectively. Shadow cure length is maximized by increasing sample depth while decreasing effective irradiance.

Gel Fraction

The relationship between the four factors and the second response, gel fraction, was best fit to a linear model, defined by the equation,

$$\text{Gel Fraction} = 18.80 + 3.12(I) - 0.36(D) + 2.45(T) + 2.51(A) \quad (7-4)$$

where I is effective irradiance, D is sample depth, T is exposure time, and A is exposure area. The model has an F-value of 21.02. An F-value of that magnitude translates to a < 0.01% chance that the model is a result of noise. All variables were found to have a statistically significant effect on the response with the exception of sample depth (see Appendix C).

As would be expected in a photopolymerization reaction under illumination, effective irradiance, exposure time, and exposure area all influence the gel fraction fairly equally, as displayed by their respective coefficients in Equation 7-4. Additionally, increasing all three of these factors across the design space increases the gel fraction (Figures 7-14 and 7-15). Sample depth, the most influential factor in the shadow cure length response, has almost no effect on the gel fraction response (Figure 7-15). In fact, the only consistent guideline that will increase both the gel fraction and shadow cure length responses is to maximize the exposure time. For the other three factors, those that must be minimized to increase shadow cure length must be maximized to increase the gel fraction and vice versa. Likely these opposing trends are a result of the polymer surrounding the light-cured section. Increasing the amount of polymer created in this region increases the gel fraction while also decreasing the lateral diffusion of the active centers needed for shadow cure length.

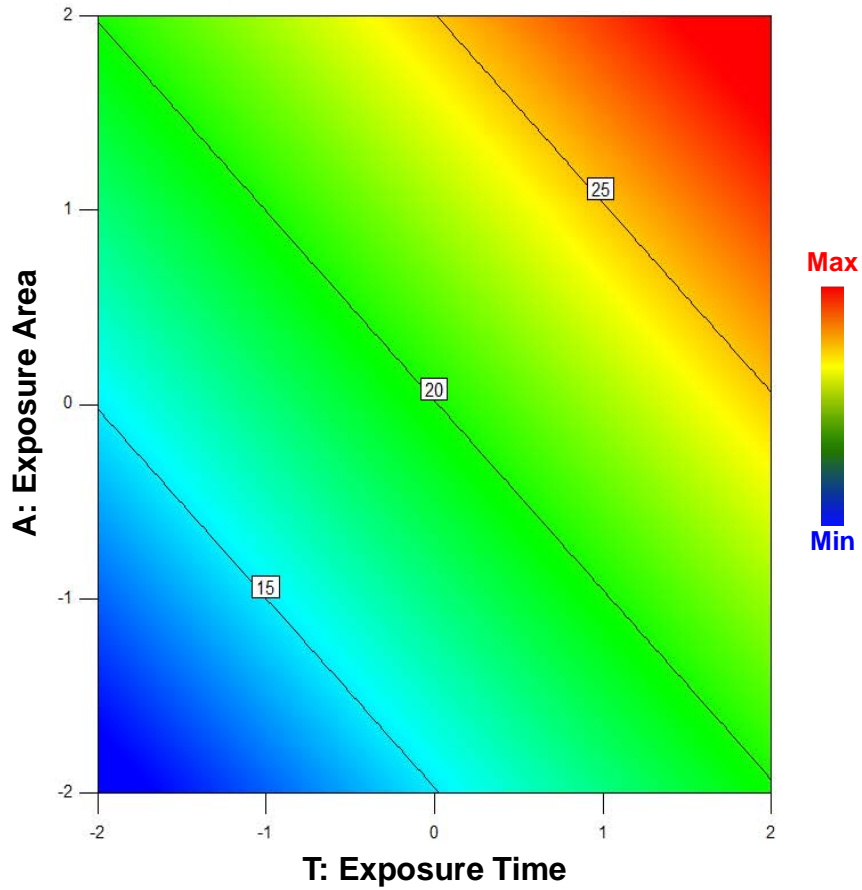


Figure 7-14. Response surface depicting the influence of exposure area and exposure time on gel fraction. Effective irradiance and sample depth were held constant at coded values of 0.49 and 1, respectively. The gel fraction is maximized by increasing both exposure area and exposure time.

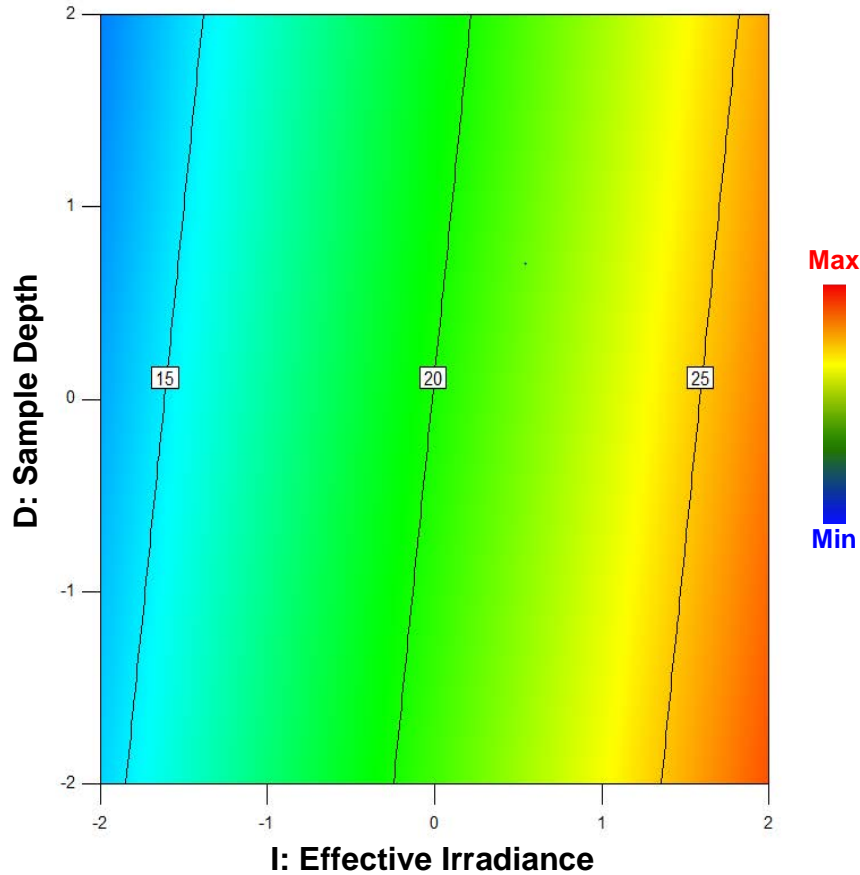


Figure 7-15. Response surface depicting the influence of sample depth and effective irradiance on gel fraction. Exposure time and exposure area were held constant at coded values of 0.59 and -0.08, respectively. The gel fraction is maximized by decreasing sample depth and increasing effective irradiance.

Qualitative observations of the gel fraction after separation from the sol fraction continue to point to the restrictiveness of the light-cured section. The gel fraction of each sample was found to contain two distinct forms of cross-linked polymer: a highly cross-linked section and more loosely cross-linked fragments (Figure 7-16). The highly cross-linked section of each gel fraction was identified as the light-cured section of each sample with additional shadow cure growth; whereas, the more loosely cross-linked fragments made up the remainder of the shadow cure growth, which was more distant from the light-cured section. Each light-cured section (with proximal shadow cure) is so highly cross-linked, in comparison to the other recovered portion of the gel fraction, that it retains its shape, the growth that occurred along the mold sides remains smooth, and it

appears as though no sol fraction was removed (Figure 7-16, inserts). In contrast, the gel fraction of the shadow-cure growth more distant from the light-cured section retains no shape, is made of numerous small domains, and is stiff but compressible, not unlike spun sugar.

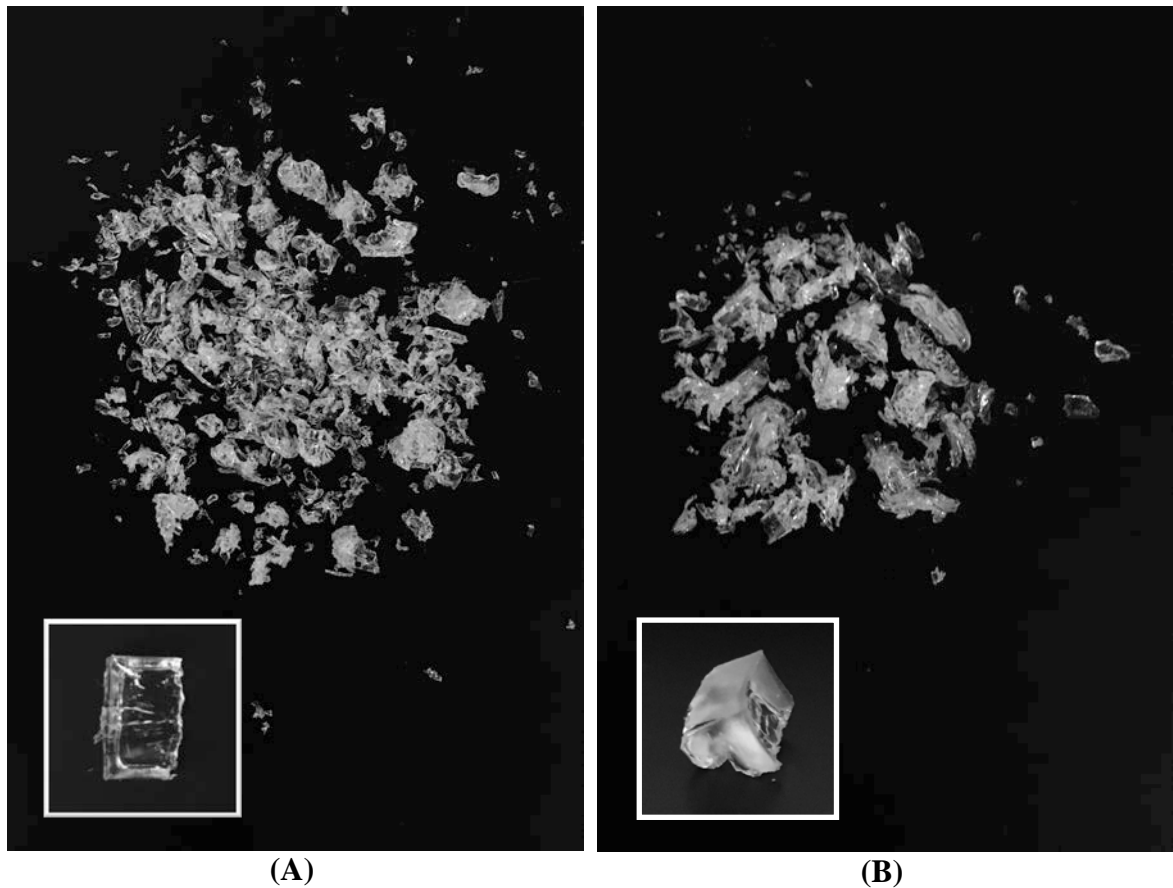


Figure 7-16. Gel fractions of two shadow-cured samples. Although the shadow-cure regions are made up of many small, cross-linked domains, each light-cured section and the shadow-cure formed in close proximity (inserts) remains completely intact after the sol fraction is removed, suggesting they are each one highly cross-linked domain. As this highly cross-linked domain increases in size, the lower cross-linked shadow-cure domains decrease.

In Figure 7-16, it is evident that the dense network of the light-cured section restricts shadow cure length. Sample A was cured with an effective irradiance of 55 mW/cm² for 5.5 minutes in a 9-mm deep mold with a 0.5 cm² exposure area. The thickness of the highly cross-linked section varies from 1.5 mm to 4 mm. Sample B was

cured with an effective irradiance of 92 mW/cm² for 5 minutes in a 7.5-mm deep mold with a 0.6 cm² exposure area. The thickness of its highly cross-linked section ranges from 3 mm to 7 mm. The effect of such a thick, dense network is clearly seen on the more loosely cross-linked domain: that of Sample B is less than that of Sample A. Moreover, it is this second (loosely) cross-linked network that comprises the shadow cure length; thus, Sample A's larger portion indicates it has a greater shadow cure length – 31.1 mm compared to Sample B's 18.7 mm. Note, the mold lengths were the same for both samples, providing equal opportunity for the shadow cure to grow.

Model Accuracy

To confirm the trends illustrated by the model, the model's accuracy was verified using 10 checkpoint (CP) samples (Table 7-4, see Appendix C for experimental conditions). These samples were external to the model, and their experimentally determined shadow cure length and gel fraction were compared to those predicted by the model.

Table 7-4. Model accuracy of the CCD was verified using ten checkpoints external to the model. The model accurately predicts gel fraction, but is only moderately accurate in predicting shadow cure length. Standard deviation of the shadow cure length response is 2.24. Standard deviation of the gel fraction response is 0.03.

	Shadow Cure Length (mm)				Gel Fraction			
	Exp.	Pred.	% Error	Within Std. Dev.	Exp.	Pred.	% Error	Within Std. Dev.
CP 1	23.4	20.3	13.2		0.21	0.19	9.5	✓
CP 2	13.2	12.0	9.1	✓	0.12	0.14	14.2	✓
CP 3	18.7	20.5	8.8	✓	0.11	0.26	57.7	
CP 4	24.4	22.1	9.4		0.24	0.23	4.2	✓
CP 5	16.6	17.6	5.7	✓	0.19	0.18	5.3	✓
CP 6	16.8	21.9	23.3		0.20	0.19	5.0	✓
CP 7	18.9	20.4	7.4	✓	0.16	0.16	0	✓
CP 8	18.7	21.9	14.6		0.22	0.21	4.5	✓
CP 9	14.0	38.3	63.4		0.02	0.05	40.0	✓
CP 10	15.6	17.7	11.9	✓	0.19	0.18	5.3	✓

For shadow cure length, the predicted values of 5 of the 10 checkpoint samples were within the 2.24 mm standard deviation of their corresponding experimental values. If the

standard deviation were extended to 3.2 mm, 8 of the 10 samples would fall within the standard deviation. Overall, it is believed that the model adequately predicts shadow cure length, but that the heterogeneity of the network most likely increases the error. Additionally, an important unknown factor not included in the model may account for discrepancies between the predicted and experimental values. The model more accurately predicted the gel fraction of the checkpoint samples. Nine of the 10 samples were within the standard deviation of 0.03.

The model was also rerun including only those variables and interactions considered statistically significant, as well as variables needed to maintain hierarchy. For example, effective irradiance (I) was determined to be insignificant for shadow cure length, however one of its interactions (ID) is significant, and so the variable is included. Reducing the model to statistically significant variables was done in an attempt to improve the accuracy of the model, especially in predicting shadow cure length; however, the new model demonstrated no improvement. Only half of the checkpoint samples still fell within the standard deviation for shadow cure length, although the new model changed which checkpoint samples were in acceptable agreement. Gel fraction predictions fared worse with the new model, with only 8 of 10 samples falling within the standard deviation.

7.4 Conclusions

EEC has significant shadow cure growth in both vertical and lateral directions. The majority of cationic active center diffusion takes place within the first 4 hours, with increasing conversion thereafter. The light-cured section restricts growth, with minimal conversion in a cavity directly beneath it even after 2 weeks post-illumination. Shadow cure responds to physical cues, growing symmetrically around angles and corners. Moreover, shadow cure can propagate in restricted areas, such as cracks and crevices; however, allowing the active centers to first diffuse vertically downward, then laterally into the crevice improved the length and thickness of the resulting cured polymer.

The central composite design, used to ascertain trends and interactions of processing variables, modeled the shadow cure length response as a two-factor interaction model and the gel fraction response as a linear model. Shadow cure length was found to

be highly dependent on the sample depth, while the gel fraction was largely independent of the sample depth variable. The design further predicts that shadow cure length is maximized with increasing sample depth and decreasing effective irradiance, exposure area, and exposure time. In contrast, the gel fraction is maximized with decreasing the sample depth and increasing the other three variables. Checkpoint samples, external to the design, confirmed that the shadow cure length model was moderately predictive, with 5 of 10 samples falling within the standard deviation. The gel fraction model fared better, correctly predicting 9 of 10 checkpoint samples within the standard deviation.

These findings can be used to enhance understanding of active center mobility in cationic systems, and to encourage and control shadow cure growth. Ultimately, providing a fundamental framework for cationic shadow cure will expand the possibilities of using photopolymerization in light-restricted applications.

7.5 References

- (1) Fouassier, J.-P. *Photoinitiation, Photopolymerization, and Photocuring: Fundamentals and Applications*; Hanser/Gardner Publication Inc.: Cincinnati, **1995**.
- (2) Koleske, J. V. *Radiation Curing of Coatings*; West Conshohocken, Penn.: ASTM ; Bethesda, MD : Radtech International, North America, **2002**.
- (3) Decker, C. The Use of UV Irradiation in Polymerization. *Polym. Int.* **1998**, *45* (2), 133–141.
- (4) Chatani, S.; Kloxin, C. J.; Bowman, C. N. The Power of Light in Polymer Science: Photochemical Processes to Manipulate Polymer Formation, Structure, and Properties. *Polym. Chem.* **2014**, *5* (7), 2187–2201.
- (5) Ficek, B. A.; Thiesen, A. M.; Scranton, A. B. Cationic Photopolymerizations of Thick Polymer Systems: Active Center Lifetime and Mobility. *European Polymer Journal* **2008**, *44* (1), 98–105.
- (6) Odian, G. *Principles of Polymerization*, 4 ed.; John Wiley and Sons, Inc., **2004**.
- (7) Brazel, C. S.; Rosen, S. L. *Fundamental Principles of Polymeric Materials*, 3rd ed.; Hoboken, NJ, **2012**; pp 1–427.
- (8) Sipani, V.; Kirsch, A.; Scranton, A. B. Dark Cure Studies of Cationic Photopolymerizations of Epoxides: Characterization of Kinetic Rate Constants at High Conversions. *J. Polym. Sci. A Polym. Chem.* **2004**, *42* (17), 4409–4416.
- (9) Hoppe, C.; Ficek, B. A.; Eom, H. S.; Scranton, A. B. Cationic Photopolymerization of Epoxides Containing Carbon Black Nanoparticles. *Polymer* **2010**, *51* (26), 6151–6160.
- (10) Socrates, G. G. *Infrared and Raman Characteristic Group Frequencies: Tables and Charts*, 3rd ed.; John Wiley & Sons, LTD: Chichester, **2001**.

CHAPTER 8

TRANSFERABLE SHADOW CURE: A NEW APPROACH TO ACHIEVING CATIONIC PHOTOPOLYMERIZATION IN LIGHT-RESTRICTED AREAS^Y

8.1 Introduction

As shown in Chapter 7, long-lived cationic active centers are able to propagate in areas unexposed to the initiating light, or *shadow cure*. Cationic photopolymerization is best suited for applications that exploit the advantages of its dark- and shadow-cure ability, that is, applications where free-radical photopolymerization is ineffective.^{1,2} In light-rich applications, free-radical photopolymerization is favored for its fast reaction rate, reaching final conversions in seconds, whereas cationic reactions often take minutes, sometimes even hours. Yet, the high termination rate of free-radical reactions prevents significant dark or shadow cure, therefore requiring illumination throughout the full length of the reaction as well as sufficient exposure of the entire surface area and depth of the film. These requirements limit the use of free-radical photopolymerization in light-restricted areas: cracks, crevices, thick films, highly pigmented or filled coatings, complex geometries, and between opaque objects. If a feasible method of cationic shadow cure is developed, it can expand the advantages and use of photopolymerization to these areas, which have previously been inaccessible due to light penetration issues.

Through the work discussed in Chapter 7, it was established that shadow cure can be controlled through the use of processing variables as well as physical cues. Furthermore, it was shown that shadow cure can be made to grow in the confined areas of cracks and crevices; however, shadow cure growth in these spaces was best encouraged by illuminating a well of resin, external and orthogonal to the crevice. The necessity of an external well of resin is admittedly cumbersome, wasteful, and unlikely to be feasible in all but the most specialized of applications. Thus, this challenge must be overcome in order to make use of cationic photopolymerization's full potential.

In this chapter, a new method of shadow cure is described and investigated. This method, entitled *transferable shadow cure*, effectively separates the initiation and

^Y This chapter is based on the patent: Schissel, S. M., Kaalberg, S. M., Jessop, J. L. P. "Transferrable Shadow Cure Method." U.S. Patent 15141800, filed April 2016. Patent Pending.

propagation mechanisms, allowing for the active-center-containing monomer to be transferred to light-restricted areas where it polymerizes. Unlike the method presented in Chapter 7, no liquid resin remains after the reaction, and no external well is needed to polymerize in confined areas. Additionally, pigments and fillers can be added to the active-center-containing monomer.

Shadow cure kinetics were monitored using Raman spectroscopy and compared to those of light and dark cure. Dynamic mechanical analysis was used to compare the physical properties of light cure and shadow cure films. Qualitative studies were undertaken to demonstrate the effect of adding pigments and fillers to shadow cure samples. Finally, a central composite design (CCD) was completed to ascertain the effects of sample depth, effective irradiance, exposure area, and exposure time on shadow cure conversion, gel fraction, and the weight percent of the light-cured section.

8.2 Experimental

8.2.1 Materials

The cationic dicycloaliphatic epoxide monomer 3,4-epoxy-cyclohexylmethanyl 3,4-epoxycyclohexane carboxylate (EEC, Sigma Aldrich, Figure 8-1) was chosen for its industrial relevance and high reactivity. The photoacid generator 4-(2-hydroxyl-1-tetradecyloxy)-phenyl] phenyliodonium hexafluoroantimonate (DAI, trade name PC-2506, Polyset) was used to initiate the cationic ring-opening polymerization of EEC. In addition, the photoacid generator 4-isopropyl-4'-methyldiphenyliodonium tetrakis(pentafluorophenyl)borate (MTB, TCI) was used to compare the effect of the counterion size.

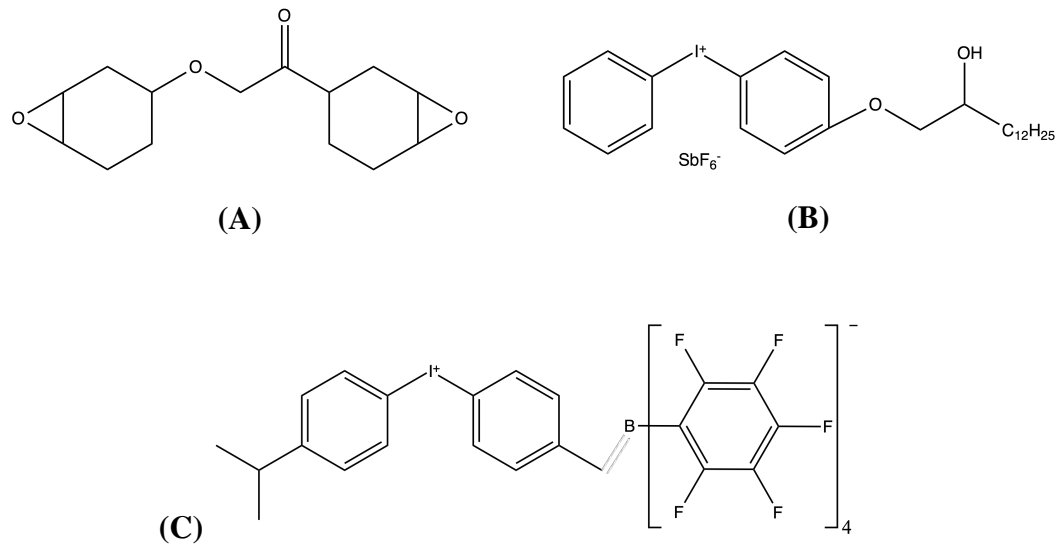


Figure 8-1. Monomer (EEC, A) and photoinitiators (DAI, B and MTB, C) used in this study.

Carbon black (Nipex® 35, Degussa) and titanium (IV) oxide (Sigma Aldrich) were used to demonstrate the effect of pigment on the polymerization. Similarly, calcium carbonate (Sigma Aldrich), barium sulfate (Sigma Aldrich), and yellow polyethylene particles (G17SE111C50-2 Extra Traffic Yellow, PolyArmor USA) were used to demonstrate the effect of fillers.

8.2.2 Methods

Molds

Molds were created using polydimethylsiloxane (PDMS, Alumilite Quick Set RTV Silicone Rubber) and were allowed to set for at least 24 hours before first use. PDMS was chosen as a mold material for several reasons. It has an inert surface chemistry, which prevents bonding between the newly formed polymer and the mold, avoids favorable or adverse influence on the polymerization reaction, and the flexibility PDMS provides also eases sample removal and mold cleaning, allowing for repeated use. Additionally, the PDMS used in these studies has been shown to be a very poor transmitter of light, which ensures the shadow cure reported is the result of active center diffusion (see Appendix C).

Note on Terminology

In this work, films produced by the transferable shadow cure method are compared to traditional photopolymerization, or *light cure*. It is recognized that these light cure films undergo dark cure, that is, further propagation post-illumination in areas exposed to the initiating light. In fact, the kinetic and physical property development that occurs over time in these films is attributed to dark cure. However, for simplicity, these films will be referred to as light-cure films and not light/dark cure films.

Photopolymerizations

All samples referenced in this work contained 0.5 wt% photoinitiator and were initiated using an Omnicure S1000 mercury arc lamp (Excelitas, 250-450 nm band pass filter) with an adjustable collimating lens attachment (Lumen Dynamics, Model No. 810-00041). The distance between the collimating lens and the sample surface was set at 20 cm to ensure a consistent irradiance profile over the entire exposure area. The effective irradiance was measured by a radiometer (Versaprobe Pro, Con-Trol Cure). The exposure area to volume ratio was controlled using a three dimensional spacer, and all samples were irradiated at the surface (Figure 8-2). Both illumination and shadow cure occurred at ambient temperature ($\sim 21^{\circ}\text{C}$). After illumination, samples were stored in the dark until characterization.

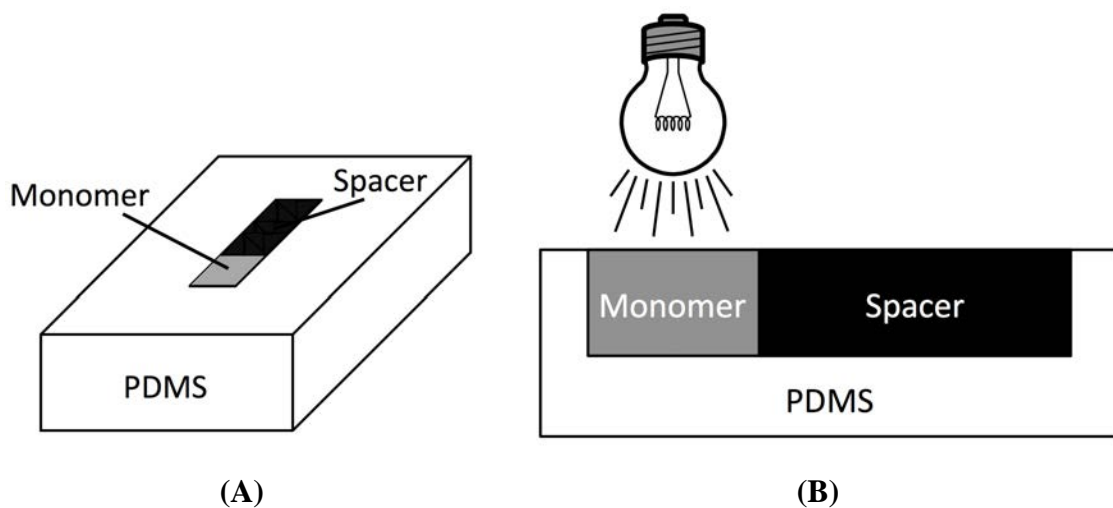
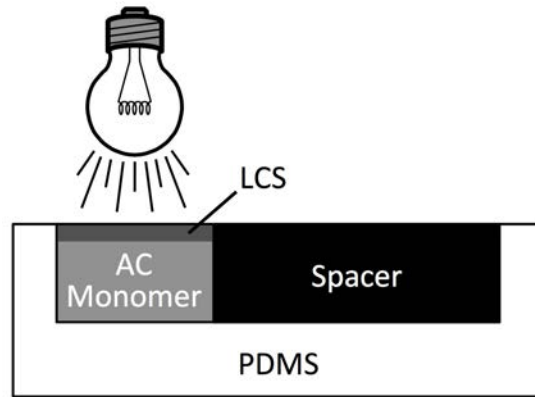


Figure 8-2. 3-D schematic of a rectangular mold with a spacer to control the monomer surface area to volume ratio (A), and a cross section of the same rectangular mold (B).

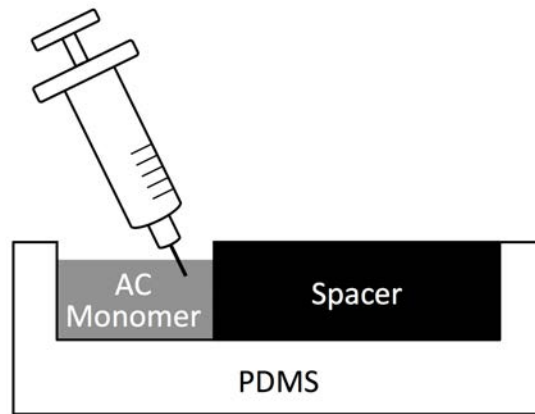
Transferable Shadow Cure Method

The transferable shadow cure method results from the recognition that the solid polymer formed during illumination on the surface of the monomer, the light-cured section (LCS, Figure 8-3), restricts active center mobility. It was repeatedly shown in Chapter 7 that minimal shadow cure occurred directly beneath the light-cured section. Therefore, after illumination, this solid polymer is removed from the surface of the monomer and discarded (Step 1, Figure 8-3). Remaining beneath the LCS is active-center-containing monomer (AC monomer). During illumination, active centers diffuse out of the LCS and into the monomer; because these active centers are not entangled in the network of the LCS, their propagating chains must be relatively short. Additionally, it is expected that some of the active centers are formed in the monomer from the reduced effective irradiance that penetrates below the depth of the LCS. Therefore, transferable shadow cure is more technically a combination of light cure, dark cure, and shadow cure, though the majority of polymerization is shadow cure. Once the AC monomer is accessible, it can be transferred, as a liquid, to wherever the polymer is wanted: mold, crevice, etc. (Step 2, Figure 8-3). If pigments or fillers are needed, they can be added to the AC monomer. By including additives post-illumination, they do not impede initiation by reducing optical clarity. Finally, the AC monomer is allowed to polymerize (Step 3, Figure 8-3).

Step 1:



Step 2:



Step 3:

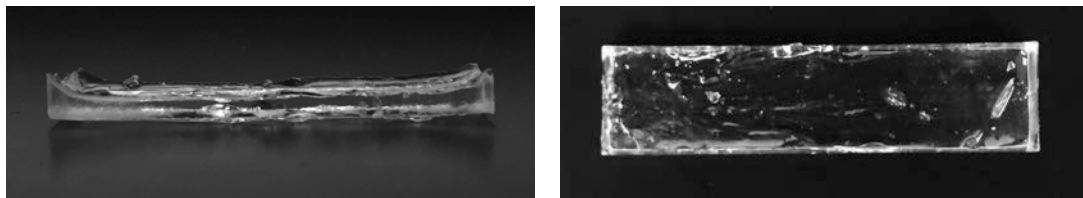


Figure 8-3. Transferable shadow cure method. Step 1: The sample is illuminated, and, post-illumination, the light-cured section (LCS) is removed. Step 2: The active-center-containing monomer (AC monomer) is transferred to the desired location. Step 3: The AC monomer is allowed to polymerize.

TSC in Complex Geometries with Pigments, and Fillers

An EEC+DAI formulation, initiated at 30 mW/cm² with a 1 cm² exposure area for 5 minutes in a 6-mm deep mold, was used for all geometry and additive investigations. The LSC was removed immediately post-illumination, and any pigments or fillers were added then to the AC monomer before transferring it. In pigment studies, ~ 1 wt% carbon black or titanium white was added to the AC monomer. Up to 10 wt% of barium sulfate and calcium carbonate were added the AC monomer when investigating fillers. In studies involving the yellow polyethylene particles, the concentration of the particles is estimated to be 3 to 5 wt%, but the particles were not weighed.

Raman Spectroscopy for Kinetic Characterization

For kinetic characterization, light cure samples were polymerized in 1-mm ID quartz capillary tubes for 5 minutes with an effective irradiance of 30 mW/cm². Transferable shadow cure samples were initiated using identical conditions in a 6-mm deep mold with a 1 cm² exposure area. The LCS section was removed immediately post-illumination, and the AC monomer was transferred to the quartz capillary tube. The first Raman spectra was collected within two minutes after illumination.

Raman spectra were collected using a holographic probehead (Mark II, Kaiser Optical Systems, Inc.) equipped with a single-mode excitation fiber, 785-nm near-infrared laser, and a 10x non-contact sampling objective. The probehead was connected to a modular research Raman spectrograph (HoloLab 5000R, Kaiser Optical Systems, Inc.). Three to five spectra were gathered for each sample with an exposure time of 1 second and 3 accumulations. Laser power was recorded at ~ 200 mW.

The epoxide conversion (α) was calculated from the collected Raman spectra using Equation 8-1:

$$\alpha = \left(1 - \frac{I_{rxn}(P)/I_{ref}(P)}{I_{rxn}(M)/I_{ref}(M)} \right) \quad (8-1)$$

where $I_{rxn}(M)$ and $I_{rxn}(P)$ are the peak intensities of the reactive band for the monomer and polymer, respectively. Similarly, $I_{ref}(M)$ and $I_{ref}(P)$ are the peak intensities of the

reference band for the monomer and polymer, respectively. The reactive band, representing the epoxide ring, is located at 790 cm^{-1} , and the reference band, representative of the $-\text{CH}_2-$ vibration, is located at 1445 cm^{-1} .^{3,4}

Reported conversion values are the average of three sample replicates. Over the extended monitoring of the samples (300 + days), some of the samples cracked or pulled away from the walls of the capillary tubes in areas, causing distortion of Raman spectra and inaccurate conversion calculations. Because of this, decreases in conversion greater than 5% from the previous data point that were also inconsistent with the other two replicates were removed from the average. Less than 10% of the conversion data was removed for this reason.

Dynamic Mechanical Analysis for Physical Property Characterization

A dynamic mechanical analyzer (DMA, Q800 TA Instruments) equipped with a film tension clamp was used to find the glass transition temperature (T_g), the full width at half maximum (FWHM) of the $\tan \delta$ peak, the maximum height of the $\tan \delta$ peak, and an estimate of the cross-link density. Films for DMA characterization were prepared by forming a mold consisting of two silanized (Rain-X® washed) glass microscope slides separated by two glass coverslips (total thickness $\sim 300\ \mu\text{m}$). The EEC+DAI formulation was injected into the mold via syringe for the light films and then exposed to initiating illumination. Transferable shadow cure films were initiated in a 6-mm deep mold, the LSC was removed immediately after illumination, and the AC monomer was transferred to the mold. The effective irradiance used to initiate both types of films was 30 mW/cm^2 for 5 minutes. After 6 days of dark storage, the films were removed from the molds and cut into 6.25 mm x 25 mm strips. A mono-frequency strain, temperature ramp sequence was used to collect $\tan \delta$ values as a function of temperature at a constant oscillating frequency of 1 Hz and a sinusoidal strain of 0.05%. Temperature was increased at a rate of 3°C/min from 0°C to 250°C on the first DMA sequence and from 0°C to 300°C on the second. The temperature ramp was repeated twice for each sample because annealing can occur at the elevated temperatures experienced in the first sequence. All property values are reported from the second DMA sequence unless otherwise noted. The polymer T_g

was taken as the maximum of the $\tan \delta$ peak. The cross-link density (ν_e) was estimated using the equation

$$\nu_e = \frac{E'}{3RT} \quad (8-2)$$

where E' is the storage modulus, R is the ideal gas constant, and T is absolute temperature. The cross-link density was calculated for the last 50 values of E' ; the reported value is an average of those densities.

Central Composite Designs

In an effort to control and predict the conversion of transferable shadow cure in an EEC+DAI system, a central composite design (CCD) was constructed using the software Design Expert® (Version 9.0.6.2, State-Ease, Inc.). A CCD is a design constructed on the principles of design of experiments (DOE), which strategically adjusts the levels of the experiment variables (factors) in order to reduce the number of samples needed to effectively demonstrate how these variables, and their interactions, influence measurable outcomes (responses) over the tested variable range (design space). A CCD was chosen because of its ability to include multiple factors and factor interactions for five levels.

The factors varied in the design were effective irradiance, exposure area (area of the sample exposed to UV light), exposure time, and sample depth (Table 8-1). Preliminary studies have shown these factors to be important in controlling shadow cure (Chapter 7). The design space was chosen to be identical to that reported in Chapter 7 to enable comparison of the two shadow cure methods.

Table 8-1. Factor levels for the four factors used in the first central composite design (CCD 1).

Factor Level:	-2	-1	0	+1	+2
Eff. Irradiance (mW/cm ²)	10	32.5	55	77.5	100
Sample Depth (mm)	3	4.5	6	7.5	9
Exposure Time (min)	1	3.25	5.5	7.75	10
Exposure Area (cm ²)	0.3	0.4	0.5	0.6	0.7

In order to account for the different ranges for each factor in the design, coded space is used (Table 8-1). All factors have the same range in coded space. Additionally, coded space allows factors to be weighed equally in the design. For example, an exposure area of 0.7 cm² is as influential to the design as effective irradiance of 100 mW/cm², because both are assigned a coded value of +2. In a five-level CCD, the coded space ranges from -2 to +2.

The CCD was calculated using 30 samples, 6 of which were replicates of the center point (all factors set to coded level 0) used to estimate the experimental error. Immediately after illumination, the LCS and the spacer were removed. The samples were left in the mold, and no intentional mixing was performed. Samples were stored in the dark for 6 days before being removed for testing. Extra checkpoint samples, cured using variable values within the design space, were made to check the validity of the design (see Appendix D). These samples were not included in the calculation of the design, but rather the design was used to predict the responses of these samples. Then the predicted and experimental values were compared. All samples, including checkpoint samples, were polymerized over the same 6-day period to reduce any variation as a result of humidity fluctuations in the lab.

Three responses were measured for the design: conversion, LCS wt%, and gel fraction. The first response is defined by Equation 8-3 and was measured using Raman spectroscopy as explained above. Instead of using a capillary tube, the solid samples were placed on an aluminum Q-panel and three spectra were collected along the length of the sample. The conversion values used in the CCD are an average of these three spectra.

The second response, LCS wt%, is defined as

$$LCS\ wt\% = \left(\frac{LCS\ Mass\ (g)}{Total\ Sample\ Mass\ (g)} \right) * 100 \quad (8-3)$$

Once removed from the surface of the sample, the LCS was gently wiped with a Kimwipe to remove excess monomer before it was weighed.

The third response, the gel fraction, was measured by first collecting the mass of the initial monomer sample. After the 6 days of shadow cure, the sample was covered in

tetrahydrofuran (THF) for 24 hours to dissolve the remaining monomer. The THF solution was filtered through grade 1 filter paper (Whatman) to separate the gel fraction, which was further rinsed with clean THF. The gel fraction was then placed in the oven at 80°C for 1 hour to evaporate any remaining solvent, weighed, and then compared to the initial sample mass in Equation 8-4.

$$Gel\ Fraction = \left(\frac{Crosslinked\ Mass\ (g)}{Sample\ Mass\ (g)} \right) * 100 \quad (8-4)$$

After determining the results for the first CCD (CCD), a second CCD (CCD 2) was constructed. CCD 2 was set up identical to CCD 1, with the exception of the design space (Table 8-2). A broader range of effective irradiances and shorter exposure times were chosen to investigate the transferable shadow cure method. In addition, the third response, gel fraction, was replaced with a second conversion collection 13 weeks post-illumination to determine whether the shadow cure kinetics could be still be predicted.

Table 8-2. Factor levels for the four factors used in the second central composite design (CCD 2).

Factor Level:	-2	-1	0	+1	+2
Eff. Irradiance (mW/cm ²)	10	50	90	130	170
Sample Depth (mm)	3	4.5	6	7.5	9
Exposure Time (s)	10	50	90	130	170
Exposure Area (cm ²)	0.3	0.4	0.5	0.6	0.7

8.3 Results and Discussion

This study investigated the kinetic and physical properties of polymers produced via transferable shadow cure using Raman spectroscopy and dynamic mechanical analysis, respectively. Qualitative experiments tested the ability to include pigments and fillers in samples produced by the transferable shadow cure method, as well as the ability to cure those samples in molds of complex geometry. Two central composite designs of different design spaces were used to model the influence of effective irradiance, exposure

time, exposure area, sample depth, and their interactions on transferable shadow cure conversion, gel fraction, and LCS wt%.

8.3.1 Kinetic Characterization

A long-term study was undertaken to compare the kinetics of the transferable shadow cure method to those of traditional light cure (and its continued dark cure). In addition, two photoacid generators, DAI and MTB, were compared to determine what effects, if any, the size of the counterion had on the polymerizations. The first data point, 0 days, was collected within 2 minutes post-illumination for both the light-cure and shadow-cure samples (Figure 8-4). Despite all solid polymer (*i.e.*, the LCS) being removed from the shadow-cure sample initially, the two polymerization methods produce fairly similar conversions: light cure ~ 10% and shadow cure ~3.5%. However, the continued propagation of the light-cured samples increases the conversion to ~35% conversion after 1 day. This dark cure further increases the conversion to 45% over the next 6 days, after which the propagation rate (slope of the line) slows considerably. In contrast, the shadow-cured samples only increase to ~10% conversion after 1 day, but continues to increase to about ~26 to 30% conversion on Day 15 before the propagation rate slows significantly. At 15 days post-illumination, the light-cure samples have ~ 15% greater conversion than the shadow-cure samples. This difference remains constant over the next 300+ days.

It was hypothesized that the counterion size may impact the kinetics, especially for the transferable shadow cure, since any trapped counterions would be removed with the LCS. Sipani estimated the anion size of DAI and MTB to be 4.25 Å and 10.25 Å, respectively.⁵ However, even with the MTB counterion 14 times more voluminous than that of DAI, little difference is seen in kinetics when the photoacid generator is switched (Figure 8-4). In the light-cure samples, the conversion never differs more than ~ 3%, with final conversions of 58 (MTB) and 55% (DAI). This difference in conversion increases to ~ 5% in the DAI- and MTB-initiated shadow-cure samples between 15 and 30 days post-illumination. Yet, the last recorded conversions are nearly identical at 41 (MTB) and 42% (DAI).

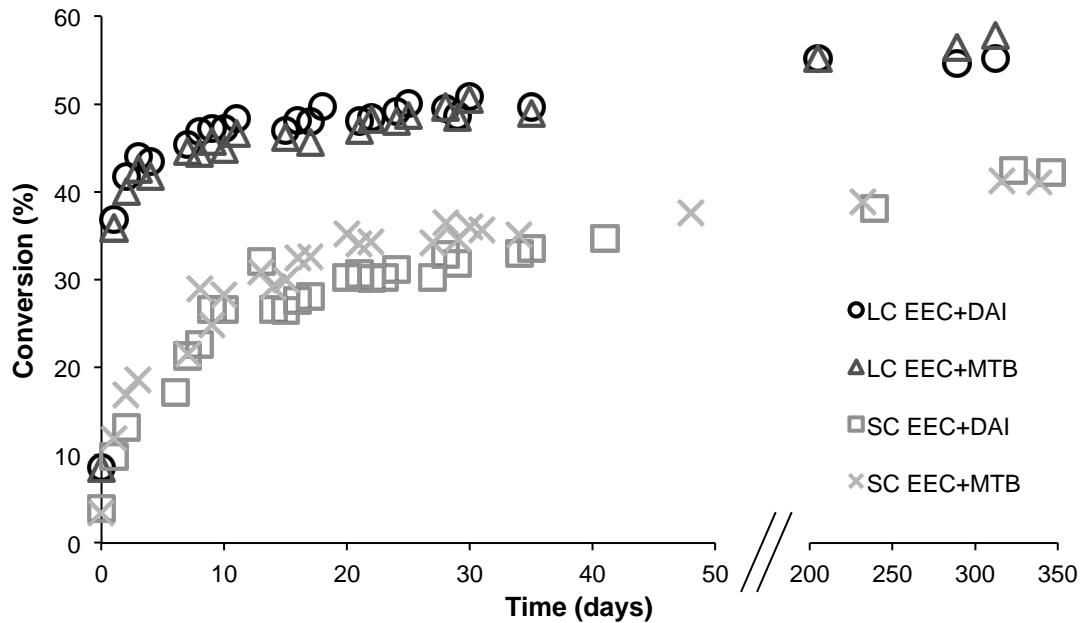


Figure 8-4. Long-term kinetic comparison between light-cure samples (LC, with continued dark cure) and shadow-cure samples (SC) of EEC with two different photoacid generators (DAI and MTB). The reactions were monitored via Raman spectroscopy. Light-cure samples maintain a higher conversion (~15%) than shadow-cure samples even after 300+ days.

Although the transferable shadow cure samples do not reach the conversion of the light-cure samples, it is impressive that they are able to reach within ~ 15% conversion despite having a majority of the active centers removed in the LSC. One reason the shadow-cure samples may be able to achieve 40% conversion with a reduced concentration of active centers is the difference in network formation between the two photopolymerization methods. Comparing the gel fractions, light-cure EEC is made of a single cross-linked domain and shadow-cure EEC is made of numerous smaller cross-linked domains (Figure 8-5). These smaller domains may have allowed for increased active center mobility.

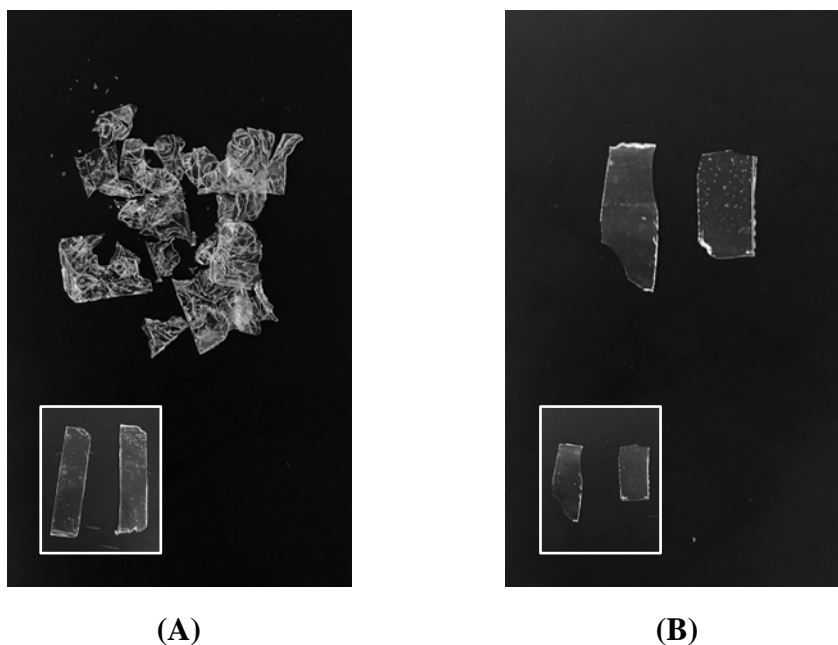
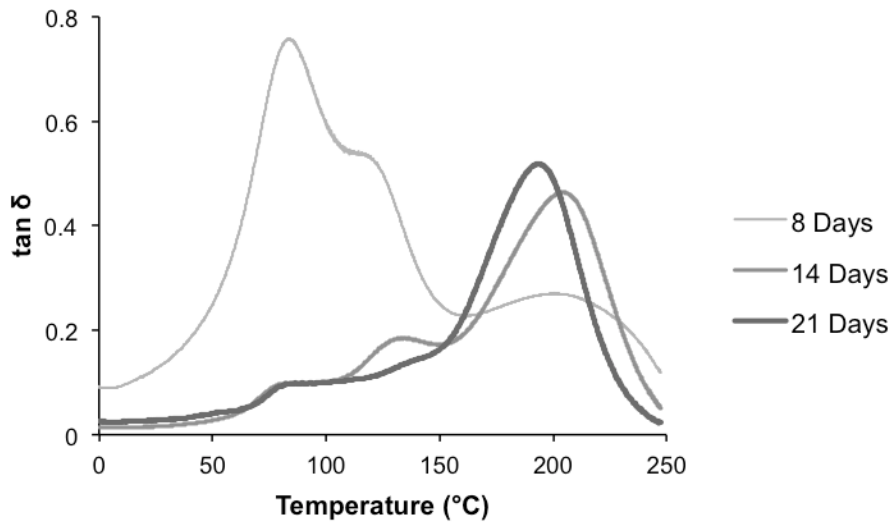


Figure 8-5. A comparison of the transferable shadow cure network (A) and light-cure network (B) of EEC after being dissolved in THF. The light cure network is a single cross-linked domain, whereas the shadow-cure network is composed of numerous smaller cross-linked domains. The inserts show the films before the sol extraction.

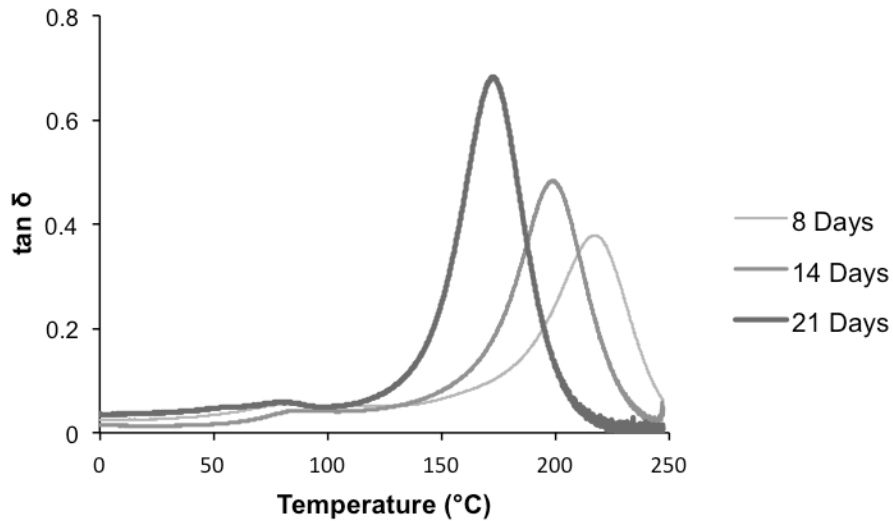
8.3.2 Physical Property Characterization

Using DMA, the impact of the kinetic and network differences on the physical properties of light- and shadow-cure EEC films was investigated over several weeks. Normally, only the $\tan \delta$ of the second temperature ramp sequence is considered, as the elevated temperatures of the first ramp can increase conversion through the increased mobility of the long-lived cationic active centers when the polymer is above its T_g . However, in comparing light and shadow cure, the $\tan \delta$ of the first temperature ramp sequence is informative. The diversity of the shadow-cure network 8 days post-illumination is evident in the double-peak $\tan \delta$ profile of this first temperature ramp (Figure 8-6.A). At later time points (14 and 21 days post-illumination), this secondary peak at $\sim 85^\circ\text{C}$ reduces to a shoulder of the primary $\tan \delta$ peak at $\sim 200^\circ\text{C}$. Although this secondary peak could be caused by the abundance of plasticizing monomer, the conversion only increases from $\sim 22\%$ at 8 days to ~ 26 and 30% conversion at 14 and 21 days, respectively (estimated from Figure 8-4). Such small conversion increases would not be expected to diminish such a prominent secondary peak; yet, even small

increases in conversion can have a large impact on the incorporation of short polymer chains, small cross-link domains, and increases in cross-link density. In contrast, the light-cure films only have a slight increase in the baseline of the $\tan \delta$ profile at $\sim 85^\circ\text{C}$, suggesting better network homogeneity (Figure 8-6.B).



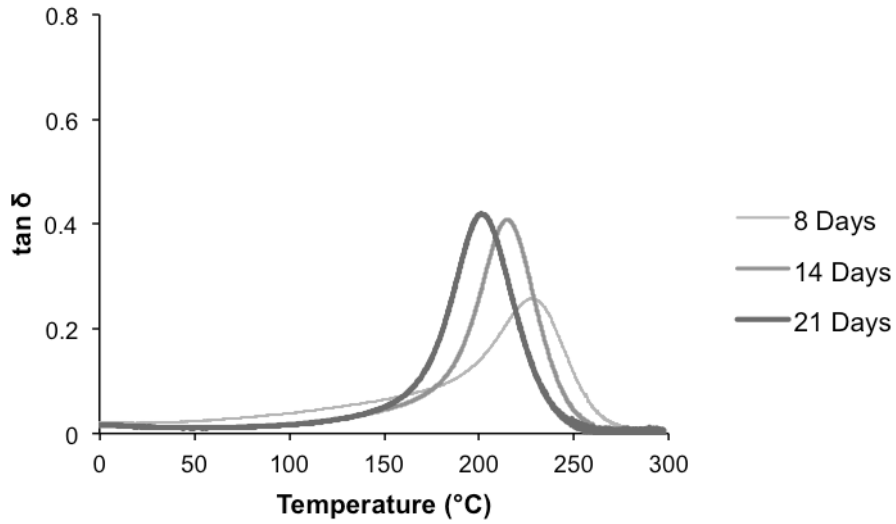
(A)



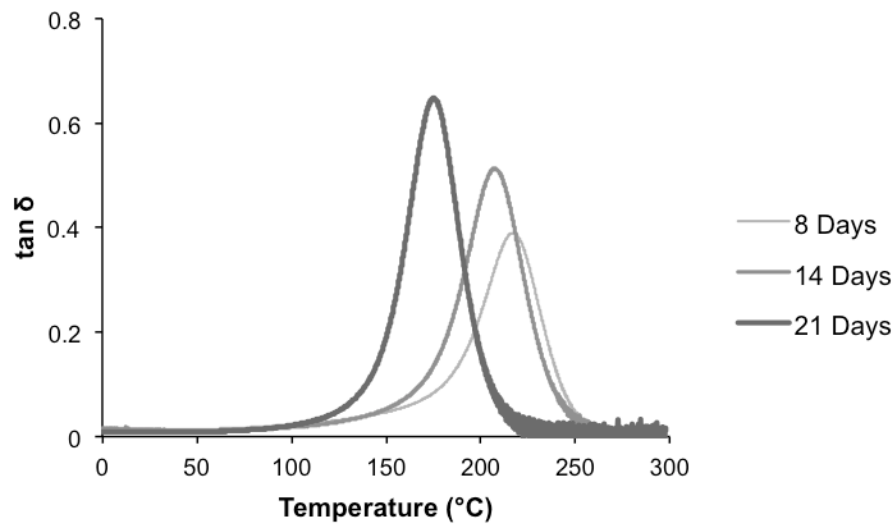
(B)

Figure 8-6. Comparison of the $\tan \delta$ curves of the first DMA temperature ramp sequence for EEC polymerized by transferable shadow cure (A) and light cure (B) at 8, 14, and 21 days post-illumination.

In both the first temperature sequence $\tan \delta$ profiles of light-cure and shadow-cure films, the maximum of the polymer peak occurs at lower temperatures as the time after illumination is increased (Figure 8-6). The exception to this trend is the 8-day shadow-cure profile, which has its primary peak maximum at a similar temperature to the 14-day profile ($\sim 210^\circ\text{C}$). This trend is also observed in the $\tan \delta$ profiles of the second temperature sequence for both film types (Figure 8-7). In the shadow-cure films, this trend could be attributed, again, to conversion; however, conversion estimates (from Figure 8-4) of the light-cure films are fairly constant at $\sim 48\%$ for 8 to 21 days post-illumination. Instead, this trend is thought to be related to the polymer network. With a more flexible network, the annealing effects should theoretically be greater, driving the film to a higher cross-link density, and increasing the cross-link density can increase the T_g of a polymer. As previously discussed, the shadow-cure network 8 days post-illumination is underdeveloped compared to the later time points. This underdevelopment of the network is less obvious in the light-cure films, though network changes could be accomplished within the error of the conversion measurement ($\sim 4\%$). Therefore, T_g and the cross-linking density should decrease with increasing time post-illumination because, before annealing in the DMA, the network is more rigid at later post-illumination times. These trends are observed in Figure 8-8.



(A)

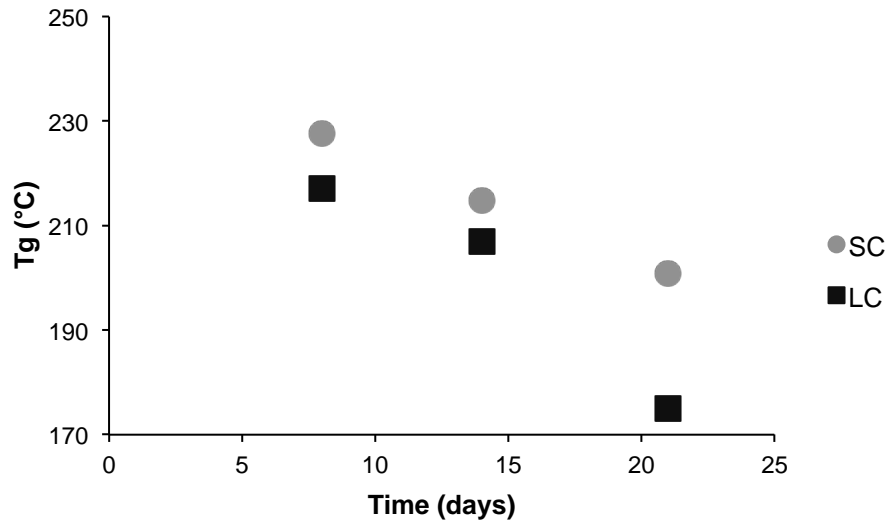


(B)

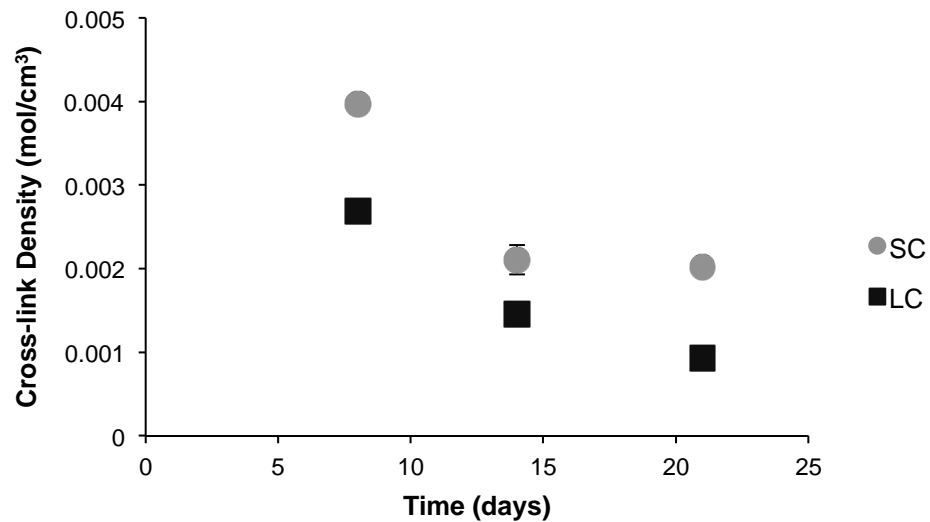
Figure 8-7. Comparison of the $\tan \delta$ curves of the second DMA temperature ramp sequence for EEC polymerized by transferable shadow cure (A) and light cure (B) at 8, 14, and 21 days post-illumination.

Further evidence in support of this theory is found in comparing the T_g and estimated cross-link density values of the light-cure and shadow-cure films. Not only does T_g decrease with increasing time post-illumination, but the shadow-cure films, at all three time points, have a greater T_g than the corresponding light-cure films (Figure 8-8.A).

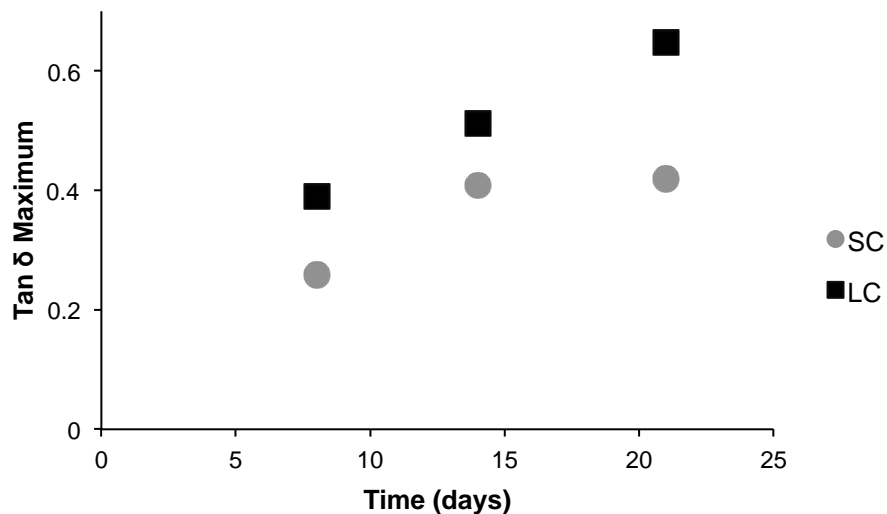
Furthermore, the shadow-cure films all have a higher estimated cross-link density than the light-cure films (Figure 8-8.B). Other similarities between the two film types include a broad tail before the $\tan \delta$ peak, which diminishes with increasing time post-illumination (Figure 8-7) and an increasing $\tan \delta$ peak height with increasing time post-illumination, indicative of the dampening properties of the films (Figure 8-8.C).



(A)



(B)



(C)

Figure 8-8. Comparison of the T_g (A), cross-link density (B), and maximum peak height of the $\tan \delta$ profile for EEC polymerized by transferable shadow cure and light cure at 8, 14, and 21 days post-illumination. T_g and cross-link density both decrease with increasing time post-illumination and polymerization by shadow cure. The $\tan \delta$ maximum increases with increasing time post-illumination and polymerization by shadow cure. Values were calculated from the second DMA temperature ramp sequence.

8.3.3 TSC in Complex Geometries with Pigments, and Fillers

The efficacy of transferable shadow cure used with pigments and fillers and in complex geometries was determined qualitatively, as these are the intended applications of the method. Not surprisingly, the shadow cure conformed easily to complex geometries, since illumination occurs in a standard rectangular mold and only the liquid AC monomer is transferred. Polymerization in cracks and crevices is also not hampered, unlike the original shadow cure method (Chapter 7), as evidenced by the ability to produce shadow cure DMA films in 300 μm molds. Furthermore, the addition of carbon black and titanium white had no apparent effect on the resulting shadow-cure polymer. These are two of the most difficult pigments for traditional photopolymerization to overcome because they efficiently absorb and reflect light, respectively; yet they do not interfere with initiation in the transferable shadow cure method because they are added to

the AC monomer post illumination. Figure 8-9 illustrates how effective titanium white and carbon black are at inhibiting photopolymerization. Only small pieces of solid polymer are formed when the pigment is added prior to illumination (Figure 8-9, A and C), but when the pigment was added after illumination, the entire volume of AC monomer polymerized (Figure 8-9, B and D). The pigments were also able to be homogenously mixed into the AC monomer post-illumination, and no phase separation was observed during the final stages of polymerization.

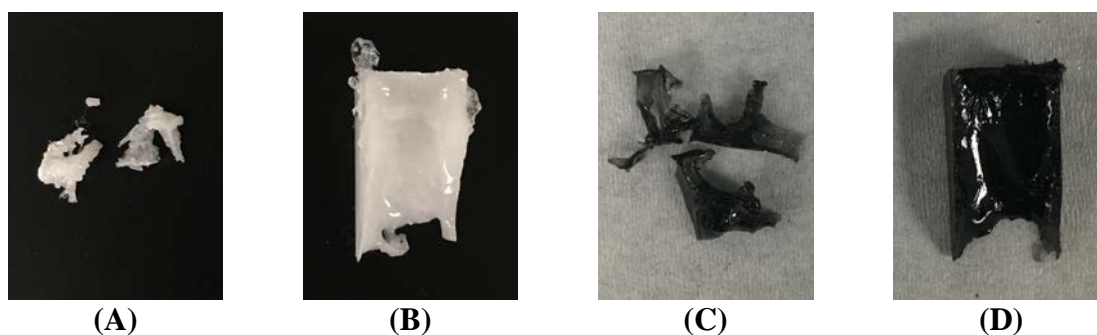


Figure 8-9. Polymer produced from transferable shadow cures samples, of the same size, with pigment added before illumination (A and C) and after illumination (B and D). When pigment was added after illumination, the entire volume of AC monomer polymerized.

Likewise, even adding 10 wt% of the fillers calcium carbonate and barium sulfate had no observable adverse effect on the polymerization. It is expected that the types and concentrations of additives that can be used with the transferable shadow cure method without negatively impacting the final conversion of the polymer is limited by miscibility, basicity (which will neutralize the acid of the active center), viscosity (which may limit active center diffusion), and hydroxyl concentration (which will promote the AM cationic propagation mechanisms, see Chapter 6).

The culmination of these investigations into pigments and geometries is depicted in Figure 8-10. In addition, these examples illustrate that the AC monomer can be layered to achieve a thick and/or multicolored polymer (Figure 8-11). Within approximately five minutes after being transferred to the mold, the AC monomer forms a thin barrier on the surface, which has enough structural integrity that another layer of AC monomer may be added on top of it without mixing. Some of these layers are visible in

the yellow portion of the polymer in Figure 8-11; the polyethylene particles that were added for their yellow color were not weighed, so the concentration varies layer by layer.



Figure 8-10. Examples of using the transferable shadow cure method to produce pigmented polymers in complex geometries.

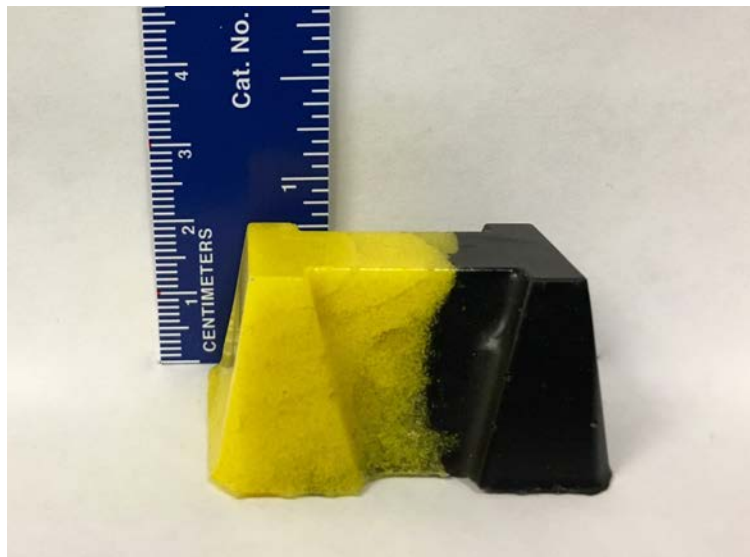


Figure 8-11. Thick polymers can be produced by layering the active-center-containing monomer. Shown is a 2-cm thick polymer made using the transferable shadow cure method, though even thicker polymers can be produced.

8.3.4 Central Composite Design 1

As in Chapter 7, a CCD was used to model responses to the factors and possible factor interactions that influence shadow-cure growth. In this CCD, the same four factors were examined (*i.e.*, effective irradiance, exposure time, exposure area, and sample depth), but three responses were measured: conversion, gel fraction, and LCS wt%. The conversion response was chosen because of its relevance to eventual applications. Generally, higher conversions are wanted because they reduce the probability of unreacted monomer migrating out of the film or coating, and they provide better physical properties. The gel fraction response was included for comparison to the original shadow cure method CCD, discussed in Chapter 7, to determine if the two methods responded to the factors similarly. In addition, the gel fraction could provide insight as to network formation, which also influences the physical properties. Finally, LCS wt% was included as a response to determine if the factors promoting the formation of a thicker LCS positively or negatively impact the conversion generated by the shadow cure. When the thickness of the LCS is increased, the total active center concentration should increase; however, the thickness may also decrease active center mobility into the monomer below.

Conversion

Evaluation of the relationship between the four factors and the first response, shadow cure conversion, determined it was best fit to a linear model, defined by the equation,

$$\text{Avg. Conversion} = 0.44 + 0.017(I) - 0.02(D) + 0.015(T) - 0.0056(A) \quad (8-5)$$

where I is effective irradiance, D is sample depth, T is exposure time, and A is exposure area. The statistical significance of the model and its factors were determined using the analysis of variance (ANOVA) technique, which uses the Fisher statistical test (F-test). The model has an F-value of 26.13. An F-value of that magnitude translates to a <0.01% chance that the model is a result of noise. All variables were demonstrated to have a statistically significant effect on the response, except exposure area (see Appendix D).

To be statistically significant, the probability that the magnitude of the F-value associated with each variable/interaction did not affect the response must be less than 5%.

Sample depth (D), with a coefficient of 0.02, is the most impactful factor on conversion, followed closely by effective irradiance (I) and exposure time (T). Increasing the sample depth increases the volume of monomer that needs to be polymerized without maintaining a proportional increase in the active center concentration due to light attenuation, thus decreasing conversion. This trend is illustrated in the response surface (Figure 8-12). In order to maximize conversion, effective irradiance and exposure time must also be increased (Figures 8-12 and 8-13). Together, these variables increase the initiating energy in the system, which in classical kinetics, increases the rate of initiation, creating more propagating active centers.⁶

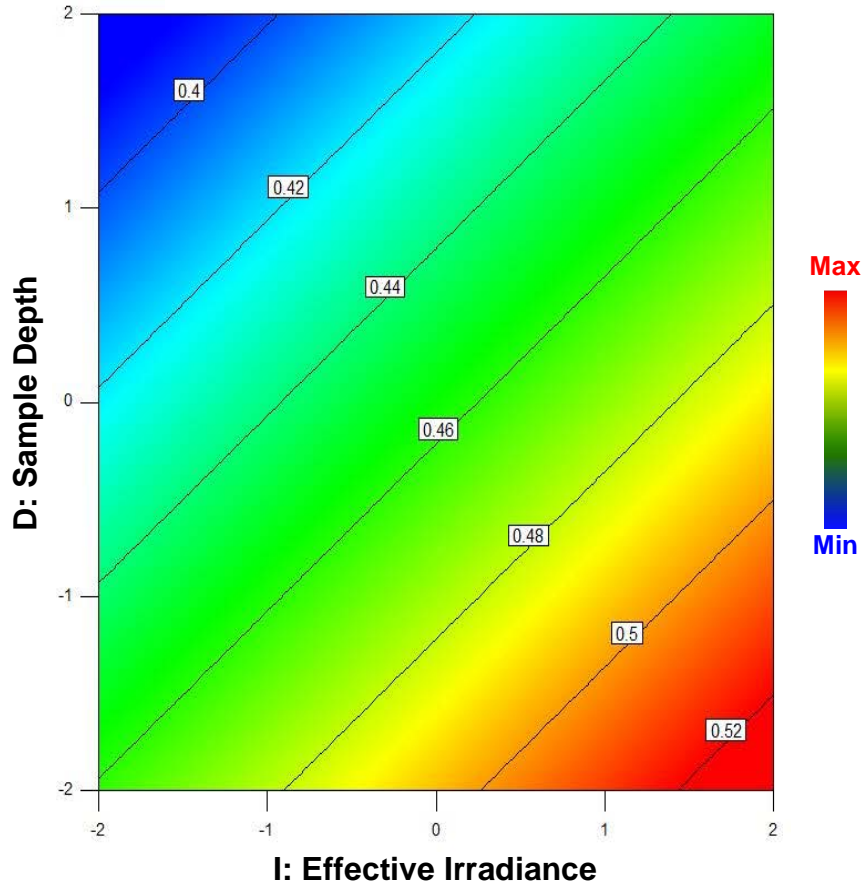


Figure 8-12. CCD 1 response surface depicting the influence of sample depth and effective irradiance on average shadow cure conversion. Exposure time and exposure area were held constant at coded values of 0.9 and -1, respectively. Shadow cure conversion is maximized by decreasing sample depth while increasing effective irradiance.

Exposure area (A) is the factor with the least impact on shadow cure conversion, with its coefficient in the model equation an order of magnitude smaller than the other three factors (Equation 8-5). The low impact of exposure area on the conversion likely relates to the experimental setup. A spacer was used to control the exposure area to volume ratio; therefore, for a mold of a constant depth, if the exposure area was increased, the volume of monomer increased proportionally. Ideally, with this constant surface area to volume ratio, conversion should be independent of exposure area. Nevertheless, the model predicts that the exposure area should be minimized to maximize conversion (Figure 8-12). This departure from the ideal is small however. Over the full

range of exposure area covered in the design space, the conversion is only predicted to change by 2%, all other factors held constant.

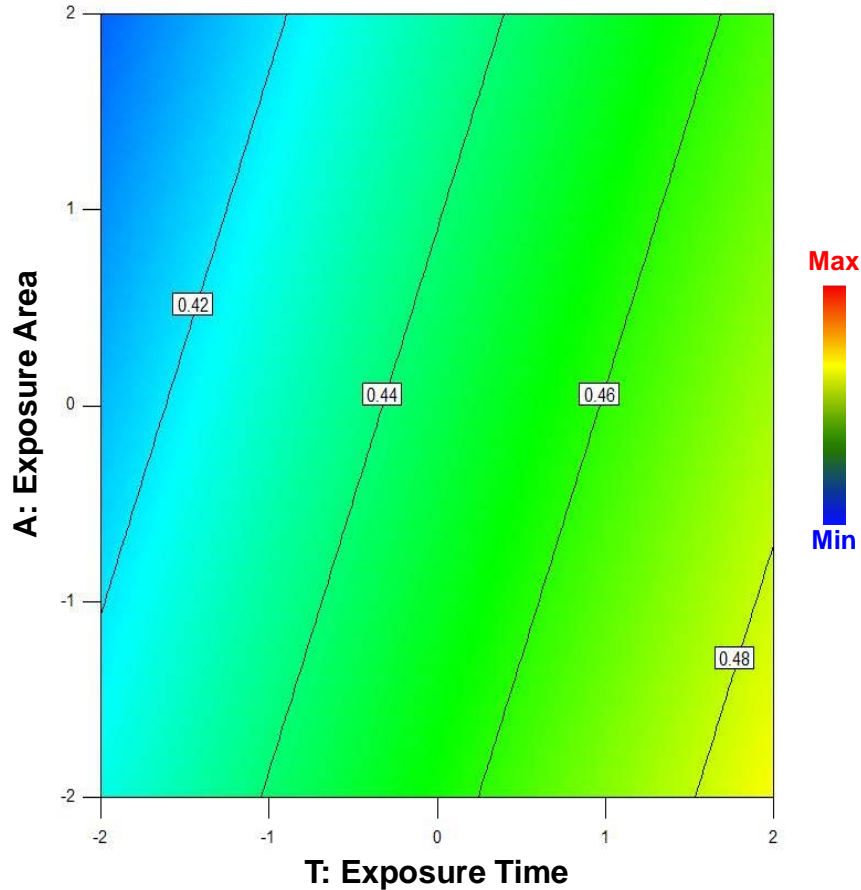


Figure 8-13. CCD 1 response surface depicting the influence of exposure area and exposure time on average shadow cure conversion. Effective irradiance and sample depth were held constant at coded values of 0.4 and 1, respectively. Shadow cure conversion is maximized by decreasing exposure area and increasing exposure time.

Gel Fraction

The second response, gel fraction, was unable to be modeled. After dissolving the CCD samples in THF, then removing and drying the gel fraction, it was found that 35 of the 40 samples (including the 10 checkpoint samples) had a gel fraction greater than 1. A second attempt was made to drive off any remaining THF by placing the samples back into the oven for an additional 2 hours at 100°C, but the gel fraction values remained

constant. It is believed that discrepancy in gel fraction is due to the copolymerized of some THF into the epoxide network. While THF, as a cyclic ether, can be acid catalyzed, it was not expected to polymerize under the presented conditions. Furthermore, there was no evidence that the THF copolymerized with samples produced via the original shadow cure method (Chapter 7), which indicates that gel fraction of these samples was sufficiently low that the copolymerization with THF did not increase even 1 of the 40 samples to a gel fraction greater than 1, or that two methods of shadow cure are sufficiently different to cause copolymerization in samples of the transferable shadow cure method but not in samples of the original shadow cure method. If the latter is considered as a possibility, the only conceivable difference is the accessibility of the active centers. Besides the change in method, the CCD samples were cured at the same conditions, with the same design space, and with the same formulation.

LCS Wt%

Evaluation of the relationship between the four factors and the third response, LCS wt%, determined it was best fit to a quadratic model, defined by the equation,

$$\begin{aligned} LCS\ Wt\% = & 12.06 + 9.54(I) - 3.36(D) + 5.87(T) + 1.93(A) - 2.19(ID) \\ & + 4.56(IT) + 0.62(IA) - 2.03(DT) + 0.19(DA) + 1.26(TA) \quad (8-6) \\ & + 2.51(I^2) - 0.048(D^2) + 0.59(T^2) + 0.058(A^2) \end{aligned}$$

where I is effective irradiance, D is sample depth, T is exposure time, and A is exposure area. The model has an F-value of 28.12. An F-value of that magnitude translates to a < 0.01% chance that the model is a result of noise. Simplified to only include variables and interactions that have a statistically significant effect on the response, Equation 8-6 becomes

$$\begin{aligned} LCS\ Wt\% = & 12.06 + 9.54(I) - 3.36(D) + 5.87(T) + 1.93(A) - 2.19(ID) \\ & + 4.56(IT) - 2.03(DT) + 2.51(I^2) \quad (8-7) \end{aligned}$$

Unsurprisingly, effective irradiance (I) has the largest impact on the magnitude of the response. Not only does effective irradiance itself have the largest coefficient in

Equation 8-6, but its interactions with sample depth (D) and exposure time (T) are also statistically significant. As the model predicted for the conversion response, increasing effective irradiance and decreasing the sample depth maximizes the LCS wt% (Figure 8-14). And, as previously mentioned, manipulating the effective irradiance and sample depth this way will increase the concentration of propagating active centers and produce more polymer; thus, the model is in agreement with known photopolymerization kinetics.⁶

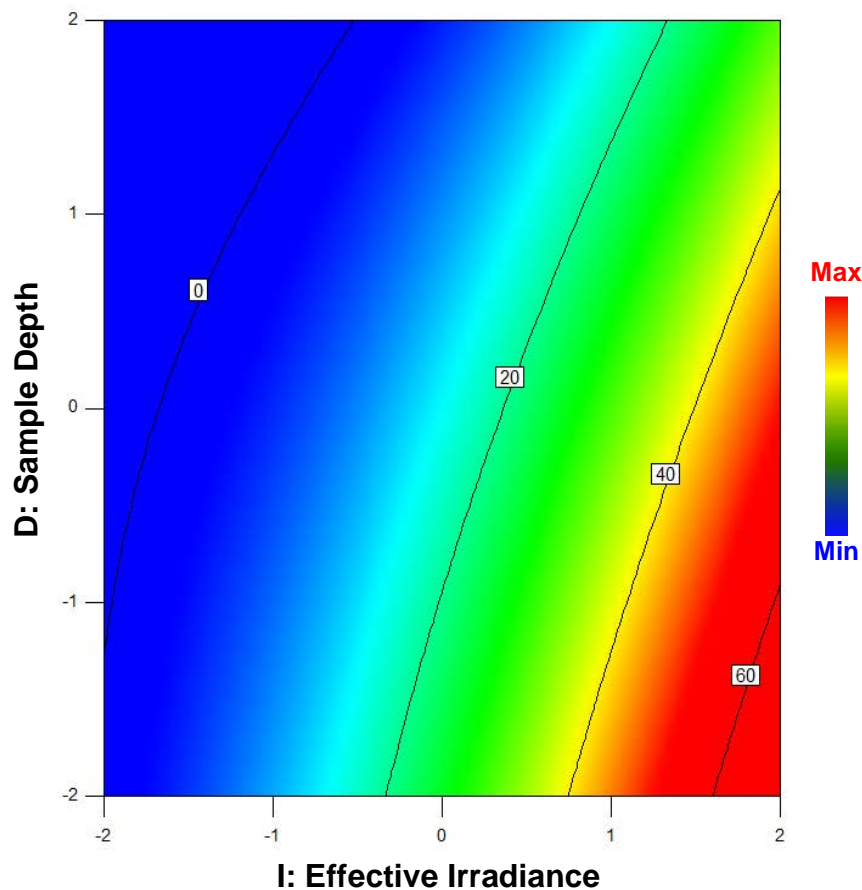


Figure 8-14. CCD 1 response surface depicting the influence of sample depth and effective irradiance on LCS wt%. Exposure time and exposure area were held constant at coded values of 0.9 and -1, respectively. The LCS mass is maximized by decreasing sample depth while increasing effective irradiance.

Also similar to the conversion response, the LCS wt% is increased by increasing exposure time (Figure 8-15). The one factor in opposition to the conversion response

model is exposure area. Instead of decreasing the exposure area to increase the response, the exposure area is increased to increase the LCS wt%. As with the conversion model, exposure area has little impact on the LCS wt% in comparison to the other factors, and, ideally the LCS wt% response should be independent of exposure area because of the constant surface area to volume ratio. The departure from the ideal, in this case, is thought to be human error. Larger LCS's are easier to remove from the sample and are more likely to remain whole.

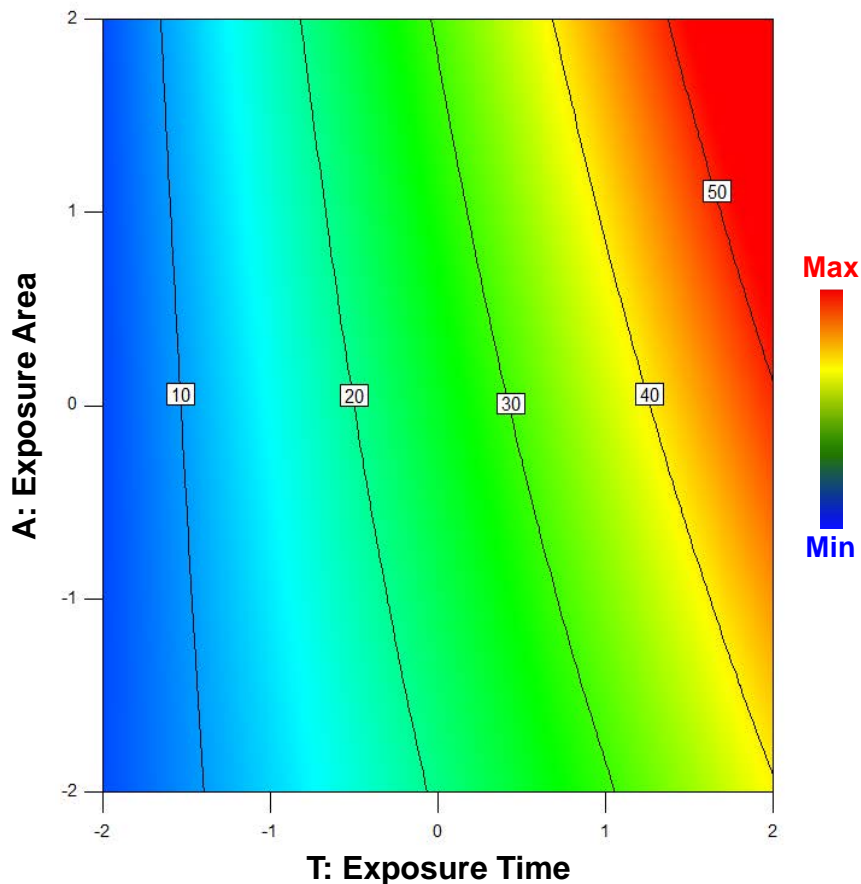


Figure 8-15. CCD 1 response surface depicting the influence of exposure area and exposure time on LCS wt%. Effective irradiance and sample depth were held constant at coded values of -0.2 and 1, respectively. LCS is maximized by increasing exposure area and exposure time.

In comparing the two responses (conversion and LCS wt%), the CCD predicts promoting one will promote the other. Within the design space of the CCD, this prediction implies two scenarios. In both scenarios, increasing the LCS wt% will

decrease the remaining monomer portion, increasing the active center concentration in the monomer. First, consider a scenario where the shadow cure only relies on the active center concentration beneath the LCS. Increasing the effective irradiance and exposure time will increase the active center concentration of the system, including below the LCS. If the resulting shadow cure only relies on the active center concentration beneath the LCS, then increasing the LCS wt% and, in turn, decreasing active center mobility out of the LCS does not negatively affect the conversion. In the second scenario, shadow cure is dependent on active center diffusion from the LCS. In this scenario, it is likely that, above a minimum LCS thickness and all other variables held constant, there is a set LCS thickness through which the active centers can diffuse to reach the monomer below. This set thickness is, of course, at the bottom of the LCS and at the interface with the monomer. Increasing the effective irradiance and exposure time will create a thicker LCS with a more dense network; however, because of the light gradient (which follows the Beer-Lambert Law), the bottom portion of the LCS, always the farthest portion from the initiating light, is least likely to change in cross-link density or conversion compared to the rest of the LCS. Therefore, diffusion out of this bottom portion is not expected to change and should not affect active center mobility. Furthermore, these two scenarios are not mutually exclusive and may coexist to increase shadow cure conversion with increasing LCS wt%.

8.3.5 Central Composite Design 2

Despite being an accurate and predictive model (see section below), it is acknowledged the range of conversions, in particular, produced in the design space of CCD 1 is not very broad (~12 % conversion). In addition, it is recognized that this narrow conversion range may provide an illusion of accuracy. In an attempt to prove that shadow cure conversion can be modeled over a wider range, a broader scope of effective irradiances and shorter exposure times were investigated in the CCD 2 (Table 8-2).

Conversion

As in the first CCD, the conversion response for CCD 2 was best fit to a linear model. The model is defined by the equation

$$\text{Avg. Conversion} = 0.4 + 0.025(I) - 0.012(D) + 0.028(T) - 0.0013(A) \quad (8-8)$$

where I is effective irradiance, D is sample depth, T is exposure time, and A is exposure area. The model has an F-value of only 3.92. An F-value of that magnitude translates to a 1.33% chance that the model is a result of noise. Compared to CCD 1, the F-value of this model is low. Moreover, the relative effect of certain factors on the response changed. Here, the rank of the variables is $T > I > D > A$ from most to least impactful (Equation 8-8). In CCD 1, the rank of variables is $D > I > T > A$ (Equation 8-5). In addition, all factors were statistically significant except exposure area in CCD 1; however, in CCD 2, only effective irradiance and exposure time are significant. The general trends of the two models remain the same: increasing effective irradiance and exposure time while decreasing sample depth and exposure area will maximize conversion (Figures 8-16 and 8-17).

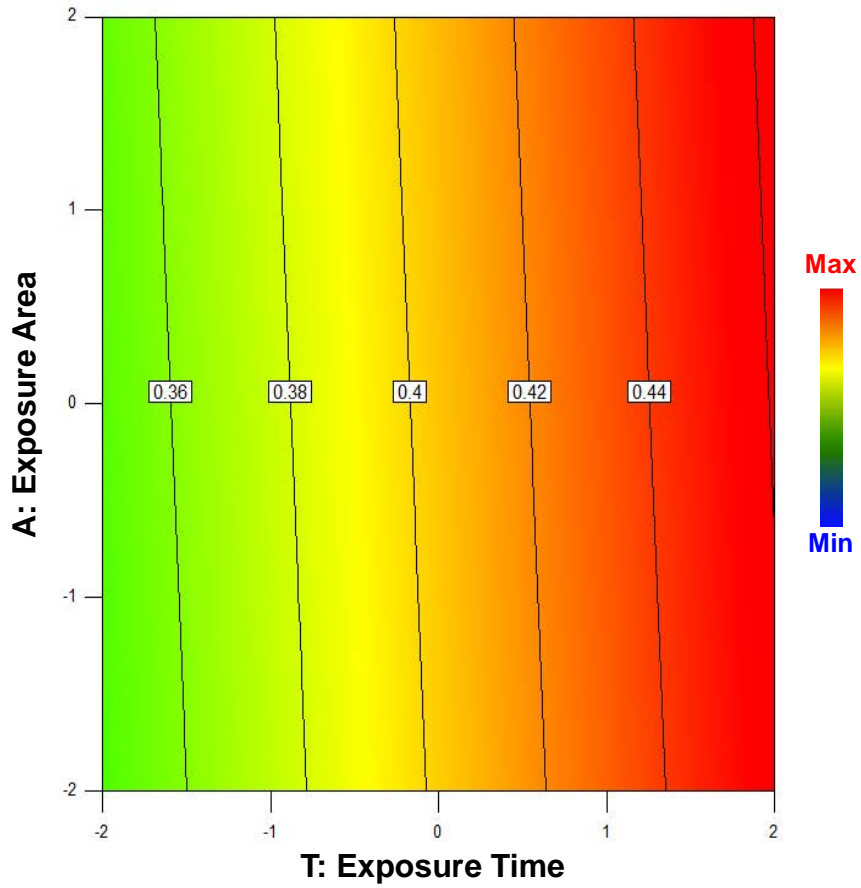


Figure 8-16. CCD 2 response surface depicting the influence of exposure area and exposure time on average shadow cure conversion. Effective irradiance and sample depth were held constant at coded values of 1 and 0.6, respectively. Shadow cure conversion is maximized by increasing exposure time.

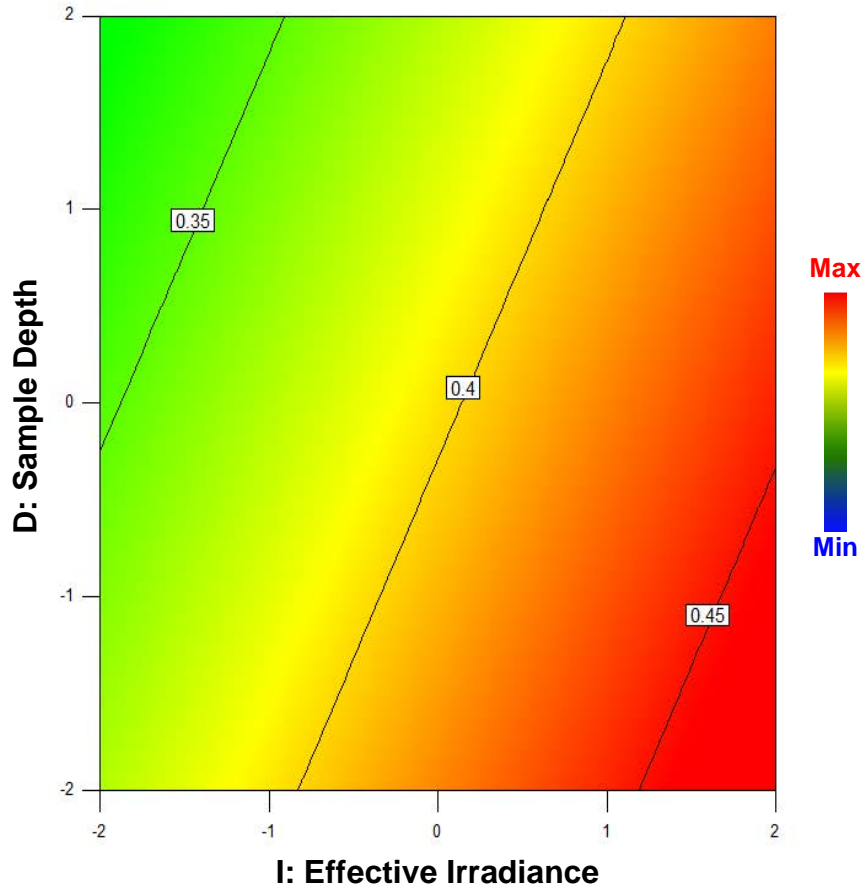


Figure 8-17. CCD 2 response surface depicting the influence of sample depth and effective irradiance on average shadow cure conversion. Exposure time and exposure area were held constant at coded values of -0.2 and 0.4, respectively. Shadow cure conversion is maximized by decreasing sample depth while increasing effective irradiance.

Conversion (13 weeks)

Because the gel fraction response of the CCD 2 samples was not undertaken, the sample conversion could be collected again at 13 weeks post-illumination. This 13-week conversion response was fitted to a linear model, just as the first, defined by the equation

$$\begin{aligned} & \text{Avg. Conversion (13 wks)} \\ & = 0.59 + 0.024(I) - 0.017(D) + 0.029(T) - 0.00125(A) \end{aligned} \quad (8-9)$$

where I is effective irradiance, D is sample depth, T is exposure time, and A is exposure area. This model has an F-value of 10.39. An F-value of that magnitude translates to a

<0.01% chance that the model is a result of noise. Along with the increase in F-value, increasing the time post-illumination has increased the importance of sample depth (D), so that only exposure area (A) remains statistically insignificant. The overall trend of the conversion response and relative importance of the factors remains the same as the first CCD 2 conversion response, suggesting that there is no significant difference between cationic propagation in the short term (first 6 days post-illumination) and the long term (13 weeks post-illumination).

LCS Wt %

Although the LCS wt% was calculated for CCD 2, the model faired very poorly (see section below). The shorter exposure times made the LCS's thinner, and thus they were harder to separate from the sample and more difficult to measure, increasing the error inherent in the model.

Model Accuracy

To confirm the trends illustrated by the two CCDs, each model's accuracy was verified using 10 checkpoint samples. These samples were external to the model, and their experimentally determined conversion and LCS% were compared to those predicted by the model (see Appendix D for experimental conditions). In the first CCD, the model correctly predicted the values of 9 of the 10 checkpoint samples for the conversion response within the 0.015 standard deviation of the corresponding experimental values (Table 8-3). If the standard deviation was widened to 0.021, the model would have correctly predicted all of the checkpoint samples. Despite the narrow range of conversions, the model has proven to be accurate over the design space, especially considering the small standard deviation. The model predicting LSC wt% did not fare as well. It correctly predicted 6 of the 10 checkpoint samples with the 3.21wt% standard deviation of the experimental values. This outcome suggests that there are areas of the design space that are not well represented by the model. The two largest discrepancies, CP 2 and CP 9, for example, both have a small experimental value, which the model over predicts.

Table 8-3. Model accuracy of CCD 1 was verified using 10 checkpoints external to the model. The model accurately predicts conversion, but is only moderately accurate in predicting LCS wt%. Standard deviation of the conversion response is 0.015. Standard deviation of the LCS wt% response is 3.21wt%.

	Shadow Cure Length (mm)				Gel Fraction			
	Exp.	Pred.	% Error	Within Std. Dev.	Exp.	Pred.	% Error	Within Std. Dev.
CP 1	0.423	0.431	2.0	✓	4.0	4.5	11.6	✓
CP 2	0.441	0.462	4.6		4.2	12.3	66.0	
CP 3	0.442	0.435	1.4	✓	29.2	28.0	4.3	✓
CP 4	0.477	0.468	1.8	✓	34.9	28.6	22.2	
CP 5	0.428	0.427	0.2	✓	8.7	5.8	51.3	✓
CP 6	0.460	0.452	1.7	✓	17.1	13.9	22.8	✓
CP 7	0.443	0.441	0.6	✓	7.0	11.1	37.5	
CP 8	0.442	0.438	1.0	✓	13.6	13.0	4.0	✓
CP 9	0.363	0.351	3.3	✓	3.4	15.7	78.5	
CP 10	0.413	0.421	2.0	✓	5.0	5.0	0	✓

The second CCD, with a wider range of effective irradiances and short exposure times, did not fare quite as well as CCD 1 (Table 8-4). The model did correctly predict all 10 of the checkpoint samples for the conversion response; however, the standard deviation of the model is larger (0.049) over a similar spread of conversions (CP 8 = 0.335 to CP 6 = 0.469). This introduction of error is attributed to a broader design space. Furthermore, only 5 of the 10 checkpoint samples were correctly predicted for the LCS wt% response within the 3.5 wt% standard deviation, and the % error between the experimental and predicted samples is high. For these reasons, the CCD 2 LCS wt% model was not included in the results above.

Table 8-4. Model accuracy of CCD 2 was verified using 10 checkpoints external to the mode. The model accurately predicts conversion, but does not accurately predict LCS wt%. Standard deviation of the conversion response is 0.049. Standard deviation of the LCS wt% response is 3.5wt%.

	Shadow Cure Length (mm)				Gel Fraction			
	Exp.	Pred.	% Error	Within Std. Dev.	Exp.	Pred.	% Error	Within Std. Dev.
CP 1	0.381	0.374	1.9	✓	0.7	3.4	79.1	✓
CP 2	0.411	0.420	2.0	✓	2.0	3.3	38.1	✓
CP 3	0.402	0.427	5.9	✓	6.6	8.0	17.2	✓
CP 4	0.362	0.371	2.4	✓	2.64	7.8	66.2	
CP 5	0.424	0.415	2.1	✓	0.32	9.0	96.4	
CP 6	0.469	0.511	8.2	✓	40.8	20.7	97.0	
CP 7	0.385	0.400	3.8	✓	11.4	-3.5	429.8	
CP 8	0.335	0.316	6.0	✓	1.7	4.7	63.6	✓
CP 9	0.401	0.399	0.5	✓	6.1	2.6	131.5	✓
CP 10	0.412	0.395	4.5	✓	0.8	8.2	90.8	

Also included in CCD 2 was the conversion response 13 weeks post-illumination (Table 8-5). The model correctly predicts 7 of the 10 checkpoint samples for this response, within the standard deviation of 0.031. If the standard deviation were increased to 0.047, the model would correctly predict 10 of 10 checkpoint samples.

Table 8-5. Model accuracy of CCD 2 was verified using 10 checkpoints external to the mode. The model predicts conversion 13 weeks post-illumination with moderate accuracy. Standard deviation of the conversion (13 week post-illumination) response is 0.031.

Fractional Conversion – 13 wks				
	Exp.	Pred.	% Error	Within Std. Dev.
CP 1	0.574	0.560	2.6	✓
CP 2	0.598	0.618	3.3	✓
CP 3	0.574	0.607	5.5	
CP 4	0.569	0.600	5.0	✓
CP 5	0.611	0.603	1.2	✓
CP 6	0.656	0.691	5.1	
CP 7	0.584	0.572	2.0	✓
CP 8	0.453	0.500	9.5	
CP 9	0.588	0.557	5.6	✓
CP 10	0.599	0.595	0.9	✓

8.4 Conclusions

A new method of shadow cure was demonstrated that effectively separates the initiation and propagation mechanisms, allowing the active-center-containing monomer to be transferred, mixed with pigments and fillers, layered in thick systems, and polymerized in complex geometries. Unlike the original shadow cure method, transferable shadow cure completely solidifies in cracks and crevices and can be cured in areas where no light is possible, such as between two opaque materials. This ability to transfer the active-center-containing monomer and produce a solid polymer, without further exposure to light, greatly expands the applications of shadow cure.

Kinetic analysis of transferable shadow cure shows the majority of conversion takes place within the first 15 days post-illumination, and the shadow-cure sample results in conversions consistently ~15% less over 300+ days post-illumination than those achieved in a light-cure sample exposed to an identical effective irradiance. Physical property testing revealed transferable shadow cure films have a higher T_g and cross-link density than light-cure films, likely driven by the annealing that occurs during the first DMA temperature ramp sequence. In addition, the T_g and cross-link density values of both shadow-cure and light-cure films decrease with increasing time post-illumination.

Two central composite designs over differing design spaces were used to model how conversion and LCS wt% respond to processing variables and their interactions. Although conversion was fit to a linear design equation and LCS wt% to a quadratic design equation, both responses were maximized by increasing effective irradiance and exposure time and decreasing sample depth. Exposure area was determined to be the least impactful variable for both models. Both designs were demonstrated to be accurate in predicting the conversion of 10 checkpoints samples, though neither design achieved a broad range of conversions. The first CCD was moderately predictive of the LCS wt% response, but the second CCD, with short exposure times, was not predictive.

8.5 References

- (1) Ficek, B. A.; Thiesen, A. M.; Scranton, A. B. Cationic Photopolymerizations of Thick Polymer Systems: Active Center Lifetime and Mobility. *European Polymer Journal* **2008**, *44* (1), 98–105.
- (2) Hoppe, C.; Ficek, B. A.; Eom, H. S.; Scranton, A. B. Cationic Photopolymerization of Epoxides Containing Carbon Black Nanoparticles. *Polymer* **2010**, *51* (26), 6151–6160.
- (3) Socrates, G. G. *Infrared and Raman Characteristic Group Frequencies: Tables and Charts*, 3rd ed.; John Wiley & Sons, LTD: Chichester, **2001**.
- (4) Cai, Y.; Jessop, J. L. P. Decreased Oxygen Inhibition in Photopolymerized Acrylate/Epoxide Hybrid Polymer Coatings as Demonstrated by Raman Spectroscopy. *Polymer* **2006**, *47* (19), 6560–6566.
- (5) Sipani, V. Kinetic Studies of Cationic Photopolymerization of Epoxide Monomers, **2004**.
- (6) Odian, G. *Principles of Polymerization*, 4 ed.; John Wiley and Sons, Inc., **2004**.

CHAPTER 9 CONCLUSIONS AND RECOMMENDATIONS

9.1 Conclusions

In this work, control strategies were developed for kinetic and physical properties in three underdeveloped areas of radiation polymerization: free-radical electron beam (EB) polymerization, free-radical/cationic hybrid photopolymerization, and cationic shadow cure. Improved kinetic and physical property control in these areas has led to better understanding of the fundamental nature of radiation polymerization, which will lead to increased viability in a broader range of industrial applications.

In Chapter 3, the use of Raman spectroscopy was established for EB-polymerized films as a technique for determining conversion. Raman spectroscopy has been previously well-established for studying photopolymerization reactions; however, it was determined that peak stability is not universal under the two different initiation mechanisms. A supposedly stable peak (representative of the $-C-C-C-C-$ bond), as identified via real-time photopolymerization monitoring, was chosen to serve as a reference for EB-polymerized films, but it failed to produce the expected uniform conversion through the film depth. This failure indicates that the peak, and thus the bond it represents, is affected by EB radiation. In order to successfully use Raman spectroscopy as a quantitative technique, an oligomer containing a phenyl ring was added to the formulation so that the $C=C$ phenyl bond could be used as a reference. Confirmation of the phenyl peak stability was done by comparing the standard deviations of the phenyl:acrylate peak ratio of EB and photopolymerized films, as well as comparing the depth profile of the phenyl peak intensity of both types of films. These findings are far-reaching: Raman spectroscopy, a non-destructive method that can simultaneously determine quantitative conversion measurements of multiple functional groups (*e.g.* acrylates and epoxides), can be used for EB-polymerized films, as long as the reference peak is proven stable. Other fingerprint techniques, such as IR, that rely on a stable reference peak are expected to behave similarly, in which case these findings serve as a cautionary tale; in addition, the comparison of photopolymer and EB-polymer Raman spectra can be used to further understanding of the effects of EB radiation on specific chemical bonds.

In Chapter 4, this Raman protocol and dynamic mechanical analysis were used to determine the dose rate effects (DREs) of a 5-monomer series in terms of conversion and glass transition temperature (T_g), respectively. Practically, understanding DREs is useful for industrial scale-up, where changes in dose rate between pilot testing and production are almost unavoidable; fundamentally, understanding DREs is valuable for determining EB kinetic principles, which have been elusive due to complexities of the system. Results of this study showed that, as the size of the acrylate monomer increased across the series, the magnitude of the DRE decreased in both conversion and T_g . This strong correlation between the DRE magnitude and monomer size was attributed to chain transfer opportunities. Confirming DREs in both conversion and T_g and establishing similar DRE trends in both polymer properties are integral steps for future investigations. The necessity of a phenyl moiety for Raman measurements and adequate film properties for DMA characterization greatly limits the chemistries that can be used to study DREs. Now, the presence of DREs in conversion can, with relative certainty, confirm DREs in T_g without DMA testing, and vice versa. Moreover, from the results of this study, a preliminary predictive relationship was developed to estimate the magnitude of the T_g DRE using the T_g shift caused by changes in dose, enabling scale-up of process variables for polymers prone to dose rate effects. Taken collectively, these findings have established a rudimentary structure/processing conditions/properties relationship. Albeit preliminary and only confirmed for this 5-monomer acrylate series, understanding how the chemical structure of the starting materials and the processing conditions they undergo collectively influence the final properties of the polymer produced is vital to understanding the fundamental aspects of EB polymerization and furthering the development of EB technology.

A protocol was also developed, in Chapter 5, to compare photopolymerized and EB-polymerized films produced with equivalent initiation energies and determine the effect of the initiation mechanism on kinetic and physical properties. Previous work, to the author's knowledge, has never compared the two radiation initiation mechanisms on the basis of equal initiation energies because EB radiation is measured in J/g (base units) and photo-radiation is measured in J/cm². Yet, complete understanding of the impact of the initiation mechanism on the final polymer – another important step in fully realizing a

structure/processing conditions/properties relationship – cannot be achieved without comparing equal initiation energies, since initiation energy has a profound effect on the final properties of the polymer. The protocol, which relied on the Kenning, *et al.* model to predict the absorbed energy in the photopolymerized films, was used to produce photopolymerized films of equivalent initiation energy to the EB films studied in Chapter 4. Two sets of photopolymerized films were made: one set with scaled energy rates (Set 1) and another set with equivalent energy rates (Set 2). In comparison to the EB films, photo-initiated Set 1 films had almost no energy rate effect and achieved equal or higher conversions for all 5 monomers; however, large energy rate effects (EREs) were observed in the photo-initiated Set 2 films, more similar to the EB films. Through physical property testing (by DMA), increases in T_g as large as 15°C were caused by switching the initiation mechanism to EB radiation, as well as smaller changes in full width at half maximum (FWHM) of the $\tan \delta$ profile and the maximum height of the $\tan \delta$. The magnitude of both the EREs and physical property changes were dependent on the monomer chemistry. Understanding these differences between EB- and photopolymerized films not only improves knowledge of fundamental kinetics, but it also improves pairing of an application to the best suited radiation initiation mechanism and sets the framework for dual EB- and photo-initiated systems.

In Chapter 6, the effect of promoting the cationic activated monomer (AM) mechanism in free-radical/cationic hybrid photophotomerizations through the presence of a hydroxyl group on the (meth)acrylate monomer was investigated and compared to a non-hydroxyl-containing control. Placement of the hydroxyl group on the (meth)acrylate was hypothesized to reduce phase separation by covalent bonding the two networks while also improving the propagation rate of the epoxide. Real-time Raman spectroscopy was used to simultaneously monitor the epoxide and (meth)acrylate conversion throughout the reaction and determined that, in fact, formulations of low epoxide content with the hydroxylated (meth)acrylate increased the epoxide conversion by as much as 50% compared to identical conditions with the non-hydroxyl-containing control. The effect of promoting the AM mechanism on the (meth)acrylate kinetics was dependent on the (meth)acrylate reaction rate: the methacrylates were more greatly impacted than the acrylates because their propagation rate more closely resembles that of the epoxide.

Physical property tuning was demonstrated through DMA characterization. The T_g of each hybrid system could be manipulated by varying the concentration of epoxide. Perhaps more importantly, however, is increased network homogeneity, as illustrated by the reduction in the FWHM, gained by using the hydroxy-(meth)acrylates. The primary motivation for using free-radical/cationic hybrid formulations is the reduction of oxygen inhibition in comparison to neat free-radical photopolymerizations; yet, the slow epoxide reaction and tendency to phase separate has been problematic for hybrid systems. The results of this study demonstrate these problems can be rectified using a hydroxy-(meth)acrylate, while also demonstrating the kinetic- and property-tuning possibilities of hybrid photopolymers.

Chapter 7 focuses on controlling the long-lived active centers of cationic photopolymerizations, through the use of physical cues and processing variables, to form polymer in areas never exposed to the initiating light, or *shadow cure*. Shadow cure is a promising avenue for expanding the application of photopolymerization to light-restricted areas, but, in order to make shadow cure a viable industrial option, the active center mobility must be better understood. To this end, timed trials of a top-illuminated system in a simple, rectangular mold were undertaken to visualize the vertical and lateral propagation of the active centers. Within 4 hours, the active centers had diffused ~ 3 cm laterally from the initiating light source, as evidenced by shadow cure growth. Increasing the time post-illumination did not result in further diffusion of the active centers, but it did result in a more rigid, developed network. One notable feature of the sample produced was the presence of a cavity filled with liquid resin directly beneath the area exposed to light that persisted for at least 2 weeks post-illumination. This cavity was attributed to the heavily cross-linked network of the light-cured section restricting the mobility of the active centers in that region. Further studies of active center mobility demonstrated that shadow cure can be directed around corners or into crevices. A central composite design was used to model the effect of sample depth, effective irradiance, exposure area, and exposure time on active center diffusion limits (shadow cure length) and network formation (gel fraction). According to the model, shadow cure length is maximized by increasing sample depth, while decreasing the other three variables; in contrast, gel fraction is maximized decreasing the sample depth and increasing the other

three variables. In other words, a more developed polymer network restricts active center diffusion. These preliminary findings demonstrate that active center mobility can be controlled, and, with further research, shadow cure may be an effective alternative to thermal polymerization in light-restricted applications.

Finally, in Chapter 8, a new method of shadow cure, *transferable shadow cure*, is presented that allows for the separation of the initiation and propagation mechanisms, enabling the active-center-containing monomer to be transferred, mixed with pigments and fillers, layered in thick systems, and polymerized in complex geometries. Unlike the original shadow cure method presented in Chapter 7, transferable shadow cure completely solidifies in cracks and crevices. The transferability of this new shadow cure method permitted a comparison to light-cure samples that was impossible with the original method. Kinetic analysis of transferable shadow cure shows conversions consistently ~15% less than light-cure samples over 300+ days post-illumination. Physical property testing revealed transferable shadow cure films have a higher T_g and cross-link density than light-cure films, likely driven by the annealing that occurs during the first DMA temperature ramp sequence. In addition, the T_g and cross-link density values of both shadow-cure and light-cure films decrease with increasing time post-illumination. As in Chapter 7, a CCD was undertaken to model the effect of sample depth, effective irradiance, exposure area, and exposure time on conversion and the weight percent of the light-cured section. The model predicts both responses are maximized by increasing effective irradiance and exposure time and decreasing sample depth, which is consistent with classic photopolymer kinetics. The ability to transfer the active-center-containing monomer and produce a solid polymer, without further exposure to light, greatly expands the applications of shadow cure. Not only can transferable shadow cure provide a uniform cure in light-restricted areas or on complex geometries, but it can be used in areas where no light is possible, such as between two opaque materials, or in areas where UV light would be detrimental, such as *in-vivo* applications. By demonstrating the similarities and differences between light and shadow cure, as well as the response of shadow cure to processing variables, this work begins the fundamental study of transferable shadow cure and its optimization.

9.2 Recommendations

9.2.1 Electron-beam Polymerization

Electron-beam polymerization remains a largely untouched area of research, especially on a fundamental level. The establishment of Raman spectroscopy as an analytical tool for investigating EB polymerization, however, will enable further research into the kinetics of EB. Also, as discussed, Raman can be used to determine the effect of EB radiation on specific Raman-active bonds or groups of bonds through comparison to photopolymer spectra. This technique should first be applied to small molecules with relatively simple Raman spectra. The five-monomer series used in Chapters 4 and 5 is an ideal subject, since all of the monomer spectra contain a known reference peak and the monomer size is incrementally increased across the series. The first couple of monomers increase by a single bond, also making peak identification straightforward. Besides the percentage of the bond that is altered, comparing the peak width and location could reveal additional information about the effect of EB radiation.

Future work on the EB dose rate effect (DRE) should begin by confirming the chain transfer theory. Estimates of chain transfer can be determined by using Soxhlet extraction on EB-polymerized films of monofunctional monomers. This estimation is an imperfect process since cross-linking of polymer chains can occur under EB radiation (Chapter 1, Section 1.1.1), but it should provide a simple method determining monomers for further study. For example, preliminary results show pure EB-cured PA (phenyl acrylate) does not have any retrievable gel fraction, while pure HPOPA (2-hydroxy-3-phenoxypropyl acrylate) polymerized under the same conditions is approximately 80% gel. In addition, comparing the sol-gel results with a photopolymerized film of equivalent initiation energy could further elucidate what portion of the EB gel fraction is due to chain transfer, because chain transfer is the only mechanism for producing gel in a monofunctional photopolymerization. Selection of monomers for future DRE studies will also help confirm the chain transfer theory. Cyclohexyl acrylate, for example, provides a useful comparison to phenyl acrylate (Figure 9-1). The two monomers are identical except for the conjugation of the aromatic ring. This difference should make cyclohexyl acrylate more susceptible to chain transfer, reducing its DREs in comparison to phenyl acrylate if the chain transfer theory holds true.

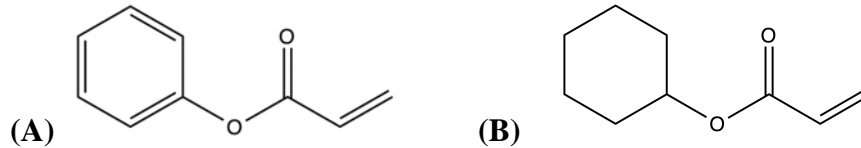


Figure 9-1. Phenyl acrylate (A) and cyclohexyl acrylate (B).

Moreover, an expanded monomer study will confirm the predictive capabilities of the 4-to-10 scale up ratio (4-fold increase in dose to 10-fold increase in line speed).

Further work comparing EB- and photoinitiation energies should verify the energy rate effects (EREs) experienced in the photopolymer films are independent of the photoinitiator by choosing a variety of Type 1 photoinitiators and repeating the study with select monomer formulations that have large energy rate effects. The question of oxygen inhibition, resulting from dissolved oxygen, should also be addressed. Dissolved oxygen can be removed from the formulations using a method proposed by Gou, *et al.*¹ This method uses the combination of a singlet oxygen generator and a singlet oxygen trapper to remove dissolved oxygen before polymerization. Additionally, directly comparing the radical concentration of the two initiation mechanisms by calculating G_i for the EB polymerization would determine whether the difference between the two mechanisms is due to difference in radical formation and side reactions or radical concentration (Equations 1-2 and 1-6). Labana has proposed a method by which G_i can be calculated using a combination of the sol-gel fractions and the reaction profile (conversion vs. time).² Although the EB reaction profile cannot be gathered in real time because of instrument limitations, it can be pieced together using several films, each receiving an increase in dose from the previous. The reaction profile should not be constructed from a single film receiving multiple, incremental doses, however, as this simulates a pulsed EB reaction, which can have different kinetics. Besides being useful for the G_i calculation, EB reactions profiles can be compared to that of the equivalent initiation energy and energy rate photopolymer films to compare propagation rates.

Another looming question that might be answered by comparing EB-initiated and photo-initiated films is why some formulations polymerize better by one initiation mechanism than the other. For example, preliminary work has shown that pure PA, BA,

PEA, and POEA are still wet, tacky films when EB-cured at 60 kGy, 20 ft/min; yet, when photopolymerized, they reach >90% conversion (though initiation energy was not matched). In contrast, pure HPOPA is well polymerized by both initiation mechanisms. Calculating G_i for the studied formulations will be important to answering this question. If a monomer has a low G_i , a low radical concentration may be to blame for low conversions. Radical stability of the primary radicals formed in EB polymerization should also be considered, as it is also a result of the monomer chemistry. If a tertiary radical is formed instead of a primary or secondary radical, it may be too stable to react in a timely manner, similar to the difference in reactions times between acrylates and methacrylates. Energy rate should also be considered when comparing the performance of a monomer by either initiation mechanism. As demonstrated in Chapter 5, energy rate is an important variable in both EB- and photopolymerization and may cause some of the discrepancies in cure, as rates between radiation methods often differ.

Beyond comparison of EB- and photopolymerization, there is potential for the two systems to work together to overcome free-radical oxygen inhibition. In Chapter 1 (Section 1.1.2), the difference in energy deposition between the two initiation mechanisms was discussed, as well as its impact on oxygen inhibition. EB polymerization is more greatly affected by oxygen inhibition because, unlike photopolymerization, the highest concentration of radicals is not at the coating surface where oxygen diffusion is most problematic. In photopolymerization, higher photoinitiator concentrations and effective irradiances can be used as an alternative to inerting with nitrogen, but these alternatives limit the depth of cure. A dual photo- and EB-initiating system might be used to overcome oxygen inhibition without inerting, while maintaining good depth of cure. Films would first be exposed to an initiating light to receive a surface cure, then they would be exposed to EB radiation to finish polymerizing the film. However, a new system such as this poses new research questions. What is the effect of a free-radical photoinitiator on EB polymerization, which is typically initiator free? Can photoinitiator only be deposited on the surface? What conversion does the photopolymerization layer need to reach to be an effective barrier against oxygen for the EB polymerization? Can the two mechanisms produce adequate film properties? And, most importantly, can such a system effectively overcome oxygen inhibition?

9.2.2 Hybrid Polymerization

Future work in hybrid systems should consider the benefits of mixing hydroxyl- and non-hydroxyl containing (meth)acrylates. It is expected that such a mixture of (meth)acrylates could be used to increase the resolution of kinetic and property tuning demonstrated in Chapter 6. Furthermore, if the miscibility of the (meth)acrylates and epoxide is low, phase separation can lead to the formation of nanophase domains, that, because of the hydroxy-(meth)acrylates, would be covalently bonded to the continuous network. Nanophase domains can be used to produce polymers with a combination of properties, such as a sturdy but flexible polymer; however, premature failure of the film or coating is problematic due to the phase separation. Bonding the phase domains together would alleviate this problem. In addition, the dark cure potential of the hybrid systems in Chapter 6 was not investigated. Further network development of the epoxide may affect the physical properties of the hybrid films. This network development is not expected to be equal across the varying concentrations of epoxide and may negatively impact the resolution achieved in property tuning. Less dark cure would be expected for hydroxyl-containing systems because of the higher conversions achieved during light cure.

9.2.3 Cationic Shadow Cure

The next step in better understanding shadow cure is the optimization of the initial polymerization rate to increase shadow cure polymerization rate and conversion. EEC has made a good test case because its initial polymerization is slow enough to allow decent shadow cure conversion; however, the rate of shadow cure is likely too slow (15 days for the majority of conversion) for industrial applications. Through analysis of the kinetics of multiple epoxides, a fundamental relationship between the light cure propagation rate and the shadow cure propagation rate will further understanding of post-illumination kinetics, as well as predict which cationic monomers are best suited for shadow cure applications.

In addition to optimizing the rate of shadow cure, controlling the pot life of the active-center-containing monomer will also be an important aspect of increasing shadow cure applications. If the shadow cure propagation rate is increased, controlling the pot

life will become even more difficult. Currently, EEC will only flow easily for 5 to 10 minutes after illumination, though it does remain mobile for hours. Ideally, the pot life should be easily variable for different applications. Polymerization at reduced temperatures is one option for controlling pot life. It is well established that rate constants are a function of temperature, and reducing the temperature would reduce the polymerization rate. In theory, polymerizing at temperatures just below room temperature should increase the pot life by minutes or hours; colder temperatures might extend the pot life for days or weeks. However, if polymerized too close to the freezing temperature of the monomer, it may be difficult to balance melting and propagation – by the time the monomer is warm enough to flow and be transferred, enough polymerization may have taken place to hinder flow, negating the purpose of the reduced temperature. Moreover, the initiation rate will also be decreased at reduced temperatures and the exposure will need to be adjusted accordingly.

Another avenue for additional investigations of shadow cure is using a pulsed, low effective irradiance exposure to produce active-center-containing monomer without a light-cured section. Because of the increased time for active center diffusion between pulses and the increased diffusion due to little to no network formation, the active center concentration in the monomer should be better distributed and may be able to be increased above the concentrations achievable under constant exposure without forming solid polymer. Increased active center concentrations would lead to higher shadow cure conversion, and the absence of a light-cured section would remove a processing step.

An alternative option for streamlining the transferable shadow cure method is the development of an apparatus to be used with the method. To this end, a syringe has been designed where the polymerization could take place in the syringe barrel, initiated by a light guide routed through the syringe plunger.³ Using a syringe would make the system easily portable post-illumination, and the narrowed tip would trap the light-cured section in the syringe barrel when the active-center-containing monomer is ejected in the desired location. An opaque syringe barrel would prevent premature initiation of the formulation from ambient light and would protect the user from the UV light source. Furthermore, if a glass (or similar material) syringe was used, in addition to the opaque outer coating, an inner coating or partial coating could be used to eliminate or restrict light guiding. The

presence of light guiding, if controlled, could increase the active center concentration throughout the depth of the formulation without forming solid polymer, increasing conversion. Although, if light guiding were used, transferable dark cure may be a more appropriate term.

9.3 References

- (1) Gou, L.; Opheim, B.; Coretsopoulos, C. N.; Scranton, A. Consumption of the Molecular Oxygen in Polymerization Systems Using Photosensitized Oxidation of Dimethylantracene. *Chemical Engineering Communications* **2006**, *193* (5), 620–627.
- (2) Labana, S. S. Kinetics of High-Intensity Electron-Beam Polymerization of a Divinyl Urethane. *Journal of Polymer Science Part A-1: Polymer Chemistry* **1968**, *6* (12), 3283–3293.
- (3) Schissel, S. M., Kaalberg, S. M., Jessop, J. L. P. “Transferrable Shadow Cure Method.” U.S. Patent 15141800, filed April **2016**. Patent Pending.

APPENDIX A
SUPPLEMENTAL INFORMATION FOR CHAPTER 5 (EB/UV COMPARISON)

A.1 Dose Equivalents for Photo-initiated Films

Table A-1. Estimated dose equivalent for the Set 1 photo-initiated films.

	Ideal				Actual				
	Dose (kGy)	Line Speed (ft/min)	E.I. @ Sample (mW/cm ²)	Lamp E.I. (mW/cm ²)	Lamp E.I. (mW/cm ²)	E.I. @ Sample (mW/cm ²)	Conversion Factor (cm ² /g)	Time (s)	Dose (kGy)
PA	15	20	3.4	3.8	3.8	3.5	44.9	100	15.7
		100	17.1	18.9	19.4	17.8	44.4	20	15.9
		200	34.1	37.8	38.2	35.1	45.7	10	16.0
	30	20	6.8	7.6	7.7	7.1	45.5	100	32.2
		100	34.1	37.8	38	34.9	44.5	20	31.1
		200	68.3	75.6	75.5	71.3	44.5	10	31.7
	60	20	13.7	15.1	16	14.7	43.9	100	64.6
		100	68.3	75.6	75.5	71.3	44.2	20	63.0
		200	136.5	151.2	150.5	138.4	43.3	10	59.9
BA	15	20	3.5	3.9	4.1	3.8	44.7	100	16.9
		100	17.4	19.2	19.0	17.5	44.9	20	15.7
		200	34.9	38.5	38.6	35.5	44.9	10	15.9
	30	20	7.0	7.7	7.4	6.8	43.2	100	29.4
		100	34.9	38.5	38.9	35.8	42.8	20	30.6
		200	69.8	77.0	77.5	71.3	43.6	10	31.1
	60	20	14.0	15.4	15.6	14.3	44.5	100	63.9
		100	69.8	77.0	77.5	71.3	45.1	20	64.3
		200	139.5	154.0	153.5	141.2	41.9	10	59.1

Table A-1. Continued.

	Ideal				Actual				
	Dose (kGy)	Line Speed (ft/min)	E.I. @ Sample (mW/cm ²)	Lamp E.I. (mW/cm ²)	Lamp E.I. (mW/cm ²)	E.I. @ Sample (mW/cm ²)	Conversion Factor (cm ² /g)	Time (s)	Dose (kGy)
PEA	15	20	3.2	3.5	3.8	3.5	55.8	100	19.5
		100	16.0	17.7	17.2	15.8	51.0	20	16.2
		200	32.0	35.3	33.1	30.4	54.9	10	16.7
	30	20	6.4	7.1	6.0	5.5	51.1	100	28.2
		100	32.0	35.3	35.3	32.5	45.6	20	29.6
		200	64.0	70.6	70.7	65.0	44.7	10	29.1
	60	20	12.8	14.1	13.4	12.3	45.5	100	56.0
		100	64.0	70.6	70.3	64.6	44.7	20	57.8
		200	128.0	141.2	141.3	129.4	45.6	10	60.0
POEA	15	20	3.5	3.8	3.7	3.4	42.2	100	14.3
		100	17.2	19.1	20.0	18.4	43.7	20	16.1
		200	34.5	38.1	37.5	34.5	42.3	10	14.6
	30	20	6.9	7.6	7.0	6.6	43.2	100	28.7
		100	34.5	38.1	37.5	34.5	45.0	20	31.0
		200	69.0	76.2	76.2	70.1	43.3	10	30.3
	60	20	13.8	15.2	15.0	13.8	43.7	100	60.3
		100	69.0	76.2	76.2	70.1	43.2	20	60.6
		200	137.9	152.4	152.9	140.6	43.6	10	61.3

Table A-1. Continued.

	Ideal				Actual				
	Dose (kGy)	Line Speed (ft/min)	E.I. @ Sample (mW/cm ²)	Lamp E.I. (mW/cm ²)	Lamp E.I. (mW/cm ²)	E.I. @ Sample (mW/cm ²)	Conversion Factor (cm ² /g)	Time (s)	Dose (kGy)
HPOPA	15	20	3.4	3.7	3.9	3.6	48.7	100	17.5
		100	16.8	18.5	19.1	17.6	45.9	20	16.1
		200	33.5	37.0	37.5	34.5	46.0	10	15.8
	30	20	6.7	7.4	7.4	6.8	55.3	100	37.6
		100	33.5	37.0	37.5	34.5	48.7	20	33.6
		200	67.0	74.0	74.5	68.5	45.3	10	31.0
	60	20	13.4	14.8	15.5	14.3	50.3	100	71.6
		100	67.0	74.0	74.5	68.5	50.9	20	69.8
		200	134.0	148.0	148.4	136.5	48.0	10	65.6

Table A-2. Estimated dose equivalent for the Set 2 photo-initiated films.

	Ideal					Actual			
	Dose (kGy)	Line Speed (ft/min)	Conversion Factor (cm ² /g)	E.I. @ Sample (mW/cm ²)	Lamp E.I. (mW/cm ²)	Lamp E.I. (mW/cm ²)	E.I. @ Sample (mW/cm ²)	Time (s)	Dose (kGy)
PA	15	20	44.0	171	189	190	172	2	15.1
		100	44.0	853	944	950	859	0.4	15.1
		200	44.0	1707	1887	1890	1708	0.2	15.0
	30	20	44.0	341	374	380	344	2	30.2
		100	44.0	1707	1887	1780	1609	0.4	28.3
		200	44.0	3413	3774	3800	3436	0.2	30.2
	60	20	44.0	683	755	749	677	2	59.5
		100	44.0	3413	3774	3770	3409	0.4	59.9
		200	44.0	6826	7548	7540	6820	0.2	59.9
BA	15	20	43.0	174	193	200	181	2	15.6
		100	43.0	872	965	970	877	0.4	15.1
		200	43.0	1744	1930	1940	1554	0.2	13.4
	30	20	43.0	349	386	390	353	2	30.4
		100	43.0	1744	1930	1900	1717	0.4	29.5
		200	43.0	3488	3860	3900	3525	0.2	30.3
	60	20	43.0	698	772	755	683	2	58.8
		100	43.0	3488	3860	3830	3463	0.4	59.6
		200	43.0	6975	7720	7690	6950	0.2	59.8

Table A-2. Continued

	Ideal				Actual				
	Dose (kGy)	Line Speed (ft/min)	Conversion Factor (cm ² /g)	E.I. @ Sample (mW/cm ²)	Lamp E.I. (mW/cm ²)	Lamp E.I. (mW/cm ²)	E.I. @ Sample (mW/cm ²)	Time (s)	Dose (kGy)
PEA	15	20	46.9	160	177	180	163	2	15.3
		100	46.9	800	885	889	804	0.4	15.1
		200	46.9	1600	1770	1700	1537	0.2	14.4
	30	20	46.9	320	354	340	308	2	28.9
		100	46.9	1600	1770	1700	1537	0.4	28.8
		200	46.9	3200	3540	3510	3174	0.2	29.8
	60	20	46.9	640	708	710	642	2	60.2
		100	46.9	3200	3540	3510	3174	0.4	59.5
		200	46.9	6398	7080	6980	6310	0.2	59.2
POEA	15	20	43.5	172	191	190	172	2	15.0
		100	43.5	862	954	955	863	0.4	15.0
		200	43.5	1724	1907	1880	1700	0.2	14.8
	30	20	43.5	345	381	380	344	2	29.9
		100	43.5	1724	1907	1880	1700	0.4	29.6
		200	43.5	3449	3814	3800	3435	0.2	29.9
	60	20	43.5	670	763	755	683	2	59.4
		100	43.5	3449	3814	3800	3435	0.4	59.8
		200	43.5	6898	7628	7600	6870	0.2	59.8

Table A-2. Continued

	Ideal				Actual				
	Dose (kGy)	Line Speed (ft/min)	Conversion Factor (cm ² /g)	E.I. @ Sample (mW/cm ²)	Lamp E.I. (mW/cm ²)	Lamp E.I. (mW/cm ²)	E.I. @ Sample (mW/cm ²)	Time (s)	Dose (kGy)
HPOPA	15	20	43.6	172	190	190	172	2	15.0
		100	43.6	860	952	950	860	0.4	15.0
		200	43.6	1719	1904	1900	1717	0.2	15.0
	30	20	43.6	344	381	385	348	2	30.4
		100	43.6	1719	1904	1910	1727	0.4	30.1
		200	43.6	3439	3808	3820	3453	0.2	30.1
	60	20	43.6	688	762	765	692	2	60.4
		100	43.6	3439	3808	3850	3480	0.4	60.7
		200	43.6	6878	7616	7620	6885	0.2	60.1

APPENDIX B
SUPPLEMENTAL INFORMATION FOR CHAPTER 6
(HYBRID PHOTOPOLYMERIZATION)

B.1 Formulation Information

Table B-1. Mol% of hybrid formulations by functional group. Greatest difference between formulations in mol% at 20 wt% is 5.4 mol%.

	10 wt% EEC	20 wt% EEC	30 wt% EEC	40 wt% EEC	50 wt% EEC	60 wt% EEC	70 wt% EEC	80 wt% EEC	90 wt% EEC
EEC	10.3	20.5	30.7	40.7	50.8	60.7	70.6	80.5	90.3
EGMEA	89.7	79.5	69.3	59.3	49.2	39.3	29.4	19.5	9.7
EEC	8.2	16.8	25.8	35.0	44.7	54.8	65.4	76.4	87.9
HEA	91.8	83.2	74.2	65.0	55.3	45.2	34.6	23.6	12.1
EEC	11.3	22.2	32.9	43.2	53.3	63.2	72.7	82.1	91.1
EGMEMA	88.7	77.8	67.1	56.8	46.7	36.8	27.3	17.9	8.9
EEC	9.3	18.7	28.3	38.0	47.9	58.0	68.2	78.6	89.2
HEMA	90.7	81.3	71.7	62.0	52.1	42.0	31.8	21.4	10.8

B.2 Hybrid Kinetics

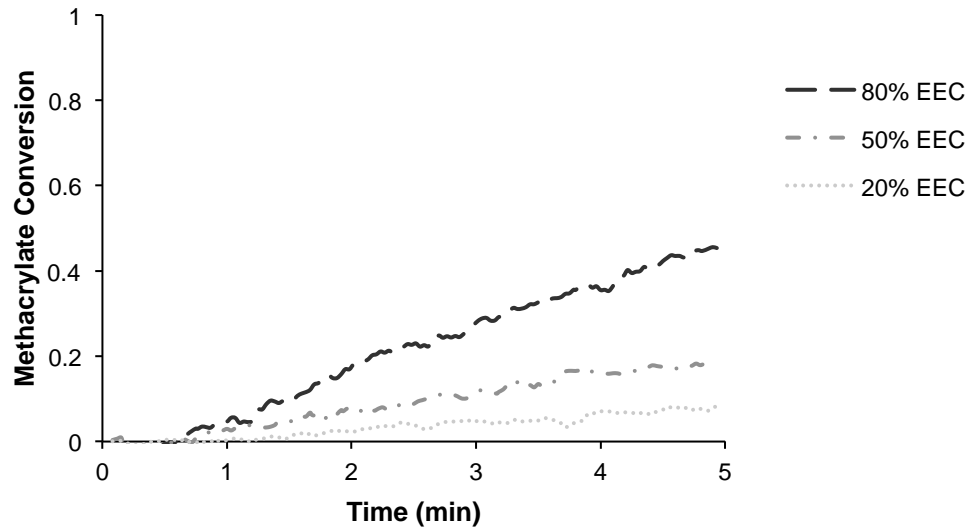


Figure B-1. EGMEMA conversion in a formulation with only 0.2 wt% DMPA as a photoinitiator, no DAI. This demonstrates that the increasing methacrylate conversion is a result of the presence of EEC, not the cationic active centers.

B.3 Viscosity Studies

Formulation viscosity was measured using a rotational cup and bob viscometer (Brookfield, Model No. DV-I+) equipped with a small sample adapter. A rotation speed of 100 RPM and S34 spindle was used for all formulations, except pure EEC. EEC required a reduced rotation speed of 3 RPM and the S18 spindle because of its higher viscosity. All samples were allowed to equilibrate to a temperature of 25°C over 30 minutes before the viscosity was recorded.

In order to use the Refutas equation, all viscosities were transformed from cP to cSt using an experimentally determined density. Graduated pipets were used to measure 1 mL of each formulation, which was then weighed.

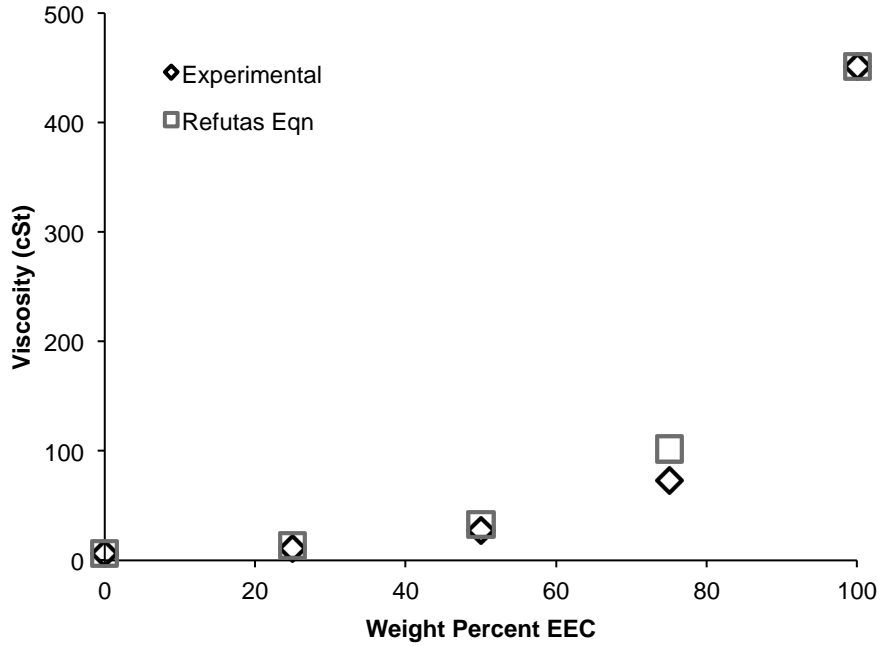


Figure B-2. Comparison of experimental and Refutas-predicted viscosities of EEC/HEMA formulations.

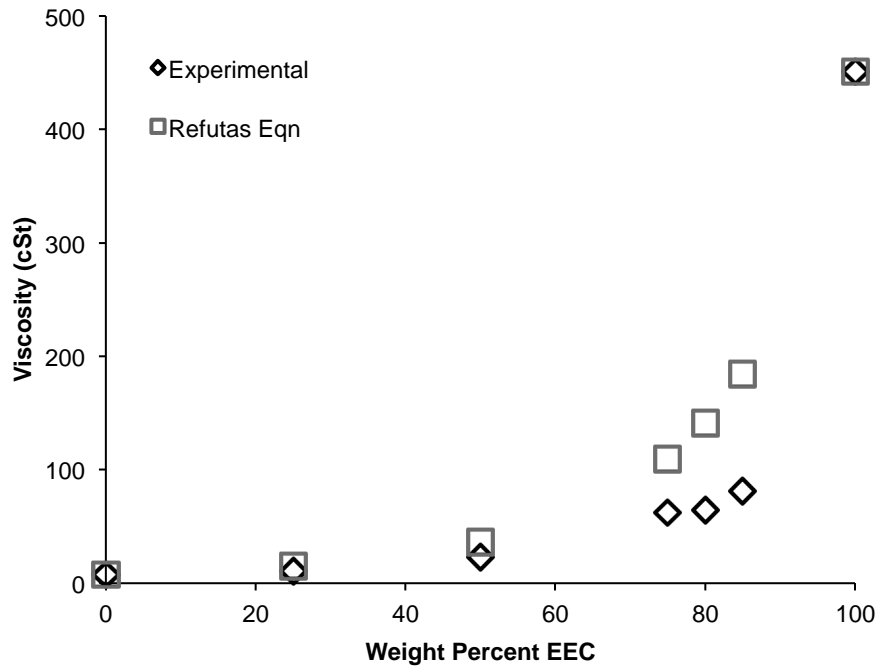


Figure B-3. Comparison of experimental and Refutas-predicted viscosities of EEC/HEA formulations.

B.4 Hybrid Physical Properties

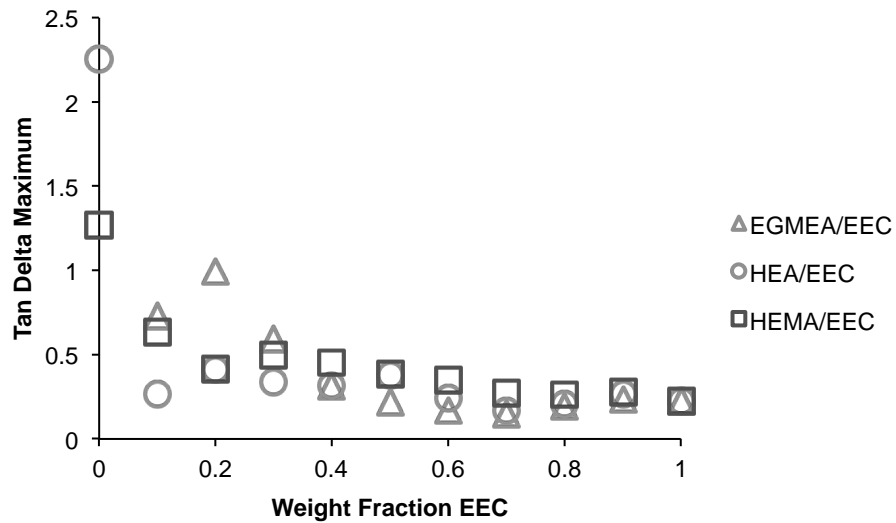


Figure B-4. Maximum height of the $\tan \delta$ for the hybrid formulations.

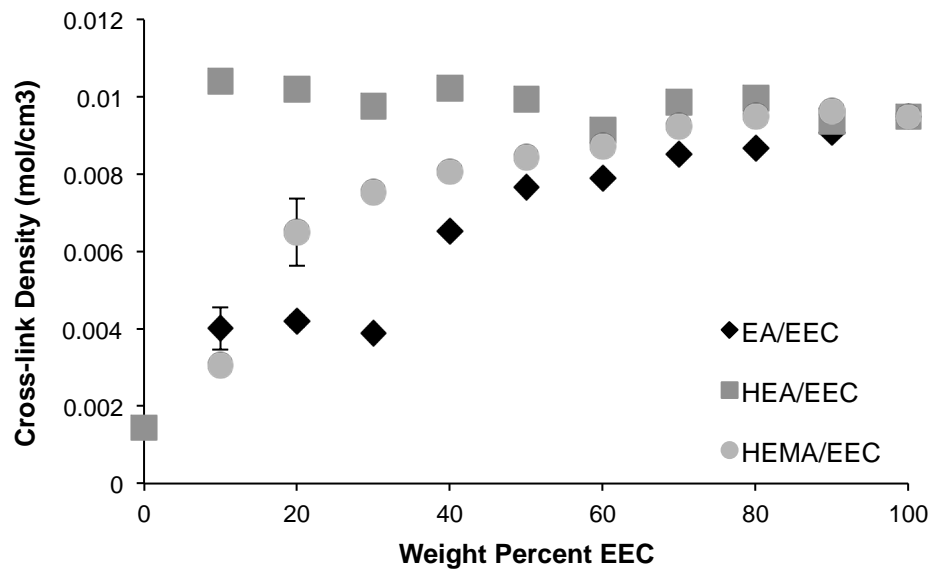


Figure B-5. Cross-link density of the hybrid formulations. Calculated from Equation 1-30.

APPENDIX C
SUPPLEMENTAL INFORMATION FOR CHAPTER 7
(ORIGINAL SHADOW CURE METHOD)

C.1 Light Interactions with PDMS

Since the majority of the shadow cure experiments are conducted in a PDMS mold, it is important to demonstrate the ability, or lack thereof, of PDMS to transmit UV light. To ensure shadow cure results were not the result of a light-guiding effect, pieces of PDMS of various thicknesses were placed under a 100 W mercury arc lamp (Efos, Model No. A4000, 250-450 nm band pass filter) and the amount of transmitted irradiance was measured using a radiometer (Versaprobe Pro, Con-Trol Cure, Table C-1). The effective irradiance was measured by placing the end of the lamp's 3 mm light guide directly onto the radiometer. To measure the transmitted irradiance, the end of the lamp's light guide was placed onto the piece of PDMS, which was placed onto the radiometer; there was no measurable space between the three objects. Very little effective irradiance is transmitted through the PDMS even at relatively high intensities (<0.4%), which suggests the shadow cure shown in the experiments is not a light-guiding effect but true diffusion of the cationic active centers.

Table C-1. Transmitted irradiance results for various PDMS thicknesses and values of effective irradiance.

Effective Irradiance (mW/cm²)	PDMS Thickness (mm)	Transmitted Irradiance (mW/cm²)
130	1.5	0.0
110	1.2	0.0
110	0.8	0.4
80	0.8	0.2
60	0.8	0.1
40	0.8	0.1
23	0.8	0.0

C.2 Preliminary Work – Hexagonal Design

A response surface for both volume of cure and length of shadow cure was generated using a hexagonal design in Design Expert 9.0 by State-Ease, Inc. Two factors were varied: sample thickness (3 to 9 mm) and effective irradiance (10 to 90 mW/cm²). The sample formulation consisted of EEC with 0.5 wt% DAI. The exposure time was held constant at 5 minutes, and the exposure area was 0.5 cm². Four center points were used.

For the first response, volume of cure, a 2FI model (2 factor interaction) was suggested in Design Expert. The response surface for volume of cure (Figure C-1) shows cure volume is maximized as thickness and effective irradiance are maximized (within the design space). The effective irradiance, sample thickness, and the interaction of the two factors were found to be significant. The standard deviation is 142.7 mm^3 off a mean of 956.0 mm^3 and an R^2 value of 0.8961. The large standard deviation and low R^2 value are most likely due to error in measurement. Volume of the cure for a sample was calculated submerging the sample in a vial of water and measuring the displaced water. Measurements were only accurate to a tenth of a mL; using a microliter pipet would provide more accurate results. Volume measurements can also be skewed by trapped air bubbles in the sample, which occur in parts of the sample that are not fully solid.

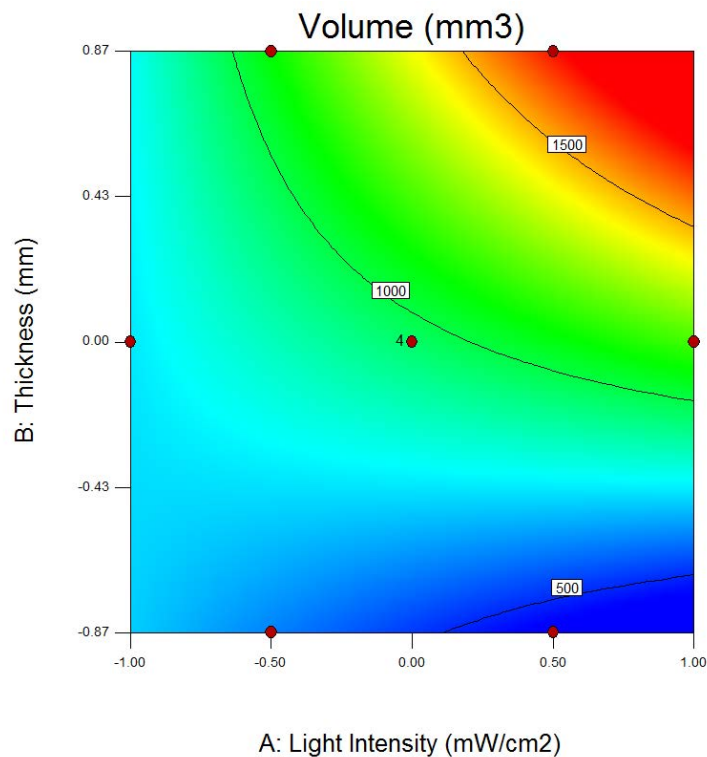


Figure C-1. Response surface of a two factor hexagonal design predicting values of cure volume for a range of effective irradiance and sample thicknesses. Generated in Design Expert.

The second response, length of shadow cure, followed a quadratic model with Factors A (effective irradiance), B (sample thickness), A^2 , and B^2 significant to the model. The response surface (Figure C-2) shows shadow cure length is maximized when sample thickness is maximized. Except for the extremes of the factor space, light intensity does not have a large affect of shadow cure length at high sample thickness.

The standard deviation was found to be 1.32 mm with a model mean of 24.8 mm and an R^2 value of 0.9916.

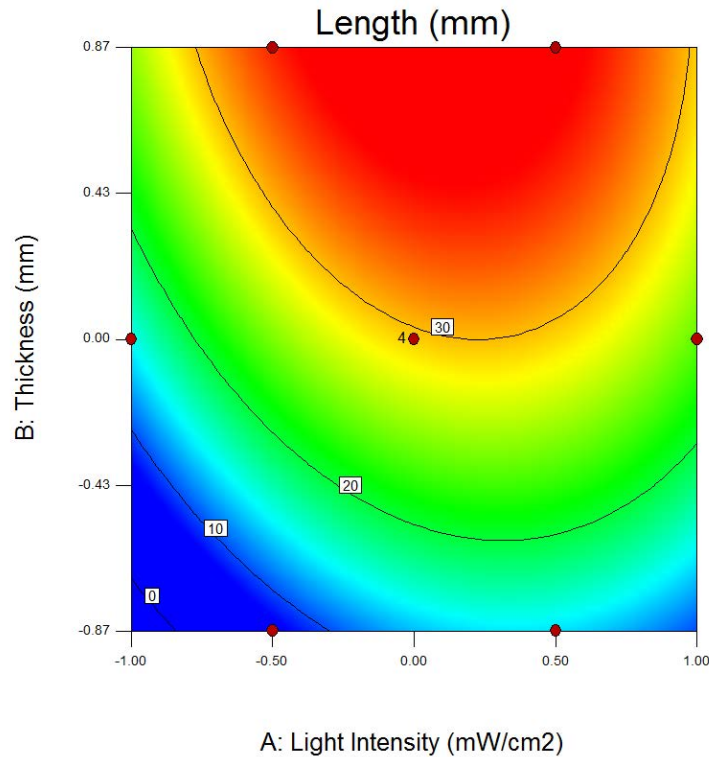


Figure C-2. Response surface of a two factor hexagonal design predicting values of shadow cure length for a range of effective irradiance and sample thicknesses. Generated in Design Expert.

Model equations were also generated for volume of cure (Equation C-1) and shadow cure length (Equation C-2) from the hexagonal design.

$$\text{Volume of Cure} = 956.0 + 213.33(A) + 435(B) + 400(AB) \quad (\text{C-1})$$

$$\text{Shad. Cure Length} = 29.5 + 4.5(A) + 12.25(B) - 10(A^2) - 4.25(B^2) \quad (\text{C-2})$$

These equations were used to predict the values of checkpoints to determine the validity of the model. Predicted values for both responses are compared to the experimentally determined values in Table C-2.

Table C-2. Comparison of predicted and experimental values for both responses. Predicted values were calculated using the model equations generated in Design Expert.

	Predicted Volume	Exptl Volume	Percent Difference	Predicted Length	Exptl Length	Percent Difference
CP 1	521 mm ³	500 mm ³	4.0%	13 mm	9 mm	30.8%
CP 2	1393 mm ³	1240 mm ³	11.0%	37 mm	35 mm	5.4%

Both model equations give a rough estimate of cure volume and shadow cure length. Increased accuracy will be obtained by refining measurement techniques, and by creating a model that includes more factors. Also, the exposure area will be considered and how its size influences the amount of shadow/dark cure.

C.3 Central Composite Design

Table C-3. Factor levels of the 30 CCD samples.

Sample	Factor Levels			
	Eff. Irradiance	Sample Depth	Exposure Time	Exposure Area
1	-2	0	0	0
2	0	0	-2	0
3	0	0	0	0
4	0	0	0	0
5	2	0	0	0
6	1	1	-1	-1
7	1	1	1	-1
8	0	-2	0	0
9	0	0	0	0
10	-1	-1	-1	1
11	0	0	0	0
12	0	0	0	-2
13	0	0	0	0
14	-1	-1	-1	-1
15	0	0	0	0
16	1	-1	1	-1
17	1	-1	1	1
18	-1	-1	1	1
19	-1	1	-1	1
20	1	1	1	1
21	-1	1	1	-1
22	-1	1	1	1
23	1	1	-1	1
24	-1	-1	1	-1
25	0	0	0	2
26	0	2	0	0
27	1	-1	-1	1
28	-1	1	-1	-1
29	0	0	2	0
30	1	-1	-1	-1

C.4 CCD Models

C.4.1 ANOVA of the Shadow Cure Length Response

Response 1 Shdw Cure Length
ANOVA for Response Surface 2FI model

Analysis of variance table [Partial sum of squares - Type III]

Source	Sum of Squares	df	Mean Square	F Value	p-value
Model	316.75	10	31.68	6.33	0.0003 significant
<i>A-Effective Irradiance</i>	3.02	1	3.02	0.60	0.4463
<i>B-Sample Depth</i>	128.90	1	128.90	25.78	< 0.0001
<i>C-Exposure Time</i>	34.37	1	34.37	6.87	0.0168
<i>D-Exposure Area</i>	0.44	1	0.44	0.089	0.7693
<i>AB</i>	64.56	1	64.56	12.91	0.0019
<i>AC</i>	15.05	1	15.05	3.01	0.0989
<i>AD</i>	0.60	1	0.60	0.12	0.7327
<i>BC</i>	52.06	1	52.06	10.41	0.0044
<i>BD</i>	6.15	1	6.15	1.23	0.2813
<i>CD</i>	11.59	1	11.59	2.32	0.1443
Residual	95.01	19	5.00		
<i>Lack of Fit</i>	90.90	14	6.49	7.90	0.0161 significant
<i>Pure Error</i>	4.11	5	0.82		
Cor Total	411.76	29			

Std. Dev. 2.24 R-Squared 0.7693
Mean 21.71 Adj R-Squared 0.6478
C.V. % 10.30 Pred R-Squared 0.3002
PRESS 288.13 Adeq Precision 10.798

Factor	Coefficient		Standard Error		95% CI		VIF
	Estimate	df	Error	Low	High		
Intercept	21.71	1	0.41	20.86	22.57		
A-Effective Irradiance	0.35	1	0.46	-0.60	1.31	1.00	
B-Sample Depth	2.32	1	0.46	1.36	3.27	1.00	
C-Exposure Time	1.20	1	0.46	0.24	2.15	1.00	
D-Exposure Area	0.14	1	0.46	-0.82	1.09	1.00	
AB	-2.01	1	0.56	-3.18	-0.84	1.00	
AC	0.97	1	0.56	-0.20	2.14	1.00	
AD	-0.19	1	0.56	-1.36	0.98	1.00	
BC	-1.80	1	0.56	-2.97	-0.63	1.00	
BD	-0.62	1	0.56	-1.79	0.55	1.00	
CD	-0.85	1	0.56	-2.02	0.32	1.00	

Final Equation in Terms of Coded Factors:

$$\begin{aligned}
 \text{Shdw Cure Length} = & \\
 & +21.71 \\
 & +0.35 * A \\
 & +2.32 * B \\
 & +1.20 * C \\
 & +0.14 * D \\
 & -2.01 * AB \\
 & +0.97 * AC \\
 & -0.19 * AD \\
 & -1.80 * BC \\
 & -0.62 * BD \\
 & -0.85 * CD
 \end{aligned}$$

C.4.2 ANOVA of the Gel Fraction Response

Response 2 Gel Fraction

ANOVA for Response Surface Linear model

Analysis of variance table [Partial sum of squares - Type III]

Source	Sum of Squares	df	Mean Square	F Value	p-value
Model	531.60	4	132.90	21.02	< 0.0001 significant
<i>A-Effective Irradiance</i>	<i>234.01</i>	<i>1</i>	<i>234.01</i>	<i>37.00</i>	<i>< 0.0001</i>
<i>B-Sample Depth</i>	<i>3.14</i>	<i>1</i>	<i>3.14</i>	<i>0.50</i>	<i>0.4875</i>
<i>C-Exposure Time</i>	<i>143.69</i>	<i>1</i>	<i>143.69</i>	<i>22.72</i>	<i>< 0.0001</i>
<i>D-Exposure Area</i>	<i>150.76</i>	<i>1</i>	<i>150.76</i>	<i>23.84</i>	<i>< 0.0001</i>
Residual	158.10	25	6.32		
<i>Lack of Fit</i>	<i>154.34</i>	<i>20</i>	<i>7.72</i>	<i>10.27</i>	<i>0.0085 significant</i>
<i>Pure Error</i>	<i>3.76</i>	<i>5</i>	<i>0.75</i>		
Cor Total	689.70	29			

Std. Dev. 2.51 R-Squared 0.7708
 Mean 18.80 Adj R-Squared 0.7341
 C.V. % 13.38 Pred R-Squared 0.6488
 PRESS 242.20 Adeq Precision 16.437

Factor	Coefficient		Standard 95% CI			VIF
	Estimate	df	Error	Low	High	
Intercept	18.80	1	0.46	17.85	19.74	
A-Effective Irradiance	3.12	1	0.51	2.07	4.18	1.00
B-Sample Depth	-0.36	1	0.51	-1.42	0.70	1.00
C-Exposure Time	2.45	1	0.51	1.39	3.50	1.00
D-Exposure Area	2.51	1	0.51	1.45	3.56	1.00

Final Equation in Terms of Coded Factors:

Cross-linked Mass =

+18.80

+3.12 * A

-0.36 * B

+2.45 * C

+2.51 * D

C.5 Model Accuracy

Table C-4. Checkpoint samples. Standard deviation of shadow cure length = 2.24 mm. Standard deviation of gel fraction = 0.03.

	Factor Levels				Shadow Cure Length (mm)				Gel Fraction			
	EI	SD	ET	EA	Exp.	Pred.	% Error	Within Std. Dev.	Exp.	Pred.	% Error	Within Std. Dev.
CP 1	-1.53	0	1.56	0.5	23.4	20.3	13.2		0.21	0.19	9.5	✓
CP 2	1.14	-1	-1.56	-2	13.2	12.0	9.1	✓	0.12	0.14	14.2	✓
CP 3	1.64	1	-0.22	1	18.7	20.5	8.8	✓	0.11	0.26	57.7	
CP 4	0.7	-1	0.22	0.5	24.4	22.1	9.4		0.24	0.23	4.2	✓
CP 5	-0.64	-1	-0.78	1	16.6	17.6	5.7	✓	0.19	0.18	5.3	✓
CP 6	-0.2	-0.33	0.67	-0.5	16.8	21.9	23.3		0.20	0.19	5.0	✓
CP 7	0.44	0	-0.56	-1	18.9	20.4	7.4	✓	0.16	0.16	0	✓
CP 8	-0.44	0	0.78	0.5	18.7	21.9	14.6		0.22	0.21	4.5	✓
CP 9	-1.92	2	-1.33	-1.5	14.0	38.3	63.4		0.02	0.05	40.0	✓
CP 10	-1.32	-1	-0.22	1.5	15.6	17.7	11.9	✓	0.19	0.18	5.3	✓

Table C-5. Statistical Variables Only. Standard deviation of shadow cure length = 2.32 mm. Standard deviation of gel fraction = 0.03.

	Factor Levels				Shadow Cure Length (mm)				Gel Fraction			
	EI	SD	ET	EA	Exp.	Pred.	% Error	Within Std. Dev.	Exp.	Pred.	% Error	Within Std. Dev.
CP 1	-1.53	0	1.56	0.5	23.4	23.0	13.2	✓	0.21	0.19	9.5	✓
CP 2	1.14	-1	-1.56	-2	13.2	17.4	9.1		0.12	0.14	14.2	✓
CP 3	1.64	1	-0.22	1	18.7	21.5	8.8	✓	0.11	0.26	57.7	
CP 4	0.7	-1	0.22	0.5	24.4	21.7	9.4		0.24	0.23	4.2	✓
CP 5	-0.64	-1	-0.78	1	16.6	15.5	5.7	✓	0.19	0.17	5.3	✓
CP 6	-0.2	-0.33	0.67	-0.5	16.8	21.9	23.3		0.20	0.19	5.0	✓
CP 7	0.44	0	-0.56	-1	18.9	21.2	7.4	✓	0.16	0.16	0	✓
CP 8	-0.44	0	0.78	0.5	18.7	22.5	14.6		0.22	0.21	4.5	✓
CP 9	-1.92	2	-1.33	-1.5	14.0	36.6	63.4		0.02	0.06	40.0	
CP 10	-1.32	-1	-0.22	1.5	15.6	15.6	11.9	✓	0.19	0.18	5.3	✓

C.6 Factor Math

Variables/Definitions:

Real = unaltered value with units, *e.g.* 30 mW/cm²

Coded = value transformed into coded design space, unitless

Max = maximum value

Min = minimum value

R = Real value, to be converted into coded design space

C = Coded value, converted real value

$$\frac{(Real\ Max - Real\ Min)}{(Coded\ Max - Coded\ Min)} = A \quad (C-3)$$

$$\frac{(R - Real\ Min)}{A} = B \quad (C-4)$$

$$C = B + Coded\ Min \quad (C-5)$$

Effective Irradiance Example:

Real Max = 100 mW/cm²

Coded Max = 2

Real Min = 10 mW/cm²

Coded Min = -2

R = 53.2 mW/cm²

$$\frac{(100 - 10)}{(2 - [-2])} = 22.5 \quad (C-6)$$

$$\frac{(53.2 - 10)}{22.5} = 1.92 \quad (C-7)$$

$$C = 1.92 + [-2] = -0.08 \quad (C-8)$$

Sample Depth Example:

Real Max = 9 mm

Coded Max = 2

Real Min = 3 mm

Coded Min = -2

R = 5.5 mm

$$\frac{(9 - 3)}{(2 - [-2])} = 1.5 \quad (C-9)$$

$$\frac{(5.5 - 3)}{1.5} = 1.67 \quad (C-10)$$

$$C = 1.67 + [-2] = -0.33 \quad (C-11)$$

Exposure Area Example:Real Max = 0.7 cm²Real Min = 0.3 cm²R = 0.35 cm²

Coded Max = 2

Coded Min = -2

$$\frac{(0.7 - 0.3)}{(2 - [-2])} = 0.1 \quad (\text{C-12})$$

$$\frac{(0.35 - 0.3)}{0.1} = 0.5 \quad (\text{C-13})$$

$$C = 0.5 + [-2] = -1.5 \quad (\text{C-14})$$

Exposure Time Example:

Real Max = 10 min

Real Min = 1 min

R = 4 min

Coded Max = 2

Coded Min = -2

$$\frac{(10 - 1)}{(2 - [-2])} = 2.25 \quad (\text{C-15})$$

$$\frac{(4 - 1)}{2.25} = 1.33 \quad (\text{C-16})$$

$$C = 1.33 + [-2] = -0.67 \quad (\text{C-17})$$

APPENDIX D
SUPPLEMENTAL INFORMATION FOR CHAPTER 8
(TRANSFERABLE SHADOW CURE METHOD)

***Note:** The central composite design (Section C.3, Table C-3) and the factor math (Section C.6) are identical to that used in Chapter 7.

D.1 Shadow Cure Kinetics

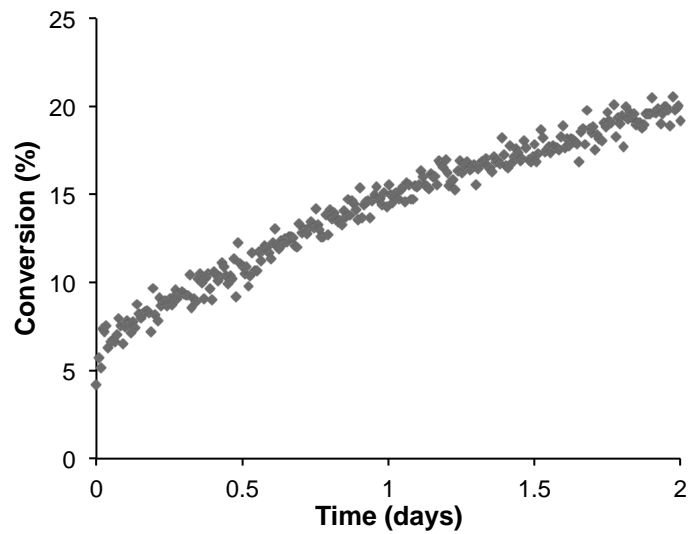


Figure D-1. Conversion of a transferrable shadow cure sample monitored by real-time Raman spectroscopy and initiated with 30 mW/cm^2 effective irradiance. Data points were collected every 10 minutes over a 2-day period.

D.2 CCD Models

D.2.1 ANOVA for CCD1, Avg Conversion

ANOVA for Response Surface Linear model

Analysis of variance table [Partial sum of squares - Type III]

Source	Sum of Squares	df	Mean Square	F Value	p-value	
Model	0.023	4	5.750E-003	26.13	< 0.0001	significant
<i>A-Effective Irradiance</i>	<i>7.046E-003</i>	<i>1</i>	<i>7.046E-003</i>	<i>32.02</i>	<i>< 0.0001</i>	
<i>B-Sample Depth</i>	<i>9.440E-003</i>	<i>1</i>	<i>9.440E-003</i>	<i>42.91</i>	<i>< 0.0001</i>	
<i>C-Exposure Time</i>	<i>5.764E-003</i>	<i>1</i>	<i>5.764E-003</i>	<i>26.20</i>	<i>< 0.0001</i>	
<i>D-Exposure Area</i>	<i>7.496E-004</i>	<i>1</i>	<i>7.496E-004</i>	<i>3.41</i>	<i>0.0768</i>	
Residual	5.500E-003	25	2.200E-004			
<i>Lack of Fit</i>	<i>4.894E-003</i>	<i>20</i>	<i>2.447E-004</i>	<i>2.02</i>	<i>0.2245</i>	<i>not significant</i>
<i>Pure Error</i>	<i>6.068E-004</i>	<i>5</i>	<i>1.214E-004</i>			
Cor Total	0.028	29				

Std. Dev.	0.015	R-Squared	0.8070
Mean	0.44	Adj R-Squared	0.7761
C.V. %	3.40	Pred R-Squared	0.7090
PRESS	8.294E-003	Adeq Precision	19.173

Factor	Coefficient		Standard Error	95% CI		VIF
	Estimate	df		Low	High	
Intercept	0.44	1	2.708E-003	0.43	0.44	
A-Effective Irradiance	0.017	1	3.028E-003	0.011	0.023	1.00
B-Sample Depth	-0.020	1	3.028E-003	-0.026	-0.014	1.00
C-Exposure Time	0.015	1	3.028E-003	9.261E-003	0.022	1.00
D-Exposure Area	-5.589E-003	1	3.028E-003	-0.012	6.471E-004	1.00

Final Equation in Terms of Coded Factors:

Average Conversion =

+0.44

+0.017 * A

-0.020 * B

+0.015 * C

-5.589E-003 * D

D.2.2 ANOVA for CCD1, LCS wt%

ANOVA for Response Surface Quadratic model

Analysis of variance table [Partial sum of squares - Type III]

Source	Sum of Squares	df	Mean Square	F Value	p-value Prob > F	
Model	4062.70	14	290.19	28.12	< 0.0001	significant
<i>A-Effective Irradiance</i>	<i>2184.90</i>	<i>1</i>	<i>2184.90</i>	<i>211.68</i>	<i>< 0.0001</i>	
<i>B-Sample Depth</i>	<i>271.00</i>	<i>1</i>	<i>271.00</i>	<i>26.26</i>	<i>0.0001</i>	
<i>C-Exposure Time</i>	<i>828.26</i>	<i>1</i>	<i>828.26</i>	<i>80.25</i>	<i>< 0.0001</i>	
<i>D-Exposure Area</i>	<i>89.15</i>	<i>1</i>	<i>89.15</i>	<i>8.64</i>	<i>0.0102</i>	
<i>AB</i>	<i>76.43</i>	<i>1</i>	<i>76.43</i>	<i>7.40</i>	<i>0.0158</i>	
<i>AC</i>	<i>332.56</i>	<i>1</i>	<i>332.56</i>	<i>32.22</i>	<i>< 0.0001</i>	
<i>AD</i>	<i>6.14</i>	<i>1</i>	<i>6.14</i>	<i>0.59</i>	<i>0.4527</i>	
<i>BC</i>	<i>66.25</i>	<i>1</i>	<i>66.25</i>	<i>6.42</i>	<i>0.0229</i>	
<i>BD</i>	<i>0.57</i>	<i>1</i>	<i>0.57</i>	<i>0.055</i>	<i>0.8178</i>	
<i>CD</i>	<i>25.31</i>	<i>1</i>	<i>25.31</i>	<i>2.45</i>	<i>0.1382</i>	
<i>A^2</i>	<i>173.02</i>	<i>1</i>	<i>173.02</i>	<i>16.76</i>	<i>0.0010</i>	
<i>B^2</i>	<i>0.063</i>	<i>1</i>	<i>0.063</i>	<i>6.100E-003</i>	<i>0.9388</i>	
<i>C^2</i>	<i>9.44</i>	<i>1</i>	<i>9.44</i>	<i>0.91</i>	<i>0.3540</i>	
<i>D^2</i>	<i>0.094</i>	<i>1</i>	<i>0.094</i>	<i>9.079E-003</i>	<i>0.9253</i>	
Residual	154.82	15	10.32			
<i>Lack of Fit</i>	<i>122.26</i>	<i>10</i>	<i>12.23</i>	<i>1.88</i>	<i>0.2524</i>	<i>not significant</i>
<i>Pure Error</i>	<i>32.56</i>	<i>5</i>	<i>6.51</i>			
Cor Total	4217.52	29				

Std. Dev. 3.21 R-Squared 0.9633
 Mean 14.54 Adj R-Squared 0.9290
 C.V. % 22.09 Pred R-Squared 0.8219
 PRESS 751.13 Adeq Precision 19.968

Factor	Coefficient		Standard Error		95% CI		VIF
	Estimate	df	Error	Low	High		
Intercept	12.06	1	1.31	9.26	14.85		
A-Effective Irradiance	9.54	1	0.66	8.14	10.94	1.00	
B-Sample Depth	-3.36	1	0.66	-4.76	-1.96	1.00	
C-Exposure Time	5.87	1	0.66	4.48	7.27	1.00	
D-Exposure Area	1.93	1	0.66	0.53	3.33	1.00	
AB	-2.19	1	0.80	-3.90	-0.47	1.00	
AC	4.56	1	0.80	2.85	6.27	1.00	
AD	0.62	1	0.80	-1.09	2.33	1.00	
BC	-2.03	1	0.80	-3.75	-0.32	1.00	
BD	0.19	1	0.80	-1.52	1.90	1.00	
CD	1.26	1	0.80	-0.45	2.97	1.00	
A ²	2.51	1	0.61	1.20	3.82	1.05	
B ²	-0.048	1	0.61	-1.36	1.26	1.05	
C ²	0.59	1	0.61	-0.72	1.89	1.05	
D ²	0.058	1	0.61	-1.25	1.37	1.05	

Final Equation in Terms of Coded Factors:

$$\begin{aligned}
 \text{Light-Cure Mass} = & \\
 & +12.06 \\
 & +9.54 * A \\
 & -3.36 * B \\
 & +5.87 * C \\
 & +1.93 * D \\
 & -2.19 * AB \\
 & +4.56 * AC \\
 & +0.62 * AD \\
 & -2.03 * BC \\
 & +0.19 * BD \\
 & +1.26 * CD \\
 & +2.51 * A^2 \\
 & -0.048 * B^2 \\
 & +0.59 * C^2 \\
 & +0.058 * D^2
 \end{aligned}$$

D.2.3 ANOVA for CCD2, Average Conversion

ANOVA for Response Surface Linear model

Analysis of variance table [Partial sum of squares - Type III]

Source	Sum of Squares	df	Mean Square	F Value	p-value	
Model	0.037	4	9.282E-003	3.92	0.0133	significant
<i>A-Effective Irradiance</i>	<i>0.015</i>	<i>1</i>	<i>0.015</i>	<i>6.21</i>	<i>0.0197</i>	
<i>B-Sample Depth</i>	<i>3.473E-003</i>	<i>1</i>	<i>3.473E-003</i>	<i>1.47</i>	<i>0.2374</i>	
<i>C-Exposure Time</i>	<i>0.019</i>	<i>1</i>	<i>0.019</i>	<i>7.98</i>	<i>0.0092</i>	
<i>D-Exposure Area</i>	<i>4.283E-005</i>	<i>1</i>	<i>4.283E-005</i>	<i>0.018</i>	<i>0.8941</i>	
Residual	0.059	25	2.370E-003			
<i>Lack of Fit</i>	<i>0.059</i>	<i>20</i>	<i>2.947E-003</i>	<i>50.57</i>	<i>0.0002</i>	<i>significant</i>
<i>Pure Error</i>	<i>2.914E-004</i>	<i>5</i>	<i>5.829E-005</i>			
Cor Total	0.096	29				

Std. Dev. 0.049 R-Squared 0.3853
 Mean 0.40 Adj R-Squared 0.2869
 C.V. % 12.11 Pred R-Squared 0.0608
 PRESS 0.091 Adeq Precision 6.661

Factor	Coefficient Estimate	Standard Error	95% CI Low	95% CI High	VIF
Intercept	0.40	1 8.888E-003	0.38	0.42	
A-Effective Irradiance	0.025	1 9.937E-003	4.290E-003	0.045	1.00
B-Sample Depth	-0.012	1 9.937E-003	-0.032	8.435E-003	1.00
C-Exposure Time	0.028	1 9.937E-003	7.603E-003	0.049	1.00
D-Exposure Area	1.336E-003	1 9.937E-003	-0.019	0.022	1.00

Final Equation in Terms of Coded Factors:

$$\begin{aligned} \text{Average Conversion} &= \\ &+0.40 \\ &+0.025 \quad * A \\ &-0.012 \quad * B \\ &+0.028 \quad * C \\ &+1.336E-003 \quad * D \end{aligned}$$

D.2.4 ANOVA for CCD2, Average Conversion 13 wks Post-Illumination

ANOVA for Response Surface Linear model

Analysis of variance table [Partial sum of squares - Type III]

Source	Sum of Squares	df	Mean Square	F Value	p-value
Model	0.040	4	0.010	10.39	< 0.0001 significant
<i>A-Effective Irradiance</i>	<i>0.014</i>	<i>1</i>	<i>0.014</i>	<i>14.21</i>	<i>0.0009</i>
<i>B-Sample Depth</i>	<i>6.757E-003</i>	<i>1</i>	<i>6.757E-003</i>	<i>6.96</i>	<i>0.0141</i>
<i>C-Exposure Time</i>	<i>0.020</i>	<i>1</i>	<i>0.020</i>	<i>20.34</i>	<i>0.0001</i>
<i>D-Exposure Area</i>	<i>3.743E-005</i>	<i>1</i>	<i>3.743E-005</i>	<i>0.039</i>	<i>0.8459</i>
Residual	0.024	25	9.703E-004		
<i>Lack of Fit</i>	<i>0.023</i>	<i>20</i>	<i>1.164E-003</i>	<i>5.98</i>	<i>0.0283</i> significant
<i>Pure Error</i>	<i>9.739E-004</i>	<i>5</i>	<i>1.948E-004</i>		
Cor Total	0.065	29			

Std. Dev. 0.031 R-Squared 0.6243
 Mean 0.59 Adj R-Squared 0.5642
 C.V. % 5.29 Pred R-Squared 0.4288
 PRESS 0.037 Adeq Precision 11.115

Factor	Coefficient	Standard Error	95% CI		VIF
	Estimate		Low	High	
Intercept	0.59	1 5.687E-003	0.58	0.60	
A-Effective Irradiance	0.024	1 6.358E-003	0.011	0.037	1.00
B-Sample Depth	-0.017	1 6.358E-003	-0.030	-3.684E-003	1.00
C-Exposure Time	0.029	1 6.358E-003	0.016	0.042	1.00
D-Exposure Area	-1.249E-003	1 6.358E-003	-0.014	0.012	1.00

Final Equation in Terms of Coded Factors:

$$\begin{aligned} \text{2nd Chk Conversion} &= \\ &+0.59 \\ &+0.024 * A \\ &-0.017 * B \\ &+0.029 * C \\ &-1.249E-003 * D \end{aligned}$$

D.2.5 ANOVA for CCD2, LCS wt%

ANOVA for Response Surface 2FI model

Analysis of variance table [Partial sum of squares - Type III]

Source	Sum of Squares	df	Mean Square	F Value	p-value	
Model	543.77	10	54.38	4.56	0.0022	significant
<i>A-Effective Irradiance</i>	141.08	1	141.08	11.84	0.0027	
<i>B-Sample Depth</i>	55.68	1	55.68	4.67	0.0436	
<i>C-Exposure Time</i>	49.20	1	49.20	4.13	0.0564	
<i>D-Exposure Area</i>	16.87	1	16.87	1.42	0.2488	
<i>AB</i>	75.05	1	75.05	6.30	0.0213	
<i>AC</i>	119.81	1	119.81	10.05	0.0050	
<i>AD</i>	57.89	1	57.89	4.86	0.0401	
<i>BC</i>	12.96	1	12.96	1.09	0.3101	
<i>BD</i>	4.04	1	4.04	0.34	0.5671	
<i>CD</i>	11.18	1	11.18	0.94	0.3448	
Residual	226.42	19	11.92			
<i>Lack of Fit</i>	218.38	14	15.60	9.71	0.0101	significant
<i>Pure Error</i>	8.03	5	1.61			
Cor Total	770.19	29				

Std. Dev.	3.45	R-Squared	0.7060
Mean	5.43	Adj R-Squared	0.5513
C.V. %	63.60	Pred R-Squared	0.0972
PRESS	695.31	Adeq Precision	10.140

Factor	Coefficient		Standard 95% CI		95% CI	VIF
	Estimate	df Error	Low	High		
Intercept	5.43	1	0.63	4.11	6.75	
A-Effective Irradiance	2.42	1	0.70	0.95	3.90	1.00
B-Sample Depth	-1.52	1	0.70	-3.00	-0.048	1.00
C-Exposure Time	1.43	1	0.70	-0.043	2.91	1.00
D-Exposure Area	0.84	1	0.70	-0.64	2.31	1.00
AB	-2.17	1	0.86	-3.97	-0.36	1.00
AC	2.74	1	0.86	0.93	4.54	1.00
AD	1.90	1	0.86	0.096	3.71	1.00
BC	-0.90	1	0.86	-2.71	0.91	1.00
BD	-0.50	1	0.86	-2.31	1.30	1.00
CD	0.84	1	0.86	-0.97	2.64	1.00

Final Equation in Terms of Coded Factors:

$$\begin{aligned}
 \text{Light-Cure Mass} &= \\
 &+5.43 \\
 &+2.42 * A \\
 &-1.52 * B \\
 &+1.43 * C \\
 &+0.84 * D \\
 &-2.17 * AB \\
 &+2.74 * AC \\
 &+1.90 * AD \\
 &-0.90 * BC \\
 &-0.50 * BD \\
 &+0.84 * CD
 \end{aligned}$$

D.3 Model Accuracy

Table D-1. Checkpoints for CCD 1 model. Standard deviation of shadow cure conversion = 0.015. Standard deviation of LCS wt% = 3.21%.

	Factor Levels				Fractional Conversion				LCS wt%			
	EI	SD	ET	EA	Exp.	Pred.	% Error	Within Std. Dev.	Exp.	Pred.	% Error	Within Std. Dev.
CP 1	-1.53	0	1.56	0.5	0.423	0.431	2.0	✓	4.0	4.5	11.6	✓
CP 2	1.14	-1	-1.56	-2	0.441	0.462	4.6		4.2	12.3	66.0	
CP 3	1.64	1	-0.22	1	0.442	0.435	1.4	✓	29.2	28.0	4.3	✓
CP 4	0.7	-1	0.22	0.5	0.477	0.468	1.8	✓	34.9	28.6	22.2	
CP 5	-0.64	-1	-0.78	1	0.428	0.427	0.2	✓	8.7	5.8	51.3	✓
CP 6	-0.2	-0.33	0.67	-0.5	0.460	0.452	1.7	✓	17.1	13.9	22.8	✓
CP 7	0.44	0	-0.56	-1	0.443	0.441	0.6	✓	7.0	11.1	37.5	
CP 8	-0.44	0	0.78	0.5	0.442	0.438	1.0	✓	13.6	13.0	4.0	✓
CP 9	-1.92	2	-1.33	-1.5	0.363	0.351	3.3	✓	3.4	15.7	78.5	
CP 10	-1.32	-1	-0.22	1.5	0.413	0.421	2.0	✓	5.0	5.0	0	✓

Table D-2. CCD 1 model run with only significant variables. Standard deviation of shadow cure conversion = 0.016. Standard deviation of LCS wt% = 3.1%.

	Factor Levels				Fractional Conversion				LCS wt%			
	EI	SD	ET	EA	Exp.	Pred.	% Error	Within Std. Dev.	Exp.	Pred.	% Error	Within Std. Dev.
CP 1	-1.53	0	1.56	0.5	0.423	0.434		✓	4.0	3.0		✓
CP 2	1.14	-1	-1.56	-2	0.441	0.451			4.2	8.2		
CP 3	1.64	1	-0.22	1	0.442	0.441		✓	29.2	27.3		✓
CP 4	0.7	-1	0.22	0.5	0.477	0.471		✓	34.9	28.8		
CP 5	-0.64	-1	-0.78	1	0.428	0.433		✓	8.7	7.5		✓
CP 6	-0.2	-0.33	0.67	-0.5	0.460	0.449		✓	17.1	14.6		✓
CP 7	0.44	0	-0.56	-1	0.443	0.434		✓	7.0	10.9		
CP 8	-0.44	0	0.78	0.5	0.442	0.440		✓	13.6	12.8		✓
CP 9	-1.92	2	-1.33	-1.5	0.363	0.343		✓	3.4	11.3		
CP 10	-1.32	-1	-0.22	1.5	0.413	0.430		✓	5.0	7.2		✓

Table D-3. Checkpoints for CCD2 model. Standard deviation of shadow cure conversion = 0.049. Standard deviation of LCS wt% = 3.5%.

	Factor Levels				Fractional Conversion				LCS wt%			
	EI	SD	ET	EA	Exp.	Pred.	% Error	Within Std. Dev.	Exp.	Pred.	% Error	Within Std. Dev.
CP 1	-0.75	0	-0.38	0.5	0.381	0.374	1.9	✓	0.7	3.4	79.1	✓
CP 2	-0.5	-1	0.75	-2	0.411	0.420	2.0	✓	2.0	3.3	38.1	✓
CP 3	0.75	1	0.63	1	0.402	0.427	5.9	✓	6.6	8.0	17.2	✓
CP 4	0.5	-1	-0.63	0.5	0.362	0.371	2.4	✓	2.64	7.8	66.2	
CP 5	0.25	-1	-0.25	1	0.424	0.415	2.1	✓	0.32	9.0	96.4	
CP 6	1.75	-0.33	1.88	-0.5	0.469	0.511	8.2	✓	40.8	20.7	97.0	
CP 7	1.5	0	-1.88	-1	0.385	0.400	3.8	✓	11.4	-3.5	429.8	
CP 8	-1.75	0	-1.63	0.5	0.335	0.316	6.0	✓	1.7	4.7	63.6	✓
CP 9	-1.5	2	1.25	-1.5	0.401	0.399	0.5	✓	6.1	2.6	131.5	✓
CP 10	1.38	-1	-1.5	1.5	0.412	0.395	4.5	✓	0.8	8.2	90.8	

Table D-4. CCD 2 model run with only significant variables. Standard deviation of shadow cure conversion = 0.048. Standard deviation of percent LCS wt% = 3.4%.

	Factor Levels				Fractional Conversion				LCS wt%			
	EI	SD	ET	EA	Exp.	Pred.	% Error	Within Std. Dev.	Exp.	Pred.	% Error	Within Std. Dev.
CP 1	-0.75	0	-0.38	0.5	0.381	0.373	1.9	✓	0.7	3.6	80.0	✓
CP 2	-0.5	-1	0.75	-2	0.411	0.411	2.0	✓	2.0	4.9	58.4	✓
CP 3	0.75	1	0.63	1	0.402	0.438	5.9	✓	6.6	8.6	22.4	✓
CP 4	0.5	-1	-0.63	0.5	0.362	0.397	2.4	✓	2.64	8.4	68.5	
CP 5	0.25	-1	-0.25	1	0.424	0.401	2.1	✓	0.32	8.9	96.4	
CP 6	1.75	-0.33	1.88	-0.5	0.469	0.498	8.2	✓	40.8	21.0	94.1	
CP 7	1.5	0	-1.88	-1	0.385	0.386	3.8	✓	11.4	-5.0	326.9	
CP 8	-1.75	0	-1.63	0.5	0.335	0.313	6.0	✓	1.7	5.4	68.1	
CP 9	-1.5	2	1.25	-1.5	0.401	0.400	0.5	✓	6.1	4.9	22.9	✓
CP 10	1.38	-1	-1.5	1.5	0.412	0.394	4.5	✓	0.8	10.7	92.9	

Table D-5. Checkpoints for CCD2 model, 13 wk shadow cure conversion. Standard deviation of shadow cure conversion, 13 week post-illumination = 0.031. CCD 2 model run with only significant variables, 3rd column section. Standard deviation = 0.031.

	Factor Levels				Shadow Cure Conversion – 13 wk				Sig Variables Conversion – 13 wk			
	EI	SD	ET	EA	Exp.	Pred.	% Error	Within Std. Dev.	Exp.	Pred.	% Error	Within Std. Dev.
CP 1	-0.75	0	-0.38	0.5	0.574	0.560	2.6	✓	0.574	0.560	2.5	✓
CP 2	-0.5	-1	0.75	-2	0.598	0.618	3.3	✓	0.598	0.615	2.9	✓
CP 3	0.75	1	0.63	1	0.574	0.607	5.5		0.574	0.608	5.7	
CP 4	0.5	-1	-0.63	0.5	0.569	0.600	5.0	✓	0.569	0.600	5.1	✓
CP 5	0.25	-1	-0.25	1	0.611	0.603	1.2	✓	0.611	0.605	1.0	✓
CP 6	1.75	-0.33	1.88	-0.5	0.656	0.691	5.1		0.656	0.691	5.0	
CP 7	1.5	0	-1.88	-1	0.584	0.572	2.0	✓	0.584	0.571	2.2	✓
CP 8	-1.75	0	-1.63	0.5	0.453	0.500	9.5		0.453	0.500	9.6	
CP 9	-1.5	2	1.25	-1.5	0.588	0.557	5.6	✓	0.588	0.555	5.9	
CP 10	1.38	-1	-1.5	1.5	0.599	0.595	0.9	✓	0.599	0.596	0.6	✓

APPENDIX E RAMAN HOW-TO AND TROUBLESHOOTING GUIDE

E.1 Raman How-To Guide

Note: Presented here are some helpful procedures for routine Raman use and/or maintenance. Additional information can also be found in the official Kaiser manual: *Raman Microprobe Operations Manual 2006988 R2*.

- 1. How to check the diameter of the laser beam.**
 - aka, the knife-edge test.
 - See Procedure Alpha
- 2. How to adjust the power output of the laser.**
 - See Procedure Beta
- 3. How to determine the resolution of a confocal fiber and objective.**
 - See Procedure Gamma
- 4. How to check the shape of the laser beam.**
 - See Procedure Delta
- 5. How to check laser hours and other laser information.**
 - See Procedure Epsilon
- 6. How to check whether a fiber has been broken.**
 - See Procedure Zeta
- 7. How to clean a microscope objective.**
 - See Procedure Eta
- 8. How to align the microscope objectives.**
 - See Procedure Theta
- 9. How to set up a line or depth scan using confocal microscopy.**
 - See Procedure Iota
- 10. How to switch the probehead capillary tube sample holder to the cuvette sample holder.**
 - See Procedure Kappa
- 11. How to adjust the Z-range of the microscope stage.**
 - See Procedure Lambda

- 12. How to perform a laser box adjustment.**
 - See Procedure Mu
- 13. How to change the light bulb (white light) on the microscope.**
 - See Procedure Nu
- 14. How to set up the probehead for film or real-time film measurements.**
 - See Procedure Xi
- 15. How to check if the spectrometer CCD is working properly.**
 - See Procedure Omicron
- 16. How to find the sample surface during confocal collection.**
 - See Procedure Pi
- 17. How to check the dark spectrum and collect a new one.**
 - See Procedure Rho
- 18. How to optimize the Raman microscope.**
 - See Procedure Sigma
- 19. How to calibrate the motorized stage.**
 - See Appendix B.3 (page 52) of the Kaiser Raman Microprobe Operations Manual
- 20. How to set up a hyper terminal to access the motorized stage programming.**
 - See 8.4 Appendix D of the ProScan, Prior Scientific, Microscope Automation System Operating Instructions
 - The *Micro* software must be closed in order to set up a hyper terminal.
 - In step 4, select COM PORT 1.
- 21. How to check/replace the microscope lamp house wiring.**
 - See Procedure Tau
- 22. How to check the microscope z-axis motor.**
 - See Procedure Upsilon

E.2 Raman Troubleshooting Guide

Note: For each problem presented here, there is a list of troubleshooting steps that should, hopefully, rectify that problem. These steps are ordered from most likely/least invasive to least likely/most invasive. If Step A solves the problem, do not continue on to Step B. Only continue on to the next step if the previous step was ineffective. If none of the troubleshooting steps fix the problem, contact Kaiser. Additional information can also be found in the official Kaiser manual: *Raman Microprobe Operations Manual 2006988 R2*.

1. Laser power is below normal.

- Typical power levels should be approximately 330 mW out of the laser box coupling, 220 mW out of the probehead, and 10-15 mW out of the microscope 10x objective.

A. Check fiber connections to make sure they are tight.

B. Check to see if the laser is set to full source power. The screen on the laser box should read POWER SET 397 mW. If not, see Procedure Beta.

C. Check fibers to see whether they have been cracked or damaged. See Procedure Zeta.

D. Check power levels out of the laser box coupling, the probehead, and the microscope. If the power level is low out of the laser box, continue to Step E. If the power level is normal out of the laser box, skip to Step G.

E. If the power level is low out of the laser box, check for chips or cracks on the laser box coupling.

F. Following Step E, if the power level is still low out of the laser box, perform a laser box adjustment. See Procedure Mu.

G. If the power level is normal out of the laser box, but low coming out of the probehead or microscope, try cleaning the objective. See Procedure Eta.

H. Following Step G, if the power is still low coming out of the microscope, perform an optimization of the Raman microscope. See Procedure Sigma.

2. There is no Raman spectrum of the sample.

- Check to make sure the shutter is open on the laser box. If using the microscope, check to make sure the shutter on the microscope is open. This shutter is

located on the top of the microscope on the right-hand side, and, if open, there should be a red light on the front of the microscope.

- A. Check fiber connections to make sure they are tight.
- B. Check laser power. If the laser power is low, refer to Problem 1.
- C. Use the default sample, a silicon wafer, to see if it has a spectrum. Silicon should have one prominent peak at approximately 520 cm^{-1} . If the silicon spectrum appears correctly, the problem is most likely with your sample. Either it is not Raman active, or possibly it is a weak Raman scatterer. If using the microscope, switch to the probehead, which has much more laser power. If the spectrum must be collected using the microscope, increasing the sample concentration, lengthening the exposure time, or increasing the number of accumulations might be beneficial.
- D. Check the dark spectrum. See Procedure Rho.
- E. Clean the objective. See Procedure Eta.
- F. Check to make sure the spectrometer is working correctly. See Procedure Omicron.

3. The Raman spectrum is distorted.

- A common distortion of sample spectrum occurs when the sample is polymerized. Often, the polymer sample has more fluorescence under the baseline than the monomer sample. This type of distortion is inherent to the sample and cannot be fixed. Heating of the sample, such as annealing or a run through the DMA, can also distort the spectrum or make the spectrum disappear. In this case, sometimes the sample spectrum returns with time.

- A. Check the sample. A rough sample surface can scatter the laser beam and make laser collection difficult. Focusing deeper into a sample with a rough surface can sometimes improve the spectrum; although, a smooth surface sample is best.
- B. Check the substrate. Using glass as a sample holder can drastically increase the amount of fluorescence and should be avoided. Quartz can be a good substrate, depending on the grade. Most often, Jessop lab uses aluminum Q-panels or DSC pans when using the microscope and quartz capillary tubes or cuvettes when using the probehead. Pure metals are Raman inactive and make excellent substrates; however, oxidized metals are Raman active. All other substrates should be tested before being used for Raman experiments.

C. If using the probehead in conjunction with the UV light, check the orientation of the light. The light must be completely orthogonal to the Raman laser. If the light is even slightly angled into the laser, it will be collected with the Raman scattering and will distort the Raman spectrum. After inserting the tip of the light guide securely in the sample holder, adjust the light guide fiber so that it arches toward the bulk of the probehead. This will ensure that even if the light is slightly angled, it is angled away from the laser.

D. Check the laser power. If the power is too low, bonds that scatter weakly may not appear. If the laser power is low, refer to Problem 1. If the laser power cannot be improved, lengthening the exposure time or increasing the number of accumulations might be beneficial.

E. Make sure the filter and calibration settings are correct. Below the spectrum window, the box next to Cosmic Ray Filter should be checked. To the right of the spectrum window, the boxes next to Dark Subtract and Intensity Calibration should also be checked.

F. Check the dark spectrum. See [Procedure Rho](#).

G. Recalibrate the instrument.

H. Use the default sample, a silicon wafer, to see if it has a spectrum. Silicon should have one prominent peak at approximately 520 cm^{-1} . If the silicon spectrum appears correctly, the problem is most likely with your sample.

I. Clean the objective. See [Procedure Eta](#).

J. Check to make sure the spectrometer is working correctly. See [Procedure Omicron](#).

4. Wavelength and/or intensity calibration fails because light intensity is too low.

A. If using the microscope, make sure the front dial is set to channel 2 and the microscope shutter is open (upper right-hand side). The laser shutter should be closed.

B. Check to make sure the calibration accessory tightly cups the end of the objective. This is usually more problematic with the microscope.

C. Reconnect the collection fiber.

5. Wavelength calibration fails because not all wavelengths were detected.

A. Check to make sure the calibration accessory tightly cups the end of the objective. This is usually more problematic with the microscope.

B. Check to make sure the spectrometer is working correctly. See [Procedure Omicron](#).

6. The microscope light (white light) does not turn on.

- This is often accompanied by a buzzing or humming sound when the light switch is flipped to the on position.

A. Check the black toggle switch on the right-hand side of the microscope to make sure it hasn't been bumped. This switch changes whether power is directed to the upper light box or the lower light box (currently removed).

B. Check the brightness level. Brightness is controlled by the lowest, horizontal, black wheel on the left side of the base of the microscope. If the brightness wheel is rotated completely to one end, it is possible for there to be no light.

C. Change the light bulb. See [Procedure Nu](#).

D. Check/replace the wiring of the light house box. See [Procedure Tau](#).

7. The microscope light (white light) is dim.

A. Repeat the troubleshooting steps of Problem 6, beginning with Step B.

8. The sample cannot be focused on the microscope.

A. Clean the microscope objective. See [Procedure Eta](#).

B. Adjust the Z-range of the stage. See [Procedure Lambda](#).

9. The microscope stage does not move in the Z-direction when commanded by the computer.

A. Remove the motor from the right-hand side course adjust and ensure the motor turns freely. See [Procedure Upsilon](#).

B. Check the stage programming. See 8.4 Appendix D of the ProScan, Prior Scientific, Microscope Automation System Operating Instructions to set up a hyper terminal to access the programming.

10. The microscope stage does not move with a consistent step size.

- *i.e.*, the stage is initially at $z = 0$, a move to $z = -1000$ is entered into the computer, then the stage is asked to return to $z = 0$; however, upon returning to $z = 0$, the visual focus is not the same as the original $z = 0$, thus the stage has not returned to the same location.

A. Recalibrate the stage. See Appendix B.3 (page 52) of the Kaiser Raman Microprobe Operations Manual.

B. Remove the motor from the right-hand side course adjust and check to see if the motor accurately follows the computer commands. See Procedure Upsilon.

C. Check the stage programming. See 8.4 Appendix D of the ProScan, Prior Scientific, Microscope Automation System Operating Instructions to set up a hyper terminal to access the programming.

11. The microscope stage does not move when commanded by the joystick.

A. Check to make sure the connection to stage is tight.

B. Check the joystick programming. See 8.4 Appendix D of the ProScan, Prior Scientific, Microscope Automation System Operating Instructions to set up a hyper terminal to access the programming. If the joystick moves the stage in the X and Y directions, but the buttons do not cause the Z-motor to engage, then the buttons need to be reprogrammed.

12. The laser beam diameter is large.

A. Optimize the Raman microscope. See Procedure Sigma. *DO NOT ATTEMPT WITHOUT APPROVAL* The microscope was optimized by Kaiser in Fall 2013.

13. The laser beam is not circular.

A. Optimize the Raman microscope. See Procedure Sigma. *DO NOT ATTEMPT WITHOUT APPROVAL* The microscope was optimized by Kaiser in Fall 2013.

E.3 Procedures

Procedure Alpha: Knife-Edge Test

Purpose: This procedure provides information about the laser diameter and the laser spot shape. A large laser diameter or non-circular shape can decrease resolution when attempting confocal line or depth scans; therefore, it is important to establish the status of the laser spot before using the Raman microscope in confocal mode.

Items Needed:

- * Laser safety glasses
- * Laser power meter
- * Tin foil
- * Lab tab

A. Turn on the Raman laser, microscope, and *Micro* software as for regular use. Let it warm up.

B. Make sure the power meter head is attached to a glass microscope slide (Figure E-1). If not, attach the head using double-sided tape.



Figure E-1. The power meter head is attached to a glass microscope slide by double-sided tape so that it can be secured to the microscope stage using the spring-loaded stage clip.

C. Take a piece of tin foil and use it to cover approximately half of the receiving window on the measuring head of the power meter (Figure E-2). Mold the foil so that it lays flat in the receiving window. Use the lab tape to secure the foil, taking care to not place any tape on the receiving window.



Figure E-2. Power meter head partially covered with tin foil in preparation for the knife-edge test.

D. Place the power meter head on the microscope stage and secure the attached glass slide using the spring-loaded stage clip.

E. Set the microscope to channel 1 (white light), engage the 10x objective, and select the Video On button in the software. Use the video image to visually focus on the tin-foil-covered half of the power meter receiving window.

F. Use the joystick to position the focus point near the edge of the tin foil.

G. Turn on the power meter using the sliding switch on the left-hand side.

H. Put on laser safety glasses.

I. Set the microscope to channel 2 (laser) and open the laser shutter. Check that the power meter still reads 0 mW. If the power is greater than 0 mW, use the joystick to reposition the focus point farther away from the edge of the tin foil.

J. In the Video On window, use the Set Zero button to set the current location of the stage to 0,0,0 (Figure E-3).

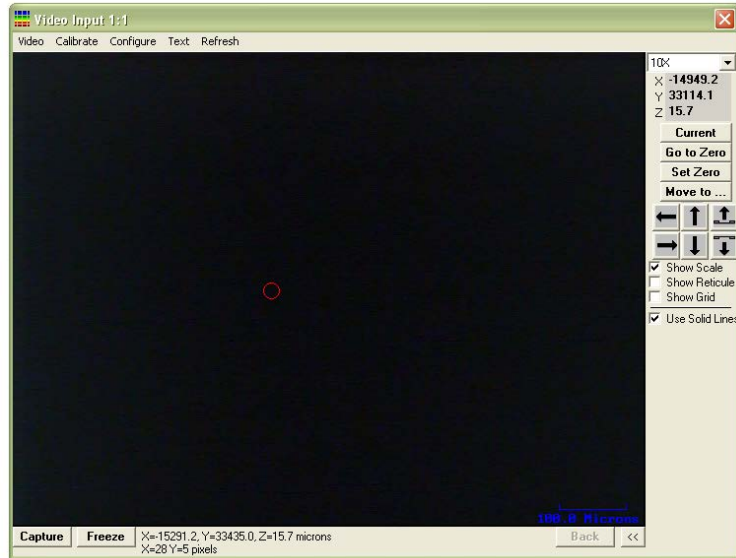


Figure E-3. Screen shot of the Video On window.

K. In the Video On window, type in a value in the X-axis box to move the stage. Moving the stage in 1 micron increments is optimal, however, 10 micron increments are also acceptable. Typing a positive value will move the stage right, and typing in a negative value will move the stage left. Move the stage so that the laser focus point moves toward the edge of the tin foil and closer to the uncovered power meter receiving window. If the set-up is identical to that shown in Figures E-1 and E-2, use a positive step to move the stage to the right.

L. Record the stage location and power meter value.

M. Repeat steps K and L until the laser power value has reached a maximum and remains constant for at least five additional stage movements. At this point, the laser focus point should be entirely on the uncovered portion of the power meter receiving window.

O. Shutter the laser and adjust the tin foil covering the power meter receiving window so that the foil edge is now 90° from the previous position.

P. Repeat steps D through M, this time moving the stage along the Y-axis.

Q. Graph data in Excel. The laser diameter is the difference in position as the laser power increases. In Figure E-4, the laser diameter is approximately $100\ \mu\text{m}$. If the shape of X-axis data matches that of the Y-axis data, the laser spot is circular. The data in Figure E-4 shows the laser spot is almost circular, but the diameter of the X-axis is about $30\ \mu\text{m}$ longer than that of the Y-axis.

R. Shut off the Raman.

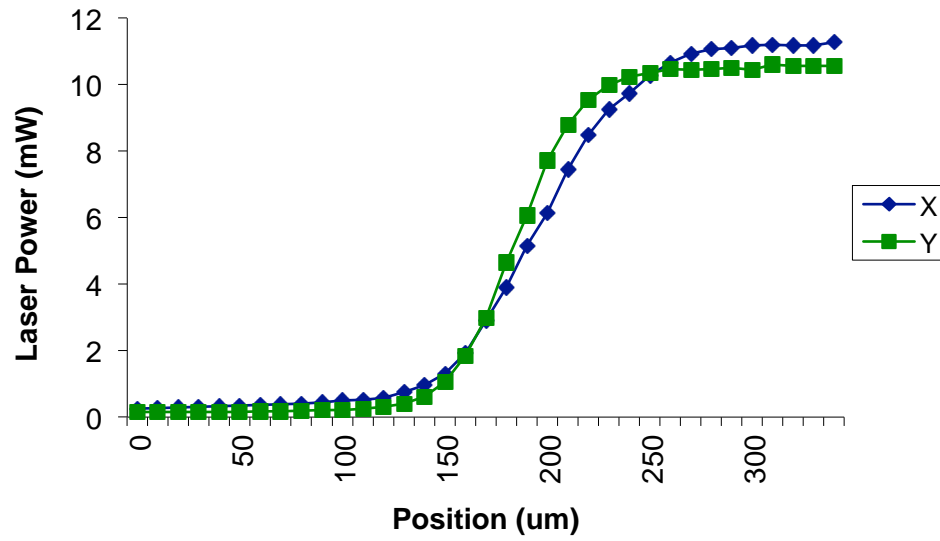


Figure E-4. Example of data from a knife-edge test. Data was collected in December 2013.

Procedure Beta: Changing the Laser Source Power

Purpose: This procedure is useful for reducing laser power to the sample, either through the probehead or microscope, to prevent sample burning or vaporization. Also, this procedure is necessary to safely view the laser without laser goggles or the laser spot as it appears on the microscope camera. Viewing the laser at full power is harmful to one's eyes and should never be done; however, sometimes it is necessary, especially when troubleshooting a problem, to visualize the laser. It is safe to view the laser if the power is that of a laser pointer, approximately 3 to 5 mW. Similarly, after the removal of the video attenuator (Oct. 2013), it is harmful to the camera to view the laser at full power. After reducing the laser source power, it is possible to view the laser spot size and shape on the microscope video tab.

A. Turn on the Raman laser and microscope/probehead as for regular use. Let it warm up.

B. Locate the set of four buttons on the top of the laser box. The top button, labeled with a curved arrow in a circle, will be referred to as TB. The bottom button, labeled with a file, will be referred to as BB. The POWER OUT screen, as seen in the picture below, is the default screen.

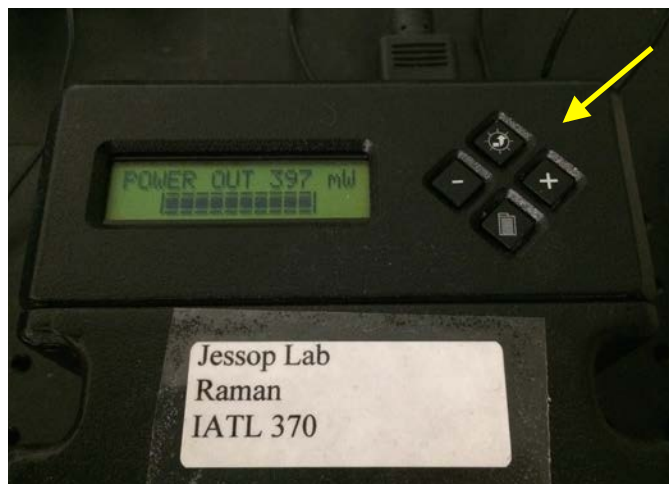


Figure E-5. Top of the laser box. The yellow arrow indicates the four buttons that control the read-out on the screen.

C. Press the BB twice. After the first press, the screen will read POWER SET. After the second press, the screen will read SETTING.

D. Once the screen reads SETTING, the – and + buttons can be used to lower and raise the source power. Maximum power is ~397 mW and can be reduced to 0 mW. This is the source power and will not be the power level measured of the laser coming out of the laser box coupling or the laser power out of the probehead or microscope objective. However, reducing the laser source power will obviously reduce the laser power in these areas.

E. Once the laser source power is at the desired level, press the TB twice. The screen should now read POWER OUT.

F. Repeat the instructions to reset the laser source power to the maximum power. The power level should always be reset to the maximum level at the end of use to be respectful to the next user. Turning off the laser does not reset the laser source power.

G. Turn off the Raman.

Procedure Gamma: Determining Fiber/Objective Resolution

Purpose: This procedure is used to determine the resolution of a confocal collection fiber/objective pair for line or depth scans.

Items Needed:

* Silicon test sample

- A.** Turn on the Raman laser, microscope, and *Micro* software as for regular use. Let it warm up.
- B.** Switch the 100- μm collection fiber to a confocal collection fiber ($\leq 20 \mu\text{m}$).
- C.** Engage the microscope objective that is to be tested.
- D.** Set the microscope to channel 1 (white light), set the silicon sample on the microscope stage, and select the Video On button in the software. Use the video image to visually focus on the silicon
- E.** Click the Set Zero button to set the location of the stage to 0,0,0. Then lower the stage until the focus is approximately 10 μm above the silicon sample (0,0, -10).
- F.** Set the microscope to channel 2 (laser), open the laser shutter, and collect a spectrum. The intensity of the silicon peak (525 cm^{-1}) should be near zero. If not, lower the stage height and try again.
- G.** Raise the stage 1 μm and collect another spectrum.
- H.** Repeat step G until the intensity of the silicon peak has maximized, then dropped back down to near zero.
- I.** Graph the data and locate the full width at half the maximum (FWHM, Figure E-6). The FWHM is the resolution of the fiber/objective pair.
- J.** Turn off the Raman.

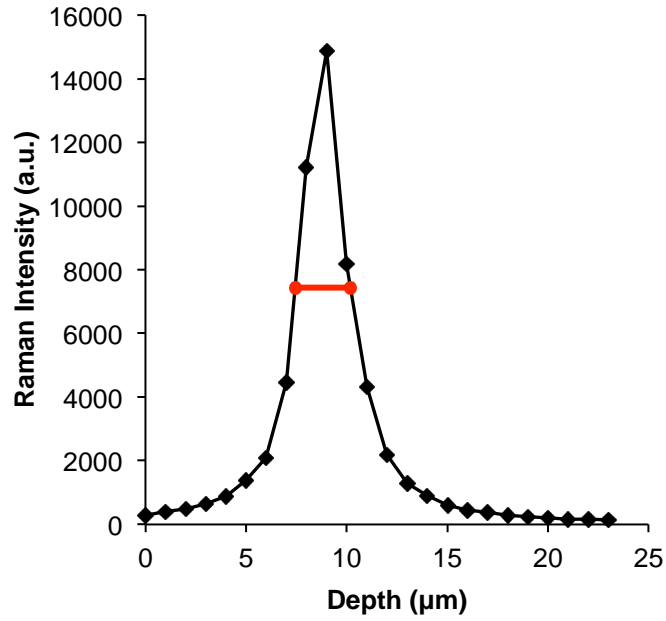


Figure E-6. Depth profile of a silicon sample. Data was collected using a 10- μm fiber, 100x objective, 5-second exposure and 2 accumulations (Nov. 2013). The depth resolution of the fiber/objective pair was taken as the FWHM and found to be 2.75 μm .

Procedure Delta: Determining Laser Beam Shape

Purpose: This procedure provides both visual and quantitative information about the laser spot shape. A laser with a non-circular shape can decrease resolution when attempting confocal line or depth scans; therefore, it is important to establish the status of the laser spot before using the Raman microscope in confocal mode. Also, a non-circular shaped laser spot occurs when the microscope optics are not fully optimized.

- A.** Turn on the Raman laser, microscope, and *Micro* software as for regular use. Let it warm up.
- B.** Use Procedure Beta to reduce the source power of the laser. The laser power should be reduced until it is less than 10 mW. This step is required to protect the microscope camera.
- C.** Set the microscope to channel 2 (laser), engage the 10x objective, and select the Video On button in the software.
- D.** Open the laser shutter. A white spot should appear on the screen (Figure E-7). This is the laser spot. If the spot is too faint to see the shape of the laser, the source power of the laser can be increased in small increments until the spot is more visible; however, too much laser power can harm the camera so use as little laser power as required and do not leave the camera on for long periods of time with the laser shutter open. If more than one 'laser spot' appears on the screen, the second spot might be a reflection of the white light. Try turning off the microscope white light using the orange switch on the left-hand side.

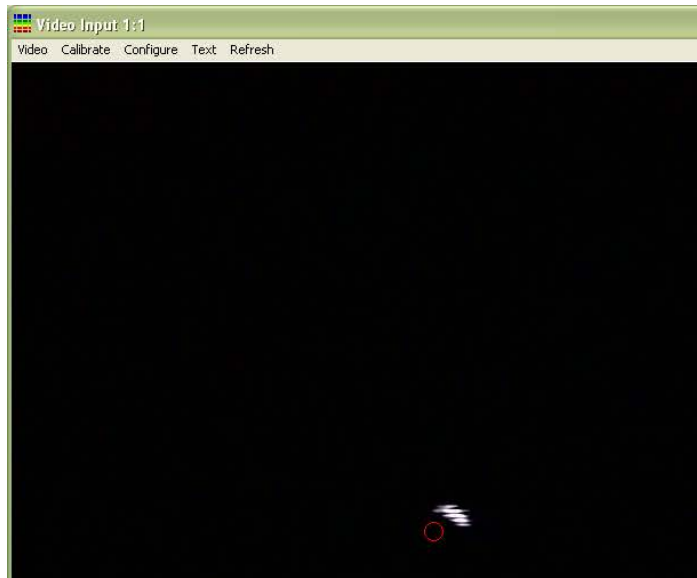


Figure E-7. An example of a non-circular laser spot. The red circle indicates where the computer thinks the laser spot is located.

E. Follow Procedure Alpha (Knife-Edge Test) for quantitative information.

F. Turn off the Raman.

Procedure Epsilon: Viewing the Laser Status

Purpose: This procedure is useful for viewing various laser status settings, such as the number of hours the laser has been used. This information can be useful in troubleshooting the health of the laser.

A. Turn on the Raman laser and microscope/probehead as for regular use. Let it warm up.

B. Locate the set of four buttons on the top of the laser box (Figure E-8). The top button, labeled with a curved arrow in a circle, will be referred to as TB. The bottom button, labeled with a file, will be referred to as BB. The POWER OUT screen, as seen in the picture below, is the default screen.

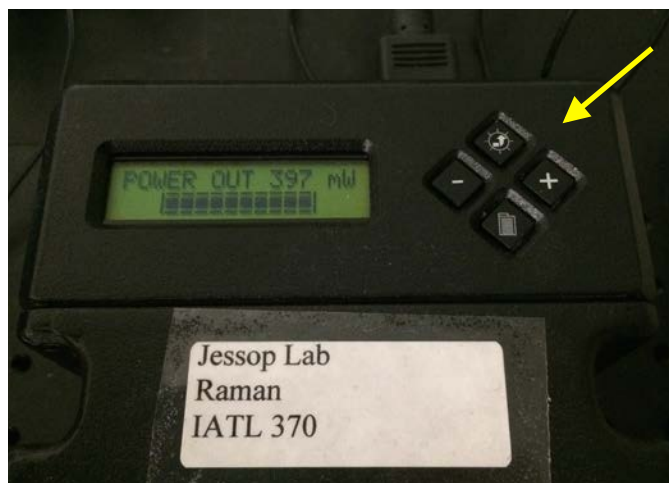


Figure E-8. Top of the laser box. The yellow arrow indicates the four buttons that control the read-out on the screen.

C. Press the BB once. The screen will read POWER SET.

D. Use the + button to scroll through the menu to Status Displays. The menu consists of the following:

- POWER SET
- Interlock ON, AUTO Restart
- Status Displays
- Units C
- Contrast Control

E. Once the screen reads Status Displays, press the BB.

F. Use the + button to scroll through the laser information. For example, at the time this was written, the laser information consisted of the following values:

- Diode 1.26A 1.82V
1.3A Limit

- TEC 0.7 A1.0V
19.0C 19.4 Set

- Diode Sink Box
19.0C 26.0 24.7

- Diode ON time
8475.3 hrs

G. To return to the default home screen (POWER SET), press the TB twice.

H. Turn off the Raman.

Procedure Zeta: Checking Optical Fibers

Purpose: This procedure is done to determine if a collection fiber is damaged.

A. Remove the fiber from its connections.

B. Inspect both ends of the fiber for cracks or chips. If a fiber end is damaged, the light is not being properly directed through the fiber and the fiber will not work.

C. Hold one end of the fiber to a white light (the table lamp or white light of the calibration box work well). Observe the opposite end of the fiber to see if the white light is transmitted. If there is a crack in the body of the fiber, the light will not be visible. If the light is visible, this indicates that the fiber is not damaged.

D. If checking a confocal fiber ($\leq 20 \mu\text{m}$), the end of the fiber must be magnified in order to observe the transmitted light. Remove the 10x objective from the microscope and hold the sampling end of the objective to the end of the fiber. If the light is properly transmitted through the fiber, it should now be visible by looking through the object.

Procedure Eta: Microscope Objective Cleaning

Purpose: Microscope objectives should be cleaned when they are knowingly contaminated through contact with a sample and periodically to ensure the collected Raman spectrum is purely a result of the intended sample and not a combination of the intended sample and whatever chemical is adhered to the objective.

Items Needed:

- * Isopropanol
- * Lens paper and/or cotton swabs

- A.** Remove the objective from the microscope by turning it counterclockwise.
- B.** Wet the lens paper or cotton swab with isopropanol.
- C.** Gently wipe. Use a new section of lens paper or new cotton swab for each wipe. Repeated use of the same lens paper/cotton swab may recontaminate the lens, or, worse, scratch the lens by pushing around a dirt particle, etc. The lens may also be soaked for a few moments in isopropanol to loosen especially stubborn material.
- D.** Dry the lens by wiping it with a dry piece of lens paper or cotton swab.
- E.** If the objective is left off of the microscope for any period of time, be sure to set the objective lens side up to prevent scratches and to prevent the inner well of the objective from collecting dust.
- F.** Replace the objective by screwing it into the microscope clockwise.

Procedure Theta: Microscope Objective Alignment

Purpose: After performing this procedure, the visual and laser focus will be at the same point in a sample for all of the objectives. This procedure is particularly useful for confocal work if a depth or line scan must begin at specific location on the sample, since the sample is usually first focused with the 10x objective, then switched to the 100x objective.

Items Needed:

- * 1.5 mm Allen wrench
- * Sample with distinctive features or multiple markers and a glass microscope slide

- Turn on the Raman microscope as for regular use.
- In the *Micro* software, select Video On.
- Make sure the red circle, indicating the laser location, is visible in the window (Figure E-9). If the red circle is not visible, click on Configure, then select Show Laser Marker.

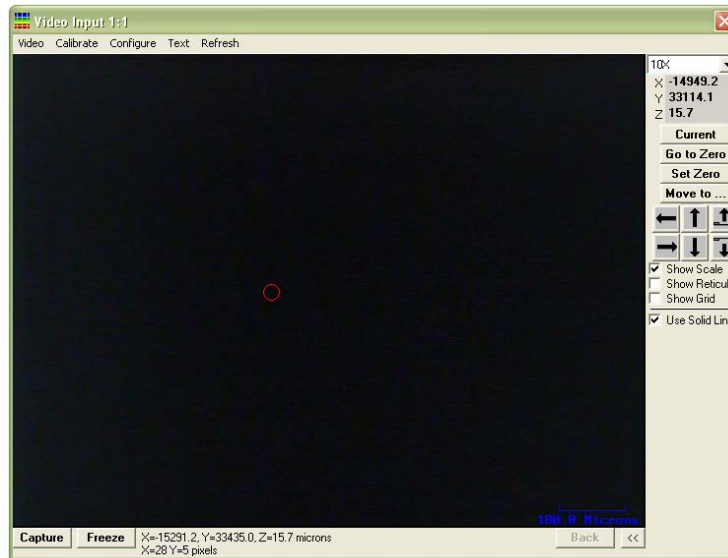


Figure E-9. Screen shot of the Video On window. Note the red circle in the middle of the window, which indicates the location of the laser.

D. Place a sample with distinctive features on the microscope stage. Make sure these features are still distinctive under 100x magnification. Alternatively, a sample can be manufactured by drawing a dot on a microscope slide with a permanent marker. Frame the dot by drawing a box in a different color; the corners of the box make it easier to distinguish a specific area of the dot. As many colors look very similar under magnification, a silver or gold Sharpie may be helpful.

E. Starting with the 10x objective, focus on the sample. Then move the stage so that a distinct feature – for example, the edge of the dot framed on the left and bottom by the edge of the box of a second color – is centered in the red circle in the Video On window.

F. Switch to the next objective and focus on the sample. Locate the distinct feature. If the distinct feature is not in the red circle on the Video On window, use the Allen wrench to manipulate the screws on either side of the objective until the distinct feature is in the red circle (Figure E-10).

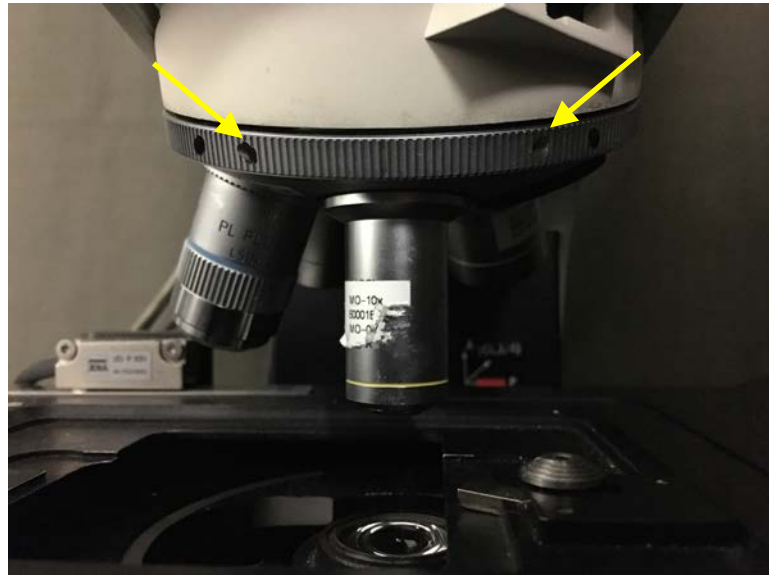


Figure E-10. The alignment of each objective is controlled by two screws located on either side of the objective (yellow arrows).

G. Repeat Step F for all objectives.

H. Turn off the Raman.

Procedure Iota: Setting Up for Confocal Measurements

Purpose: This procedure is useful for collecting Raman measurements in discreet areas/volumes of a sample instead of the bulk sample. For example, confocal measurements can be used to determine how oxygen inhibition affects conversion through the depth of a sample. Confocal measurements can be collected as a line scan at set sample depth or in a depth profile.

Items Needed:

* Confocal collection fiber ($\leq 20 \mu\text{m}$ diameter)

- A.** Turn on the Raman laser and microscope as for regular use. Let it warm up.
- B.** Calibrate the Raman, if necessary.
- C.** Making sure the laser is shuttered, remove the $100 \mu\text{m}$ collection fiber (normal collection fiber for bulk Raman measurements) and replace it with the confocal collection fiber of choice. Confocal fibers with larger diameters will have a larger collection volume (see Procedure Gamma) but will reduce the exposure time needed for adequate Raman intensity. Note, confocal fibers are directional; the silver-tipped end must be attached to the microscope. Reversing the direction of the confocal fiber could irreparably damage it.
- D.** Focus slightly above the sample using the 10x objective, then switch to the 100x objective for collection.
- E.** In the Acquire tab of the *Micro* software, select the exposure time and number of accumulations.
- F.** Automation of a depth or line scan can be done by using the Stage/Mapping tab in the software; however, currently (Summer 2016) the Z-axis movement of the stage is not reliable enough for automation of a depth scan. The X- and Y-axes are controlled by a different motor and should be ok for automation. If an automated scan is used, the user must hit the Acquire button in the Stage/Mapping tab to start the procedure.
- G.** If forgoing automation, the stage can be moved between measurements using the fine adjust. Shutter the laser and open the Video On window. Note the location of the Z axis. Use the fine adjust to move the stage, then move the mouse over the Video On window. This will refresh the Z axis location. Repeat until the stage is at the correct height for the next measurement.
- H.** Shut off the Raman and replace the confocal collection fiber with the $100 \mu\text{m}$ collection fiber.

Procedure Kappa: Switching to the Cuvette Sample Holder

Purpose: Using the cuvette sample holder instead of the normal capillary tube sample holder allows for a larger sampling volume while gathering measurements with the probehead.

Items Needed:

*3/16 inch Allen wrench

*Cuvette sample holder

A. Locate the cuvette sample holder (Figure E-11).

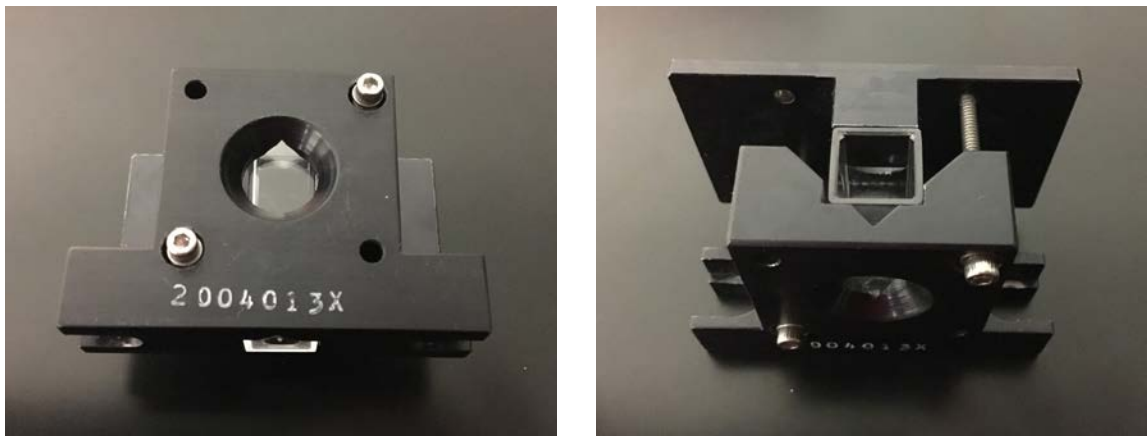


Figure E- 11. Cuvette sample holder.

B. Remove the two screws holding the capillary tube sample holder to the breadboard (Figure E-12). Note the location of the screws on the breadboard so the cuvette sample holder can be put in the same location.

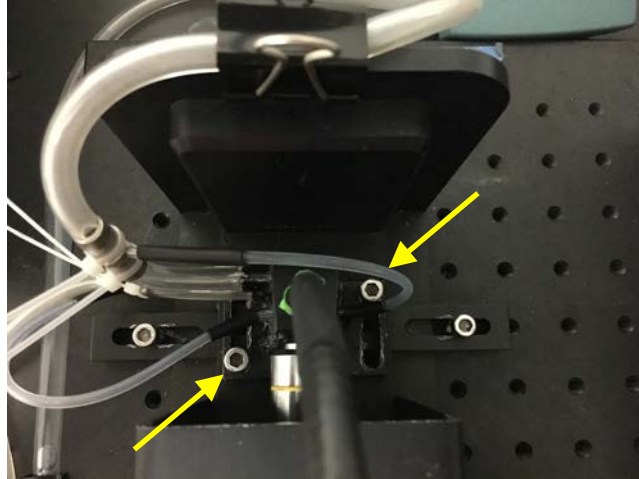


Figure E-12. Bird's eye view of the capillary tube sample holder. The screws marked with yellow arrows are removed to switch sample holders.

C. Make sure any hoses are only connected to the capillary tube sample holder before moving it off to the side.

D. Screw the cuvette sample holder to the breadboard, aligning the location of the left screw with the location of where the left (forward) screw of the capillary tube sample holder was.

Procedure Lambda: Adjusting the Z-Range of the Microscope Stage

Purpose: For particularly thick samples, the Z-range may need to be adjusted in order to properly focus on the sample.

A. Empty the stage.

B. Locate the lever on the right side of the microscope (Figure E-13).



Figure E-13. Right side of the Raman microscope. The lever needed to adjust the Z-range of the microscope stage is labeled with a yellow arrow.

C. Cup the bottom of the stage with one hand and brace for the weight of the stage. If the stage isn't caught when it's released, it will slam down on the base of the microscope.

D. Lift the lever and catch the stage. Lift the stage to approximately the height that is needed and lock the stage in at that height by replacing the lever. As with before, the coarse adjust can be used to focus from this new stage height.

Procedure Mu: Optimizing the Laser Box

Purpose: Optimizing the laser box increases the laser power to both the microscope and probehead. Over time, the mirrors inside the laser box drift and need to be realigned. Typical power values for the probehead and microscope are ~220 mW and 10-15 mW, respectively.

Items Needed:

*5/64 inch Allen wrench

*Power meter

A. Turn on the Raman laser and microscope as for regular use. Let it warm up.

B. Place the head of the power meter under the 10x objective on the microscope stage. Position the body of the power meter so that it can be easily read while working on the laser box.

C. Turn on the power meter, set the microscope to channel 2 (laser), and open the shutter on the laser. Note the starting power level.

D. Using the Allen wrench, turn the screw on the laser box labeled X-axis very slightly (Figure E-14). Check to see if the laser power increased. If it did, turn the screw again in the same direction. If not, turn the screw in the other direction. Repeat until the X-axis is optimized. Because there is a slight delay from the adjustment to the power meter reading and because it is very easy to completely unfocus the laser box, it is highly recommended that the user do not simply slowly and continuously turn the screw. Make a small adjustment, then completely stop adjusting the laser box when reading the power meter.



Figure E-14. The Raman laser box. The screws for adjusting the three axes of the internal mirrors are labeled with yellow arrows.

E. Repeat Step D for the Y-axis.

F. After optimizing the Y-axis, optimize the X-axis again. Repeat for both axes until a maximum power value is reached.

G. Repeat Step D for the Z-axis. Often, the Z-axis does not need much optimization. If a large adjustment is needed, repeat adjustment for X- and Y-axes.

H. Once the microscope is optimized, shutter the laser and switch to the probehead attachment. Open the laser, and record the probehead laser power. The optimization performed using the microscope should have also optimized the probehead laser power; however, the same procedure can be repeated using the probehead if the laser power falls below normal.

I. Turn off the Raman and the power meter.

Procedure Nu: Replacing the Microscope Light Bulb

Purpose: This procedure is used when the bulb that produces the microscope white light dies and needs to be replaced.

Items Needed:

* OSRAM microscope bulb 12 V, 100 W, HLX 64625 FCR

- A. Make sure the microscope is turned off. Unplug the microscope.
- B. Remove the lamp house shielding (Figure E-15). It lifts off vertically. There are two screws in the top of the lamp house shielding. These screws should not be engaged. They are stripped and not necessary to attach the shielding. However, if the lamp house shielding is stuck, someone may have tightened them.



Figure E-15. Microscope with (left) and without (right) the lamp house shielding (yellow arrow).

- C. Remove the old light bulb by pulling straight out and away from the lamp socket.
- D. Replace the light bulb. Press in firmly to make sure there is a good connection.
- E. Replace the lamp house shielding and plug in the microscope. Do not turn on the light without replacing the shielding as it is very bright.

Procedure Xi: Collecting Probehead Film or Real-time Film Measurements

Purpose: This procedure is useful when the laser power through the microscope is too weak for adequate Raman intensity of a film or when real-time collection is needed for a film (not including illumination). Additionally, using the probehead instead of the microscope for bulk film measurements can drastically cut down on collection time because of the higher laser power through the probehead. This procedure can also be adapted so that a hot plate, or other similar device, can be used as a substrate.

Items Needed:

- * Ring stand with two clamps
- * Ruler
- * Aluminum Q-panels or other substrate
- * Laser safety glasses

A. Turn on the Raman laser and probehead as for regular use. Let it warm up.

B. Attach both clamps to the ring stand. Use a ring stand with a flat bottom, not the tripod bottom. The flat bottom ring stand is more stable and will provide a nice sample platform.

C. Making sure the laser is shuttered, carefully remove the probehead from its holder and secure it to the ring stand (objective facing downward) using the two clamps (Figure E-16). The upper clamp should stabilize the main body of the probehead, while the second clamp should be placed around the neck of the probehead. Be aware of the position of the probehead fiber optic cable during this move; it should not be taut or bent beyond its normal radius at any point.



Figure E-16. Probehead film or real-time film measurement set-up.

D. Using the ruler, adjust the height of the probehead so that the bottom edge of the yellow line on the objective is ~ 23 mm above the base of the ring stand. This distance is the optimum focal length for the probehead.

E. Place the aluminum Q-panel, or other substrate, beneath the probehead objective. DO NOT place the film directly on the base of the ring stand. Because it is black, the paint on the ring stand will absorb the laser and begin to burn. Make sure a Q-panel, or other substrate, is always present to avoid safety hazards. In addition, stacking Q-panels is an easy way of adjusting the focal length (sample-to-objective distance).

F. The probehead can now be used to collect film or real-time film measurements. Continue with typical probehead set-up, including adjusting the exposure time, accumulations, *etc.*

G. Because the laser is more exposed than normal and $\sim 20x$ more powerful than when in a similar position directed through the microscope, take extra precaution. Wear the laser safety glasses. Avoid wearing reflective jewelry. Do not allow other people behind the curtain who are not also taking similar safety precautions.

Procedure Omicron: Checking the Spectrometer

Purpose: This procedure is used to determine if the spectrometer is in working order.

- A.** Turn on the Raman software, as for regular use.
- B.** Turn on the calibration accessory and set it for a wavelength calibration so that the orange light is turned on.
- C.** If a fiber optic cable is connected to the spectrometer, remove it.
- D.** Hold the end of the calibration accessory to the port on the spectrometer so that the orange light is directed into the port.
- E.** Collect a spectrum. If the spectrometer is in good working order, multiple peaks should appear at distinct wavelengths along the spectrum.
- F.** Turn off the calibration accessory.

Procedure Pi: Finding the Sample Surface

Purpose: This procedure is used to find the surface of a sample for Raman confocal depth measurements using collected data.

- A. Collect a confocal depth profile (Procedure Iota).
- B. Import depth profile data into HoloReact.
- C. Select a stable, non-reactive peak, and then click on Analysis and select Peak Height.
- D. In the left-hand window (Profile), click on Edit, then X Axis Mode, then select By fixed interval. In the window that appears, input the step size in the Interval box. In the Label box, input *Depth*, and in the Units box, input *microns*.
- E. Take the location of the maximum relative intensity as the sample surface. Figure E-17 shows the results of this procedure for a silicon sample. The sample surface is estimated to be 11 μm from the initial stage height.

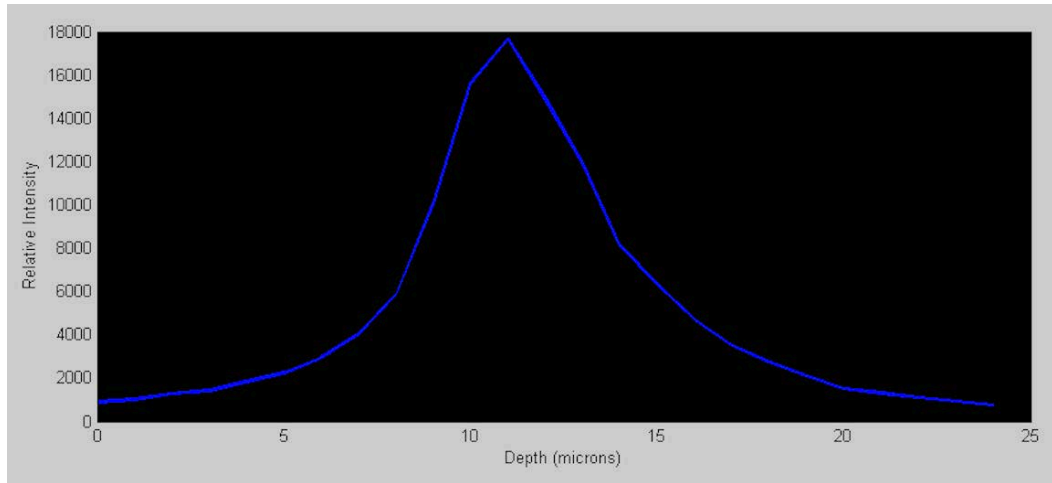


Figure E-17. Graph of the intensity of the silicon peak 525 cm^{-1} vs. depth. The sample surface is estimated to be 11 microns from the initial stage height. All spectra were collected using a confocal 10- μm collection fiber, 100x objective, 5-second exposure, and 2 accumulations. The microscope stage was moved approximately 1 μm between spectra.

Procedure Rho: Checking and Collecting a Dark Spectrum

Purpose: Occasionally, during the automated process of collecting a new dark spectrum, the Raman collects a sample spectrum instead, which makes the processed data look distorted, like a baseline without peaks, or of low Raman intensity. This procedure is helpful in identifying this problem and rectifying it. Also note that the Raman software will collect a new dark spectrum whenever the exposure time or number of accumulations is changed, so this problem can occur whenever these settings are changed.

A. Turn on the Raman laser and probehead/microscope as for regular use. Let it warm up.

B. After collecting an abnormal spectrum, locate the sub-tabs Processed, Raw, Dark, Intensity, and Background in the Acquire tab of the Raman software. Click on the Raw sub-tab. With the exception of some fluorescence distorting the baseline, the spectrum should look correct. If the spectrum does not look correct in the Raw sub-tab, check Step C, but it is not likely the problem is with the dark spectrum.

C. Click on the Dark sub-tab. The spectrum should have either a flat or a sloped baseline, but there should be no peaks. If there are no peaks present in the dark spectrum, it is not likely the problem is with the dark spectrum; however, as this procedure is noninvasive, it can be completed to definitively rule out a problem with the dark spectrum even if it is not likely. If there are peaks present in the dark spectrum, the dark spectrum must be replaced.

D. To manually collect a dark spectrum, first shutter the laser. Then click Acquire Dark in the Acquire tab.

E. Open the laser shutter and acquire a new sample spectrum. The spectrum, viewed in the Process sub-tab, should now look correct. The Raw and Dark sub-tabs can also be viewed to confirm the dark spectrum is adequate.

F. Turn off the Raman.

Procedure Sigma: Optimizing the Raman Microscope

Note: This procedure was directly copied from the *Raman Microprobe Operations Manual 2006988 R2*, pages 44 through 48, A.2 *Optimizing the Probehead, Procedure B*. Figures from the manual were also copied and included. Steps from the original procedure are in boldface font, while my notes are in regular font. Additional steps are labeled using letters to preserve the numbering of the original procedure.

Purpose: This procedure is used to correct a noncircular laser beam and to optimize the beam diameter for better confocal depth resolution.

Tools:

- * Laser safety glasses
- * Phillips head screwdriver
- * 7/64" Allen wrench
- * 5/64" Allen wrench (having both a straight and a L-shaped wrench is helpful)
- * Silicon sample
- * White sheet of paper

***IMPORTANT:** Before this procedure is started, attempt other, non-invasive procedures to solve the problem. This procedure is difficult and should not be attempted unless approval is given by Dr. Jessop. The Raman microscope was optimized by Kaiser in Fall 2013 and should not need further optimization unless moved, violently shaken, *etc.*

A. Turn on the Raman laser and microscope as for regular use. Let it warm up.

B. Make sure the laser shutter is closed.

1. Remove the five exposed Phillips flat machine screws, indicated by fat arrows in Figure A.2, from the probe head lid. (The lid is the side with the AVOID EXPOSURE laser warning label.)



Figure A.2. Probe head lid and fold mirror housing. The fat arrows indicate the five screws to remove to remove the probe head lid. Do not loosen the screws that hold the automatic shutter assembly, indicated by thin arrows.

2. Carefully lift off the lid of the probe head.

3. Remove the six Phillips flat machine screws from the edge of the fold mirror housing (Figure A.3). Red arrows.

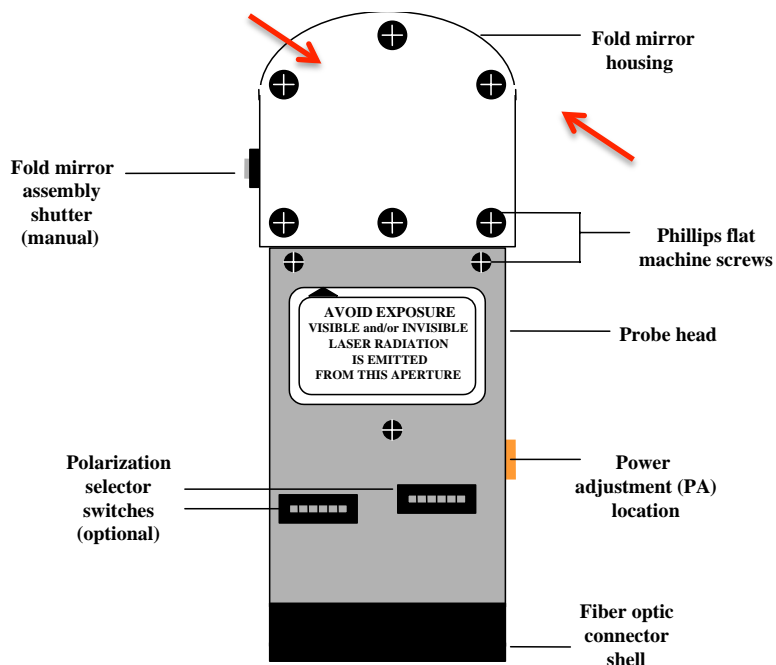


Figure A.3. Top view of the fiber optic probe head and the fold mirror housing.

4. Carefully lift off the lid of the fold mirror housing. Make sure the laser is shuttered

before you remove the lid.

- 5. Place a strong Raman scatterer, such as the silicon sample, in the focal plane of the microscope collection lens.**
- 6. Set the dial on the front of the Leica microscope to 1, reflected light mode (Figure 3.2).**
- 7. Set the reflected light switch on the microscope to illuminate the sample from above. This switch is located on the right foot of the microscope or on the top right side of the optional enclosure.**
- 8. If the microprobe is not already on, turn on the CAMERA and LASER switches on the base unit. Start *HoloGRAMS* and wait 15 minutes for the system to thermally stabilize. *HoloGrams* is labeled as *Micro* on the computer desktop.**
- 9. On the menu bar, click *Video On* to open the Video Input window.**
- 10. Rotate the nosepiece so that the lowest magnification objective is pointing at the sample. Use the 10x objective.**
- 11. While watching the image in the Video Input window, adjust the microscope stage focus so that you see a white light image of the sample on the screen. Focus on the silicon sample, as per usual.**
- 12. Repeat steps 10 and 11 for each of the other objectives. Ignore this step.**
- 13. Set the transmitted light illumination to minimum.** Translation: Set the laser source power to a minimum. To do this, see [Procedure X](#). Power should be set so that it is below 3 mW. At 3 mW, the laser is safe to view and laser goggles are not required.
- 14. Set the dial on the Leica microscope to 2, transmitted light / Raman mode (Figure A.7).** Lay the white sheet of paper on top of the microscope, covering the exposed mirrors. Open the laser shutter. Carefully lift the paper slightly, keeping it horizontal. Check to make sure there is no stray laser hitting the paper. If the paper remains blank, it can be removed and it is safe to view the mirrors with the laser shutter open.
- 15. On the Acquire control panel, click the Focus button to collect Raman spectra in Focus mode. Spectra are collected continuously at the interval that you indicate in Exposure time.** Set the exposure time to 250 ms. Once in Focus mode, you should be able to see a single, distinct peak from the silicon sample. If the intensity is too low, you can raise the laser source power, but laser goggles must be worn.

16. Adjust the probe head at the spatial filter (SF in Figure A.14). Use the 5/64” Allen wrench. The small cylindrical brass holder contains a focusing lens that focuses the laser light onto the spatial filter (slit). Carefully adjust the setscrews indicated by the large arrows in Figure A.14 to translate the laser light across the slit until the Raman intensity is maximized. Before adjusting anything, record the intensity value of the silicon peak and the value of the source power. Ideally, at the end of the optimization, the intensity value (at the same source power) should be larger than this initial value.

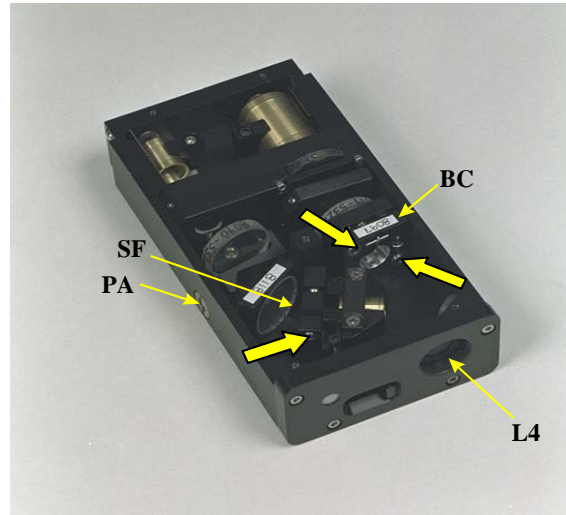


Figure A.14. Probe head optics: power adjustment screw (PA), beam combiner (BC) and slit (spatial filter, SF). Large arrows indicate adjustments for the slit and the beam combiner. In the Raman microprobe, L4 is the entrance to the fold mirror housing.

17. If the laser spot is not visible in the Video Input window, remove the video filter (Appendix D, Section D.3, steps 1–3). The video filter protects the camera. If removed, the laser output power should never be above 10 mW with the camera on. If the source power must be raised for better intensity, the camera should be off. After removing the video filter, the image in the Video Input window might be confusing. The large, bright shape with diffuse edges is not your laser beam. The laser beam will be a tiny spot, usually off to the side (though, it can sit behind this bright spot). If you move the stage up and down, your laser beam will probably change shape and travel a bit, whereas the bright spot generally stays in the same place.

18. If you do not see laser light on the silicon test sample on the translation stage, adjust mirror M3 in the fold mirror housing (Figure A.12) to obtain a laser spot. With the laser spot visible on the Video Input window, move the translation stage up and down (in the Z direction) and observe the shape of the laser spot. The laser spot should change size but not shape. If the spot appears to be changing shape as the stage is being focused and defocused, carefully adjust the two tilt adjustments on the

M3 mirror in the fold mirror housing (Figure A.12). When this has been correctly accomplished, a pattern similar to that in Figure A.13a should be observed whose overall shape should not be changed by repeated defocusing and refocusing of the image. If the other patterns in Figure A.13 are observed, contact Kaiser for assistance. Optimizing M3 is probably the hardest part of this procedure. There are two ways to monitor its adjustment: intensity and the defocused shape of the laser beam. It is best to alternate between these two for best results. Remember to record an initial intensity value before starting adjustments. Using intensity, follow steps 15 and 16. However, there are two screws to optimize on the M3. Optimize the location of the first screw, then optimize the second, and then optimize the first again. The adjustment of one screw affects the location of the second, so alternating between the two screws is necessary. Once an optimum intensity has been reached (record the value!), stop the focus function and turn on the video. If the source power is greater than 10 mW, reduce it to a safe value, then turn the camera back on, then turn on the video. The laser beam should be circular and it should retain that shape as it is focused and defocused; furthermore, it should stay approximately in the same location on the screen as the focus is changed. The other way to monitor the adjustment is to use the defocused shape of the laser beam. In theory, an optimized laser beam should remain circular even if it is defocused. Therefore, make adjustments to optimize M3 in the same manner as before, but now the goal is to make the defocused laser spot circular. Check and see how these adjustments have affected your intensity.



Figure A.12. Location of adjustments for M3 in the fold mirror housing.

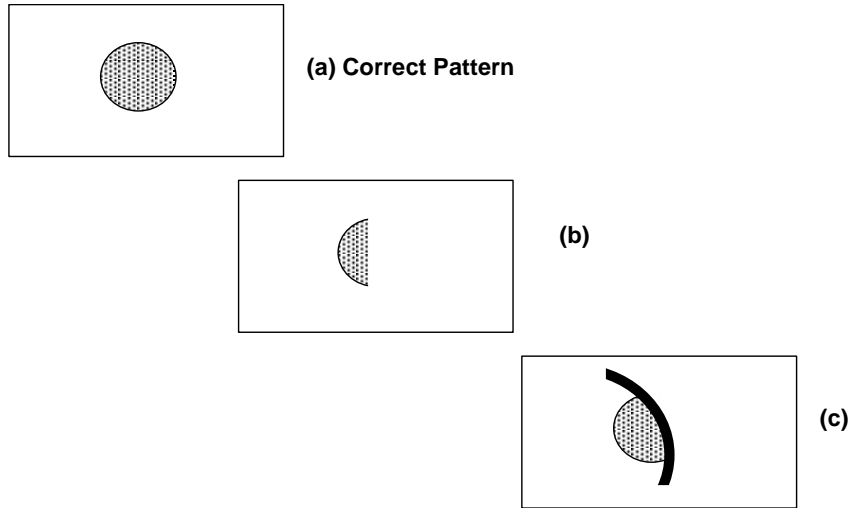


Figure A.13. Possible laser spot patterns observed on a sample on the microscope stage.

19. Use a 5/64" Allen wrench to adjust the vertical and horizontal movement of the beam combiner (Figure A.14) and observe the Raman signal increase or decrease with each adjustment. Continue this process until the Raman intensity (e.g., for silicon, the 520 cm^{-1} band) is maximized. It is necessary to repeat this step because changing the angle of the beam combiner deviates the reflection path of the laser off the beam combiner and thus the laser path with respect to M3. As with the M3 adjustments, toggle back and forth between the two screws for the greatest optimization.

20. Optimize the slit position by following the procedure below. It is assumed at this point that the silicon test sample is mounted on the microscope stage, that the microscope is focused on the sample, and that the dial on the front of the microscope is set to 2, transmitted light/Raman mode. I did not optimize the slit position. Skip to step 21.

On the Acquire control panel, set the exposure time to 1 second and click Focus. *HoloGRAMS* acquires a spectrum continually every second.

Remove the plastic plug in the top of the pre-filter stage light shield. A 1/8" Allen wrench fits through the hole to the brass knob directly underneath (Figure A.15).

Translate lens L3 by rotating the brass knob located near the slit holder. This translation moves the image of the optical fiber diameter across the slit. Adjust this

translation until the number of counts observed from the Raman spectrum of silicon is maximized.

Record the maximum number of counts for later use.

If the number of counts being observed from the silicon test sample is maximized, or if the system is being installed for the first time, proceed to the next step. The objective and the laser power at the sample need to be the same as for the factory-recorded spectrum in order to make a direct comparison. Also note that other changes such as a different camera, grating, slit, or optical fiber will influence the observed intensity from the silicon test sample.

21. If you removed the video filter, replace it (Appendix D, Section D.3, steps 4– 6).

22. Replace the probe head lid and tighten all screws.

23. Replace the fold mirror housing cover and tighten all screws.

24. Using a laser power meter, measure the maximum laser power at the sample for each objective and record this information for future reference. If you do not have a laser power meter, record the maximum number of counts recorded from the sample for future reference. It is recommended that you save the spectra.

25. Close the shutter in the fold mirror housing (Figure 3.3).

26. Remove the silicon test sample from the microscope stage and retain for future use.

27. If you are not going to use the instrument again immediately, turn off the laser and the CCD camera (Figure 3.1).

For optimum performance, recalibrate the instrument using the Raman Calibration Accessory.

Procedure Tau: Checking and/or Replacing the Microscope Lamp House Wiring

Purpose: This procedure is to be performed if the microscope white light is not fixed by replacing the light bulb. Additionally, discoloration of the lamp socket or wires is an indication the lamp socket or wiring made need to be replaced.

Items Needed (for replacement only):

- * Lamp house shielding cable (part # 11301380080000)
- * Fassung GY 6,35 – Lamp socket (part # 11302033070108)
- * Small Phillips head screwdriver
- * 7/64 inch Allen wrench

A. Make sure the microscope is turned off. Unplug the microscope.

B. Remove the lamp house shielding. It lifts off vertically. There are two screws in the top of the lamp house shielding. These screws should not be engaged. They are stripped and not necessary to attach the shielding. However, if the lamp house shielding is stuck, someone may have tightened them.

C. Remove the light bulb.

D. Locate the screw at the base of the lamp house (Figure E.18, yellow arrow) to disconnect it from the microscope using the Allen wrench.

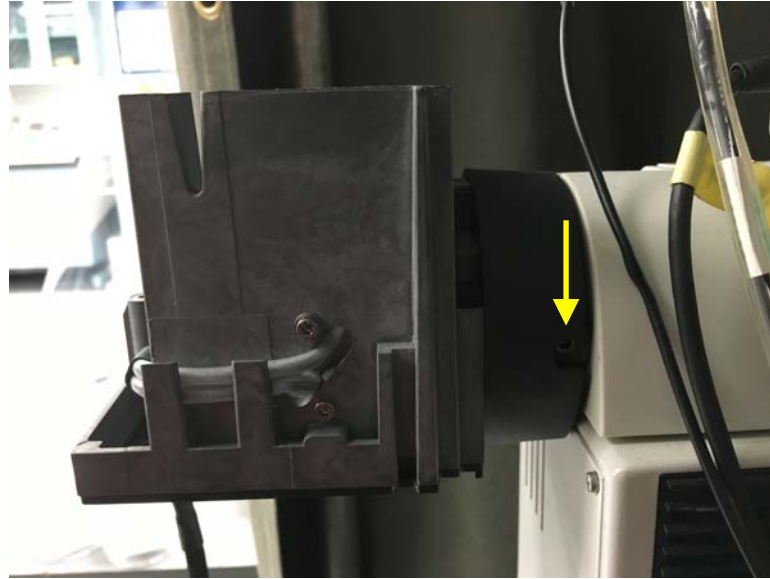


Figure E-18. Side view of lamp house after the shielding has been removed. The yellow arrow indicates the screw that will release the lamp house from the back of the microscope.

E. Use the Allen wrench to remove the two screws on the outside of the lamp house (Figure E.18). This will disconnect the lamp socket from the wall of the lamp house.

F. Use the Phillips screwdriver to remove the two screws in the lamp socket. One screw is visible on the front (Figure E.19, yellow arrow). The other screw is located on the back of the lamp socket. This will disconnect the lamp socket from the wires. Note any discoloration of the lamp socket or the ends of the wires that were connected to the lamp socket. If any discoloration is visible, it is advisable to replace the lamp socket and/or the wiring. If no discoloration is visible, try replacing the wiring first.



Figure E-19. Inside of the lamp house with the shielding removed. The yellow arrow indicates one of the two screws that connects the lamp socket to the wiring.

G. Push the raw ends of the wiring into the lamp socket, making sure the connection is tight. Order does not matter.

H. In reverse order, replace the screws removed in steps D through F.

I. Replace light bulb and lamp house shielding.

Procedure Upsilon: Checking the Microscope Z-axis Motor

Purpose: This procedure is used to check that the z-axis motor on the Raman microscope is rotating freely and accurately.

Items Needed:

* Tape

- A. Turn on the microscope and software as for regular use.
- B. Remove the z-axis motor from the right-hand course adjust by releasing the pressure screw. Only the motor should be released. The cuff that holds the motor on the course adjust should remain.
- C. Either use the buttons on the joystick to move the motor or control the motor by adjusting the z-axis using the Video On window in the *Micro* software. The silver gear in the center of the motor should turn freely. If not, call Kaiser.
- D. To check the accuracy of the motor, attach a piece of tape to the side of the silver gear, aligned with one part of the gear (this part of the gear could also be marked with a permanent marker).
- E. Command the z-axis to move a set distance in the Video On window in the *Micro* software. Note how many turns the gear made during this move.
- F. Now command the z-axis to move the same set distance in reverse (*i.e.* if the z-axis started at 0 and then was commanded to move 100 μm , type in a move of -100 μm). If the motor responded accurately to the computer's commands, the gear should have turned the same number of times as before, and the gear should align with the piece of tape.
- G. Replace the motor by placing it in the cuff on the course adjust and tightening the pressure screw. Make sure the gear on the motor is aligned with the gear inside the cuff, or the motor will not be able to properly move the stage.
- H. Turn off the microscope.